The Supermassive Black Hole at the Centre of our Galaxy

By

Ecaterina Marion Howard

A thesis submitted to Macquarie University

for the degree of

Doctor of Philosophy

Department of Physics and Astronomy

March 2015

Supervisor: Prof. Mark Wardle

Typeset in LaTeX 2_ε.

Except where acknowledged in the customary manner, the material presented in this thesis is, to the best of my knowledge, original and has not been submitted in whole or part for a degree in any university.

Ecaterina Marion Howard

Abstract

Sgr A*, the supermassive black hole at the center of the Galaxy, is variable in radio, sub-millimeter, millimeter, near-IR and X-rays. The flare activity is thought to arise from the innermost regions of the accretion flow, within ten gravitational radii of the black hole.

General relativistic effects play therefore a substantial role in determining the flaring properties of Sgr A*. Our goal is to study the processes responsible for the variable emission from Sgr A*, and to analyse the relativistic signatures in the emission and ultimately test General Relativity by constraining the parameters of the black hole.

We model the variable emission from a compact source within the accretion disk, orbiting in the equatorial plane close to the event horizon, near the marginally stable orbit of a black hole. Based on our developed scenario, we estimate the black hole spin. We take into account all special and general relativistic effects, and search for relativistic signatures in the resulting light curves and find that they may play a significant role in Sgr A* variability.

Motivated by the apparent periodicity in some Sgr A* light curves, and the clear sub-structure, suggestive of lensing and Doppler beaming effects, together with the presence of time lags at radio wavelengths, we develop a general relativistic time-dependent model that aims to understand the variable emission and the black hole properties.

The model incorporates a bubble of synchrotron-emitting electrons orbiting close to the black hole and cooling via synchrotron emission and adiabatic expansion. The model reproduces the observed time delays at radio wavelengths, the shape and structure of the flares, the periodic orbital dynamics and confirms the presence of variability at sub-orbital scales due to lensing and Doppler beaming. We obtain good matches with the observed light curves in NIR/X-Ray and radio. Further analysis of Sgr A* variability at orbital timescales will allow us to test General Relativity and the validity of the Kerr metric.

Contents

1

Introduction

Almost 40 years have elapsed since the discovery of Sgr A* (Balick & Brown 1974), the compact radio, infrared, and X-ray source located at the dynamical center of Milky Way (Eisenhauer et al. 2005). Observations of stellar orbits in the immediate proximity of a mass of $\sim 4 \times 10^6 M_\odot$ within 45 AU of Sgr A* (e.g., Schödel et al. 2003; Ghez et al. 2003) have shown evidence of a super-massive black hole (SMBH) at the center of our Galaxy (Eckart & Genzel 1996, Ghez et al. 1998, 2000, 2003, 2005a, 2008, Eisenhauer 2003, 2005, Gillessen et al. 2009). Recent observations of variability in the radio, near-infrared and X-ray observations have brought significant insight into the relative importance of different emission mechanisms, including synchrotron, synchrotron self-Compton (SSC), and bremsstrahlung (e.g. Baganoff et al. 2001, 2002, 2003, Eckart et al. 2003, 2004, 2006ab, 2008ab, 2009, Porquet et al. 2003, 2008, Genzel et al. 2003, Belanger et al. 2006, Yusef-Zadeh et al. 2006ab, 2007, 2008, 2009, Marrone et al. 2009, Dodds-Eden et al. 2009).

Multi-wavelength observations in sub-millimeter, X-ray and infrared bands provide evidence that the SgrA* luminosity is many orders of magnitudes below the average luminosity of an SMBH in active galactic nuclei(AGN) of a comparable mass. Indeed, Sgr A* is the faintest SMBH so far observed. Fortunately, due to its proximity Sgr A* is still bright enough to be studied in detail. Its luminosity seems to be caused by the accreting thermal winds from the cluster of massive stars in the near vicinity (see Melia, 1992). The question is why Sgr A* is so dim.

Several models attempted to explain this faint emission (e.g., Melia & Falcke 2001; Yuan, Quataert & Narayan 2003; Goldston, Quataert & Tgumenshchev 2005; Liu & Melia 2001; Liu, Melia & Petrosian 2006). Firstly, the ADAF model (Narayan et al. 1998) envisages that the multi-wavelength spectrum as a two-temperature radiatively inefficient flow that is advected across the event horizon before radiating away its initial energy. Radio and sub-millimeter observations (Bower et al. 2003; Marrone et al. 2006) brought more information on the integrated electron density in an accretion area between ~10 to 1000 Schwarzschild radii, much lower than predicted by the ADAF model. Consequently, most of the material captured from stellar winds doesn't reach the event horizon. Alternative models (e.g., Yuan et al. 2003) could provide further explanation but the question whether the accreting material would remain in a convective flow (Narayan et al. 2002), a magnetically-driven low-velocity outflow (Blandford & Begelman 1999, Igumenshchev et al. 2003), or a fast jet (Yuan, Markoff & Falcke 2002) remains unanswered. By analyzing the Sgr A* flare emission, these questions could be eventually answered.

Sgr A* is visible in NIR band when flaring. Most of the NIR flares have an X-ray counterpart as well, suggesting that the underlying radiation mechanism might be synchrotron or synchrotron self-Compton emission. The spectrum of a NIR flare can be fitted with a power-law and a soft spectrum $F_\nu \propto \nu^{-\alpha}$ and $\alpha > 0$ (with F_ν, ν and α the flux density, frequency and spectral index). The spectral index value is still not well measured (Eckart et al. 2004).

Observations of Sgr A* activity have detected hourly variability in radio, millimeter and sub-millimeter wavelength bands. Radio flares were detected with a duration of about two hours, similar to the lifetime of flares observed at sub-mm and millimeter wavelengths (see Maurehan et al. 2005; Yusef-Zadeh et al. 2006a,b).

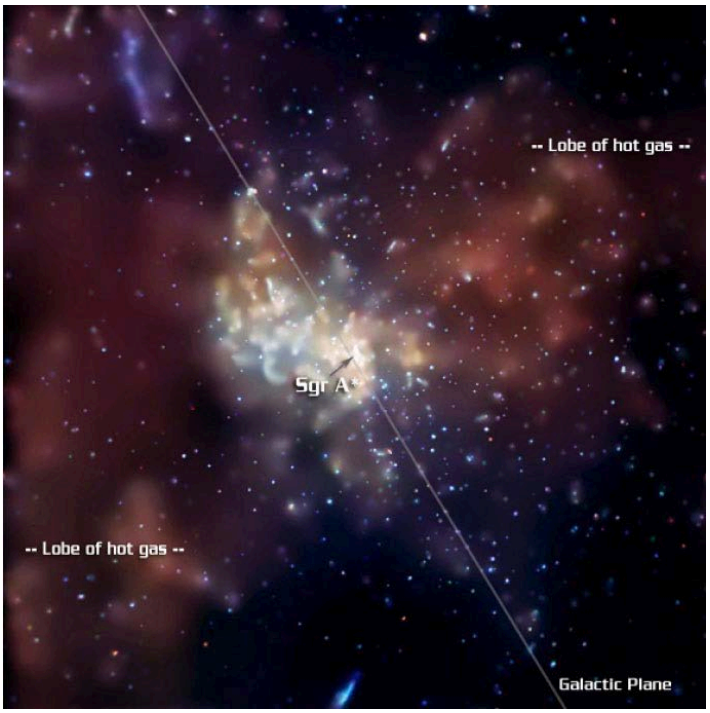

FIGURE 1.1: Chandra image of Sgr A* region, $8.4' x 8.4'$, taken in the energy bands 2.0-3.3 keV (red), 3.3 - 4.7 keV (green) and 4.7 - 8.0 keV (blue). The supermassive black hole is associated with the point source. Credit: NASA, CXC, MIT, F.K.Baganoff et al., 2003

Most observations of Sgr A* (see Figure 1.1) show strong variability, with signs of periodicity, suggesting the presence of spots of emission along with the accretion flow. It is expected indeed that strong inhomogeneities would develop in such an environment, predictions confirmed by recent general-relativistic magnetohydrodynamic simulations (Mosci-brodzka at al., 2009, Dolence et al., 2009). This could be due to particle acceleration at strong shocks or magnetic reconnection events. These mechanisms produce a distribution of compact, non-thermally emitting regions.

The emission coming from the innermost region of Sgr A* has quiescent (i.e. quasi-steady) and variable components. Variability has been detected in almost all wavelength bands and can be helpful for a quantitative analysis of the physical properties of the gas flow, for studying the radiation mechanisms in various wavelength bands and understanding the scale lengths of the variable emission. The flares could be embedded in the accretion disk or could be completely a distinctive feature within the emission region. The quiescent emission

was detected at low energies (radio and submm wavelengths) and the flares in near-IR and X-ray bands. However, the connection between the quiescent flux and the flaring activity, along with the origin of the flares is not yet understood.

A large number of mechanisms have been suggested as the origin of the variability of Sgr A*. The established direction in interpreting the flaring activity of Sgr A* is based on emission for a thin accretion disk, a disk and jet, outflow, an advection-dominated accretion flow, a radiatively inefficient accretion flow. An accretion model is developed and the predicted spectrum is then compared with the spectrum provided by the existing observational data. Various models have been produced to understand the flaring activity of Sgr A*, such as the expanding plasmon model and the orbiting hot spot model.

Most models for the Sgr A* variable emission have mainly focussed on the link between the strong flares in NIR and X-ray (Baganoff et al. 2003, Eckart et al. 2004, 2006; Yusef-Zadeh et al. 2006a; Hornstein et al. 2007), assuming that the IR emission is caused by synchrotron emission from a transient population of near-Gev electrons in a ~10–100 G magnetic field. The X-ray emission would be produced either by synchrotron emission from higher energy accelerated electrons (Yuan et al. 2003) or by the inverse Compton scattering of either the sub-mm emission produced in the surroundings or even directly by the synchrotron-self-Compton transient population (e.g. Yuan et al. 2003, 2004; Liu et al. 2004, 2006a,b). The transient population of accelerated electrons can also be produced via reconnection, acceleration in weak shocks (e.g. Yuan et al. 2003) or heating by plasma waves (Liu et al. 2006a,b) led by instabilities in the accretion flow or dissipation of magnetic turbulence. As the emission regions were proven to be compact, these models can help with understanding of the evolution of the accelerated electron populations in response to heating and radiative mechanisms (Bittner et al. 2007).

We focus on recent time variability observations of Sgr A* and aim to analyze the periodic modulation observed in Sgr A* spectrum. As the material in the accretion disk is very hot, line emission is here excluded and hence continuum emission from synchrotron radiation is only considered for modelling. The dominant radiation from a thin accretion disk is in the form of continuum emission, that provides very limited information about the environment close to the black hole. In this Thesis, we aim to model and analyse relativistic

light curves from a continuum emitting region within a thin disk. The information carried by continuum emission provides us with a significant tool to understand and analyse the inner regions near the black hole.

The periods of enhanced radiation (or flares) last in NIR around 100 minutes and they seem to be accompanied by quasi-periodic oscillations (QPOs) (Genzel et al. 2003, Eckart et al. 2004, 2006a,b, Meyer et al. 2006a,b). The event could be caused by magnetic reconnections, stochastic acceleration of electrons due to MHD waves or Magneto Rotational Instabilities (MRI) within the plasma. The continuum emission is most likely generated within the accretion disk, where the source of variability is present. Several MHD simulations confirmed that variability seems to be a fundamental property of Sgr A* disk emission. (Hawley et al. 2002; Goldston et al. 2005; Chan et al. 2009; Moscibrodzka et al. 2009).

The quasi-steady emission from radio to sub-millimeter bands is most likely synchrotron radiation from electrons from within the accretion disk spanning out radii up to 100 AU or even more from the center black hole (see Yuan et al. 2003), or close to the base of a jet (see Falcke & Markoff 2000). The electron temperature and the magnetic field strength in the accretion flow have been estimated to be $kT_e \sim 10\,\mathrm{MeV}$ and $\sim 30\,\mathrm{G}$, respectively.

Various multi-wavelength Sgr A* observations have also shown evidence that near-IR flare activity is important for understanding the X-ray and sub-mm activity (e.g., Eckart et al. 2004, 2006; Gillessen et al. 2006; Yusef-Zadeh et al. 2006). For example, near-IR synchrotron emission is produced by the transient population of ~GeV electrons in a $\sim 10\,\mathrm{G}$ magnetic field of size $\sim 10R_s$.

A number of theoretical models were introduced in order to explain the origin of the Sgr A* flaring activity as well as the low luminosity of the quiescent emission. These models include ideas like disk-star interactions (Nayakshin et al. 2004), stochastic acceleration of electrons in the inner region of the accretion disk (Liu et al. 2006), non-axisymmetric density perturbations emerging during disk evolution (Chan et al. 2009b), heating of electrons close to the core of a jet (Markoff et al. 2001; Yuan et al. 2002), sudden changes in the accretion rate of the black hole (Liu et al. 2002), trapped oscillatory modes in the inner regions of the disk as spiral patterns or Rossby waves (Tagger & Melia 2006; Falanga et al. 2007; Karas et al. 2008), non-Keplerian orbiting spots falling inward inside the plunging region created

via magnetic reconnection phenomena (Falanga et al. 2008), comet like objects trapped and tidally disrupted by the black hole (Cadez et al. 2006; Kostic et al. 2009). The analysis of the broad band and flaring spectra of the quiescent flux could provide new information on the of Sgr A* flaring activity.

In the past few years, observations of emission from accreting black holes have introduced new possibilities for astrophysical tests of relativistic effects. Observations of AGNs at various frequencies indicate the presence of time variability in the flare emission. The origin of this variation is not yet understood. Recent discoveries provide direct evidence for strong gravitational signatures in supermassive black holes with the prospect of determining the black hole's spin and the nature of the variable emission. The emission from the vicinity of the event horizon contains significant information about the physical parameters of a black hole.

Nowadays, it is widely accepted that supermassive black holes are located in the centres of most of galaxies, and thus have a fundamental influence on galactic formation and evolution. According to the unification model of AGN, they are most likely powered by the accretion of gas onto their central supermassive black holes with mass ranging from 10^5 to 10^9 $M_\odot$.

A large fraction of the accretion energy in luminous black holes is dissipated in the innermost regions of the accretion flow. Most of the power is radiated from close to the smallest accretion disc radii in the relativistic region close to the black hole event horizon (Shakura and Sunyaev 1973; Pringle 1981). Relativistic effects then affect the appearance of the spectrum from the black hole disc through Doppler, aberration, gravitational redshift and light bending effects (Page and Thorne 1974; Cunningham 1975, 1976). The dominant features in the emission spectrum seen by a distant observer, carrying unique information on the structure, geometry, and dynamics of the accretion flow in the immediate vicinity of the central black hole, provide a good tool to investigate the nature of the spacetime around the central object (Fabian et al. 1989; Laor 1991).

Emitting flaring material within the accretion disk around a black hole is orbiting at high velocities, close to the speed of light, in strong gravitational potential. The emission from such flares is distorted by Doppler shifts, length contraction, time dilation, gravitational

redshift and light bending. For a flare within the disk of the black hole, strong relativistic effects affect every aspect of the radiation coming from the source, including its spectrum, light-curve and image. A distant observer located at infinity will detect a time dependent light curve to which all parts of the orbiting blob contribute. These flux contributions will depend on the local emissivity but also on the relativistic effects and on the Doppler shift acting at any given position. The integration method used in the code takes into account the energy shift of the photons along the geodesics, the arrival timelags, and the lensing effect.

The combined impact of all these special and general relativistic effects was first calculated in the now seminal paper of Cunningham (1975), where he used a single transfer function to describe the relativistic effects. Even if such a flare is only a transient feature within the disk, it may last sufficiently long to produce observable effects. A flare is expected to arise naturally in accretion discs and to persist there for times longer than the orbital period of the flow particles.

The Thesis concentrates only on time dependent information that can be extracted from light curves. We model relativistic light curves by using ray tracing techniques in Kerr metric. Due to the asymptotical flatness of Kerr spacetime, the relativistic effects are ubiquitous and their onset could be tested observationally with sufficient spectral resolution. The direction of rotation of the black hole (and thus the direction of rotation of the flare) is arbitrarily chosen to be counter-clockwise. Comparison between observational data and our simulated light curves can't be done without taking into account the relativistic effects that influence the trajectories of the photons.

The resulting time dependent light curve can serve for diagnostics and to constrain essential parameters of the accreting black hole system. The emitting region is assumed to be either a synchrotron emitting hot spot or an expanding plasmon, both in stationary Keplerian rotation. Most of the action occurs within a very small region, within a few tens of gravitational radii from the center. In these inner regions, the relativistic effects leave their mark on the emitted radiation. We aim to provide a better insight into a number of theoretical crucial problems: (1) understand the Sgr A* flare variability at various timescales (2) understand how strong gravity affects the emission from the inner accreting regions (3) disentangle the intrinsic flaring emission from the relativistic effects and (4) determine whether the black

hole is spinning and estimate its spin parameter

Chapter 2 focuses on rotating black holes generic properties and Kerr spacetime in general, in order to later understand the relativistic behaviour of emitted light from the disk. Chapter 3 presents a description of the numerical subroutines and techniques, the geodesic ray-tracing code and the parameters used in the code. Chapter 4 investigates in detail how the relativistic effects will distort the light curves and what the observer will see from different viewing angles, at different orbital radii and for different spins of the black hole. All special and general relativistic effects are taken into consideration in order to isolate each particular imprint onto the light curves. We focus on the time-dependent information that can be extracted from light curves for a continuum emitting spot within a thin accretion disk. The profile of the light curve is caused by the interplay of gravitational lensing, Doppler and transverse Doppler shifts, relativistic beaming and gravitational redshifting. Chapter 5 studies Sgr A* flaring activity and the timescales involved in the observed variability. The study of Sgr A* flares carry direct evidence of the strong gravity physics close to a massive black hole. While the physical origin of these flares is still unknown, we attempt to search for relativistic signatures within the overall characteristics of the light curve. Our primary goal is to isolate each special and general relativistic effect studies in a previous chapter and separate them from the flux modulations caused by the intrinsic flaring, interpreted as particle injection, magnetic fluctuations, synchrotron cooling and adiabatic cooling, at various timescales. We are not concerned with resolved images of the emitting region. All necessary information is extracted from unresolved light curves of unpolarised light, continuous synchrotron emission of a hot spot or an adiabatically expanding blob, when time lags are present.

Despite uncertainties, as long as the emission region is compact, robust predictions for the spin and inclination of the black hole can be made, using relativistic ray-tracing methods, allowing us to provide estimates on the properties, the viewing geometry and the physical conditions of the Sgr A* accretion flow.

2

Rotating Black Holes

2.1 Overview

Black holes are among the most fascinating and counter-intuitive objects predicted by modern physical sciences. The existence of black holes was first postulated in the late 18th century by Reverend John Mitchell who proposed that gravity could affect light as well as matter. Subsequently in the very late 18th century Pierre-Simon Laplace reasoned that: ”it is therefore possible that the greatest luminous bodies in the universe are on this account invisible.” Both Mitchell and Laplace believed that the escape velocity, the speed necessary to escape a star′s gravity, for a sufficiently large star would be greater than the speed of light. However, the real foundations for black hole theory were laid by the discovery of Theory of General Relativity by Albert Einstein.

According to General Relativity, a black hole is a region of spacetime around a collapsed

mass with a gravitational field that has become so strong that nothing (including electromagnetic radiation) can escape from its attraction, after crossing its event horizon. The problem of such catastrophic gravitational collapse was first adressed by Chandrasekhar when he discovered the upper mass limit for ideal white dwarfs, composed of a degenerate electron-gas. The term ”black hole” was coined in 1968 by John Wheeler and has since been widely accepted as a description of these peculiar astrophysical objects.

From a mathematical point of view, classical black holes are solutions of the field equations of General Relativity. The final form of Albert Einstein′s general theory of relativity was developed in November 1915 and within two months Karl Schwarzschild had solved the field equations that determine the exact geometry of a non-rotating point mass. The exterior Schwarzschild solution describes a static and spherically symmetric spacetime of an electrically neutral point mass. The location of the point mass coincides with a singularity where the curvature of spacetime diverges to infinity. For a distant observer the singularity lies behind an event horizon located at one Schwarzschild radius. Schwarzschild black holes are global vacuum solutions of the field equations where the stress-energy tensor vanishes.

The form of the spacetime around a rotating black hole is due to Roy Kerr (1963) who found the exact solution to the general relativistic Einstein′s equations for the spacetime outside the horizon of a rotating black hole. The spacetime geometry of Kerr black holes depends on two parameters only, the black hole mass and spin. The source for a stationary and axisymmetric gravitational field is a mass shielded by two event horizons forming a ring singularity.

The Kerr solution is indeed a practical, realistic and accurate solution to be used in astrophysics as Schwarzschild solution is both static (highly unlikely in astrophysical context, as long as a black hole forms through the gravitational collapse of a rotating body) and point mass (could work in approximation, for very low spins, but not accurately as the metric form completely changes).

The Schwarzschild and Kerr metrics represent solutions of Einstein’s equations relevant for astrophysical black holes which are assumed to be electrically neutral. Nevertheless, they can be further generalised by taking of the electric charge into the consideration. The corresponding solutions are Reissner-Nordström metric for a non-rotating charged black hole,

and Kerr-Newman metric for a rotating charged black hole, respectively. Besides the mass, angular momentum and electric charge, black holes do not have any other parameters, which is often called "no-hair theorem" (this statement gets its name from a comment by John A.Wheeler 1968). Astrophysical black holes are expected to be uncharged, therefore only the mass and spin are important here.

2.2 Black hole properties

Several characteristic radii can be defined around black holes, and the most important are:

1. Schwarzschild radius R_S, representing the limiting radius below which a collapsed mass form a spherically symmetric non-rotating black hole, where G is the gravitational constant and c is the speed of light;

2. gravitational radius R_g (being a half of R_S and usually used as a unit for distance around a black hole);

3. radius of event horizon R_h (representing space-time boundary below which events cannot affect an outside observer); and

4. radius of marginally stable orbit R_{ms} (representing the minimum allowed radius of a stable circular equatorial orbit around a black hole).

Black holes in nature are classified according to their masses as: supermassive black holes (with masses $M_{BH} \sim 10^5 - 10^{10}\ M_\odot$), intermediate-mass black holes ($M_{BH} \sim 10^2 - 10^5\ M_\odot$), stellar-mass black holes ($M_{BH} < 10^2\ M_\odot$), mini and micro black holes ($M_{BH} \ll M_\odot$). A crucial event for the acceptance of black holes was the discovery of pulsars, as a clear evidence for the existence of neutron stars, therefore, as a confirmation of Chandrasekhar limit. The first identification of a stellar mass black hole came in 1972, when the mass of the rapidly variable X-ray source Cygnus X-1 was proven to be above the maximum allowed for a neutron star.

The first exact solution of Einstein's equations describing a black hole for a point mass assuming spherical symmetry is Schwarzschild solution. The radius of the event horizon is accordingly called Schwarzschild radius:

$$r_\mathrm{s} = 2r_\mathrm{g} = \frac{2GM}{c^2}, \tag{2.1}$$

where r_g is the gravitational radius which is equivalent to the mass if the geometrised units with $c = G = 1$ are used. The Schwarzschild metric in Schwarzschild coordinates is:

$$ds^2 = -\left(1 - \frac{r_s}{r}\right)dt^2 + \frac{1}{\left(1 - \frac{r_s}{r}\right)}dr^2 + r^2 d\Omega^2, \tag{2.2}$$

where $d\Omega^2 \equiv d\theta^2 + \sin^2\theta\, d\varphi^2$, t is the time measured by an observer at infinity at rest, r is the radial coordinate, θ is the latitude, and φ is the azimuthal angle.

2.3 Kerr spacetime

General Relativity tells us that mass causes gravitational redshift effects i.e. the strong pull of gravity shifts radiation emitted near masses towards the red spectral range and the intensity is reduced, too. This is mathematically included in the general relativistic Doppler factor or g–factor for short hereafter. The g–factor is a measure for both, energy shift of emission and suppression or enhancement of intensity as compared to the emitter's rest frame. g is generally a function of the velocity field of the emitter (as measured in a suitable observer's frame e.g. the zero angular momentum observer, ZAMO), the curved space–time (represented by metric coefficients), and constants of motion of the photon as discovered by Carter.

Kerr black holes belong to the stationary axially symmetric vacuum solutions family and it is depicted by two physical parameters, the mass M and the specific angular momentum a. In Boyer–Lindquist form, a Kerr black hole is defined by a line element

$$ds^2 = -\alpha^2 dt^2 + \tilde{\omega}^2(d\phi - \omega dt)^2 + \rho^2/\Delta\, dr^2 + \rho^2 d\theta^2, \tag{2.3}$$

with the lapse for rotating black holes

$$\alpha = \frac{\rho\sqrt{\Delta}}{\Sigma}. \tag{2.4}$$

Other metric functions satisfy

$$\Delta = r^2 - 2Mr + a^2, \tag{2.5}$$

$$\rho^2 = r^2 + a^2 \cos^2\theta, \tag{2.6}$$

$$\Sigma^2 = (r^2 + a^2)^2 - a^2 \Delta \sin^2\theta, \tag{2.7}$$

$$\omega = 2aMr/\Sigma^2, \tag{2.8}$$

$$\tilde{\omega} = \Sigma \sin\theta/\rho. \tag{2.9}$$

One important metric coefficient is the redshift or lapse function α that measures the amount of gravitational redshift of photons and time dilation. It holds for static black holes

$$\alpha_{\rm S} = \sqrt{1 - \frac{2M}{r}}, \tag{2.10}$$

and is known as *Schwarzschild factor*. In a good approximation, any slowly rotating mass may be described by this factor. A classical black hole horizon satisfies $\Delta = 0$ and consequently $\alpha_{\rm S} = \alpha = 0$. Since $g \propto \alpha$, the redshift influences any emission of electromagnetic radiation in the vicinity of a black hole. The observed intensity of radiation satisfies $F_\nu^{\rm obs} \propto g^3$ so that spectral flux is strongly reduced as the emitter approaches to the event horizon. For a static Schwarzschild black hole, $a = 0$, there is only one event horizon located at the Schwarzschild radius, $\mathrm{R_S} = 2M$. Kerr black holes posses two horizons with

$$r_{\rm H}^{\pm} = M \pm \sqrt{M^2 - a^2}, \tag{2.11}$$

where $r_{\rm H}^{+}$ is the outer horizon and $r_{\rm H}^{-}$ the inner horizon or Cauchy horizon. The inner Cauchy horizon can only be intersected once, being a one–way ticket towards the curvature singularity. Because of the cosmic censorship conjecture (R. Penrose, 1969), the true singularity remains hidden by the two horizons. The radius of the outer horizon is given by:

$$r_+/M = 1 + \left(1 - a^2/M^2\right)^{1/2}. \tag{2.12}$$

The conversion factor from the angular momentum $J_{\rm phys}$ (in physical units) to the angular momentum J (in geometrical units, cm^2) is: $J = (G/c^3)J_{\rm phys}$. It is convenient to make all geometrized quantities dimensionless by scaling them with the appropriate power of mass M. The dimensionless specific angular momentum, $a \equiv J/M$, spans the range $-1 \leq a \leq 1$,

where the positive/negative value refers to the motion co/counter-rotating with respect to the φ-coordinate. We will further assume co-rotational motion only ($a \geq 0$). The magnitude of a is thought to be less than 1, in order to have a regular horizon and avoid the case of naked singularity.

The equations for photon trajectories in the Kerr metric were derived by Carter (1968). Several relativistic effects, such as light bending, gravitational and Doppler shift could be computed by solving the equation of the photon orbits. Cunningham and Bardeen calculated the radiation of a point source in a circular orbit in the equatorial plane around an extreme Kerr metric black hole. (see Cunningham and Bardeen, 1972) Bardeen (1973) studied the effects of accretion from a disk of gas orbiting a black hole on its properties and showed that the Kerr metric is more appropriate for describing supermassive black holes than the Schwarzschild metric. As noted by Thorne (1974), the rotation of an astrophysical black hole is limited by the (maximum) equilibrium value $a \doteq 0.9982$ because of the capture of photons from the accretion disc and by magnetic torques (Krolik et al. 2005). The disk would extend down to about 1.23 R_g, while in the case of a non-rotating black hole it could extend down to 6 R_g.

Kerr black holes show a new feature that doesn't exist in Schwarzschild case: rotation of space–time or frame–dragging. The frame–dragging frequency already introduced as ω in Eq. (2.8), parameterizes the rotation of space as seen from infinity. Approaching the black hole, the spin steeply increases, $\omega \propto r^{-3}$. Kerr black holes posses an oblate zone where the spacetime rotation is extraordinarily strong: the ergoregion (see Figure 2.1). The outer edge of this region, the ergosphere, may be computed according to $g_{\mathrm{tt}} = 0$ and we have

$$r_{\mathrm{erg}}(\vartheta) = M + \sqrt{M^2 - a^2 \cos^2 \vartheta}. \tag{2.13}$$

The metric coefficient changes sign here: it is negative for $r > r_{\mathrm{erg}}$ and positive for $r < r_{\mathrm{erg}}$. In the equatorial plane, $\vartheta = \pi/2$, the ergosphere lies at the Schwarzschild radius, independent of the spin. For lower poloidal angles, the ergosphere approaches the event horizon and coincides with it at the poles, $\vartheta = 0$.

The natural length scale here is the gravitational radius defined by $r_{\mathrm{g}} = \mathrm{G}M/\mathrm{c}^2$ with Newton′s constant G and vacuum speed of light c. For one solar mass, $M = \mathrm{M}_\odot = 1.989 \times$

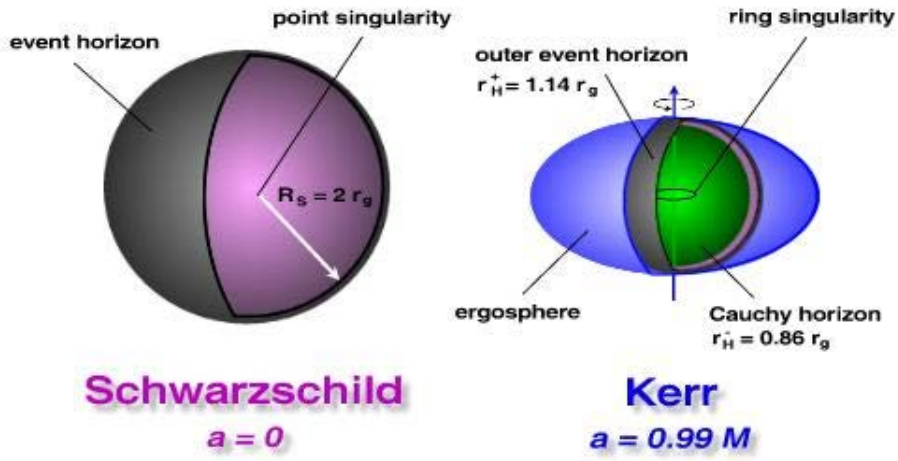

FIGURE 2.1: Architecture of static Schwarzschild (left) and rotating Kerr BHs (right). We assume the same mass. Kerr BHs are more compact than Schwarzschild BHs. Credit: A. Muller, 2004

10^{33} g, the Schwarzschild radius amounts to $R_S \simeq 3\,\mathrm{km}$. It is convenient to use geometrized units G = c = 1 so that length is measured in units of mass M. We measure black hole rotation in terms of the specific angular momentum (Kerr parameter) that holds $a = J/M = GM/c$. At first glance, the Kerr parameter can take any value between $-M$ and $+M$ but the cases $a = \pm M$ develop a naked singularity that is forbidden. As discussed earlier, accretion theory favours a limit of $|a|_{\max} = 0.998\,M$.

The metric depends on two parameters, the total mass M and the angular momentum $J = Ma$ (we assume $J \geq 0$ without loss of generality, and we use units where the velocity of light c as well as Newton's gravitational constant G are equal to 1). The metric is stationary (independent of t) and axisymmetric (independent of φ). Inside the ergosphere ($r_+ < r < r_0$) an observer must rotate in the same direction as the black hole ($d\varphi/dt > 0$). We can see the locations of the ergosphere and the horizons in Figure 2.2.

For circular orbits of a test particle in the equatorial plane $\vartheta = \pi/2$, the angular velocity is

$$\Omega = \pm \frac{\sqrt{M}}{r^{3/2} \pm a\sqrt{M}} \quad , \tag{2.14}$$

where the upper sign represents direct orbits (co-rotating) and the lower sign for retrograde

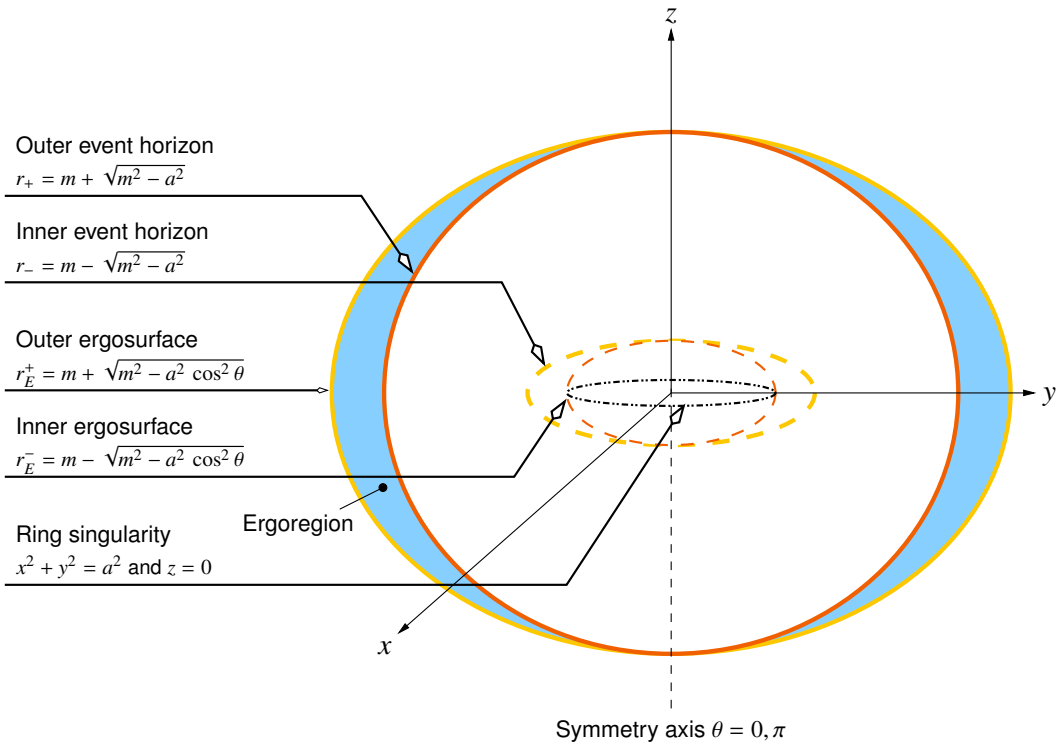

FIGURE 2.2: Location of the horizons, ergosurfaces and curvature singularity in Kerr spacetime. Credit:Matt Visser, 2008

(counter-rotating) orbits. A circular orbit will exist only for $r > r_{\rm ph}$. The photon orbit is given by

$$r_{\rm ph} = 2M\left\{1 + \cos\left[\frac{2}{3}\arccos\left(\mp\frac{a}{M}\right)\right]\right\}. \tag{2.15}$$

The orbits become bound at $r > r_{\rm mb}$, with the 'marginally bound orbit'

$$r_{\rm mb} = 2M \mp a + 2M^{1/2}(M \mp a)^{1/2}. \tag{2.16}$$

(Under an infinitesimal outward perturbation, a particle in an unbound orbit will escape to infinity.)

The two limiting cases of Kerr black holes are $a = 0$ ($J = 0$), the non-rotating (Schwarzschild) case, and the $a = M$ ($J = M^2$), the extremely rotating black hole. In $a = 0$ case, the event horizon is formed at by $r_+ = 2M$ ('Schwarzschild radius') and no ergosphere is formed. In $a = M$ case, one has $r_+ = M$ and the ergosphere will extend up to $r_0(\pi/2) = 2M$ in the equatorial plane. The characteristic radii $r_{\rm ph}$, $r_{\rm mb}$ and $r_{\rm ms}$ discussed above are given in Table 2.1.

TABLE 2.1: The photon orbit, marginally bound orbit and marginally stable orbit for Schwarzschild black hole and for extreme Kerr black hole. For the rotating black holes, there are two cases: direct and retrograde orbits.

	$r_{\rm ph}$	$r_{\rm mb}$	$r_{\rm ms}$
$a = 0$	3M	4M	6M
$a = M$ (direct)	M	M	M
$a = M$ (retrograde)	4M	$(3 + 2\sqrt{2})$M	9M

There are three significant Kerr geometry features that are most relevant to this Thesis:

1. **Event Horizon:** It is a sphere of radius $\sim GM/c^2$ around the singularity, from within which nothing may emerge — a one-way membrane.

2. **Ergosphere:** It is a region around a rotating black hole where the spacetime is dragged along with the direction of rotation at a speed greater than the local speed of light.

3. **Innermost Stable Circular Orbit (ISCO) or Marginally stable orbit:** It is the smallest orbit ($r = r_{\rm ms}$) along which a free stable particle orbits around a black hole. No stable circular motion is possible for $r < r_{\rm ms}$. In Newtonian theory, orbits at any radii were possible.

For astrophysical black holes, the black hole is an uncharged object and the gravity of the disk is negligible. The spacetime metric $g_{\mu\nu}$ will be described by the Kerr metric, determined by two parameters: total mass M_* and total angular momentum J_*.

The Kerr metric is not dependent on time t and azimuthal angle ϕ around the symmetry

axis. The other used coordinates are the Kerr-Schild coordinates, with the metric

$$\begin{aligned} g_{\mu\nu} &= \eta_{\mu\nu} + f\, k_\mu\, k_\nu, \quad \eta_{\mu\nu} = \mathrm{diag}(-1, 1, 1, 1) \\ f &= \frac{2Mr^3}{r^4 + a^2 z^2}, \\ k_t &= 1, \\ k_x &= \frac{rx + ay}{r^2 + a^2}, \\ k_y &= \frac{ry - ax}{r^2 + a^2}, \\ k_z &= \frac{z}{r}, \end{aligned} \tag{2.17}$$

with $k_\nu = (k_t, k_x, k_y, k_z)$ is a unit vector, and r is given by

$$\frac{x^2 + y^2}{r^2 + a^2} + \frac{z^2}{r^2} = 1. \tag{2.18}$$

The Kerr–Schild metric in given in the Cartesian form in order to prevent confusion with the spherical-polar Boyer–Lindquist coordinate system. The indices $\{t, \phi, r, \theta\}$ refer to the Boyer–Lindquist coordinates. In Boyer-Lindquist form, The Kerr solution exhibits a coordinate singularity at both horizons. The coordinate system can be easily transformed to suited wellbehaved coordinates such as horizon adapted coordinates, like Kerr-Schild.

On the other hand, the main advantage of the Boyer–Lindquist form is that the event horizons can be easily calculated, whereas the pathological behaviour of the standard Boyer-Lindquist formulation can be remedied by the Kerr-Schild coordinate system, circumventing the coordinate singularities at the horizon.

The Kerr-Schild frame represents the most simple horizon adapted frame. Another advantage the Boyer-Lindquist coordinate system is that the parameter t can naturally be thought of as a time coordinate, at least at large distances near spatial infinity.

The Boyer-Lindquist coordinates also minimizing the number of off-diagonal components of the metric (there is only one off-diagonal component), making the asymptotic behaviour more easily understood. While Boyer-Lindquist coordinates are more helpful and well adapted to many purposes, they are very ill-adapted to probing the coordinate singularities, found in Kerr-Schild decomposition.

2.3.1 ISCO: the Marginally Stable Orbit

The Kerr metric solution implies the presence of a radius within which the orbit of a moving particle in the equatorial plane becomes unstable. This radius is known as the Innermost Stable Circular Orbit (ISCO), referred to as the marginally stable orbit ($r_{\rm ms}$) (Bardeen, Press & Teukolsky 1972). Beyond the ISCO, the particles plunge into the black hole on nearly geodesic orbits of constant energy and angular momentum. The ISCO represents the closest orbit to the black hole, where the orbit of a particle is stable. Below this orbit, only unstable (unbound) orbits may occur.

The basic assumption is that the accretion disc is in circular orbital motion and disc extends down to the ISCO. Most of the accretion energy is released very close to the black hole at only a few gravitational radii enabling the effects of general relativity to be probed by observation. Accreting gas can efficiently lose energy and angular momentum only outside of the ISCO. The radiative behaviour of the inner disk becomes strongly dependent on the geometry of spacetime near this region. It is very difficult to recover unambiguous information about the main parameters, such as black hole spin, disk inclination angle or inner disk radius. This is because the smooth, featureless tails in the light curve do not retain enough information to break the degeneracies between the various parameters, describing the accretion disk or its emissivity.

The ISCO depends on the spin of the black hole (see Figure 2.3) and the relative orientation of the black hole angular momentum relative to the angular momentum that of the accretion flow. $r_{\rm ISCO}$ ranges from $r = 1$ ($a = 1$, i.e. the case of a maximally spinning black hole) to 6 ($a = 0$, a static black hole) and 9 for $a = -1$. The rotation limit of an astrophysical black hole of $a \doteq 0.9982$ implies that $r_{\rm ISCO} = 1.23$. The accretion process naturally causes a black hole to spin, provided the disc angular momentum is partly aligned as the black hole spin.

For values of the spin lower than $a = 1$, the radius of the marginally stable orbit will increase (see Figure 2.4). The spin of the black hole not only determines how close the disk can extend to the center, but also causes additional distortion due to the dragging of the frame. The velocity field of the accreting matter is usually treated in the approximated

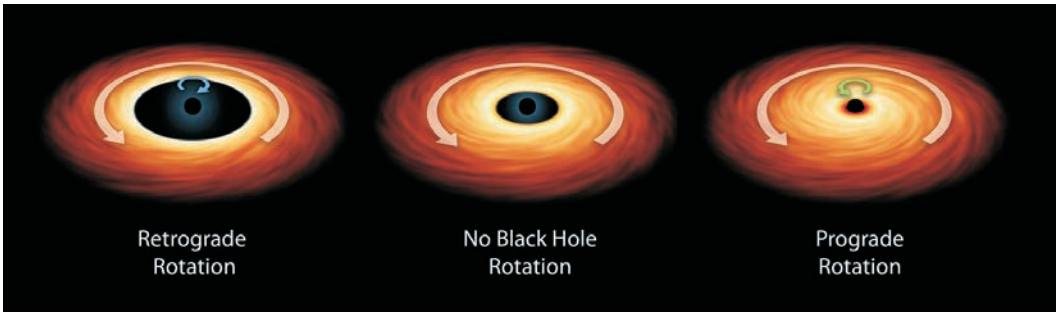

FIGURE 2.3: Relative location of the ISCO within a black hole accretion disk for a flare in retrograde rotation, for a non-rotating black hole and for a flare in prograde rotation. The disk is truncated at the inner radius of the disk $r_{\rm in}$ which in this case coincides with ISCO. Credit: NASA website, JPL-Caltech, 2013

way in models of relativistic effects: it is assumed that the matter accretes in a form of a geometrically thin accretion disk and, for prograde rotation, it is assumed that the disk rotates in the planar plane of the black hole (cf. Bardeen & Petterson 1975 for frame dragging effects on disks not in the equatorial plane). The accreting material is assumed to flow along circular equatorial geodesics for $r > r_{\rm ms}$, and to be in free fall for $r < r_{\rm ms}$.

The inner radius of the accretion disc cannot be smaller than the ISCO. This of course does not mean that there is no matter at radii lower than the ISCO but matter must spiral in (see Krolik & Hawley 2002 for alternative definitions of the "edge" of the disc). The ISCO depends on the black hole spin and on whether the disc is co– or counter–rotating with the black hole:

$$r_{\rm ISCO} = 3 + Z_2 \pm \left[(3 - Z_1)(3 + Z_1 + 2Z_2) \right]^{\frac{1}{2}} \tag{2.19}$$

where

$$Z_1 = 1 + (1 - a^2)^{\frac{1}{3}}[(1 + a)^{\frac{1}{3}} + (1 - a)^{\frac{1}{3}}] \tag{2.20}$$

$$Z_2 = (3a^2 + Z_1^2)^{\frac{1}{2}}$$

The – (+) sign applies to co– (counter–) rotating discs. Indeed, the decrease of the ISCO with a (for a corotating disc) provides a method to measure the spin.

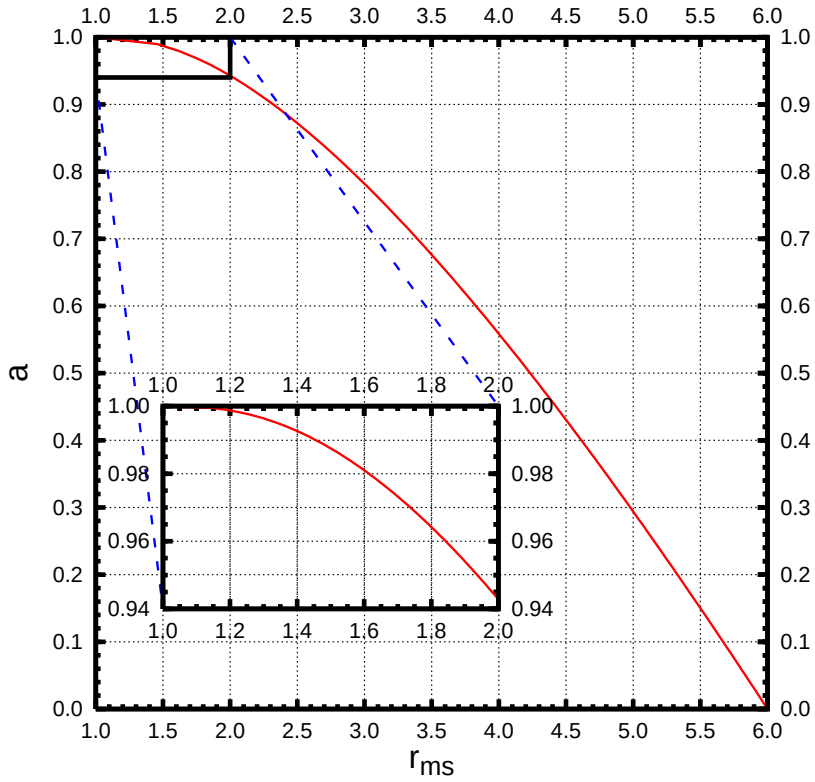

FIGURE 2.4: Relation between spin a and marginally stable orbit r_{ms}. Credit: J. Svoboda, 2010

There are two types of rotation for a black hole: a prograde black hole rotates in the same direction as its accretion disk, whereas a retrograde black hole rotates in the opposite direction. We refer to prograde rotation, if the spot (located within the accretion disk, in the equatorial plane) rotates in the same direction as the black hole (counter-clockwise) and retrograde if the spot in the disk rotates in the opposite direction as the black hole. In this way, it is possible not only to infer the black hole spin but also to find whether the Keplerian flow is in prograde or retrograde rotation. The radius of the retrograde photon is larger because of the rotation of the black hole. If the photon comes nearer to the black hole, then the rotation of the spacetime geometry would force the photon to change its direction of rotation towards the direction of rotation of the black hole. As the photon loses rotational velocity, it will fall into the black hole. Consequently, the retrograde orbits are present further away than prograde orbits (see Figure 2.5).

The velocity at the marginally stable orbit reaches a considerable fraction of the speed of

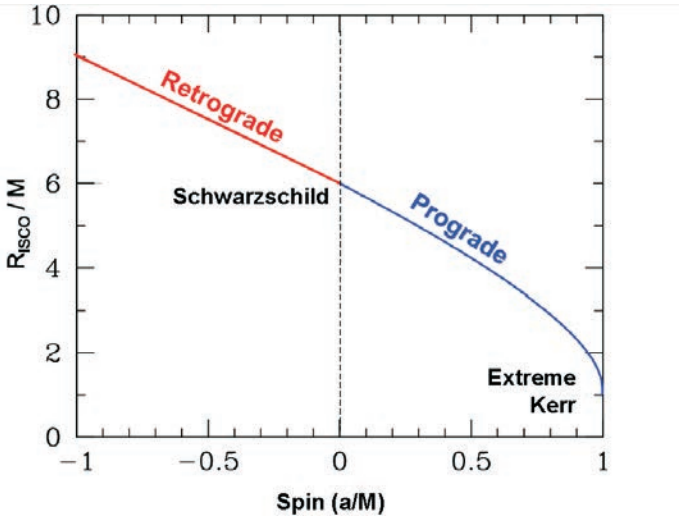

FIGURE 2.5: Black hole spins for retrograde and prograde photons.

light c (=1) and has a similar value $V(r) \approx (0.5 - 0.6)\ c$ for any value of the spin (Figure 2.6). For large spins, a small dip develops in the velocity profile near the horizon. Although it is an interesting feature, its magnitude is far too small to be recognised with existing or planned observational facilities. Despite its successes, there has not yet been a satisfactory test of general relativity in the strong gravity limit. By their very nature, studies of black holes are likely to provide the best opportunity for constraining strong field relativity.

Frame dragging slows down the particles orbiting in retrogrades orbits and acts in opposition to the disk angular momentum, causing orbits to plunge in from farther out than otherwise.(Chandrasekhar, 1983). In the case of a Kerr black hole, there are two circular photon orbits in the equatorial plane. One is a prograde orbit moving in the same direction as the black hole spin, while the other is the retrograde orbit moving against the black hole (see Figure 2.7).

The motion around a black hole follows bound orbits that are never closed. There are no perfectly circular orbits in a realistic scenario. Any eccentric orbit in either Schwarzschild geometry or in the equatorial plane of a Kerr black hole will be planar but never closed. Lense-Thirring precession will cause for any circular orbit that lies outside the equatorial plane to not be planar and take the shape of an orbital ascending node. A plasma blob that falls into the event horizon on a trajectory outside the equatorial plane would cause the geometrically thin accretion disk to become a thick disk, symmetrically spread above and

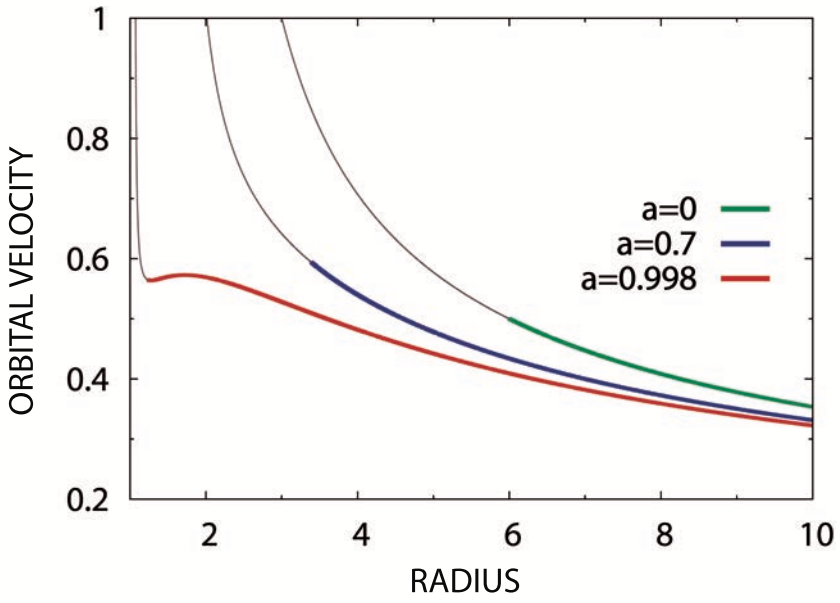

FIGURE 2.6: Orbital velocity of prograde motion near a Kerr black hole for three spins. The thick coloured part indicates the range of radii above the marginally stable orbit, where the circular motion is stable. The thin curve indicates an unstable region at small radii.

beneath the equatorial plane. The trajectory will eventually be confined onto the equatorial plane and become circular. With good approximation, we generate most of our relativistic light curves using circular orbits in the equatorial plane. We also propose a plunging scenario of a blob in non-keplerian orbital motion, falling into the event horizon of a Kerr black hole. Assuming purely azimuthal Keplerian motion of the spot, the orbital velocity (with respect to a locally non-rotating observer at the radius r) is:

$$\mathrm{v}^{(\phi)} = \frac{r^2 - 2a\sqrt{r} + a^2}{\sqrt{\Delta}\,(r^{3/2} + a)}. \tag{2.21}$$

In order to derive time and frequency as measured by a distant observer, we have to to take into account the Lorentz factor associated with the orbital motion,

$$\Gamma = \frac{\left(r^{3/2} + a\right)\sqrt{\Delta}}{r^{1/4}\ \sqrt{r^{3/2} - 3r^{1/2} + 2a}\ \sqrt{r^3 + a^2 r + 2a^2}}\,. \tag{2.22}$$

The angular velocity of orbital motion is $\Omega = (r^{3/2} + a)^{-1}$, which also determines the orbital period t_{orb}. The redshift factor g and the emission angle ϑ (with respect to the normal

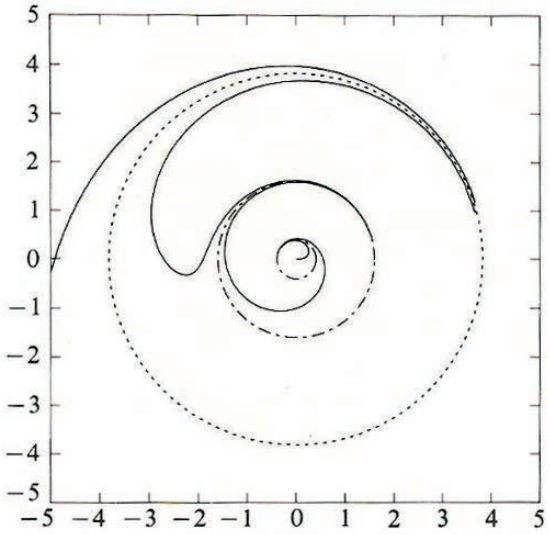

FIGURE 2.7: The orbit of a retrograde photon.(Chandrasekhar, 1983)

direction to the disc) will be

$$g = \frac{\mathcal{C}}{\mathcal{B} - r^{-3/2}\xi}, \quad \vartheta = \arccos \frac{g\sqrt{\eta}}{r}, \tag{2.23}$$

where $\mathcal{B} = 1 + ar^{-3/2}$, $\mathcal{C} = 1 - 3r^{-1} + 2ar^{-3/2}$; ξ and η are constants of motion for with the photon path in an axially symmetric and stationary spacetime. In the numerical code, the velocity is calculated in special Kerr ingoing coordinates (Kerr-Schild form), non-singular on the horizon. In approximation, the orbital period formula for $a = 0$ is accurate enough also in the case of a spinning black hole, provided that r is not very small. For instance, even for $r = 6$ (the last stable orbit in Schwarzschild metric), $T_{\rm orb}(r_{\rm ms})$ calculated for a static and for a maximally rotating ($a = 1$) black hole differ by about 7%. The relative difference decreases, almost linearly, down to about 1% at $r = 20$. The orbital period may be used in this case to estimate the black hole mass even if the angular momentum is unknown (deviations are relevant only for $r < 6$, when the radius can be used to constrain the allowed range of a).

3

Ray-Tracing in Kerr geometry

In order to analyze relativistic light curves from a localized emitting spot integrated over the surface of an accretion disk, we propose a review of the ray-tracing method in Kerr metric. We describe the principles of geodesic ray tracing and derive the observed photon flux from the black hole disk.

We use a generalized scheme and a code that requires the use of the standard X-ray spectral fitting package XSPEC (Arnaud, 1996). To explore the relativistic effects from the disc, a modified subroutine of the Karas-Yaqoob (KY) numerical code is employed (using the NASA X-Ray Spectral Fitting XSPEC Package). We adapted an existing Fortran 77 numerical code to work for broad band continuum instead of line profiles and to allow intrinsic variation of the source. The code was modified in order to integrate the expanding plasmon model, a plunging blob model, a simple particle injection model and to allow for intrinsic emmisivity of a synchrotron (continuum) emitting blob. The calculations are based

on a modified KY code (Dovciak, Karas, Yaqoob, 2004) for a single spot orbiting close to the corresponding last stable orbit. All special and general relativistic effects (the relativistic beaming, redshifts and blue-shifts, lensing effect, photon time delays) for unpolarized synchrotron emission near a Schwarzschild and Kerr black hole are all taken into consideration.

The light curves are plotted in proper time and therefore can model realistic time dependent profiles of the continuum radiation expected to be emitted by an SMBH. The code produces light curves of from a synchrotron-emitting blob of plasma. For simplicity reasons, the mapping between the rest frame emission and that seen by a distant observer is called Transfer function. Each relativistic effect has been computed for light rays emitted from the equatorial plane of the Kerr black hole and received by an observer at infinity and is stored in a separate transfer function. The transfer function includes all relativistic effects into a single function that describes the overall influence of the gravitational field on light rays emerging from the disc.

The transfer functions amplify the flux in some regions within the disk whereas in other areas it suppresses the emission. The code subroutine employs pre-stored data tables to look up and interpolate the relevant effects:(i) the Doppler shift of the photons and gravitational redshift effect, (ii) relative delay of their arrival time, (iii) magnification of radiation (gravitational lensing effect) in Kerr metric. Due to the relativistic effects and a non-axisymmetric compact emission, the impact on the light curve is asymmetric and can be used to constrain the inclination angle of the disk and the spin of the black hole, together with other emissivity parameters.

The modified code produces light amplification curves for each individual flare in keplerian orbit around the black hole, including all special and general relativistic effects. We adopt a geometrically thin and optically thick accretion disc model and we point out that general relativity effects play an important role if the configuration is sufficiently dense in a limited region, typically a few tens of gravitational radii. Calculation of the bending of light, rotational frame dragging or lensing requires the integration along photon rays (Broderick and Blandford 2006). In order to calculate the final spectrum that an observer at infinity measures when local emission from the accretion disc is given, one must first specify the intrinsic emissivity in frame co-moving with the disc medium and then perform transfer of

photons to a distant observer.

Cunningham and Bardeen (1973) analyzed light curves of a point-like source of light orbiting in the equatorial plane of a Kerr black hole. They adopted approximations of geometrical optics and presented a detailed study of periodic variations of the observed frequency-integrated observed flux. Origin of the variability was twofold: (i) energy of individual photons is affected by the Doppler effect (special relativity effect), and (ii) photon trajectories are influenced by the gravitational field of the central black hole (general relativistic effect).

The photons (null geodesics) that connect the emission from the disc with the observer can only be found by computing the full general relativistic light travel paths which connect the disc to the observer. These null geodesics are given by solutions of the geodesic equations (Carter 1968; Misner, Thorne & Wheeler 1973; Chandrasekhar 1983), which can be obtained numerically (e.g. Karas, Vokrouhlicky Polnarev 1992), but can also be given in terms of analytic functions (Rauch & Blandford 1994; Agol 1997; Cadez, Fanton & Calvani 1998), which enable them to be solved quickly and with arbitrary accuracy.

The first calculation of the spectrum of matter accreting onto a Kerr black hole was done by Cunningham (1975). His results, however, do not have the form suitable for data analysis, as they are tabulated only for a few values of the relevant parameters. So far, the most efficient procedure for the data analysis comes from the concept of the photon transfer function, which is constructed by calculating the trajectories of a large number of photons (e.g., Laor 1991).

3.1 Imaging an Accretion Disk

General relativistic radiative transfer can be applied to accreting systems in two ways. Cunningham (1975) packaged all relativistic effects for optically thick, geometrically thin disks into a single transfer function to follow from local emitted flux on the equatorial plane to the observer located at infinity, ignoring all trajectories that recross the plane. Luminet (1979) used a relation between the impact parameters at infinity and constants of the motion to shoot photon rays backwards in time from an observer's photographic plate located at infinity to

the black hole.

Numerical simulation of Kerr null geodesics is computationally expensive in certain applications. Rauch and Blandford (1994) found a method for computing null geodesics in the Kerr metric semi-analytically using the Hamilton-Jacobi formulation of the equations of motion and used it to study the primary caustic. Fanton et al. 1997 used a fast analytic version for creating line profiles and accretion disk images. Falcke et al., 1994 used it along with a simple model for the Galactic center black hole to create images of the accretion flow. All of this work used Legendre's formulation of elliptic integrals and treated the ϕ and t coordinates numerically, if at all. Other approaches have been applied to the study of emission lines and spectra from AGN accretion disks and tori as well as their quasi-periodic oscillations. Noble (2006) has generated images of the galactic center black hole Sagittarius A* (Sgr A*) using axisymmetric general relativistic MHD simulations and Broderick and Loeb studied the frequency dependence of Sgr A* position (Broderick and Loeb, 2005).

De Felice, Nobili and Calvani (1974) have computed radiation from matter moving around a black hole in different approximations and parameter space. Cunningham (1975) studied the combined effects of Doppler shifts and gravitational lensing on X-ray emission from an accretion disc. He introduced a concept of a transfer function that includes all relativistic effects and describes the overall influence of the gravitational field on photon rays emerging from the disc. He also studied the self-irradiation of the disc and its impact on the disc emission (Cunningham, 1976). Since then numerous authors have investigated emission from disc (line, blackbody, reflected, etc.) in strong gravity. When full spectral resolution is not available, power spectra of light curves provide partial information on the emission from accretion discs.

Several methods have been used to calculate the emission profiles from accretion disks around black holes. The methods can be roughly divided into three categories. The first method uses a transfer function to map the image of the accretion disk onto a sky plane (Cunningham 1975, 1976). It is Keplerian and geometrically thin, but optically thick and residing in the equatorial plane. The spacetime metric around a black hole is firstly specified, and the energy shift of the emission (photons) from each point on the disk surface is calculated. The line profile expected for an accretion disk orbiting a non-spinning Schwarzschild

black hole was described by Fabian et al. (1989); the maximal spin Kerr case was described by Laor (1991). It was not until 2004 that models became available that included spin as a parameter. Such models have been developed and implemented into XSPEC by Dovciak, Karas and Yaqoob (2004), Beckwith and Done (2004), and Brenneman and Reynolds (2006). These authors used several methods for computing the transfer of photons from the accretion disc to the observer located far away from the central black hole. Some of them assumed the black hole to be non-rotating, others performed their calculations for a rotating Kerr black hole. Karas (1994) has explored a substantially more complex case when self-gravity of the disc is not neglected. Schnittman developed a geodesic hot spot model to explain the frequency commensurabilities seen in the quasi periodic power spectra of various micro-quasars and binary black holes. The results of his model are based on a fully relativistic ray-tracing framework.

The specific intensity at each point in the sky plane is determined from the energy shift and the corresponding specific intensity at the disk surface, using the Lorentz-invariant property. The transfer-function formulation (Cunningham 1975, 1976) has been applied to line calculations in settings ranging from thin accretion rings (e.g. Gerbal and Pelat 1981) and accretion disks around Schwarzschild (e.g. Laor 1991) and rotating (Kerr) black holes (e.g. Bromley et al. 1997). The second method makes use of the impact parameter of photon orbits around Schwarzschild black holes (e.g. Fabian et al. 1989; Stella 1990; Kojima 1991). The transfer function is described in terms of elliptical functions, which are derived semi-analytically. The Jacobian of the transformation from the accretion disk to sky plane is, however, determined numerically via infinitesimal variations of the impact parameter (Bao 1992). This method can be generalized to the case of rotating black holes by using additional constants of motion (Viergutz 1993; Bao et al. 1994; Fanton et al. 1997; Cadez et al. 1998). The third method simply considers direct integration of the geodesics to determine the photon trajectories and energy shifts (Dabrowski et al. 1997; Pariev and Bromley 1998; Reynolds et al. 1999).

Let us begin with a construction of a simple image of the accretion disk, as seen by on observer at infinity. We will later consider a localized source in the accretion disk, that will be the emitting source for all our time dependent emissivity models. We present a general

formulation for ray-tracing in Kerr space-time. The trajectory of a photon in the Kerr metric can be described using 3 constants of motion (Misner, Thorne, & Wheeler 1970),

$$\begin{aligned} E &= -p_t \,, \qquad L = -p_\phi \,, \\ Q &= p_\theta^2 - a^2 E^2 \cos^2\theta + L^2 \cot^2\theta \,, \end{aligned} \tag{3.1}$$

with r, θ, ϕ and t are the Boyer–Lindquist coordinates, p is the four-momentum and $a = J/M$ is the angular momentum in units of black hole mass. We use natural units such that $G = c = 1$. In order to eliminate the inflection points along a trajectory, we solve the three second-order geodesic equations, for $r(t)$, $\theta(t)$ and $\phi(t)$.

$$\frac{d^2x^i}{dt^2} = -\Gamma^i_{\mu\nu}\frac{dx^\mu}{dt}\frac{dx^\nu}{dt} + \Gamma^0_{\mu\nu}\frac{dx^\mu}{dt}\frac{dx^\nu}{dt}\frac{dx^i}{dt} \tag{3.2}$$

Here, the Γ's are connection coefficients; Latin indices take the values 1,2,3 (with x^1, x^2 and x^3 representing r, θ and ϕ, respectively) and Greek indices range from 1 to 4; repeated Greek indices denotes summation.

To obtain an image of an accretion disk as seen by a distant observer we integrate the geodesic equations (3.2) to follow trajectories of photons which propagate from a uniform Cartesian grid of points in the observer's sky plane to the accretion disk. The uniform grid may be associated with the field imaged by pixels of a CCD detector.

The integration of equations (3.2) occurs in three steps. First, we determine the initial-value data, i.e., the phase-space location of the photons; the starting points of the trajectories are located at a large distance from the black hole. In the second stage, we integrate the equations from $t = 0$ until the photon just crossed the plane of the disk. An adaptive step 4^{th}-order Runge–Kutta method is used to calculate the trajectory. In the last step, we use a golden selection search to determine the spacetime intersection of the photon and the disk with high accuracy. We discard the photons intercepted by the black hole (determined by an inner cut-off radius) or miss the accretion disk. We save the Boyer-Lindquist coordinate of the photon-disk intersection, the flight time in the observer frame and the frequency shift for each pixel.

Figure 3.1 shows the image of a geometrically thin accretion disk around an extremely rotating black hole ($a = M$) with the inner and outer radii at $1.25R_g$ and $10R_g$, respectively. The disk is viewed at 75° with respect to the polar axis. The colors show the frequency shift

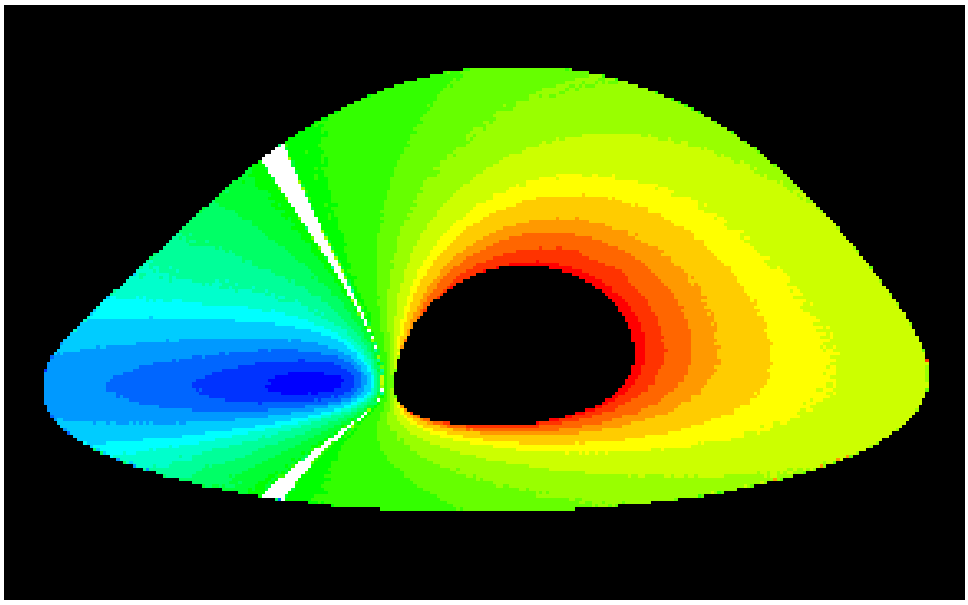

Figure 3.1: A geometrically thin and optically thick disk around a maximally-rotating black hole of mass M. The inner radius and outer radius are at $1.25M$ and $10M$. The disk is viewed at a 75° inclination angle. The color map shows the ratio of observed frequency to emitted frequency, with the blue shaded bands representing the blueshift and the red indicating the redshift. The white patch represents the zero frequency shift contour. Credit: B Bromley, 1997

of emitted photons caused by the Doppler and gravitational redshift effects. We can see the gravitational re-focus effect of photons emitted from the far side of the disk, causing the far side of the disk to appear bent towards the distant observer. The relativistic effect of frame dragging is also shown in the shape of disk and the asymmetry of the frequency shift along the contours of the fixed radius between the near and far sides of the accretion disk.

Photons have an equivalent to the ISCO for massive particles, the circular photon orbit. This orbit represents the boundary between photons that are bound and unbound to the gravitational pull of the black hole. Inside of this circular photon orbit, only particles from the front side of the disk will emit photons that reach the observer. Unless the disk is opaque, when the photosphere being placed in front of the black hole, this will produce a shadow at the circular photon orbit, where regions outside of the projection of the photon orbit at infinity appear brighter than the regions inside it. The combination of maximum path lengths at

the photon orbit together with the emission peaking near the black hole produce bright rings in these regions. The black hole shadow is a consequence of the circular photon orbit and a prediction of the presence of an event horizon (Bardeen, 1973; Broderick and Loeb, 2009).

3.2 Photon trajectories in Kerr spacetime

The motion of a photon follows the null geodesic equation $\nabla_{\mathbf{p}} \cdot \mathbf{p} = 0$, where $\mathbf{p}$ is the 4-momentum of the photon and $\nabla_{\mathbf{p}}$ is the directional derivative operator along $\mathbf{p}$. This is a set of second-order ordinary differential equations, which may be solved by the Runge-Kutta method with known initial position and momentum of the photon. We also note that in Kerr spacetime, the constants of motion include the energy of the photon E, the angular momentum along the spin axis L_z, and the norm of the 4-momentum δ) and solve the photon trajectory in the equatorial plane by the Lagrangian approach.

For a general null geodesic in Kerr spacetime, Carter (1968) has proven the separability of the Hamilton-Jacobi equation and found another constant of motion (i.e. the Carter constant $\mathscr{Q}$). If we take the partial derivatives of the Hamilton's principle function

$$S = \frac{1}{2}\delta\lambda - Et + L_z\phi + \int^r \frac{\sqrt{R(r)}}{\Delta}dr + \int^\theta \sqrt{\Theta(\theta)}d\theta\,, \tag{3.3}$$

with respect to E, L_z, δ, and $\mathscr{Q}$ then set them to zero, we obtain the equations of motion of the photons. We find that the equation governing the motion of the photon ($\delta = 0$) in r and θ is

$$\int^r \frac{dr}{\sqrt{R(r,\xi,\eta)}} = \int^\theta \frac{d\theta}{\sqrt{\Theta(\theta,\xi,\eta)}} = P\,, \tag{3.4}$$

where

$$R(r,\xi,\eta) = r^4 + \left(a^2 - \xi^2 - \eta\right)r^2 + 2M\left(\eta + (\xi - a)^2\right)r - a^2\eta\,, \tag{3.5}$$

$$\Theta(\theta,\xi,\eta) = \eta + a^2\cos^2\theta - \xi^2\cot^2\theta\,, \tag{3.6}$$

and P is the parameter along the photon trajectory. e used two impact parameters $\xi = L_z/E$ and $\eta = \mathscr{Q}/E^2$. The equations of motion for other coordinate systems (including the affine

parameter λ) are described as combinations of the integrals about r and θ

$$\lambda = \int^{r} \frac{r^2 dr}{\sqrt{R(r,\xi,\eta)}} + \int^{\theta} \frac{a^2 \cos^2\theta d\theta}{\sqrt{\Theta(\theta,\xi,\eta)}}\,, \tag{3.7}$$

$$t = E\lambda + 2M \int^{r} r\left(Er^2 - aL_z + a^2 E\right) \frac{dr}{\Delta\sqrt{R(r,\xi,\eta)}}\,, \tag{3.8}$$

$$\phi = a\int^{r} \left((r^2+a^2)E - aL_z\right) \frac{dr}{\Delta\sqrt{R(r,\xi,\eta)}} + \int^{\theta} \left(L_z \csc^2\theta - aE\right) \frac{d\theta}{\sqrt{\Theta(\theta,\xi,\eta)}}\,. \tag{3.9}$$

The upper and lower limits in the integrals about r and θ are related to the turning points of the photon trajectories which are roots of quartic Eqs. 3.5 and 3.6 but with different choices of the impact parameters. 3.9 are elliptical integrals, that can be reduced to Carlson's (1977) standard forms.

The covariant components of the 4-momentum of photon can be written

$$p_\mu = \left(p_t,\ p_r,\ p_\theta,\ p_\phi\right) = \left(-E,\ \pm E\sqrt{R}/\Delta,\ \pm E\sqrt{\Theta},\ L_z\right)\,, \tag{3.10}$$

with the signs in p_r and p_θ determined by the initial values. The impact parameters ξ and η are associated with the angular parameters α (perpendicular to the projection of the spin axis in the observer's plane) and β (parallel to the projection) of the image seen by an observer located at infinity receiving photons from different points of the disk:

$$\alpha = (rp^{(\phi)}/p^{(t)})_{r\to\infty} = -\xi/\sin\theta_0\,, \tag{3.11}$$

$$\beta = (rp^{(\theta)}/p^{(t)})_{r\to\infty} = (\eta^2 + a^2\cos^2\theta_0 - \xi^2\cot^2\theta_0)^{1/2}\,, \tag{3.12}$$

where $p^{(\alpha)}$ is the tetrad components of the photon 4-momentum, θ_0 is the inclination of the observer with respect to the black hole spin axis.

3.3 Principles of Geodesic Ray tracing

The initial conditions for a photon geodesic are described in the local orthonormal frame of a "Zero Angular Momentum Observer" (ZAMO). The spatial axes are aligned with the coordinate axes while the time axis is is orthogonal.

Far away from the black hole, the spacetime is nearly flat and the Euclidean geometry will describe the spatial direction of the photon $n^{\hat{i}}\mathbf{e}_{\hat{i}}$, from which the initial momentum in the coordinate basis is derived:

$$p_t = -E_{\rm obs}(\omega\varpi n^{\hat{\phi}} + \alpha) \tag{3.13a}$$

$$p_r = E_{\rm obs}\sqrt{\frac{\rho^2}{\Delta}}\, n^{\hat{r}} \tag{3.13b}$$

$$p_\theta = E_{\rm obs}\sqrt{\rho^2}\, n^{\hat{\theta}} \tag{3.13c}$$

$$p_\phi = E_{\rm obs}\sqrt{\varpi^2}\, n^{\hat{\phi}}, \tag{3.13d}$$

where the photon energy is measured by a distant ZAMO with $E_{\rm obs}$.

The photon trajectories are integrated backwards in time from the image plane oriented at some inclination i with respect to the axis of rotation. A photon path is integrated from the intersection with the center of a pixel in the detector grid to the point of origin on a thin disk around a black hole. The accretion disk is actually confined to a finite region with angular thickness $\Delta\theta$, which is oriented normal to the black hole rotation axis. The photon trajectory will end either at the event horizon or pass through the surfaces of colatitude (θ = const). As the trajectories can pass through the disk, the photon's position and momentum (x^μ, p_μ) can be recorded at each plane intersection, to be able to construct the image of the disk. The method is identical in form to the forward integration from the photon origin on the disk to the detector, but more computationally efficient. Each photon is assumed, with accuracy, to approach the detector camera from a direction normal to the detector plane.

In order to trace the trajectory of a photon and consequently compute the observed flux, the local flux is considered to be emitted from the surface of the disc where the conditions of integration are initially set. If we integrate all flux contributions over a fine mesh on the disc surface, the emission originating in the disk, arriving at the observer within a solid angle can be calculated at the infinity in the observer's plane.

For an infinitely thin disk ($\Delta\theta \to 0$), the image plane maps onto the source plane and in

pseudo-Cartesian coordinates:

$$x = \sqrt{r^2 + a^2}\cos\phi \tag{3.14a}$$

$$y = \sqrt{r^2 + a^2}\sin\phi. \tag{3.14b}$$

For $i > 0°$, as the photon rays are deflected by the black hole, they tend to be focused on the far side, exhibiting a strong magnification by mapping a large area in the image plane onto a small area of the source plane. For a flat disk geometry, the photon rays are not allowed to pass through the plane defined by $\theta = 0$, so we are not able to see multiple images of sources behind the black hole.

For a sufficiently high inclination and spin values, single points in the equatorial plane may be mapped to different regions in the image plane, obtaining multiple images of different regions of the disk.

Considering the entire disk, we can integrate an entire collection of mass elements moving along geodesic orbits and emitting isotropic light with energy $E_{\rm em}$ in the emitter's rest frame. For a photon with 4-momentum $p_\mu(\mathbf{x}_{\rm em})$ that intersects a particle trajectory with the 4-velocity $v^\mu(\mathbf{x}_{\rm em})$, the redshift as seen by the observer is defined

$$\frac{E_{\rm obs}}{E_{\rm em}} = \frac{p_\mu(\mathbf{x}_{\rm obs})v^\mu(\mathbf{x}_{\rm obs})}{p_\mu(\mathbf{x}_{\rm em})v^\mu(\mathbf{x}_{\rm em})}, \tag{3.15}$$

where for a distant observer at $r \to \infty$, we take $v^\mu(\mathbf{x}_{\rm obs}) = [1, 0, 0, 0]$.

We consider radiation coming from a limited area of the disk, corresponding to the emission region responsible for flaring emission. Assuming zero opacity of the source, when calculating the emission from a flat, steady-state disk, the equatorial plane is taken to be totally opaque so that rays cannot curve around and see the "underside" of the accretion disk. The collection of incident photons can be summed to obtain the light curve.

Starting at a distant observer, a collection of photon trajectories are integrated backwards in time to a fixed coordinate grid surrounding the black hole. With the spacetime position and momentum recorded at each point in the computational grid, time-dependent light curves of the dynamic spot are generated. There are two steps in backwards ray tracing. Firstly, the photon trajectories associated to a camera coordinate grid are computed. Secondly, the

relativistic radiative transfer equation is solved for each photon trajectory, using an emission model. The camera is located at a very large distance from the black hole, in such a way that the light bending effect is negligible at the observer. The camera coordinates are related to the constants of motion in Kerr metric and use corresponding impact parameters perpendicular and parallel to the black hole spin axis respectively.

Given the ray-tracing map from the accretion disk to the image plane, with each photon bundle labelled with a distinct 4-momentum and time delay, we can reconstruct time-dependent images of the disk based on time-varying emission models.

3.4 Kerr Black Hole Ray Tracer

We use the modified KY code as a ray-tracer to generate time-dependent profiles of continuum emission from the black hole disk. The integration of photon trajectories is performed twice, both forward and backward in time, in order to compute relativistic path trajectories of the photons. All relativistic effects are pre-calculated, using forward integration subroutines (Dovciak et. al. 2004), all present in FITS files. We modify only backward integration subroutines, that describe the local emission from a spot around the black hole and use the existing pre-calculated relativistic effects. All dynamical ray-tracing computations are done using photons emitted from the initial point within the accretion disk and reach the observer at infinity.

The Kerr Black Hole Ray Tracer maps emitting points in the equatorial plane of a Kerr black hole to points on the observers screen. Spectral flux of continuum emission is computed by numerical integration over the solid angle subtended by the screen. All relativistic effects such as gravitational redshift, beaming and lensing are accounted for. The complete solver will be presented later. The final formulation will take full account of all special and general relativistic effects in the photon transport and the relative motion of the emitting source. In our models the continuum emission profile originate from a thin accretion disk, the motion of the emitter in the disk being determined by the gravity and spin of the black hole as well as the space-time structure near the black hole.

The model is based on pre-calculated tables and thus the geodesics do not need to be

calculated each time one integrates the emission. The ray tracing method is shown in Figure 3.2. In general, the disk emissivity (or a non-axisymmetric area in the disk, in our case a blob) is the quantity that has to be folded into the flux integral to evaluate the observed flux from accretion disks.

We consider cases where disk material is either in a stable circular orbit (Keplerian in a relativistic sense), or, if within the marginally stable circular orbit at ISCO, it is assumed to be in free fall onto the black hole, with energy and angular momentum corresponding to the marginally stable orbit (see Cunningham 1975; also Reynolds and Begelman 1997). All material, whether in circular orbit or in free fall, is taken to lie in a slab whose thickness is small everywhere compared to the distance to the black hole (lying in thin disk). The information contained in the continuum emission profile is rich but the parameter space for the models is also fairly large.

The model parameters and light curve characteristics depend on disk radii, emissivity parameters of the source, observed inclination angle of the disk, orbital period, spin parameter of the black hole. If the black hole is rotating, we assume that the disk lies in the equatorial plane of the black hole and that the disk is corotating. This last assumption is justified by the Bardeen-Petterson (1975) effect which causes a viscous disk to stabilize in the equatorial plane of the rotating hole. With these specifications for the relativistic accretion disk system we proceed to calculate quantities relevant to our study. On the other hand, the source can corotate or counter-rotate relative to the spin direction. We study both prograde and retrograde motion of the plasmon around the black hole. Of all of these parameters, perhaps the most problematic is the disk emissivity. We assume a number of emission models, stationary and non-stationary. As a radiation mechanism, we will use an adiabatically expanding uniform blob of relativistic electrons that moves in a Keplerian orbit around the spinning black hole.

The observed radiation flux from a spot in an accretion disc is obtained by integrating the intrinsic emission over the entire spot, weighted by the transfer function $T(r_e, \varphi_e, \theta_o, a)$ determining the impact of relativistic energy change (Doppler and gravitational) as well as the lensing effect for a distant observer directed along the inclination angle θ_o:

$$F_{\rm obs}\,(\theta_o, a, E_o) = \int T(r_e, \varphi_e, \theta_o, a)\, I(r_e, E_e)\, \mathrm{d}g\, r_e\, \mathrm{d}r_e, \tag{3.16}$$

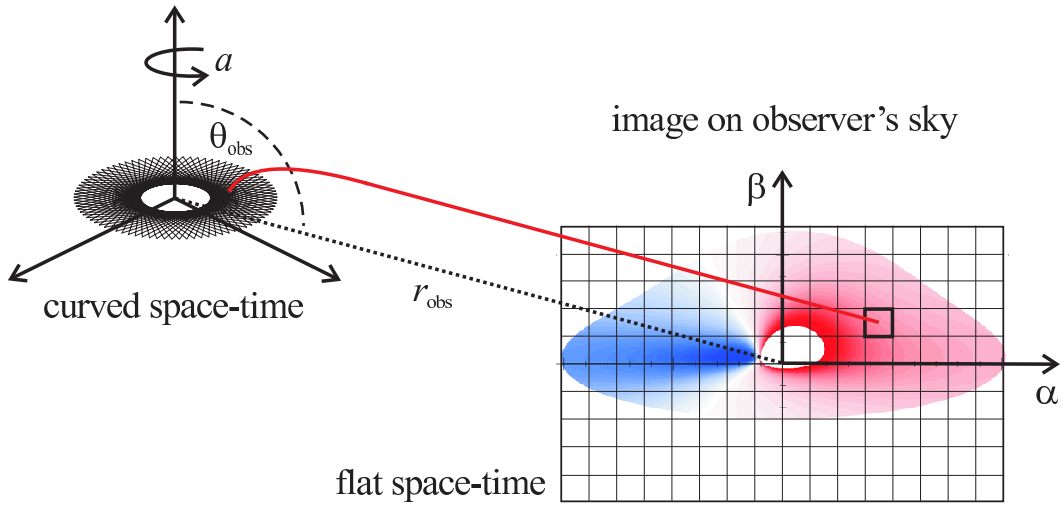

FIGURE 3.2: Schematic illustration of the ray-tracing method in the Kerr metric, showing a photon ray emitted from a radius in the accretion disk in Kerr coordinates and observed at a point of coordinates α,β on the disk image in the observer's reference frame. Image Credit: Jovanović & Popović, Copyright: Black Holes and Galaxy Formation, Nova Science Publishers Inc, Hauppauge NY, USA, 249-294 (2009).

where the index 'e' denotes quantities related to the disc and 'o' observed quantities. The integration is carried out over all possible values of the frequency shift g. The quantity $F_{\rm obs}\,(\theta_{\rm o}, a, E_{\rm o})$ is given by the integrated flux per energy bin. The integration can be carried out over the coordinates where the g-factor is computed at each place. We introduce the quantity I as the specific intensity, given by eq. (3.21). and the transfer functions given by $G_1 \equiv g^3$ and $G_2 = g^2\mu_{\rm e}\ell$. The relation for G_2 may be found from the transformation relation between the α, β coordinates and the Boyer-Lindquist coordinates of the disc r,φ. The relationship between the image plane coordinates and the local flux, expressed in Boyer-Lindquist coordinates is:

$$\frac{{\rm d}\alpha\,{\rm d}\beta}{r\,{\rm d}r\,{\rm d}\varphi} = \frac{{\rm d}S_{\rm o}}{{\rm d}S^{\perp}_{\rm loc}} \times \frac{{\rm d}S^{\perp}_{\rm loc}}{{\rm d}S_{\rm loc}} \times \frac{{\rm d}S_{\rm loc}}{{\rm d}S} = \frac{\ell\,\mu_{\rm e}}{g}, \tag{3.17}$$

where $S_{\rm o}$ is the observed element surface (i. e. in the detector frame), $S_{\rm loc}$ is the local element surface of the disc, and $\ell \equiv \frac{{\rm d}S_{\rm o}}{{\rm d}S^{\perp}_{\rm loc}}$ is the lensing factor defined as the ratio of the cross-section of the flux tube at the detector to the cross-section of the same flux tube at the disc. Using eqs. (3.19)–(3.17): $G_2 = g^2\mu_{\rm e}\ell$. In order to include the transfer function explicitly, we write

the observed flux at a particular frequency ν from an accretion disk as a function of specific intensity and frequency of a photon located at the radial location r_e:

$$F(\nu) = \int d\Omega \int d\nu_e T(\nu, \nu_e, r_e) I(\nu_e, r_e) \left(\frac{\nu}{\nu_e}\right)^3 , \tag{3.18}$$

where I is the specific intensity which is a function of the frequency ν_e of the emitted photon and the radial location r_e of the emitting material on the disk. The transfer function T determines the fraction of locally emitted energy that is ultimately detected by the observer at frequency ν. In addition to the intrinsic disk quantities ν_e and r_e, this function depends on the observed frequency, the inclination angle of the disk as given by the angle cosine μ, and the distance d between source and observer.

There are two possibilities how the observed flux is expressed:

1. in detector coordinates α, β:

$$F_{\rm obs}\,(\theta_{\rm o}, a, E_{\rm o}) = \int G_1(r_{\rm e}, \varphi_{\rm e}, \theta_{\rm o}, a)\, I(r_{\rm e}, E_{\rm e})\, {\rm d}\alpha\, {\rm d}\beta, \tag{3.19}$$

2. in Boyer-Lindquist coordinates of the disc r, φ:

$$F_{\rm obs}\,(\theta_{\rm o}, a, E_{\rm o}) = \int_0^{2\pi} \int_{r_{\rm in}}^{r_{\rm out}} G_2(r_{\rm e}, \varphi_{\rm e}, \theta_{\rm o}, a)\, I(r_{\rm e}, E_{\rm e})\, r_{\rm e}\, {\rm d}r_{\rm e}\, {\rm d}\varphi_{\rm e}, \tag{3.20}$$

where $G_1(r_{\rm e}, \varphi_{\rm e}, \theta_{\rm o}, a)$ and $G_2(r_{\rm e}, \varphi_{\rm e}, \theta_{\rm o}, a)$ are the previously introduced transfer functions.

The integration over $d\Omega$, an element of solid angle, covers the image of the disk in the observer's sky plane. The factor $(\nu/\nu_e)^3$ arises because $I_\nu/\nu^3 = I_{\nu_e}/{\nu_e}^3$ is an invariant from one observer to another, and from one event to another, along the entire trajectory of the photon. This invariant results from the principle of conservation of photons in a flux tube together with conservation of volume in phase space (Liouville's theorem holds in curved spacetime). Indeed, I_ν/ν^3 is equal, up to a power of Planck's constant, to the photon phase-space density.

We allow a to vary independently, in which case the horizon radius, $r_{\rm h}(a) \equiv 1 + \sqrt{1 - a^2}$, has to be, and indeed is, updated at each step of the procedure.

3.5 Photon flux from the black hole disc

In order to study the relativistic effects from emitting light from a Kerr black hole, it is necessary to compute the photon flux from a local proper area in the disc reaching the detector within a given solid angle and being measured in the rest frame co-moving with the disc. The flux contributions will be integrated over a mesh grid on the disc surface. The specific intensity I is defined as energy emitted at some given frequency ν into the element of solid angle Ω in unit of time t:

$$I = \frac{\mathrm{d}Nh\nu}{\mathrm{d}t\mathrm{d}\nu\mathrm{d}\Omega}, \tag{3.21}$$

where N is the total number of photons. The value of the intensity detected by an observer depends on the frequency shift of the emitted radiation. This relation may be derived from the Liouville's theorem which states that the phase-space volume Γ is invariant to the canonical transformations representing the time evolution of the system:

$$\int_\Gamma \mathrm{d}^n p\, \mathrm{d}^n q = C, \tag{3.22}$$

where n is the dimension, q expresses coordinates and p the conjugated momenta. In our application, the Liouville's theorem states that the phase-space density:

$$n = \frac{\mathrm{d}N}{\Gamma}, \tag{3.23}$$

is a constant of the Lorentz transformation. The element of the phase-space volume is dependent on the proper area S in the disc from where the emission originates:

$$\Gamma = \mathrm{d}^3 p \mathrm{d}^3 x = 4\pi p^2 \mathrm{d}p\mathrm{d}\Omega c\mathrm{d}S\,\mathrm{d}t. \tag{3.24}$$

Thus,

$$n = \frac{\mathrm{d}N}{4\pi p^2 \mathrm{dpd}\Omega\mathrm{cdSdt}}. \tag{3.25}$$

Substituting from (eq. 3.25) into (eq. 3.21) and using $p = \frac{h\nu}{c}$:

$$I(\nu) = \frac{4\pi h^4 c\mathrm{d}S\, n\nu^3}{c^3}, \tag{3.26}$$

and so

$$\frac{I}{\nu^3} = const. \tag{3.27}$$

Therefore we have

$$\frac{I_{\rm obs}}{I_{\rm em}} = \frac{{\nu_{\rm obs}}^3}{{\nu_{\rm em}}^3} = g^3. \tag{3.28}$$

This fact implies that the radiation from matter approaching the observer (blueshift) is boosted while the radiation from a matter receding from the observer (redshift) is diminished. The level of the intensity amplification (respectively diminution) depends on the values of the line-of-sight velocity.

The emission profile produced by the hot spot within the disk around a black hole is influenced by the Doppler shift, gravitational red-shift, beaming effect, and gravitational lensing effect. The changing of photon energy along a bundle of photon trajectories (geodesic congruence) can be characterized by the ratio g of the energy $E_{\rm obs}$ measured by a local inertial (rest) observer at asymptotic infinity to the emitted energy $E_{\rm em}$ measured by an observer co-moving with the plasma element on the accretion disk,

$$g = \frac{E_{\rm obs}}{E_{\rm em}} = \frac{(u^\mu p_\mu)_{\rm obs}}{(u^\mu p_\mu)_{\rm em}} = (1+z)^{-1} \ , \tag{3.29}$$

where $z \equiv (\lambda_{\rm obs} - \lambda_{\rm em})/\lambda_{\rm em}$ is the redshift as usually defined, u^μ in the denominator and numerator are the four-velocity of the emitting plasma element and the observer at infinity respectively, and p_μ is the four-momentum of the photon which propagates from the plasma element to the observer along a null geodesic. The total observed flux $F_{\rm obs}$ is determined by integrating the specific flux $\mathrm{d}F_{\rm obs}$ over all the plasma elements on the accreting disk. The specific flux $\mathrm{d}F_{\rm obs}(E_{\rm obs})$ at observed energy $E_{\rm obs}$ can be expressed as:

$$\mathrm{d}F_{\rm obs}(E_{\rm obs}) = I_{\rm obs}(E_{\rm obs})\mathrm{d}\Omega_{\rm obs} \ , \tag{3.30}$$

where $I_{\rm obs}$ is the observed specific intensity and $\mathrm{d}\Omega_{\rm obs}$ is the observed solid angle subtended by each plasma element. Using Liouville's theorem

$$I_{\rm obs}/\nu_{\rm obs}^3 = I_{\rm em}/\nu_{\rm em}^3 \tag{3.31}$$

we find

$$I_{\rm obs} = I_{\rm em}\nu_{\rm obs}^3/\nu_{\rm em}^3 = I_{\rm em}g^3 = I_{\rm em}(1+z)^{-3} \ . \tag{3.32}$$

And the observed solid angle $\mathrm{d}\Omega_{\rm obs}$ is naturally the size of the pixels in the observer's screen.

We trace every null geodesic from the observer's screen backwards towards the central black hole and search for the interactions of the trajectories with the surface of the disk. The shadowing from the observer due to the warping of the disk is taken into account. We calculate the observed flux $\mathrm{d}F_{\mathrm{obs}}$ from each plasma element, and add its contribution into a energy bin according to the observed energy of photons ($E_{\mathrm{obs}} = gE_{\mathrm{em}}$). Then we obtain the light curve profile by plotting the observed flux $\mathrm{d}F_{\mathrm{obs}}$ for all photons versus proper time. The number of bins we choose determines the spectrum resolution. We assume an optically thick disk, thus we consider only the direct photons and neglect the photons which would circulate around the black hole and strike the disk.

The properties of radiation are described in terms of photon numbers. The source appears as a point-like object to a distant observer and consequently the observer will measure the flux that enters the solid angle $\mathrm{d}\Omega_{\mathrm{o}}$, associated with the detector area $\mathrm{d}S_{\mathrm{o}} \equiv D^2\,\mathrm{d}\Omega_{\mathrm{o}}$ where D is the distance between the observer and the source. We define the total photon flux received by the detector,

$$N_{\mathrm{o}}^{S}(E) \equiv \frac{\mathrm{d}n(E)}{\mathrm{d}t\,\mathrm{d}S_{\mathrm{o}}} = \int \mathrm{d}\Omega\, N_{\mathrm{l}}(E/g)\, g^2\,, \tag{3.33}$$

where $\mathrm{d}n(E)$ is the number of photons with energy in the interval $\langle E, E + \mathrm{d}E \rangle$ and $g = E/E_{\mathrm{l}}$ is the redshift factor. We therefore have:

$$N_{\mathrm{l}}(E_{\mathrm{l}}) \equiv \frac{\mathrm{d}n_{\mathrm{l}}(E_{\mathrm{l}})}{\mathrm{d}\tau\,\mathrm{d}S_{\mathrm{l}}\,\mathrm{d}\Omega_{\mathrm{l}}} \tag{3.34}$$

the local photon flux emitted from the surface of the disc. The local flux, $N_{\mathrm{l}}(E_{\mathrm{l}})$, can also vary over the disc and in time, and it can also depend on the local emission angle. The emission that reaches the detector within a solid angle $\mathrm{d}\Omega$ originates from the proper area $\mathrm{d}S_{\mathrm{l}}$ on the disc (as measured in the rest frame co-moving with the disc). We integrate the flux contributions over a fine mesh on the disc surface. We adjust eq. (3.33) and obtain $N_{\mathrm{o}}^{S}(E)$ flux density:

$$N_{\mathrm{o}}^{S}(E) = \frac{1}{D^2}\int \mathrm{d}S\,\frac{D^2\mathrm{d}\Omega}{\mathrm{d}S}\,N_{\mathrm{l}}(E/g)\,g^2 = \frac{1}{D^2}\int \mathrm{d}S\,\frac{\mathrm{d}S_{\perp}}{\mathrm{d}S}\,\frac{\mathrm{d}S_{\mathrm{f}}}{\mathrm{d}S_{\perp}}\,N_{\mathrm{l}}(E/g)\,g^2\,. \tag{3.35}$$

Here $\mathrm{d}S_{\mathrm{f}}$ is an element of area perpendicular to light rays corresponding to the solid angle $\mathrm{d}\Omega$ at a distance D, $\mathrm{d}S_{\perp}$ is the proper area measured in the local frame of the disc and perpendicular to the photon rays, and $\mathrm{d}S$ is the coordinate area. We integrate in a two-dimensional slice of a four-dimensional space-time, which is specified by coordinates θ =

$\pi/2$ and $t = t_o - \Delta t$ with Δt being a time delay with which photons from different parts of the disc (that lies in the equatorial plane) arrive to the observer (at the same coordinate time t_o). The coordinates are t', θ, r, φ with $t' = t - \Delta t$ and $\Delta t = \Delta t(r, \theta, \varphi)$. Therefore, let us define the coordinate area by

$$\mathrm{d}S \equiv |\mathrm{d}^2S_{t'}{}^{\theta}| = \left|\frac{\partial x^{\mu}}{\partial t'}\mathrm{d}^2S_{\mu}{}^{\theta}\right| = |\mathrm{d}^2S_{t}{}^{\theta}| = |g^{\theta\mu}\mathrm{d}^2S_{t\mu}|\,. \tag{3.36}$$

The tensor $\mathrm{d}^2S_{\alpha\beta}$ is described by the two four-vector elements $\mathrm{d}x_1^{\mu} \equiv (\mathrm{d}t_1, \mathrm{d}r, 0, 0)$ and $\mathrm{d}x_2^{\mu} \equiv (\mathrm{d}t_2, 0, 0, \mathrm{d}\varphi)$ and by Levi-Civita tensor $\varepsilon_{\alpha\beta\gamma\delta}$. The time components of these vectors, $\mathrm{d}t_1$ and $\mathrm{d}t_2$, are such that the vectors $\mathrm{d}x_1^{\mu}$ and $\mathrm{d}x_2^{\mu}$ lie in the tangent space to the slice. Therefore

$$\mathrm{d}S = |g^{\theta\theta}\varepsilon_{t\theta\alpha\beta}\,\mathrm{d}x_1^{[\alpha}\mathrm{d}x_2^{\beta]}| = g^{\theta\theta}\sqrt{-\|g_{\mu\nu}\|}\,\mathrm{d}r\,\mathrm{d}\varphi = \mathrm{d}r\,\mathrm{d}\varphi\,, \tag{3.37}$$

where $g_{\mu\nu}$ is the metric tensor and $\|g_{\mu\nu}\|$ the determinant of the metric. The area $\mathrm{d}S_{\perp}$ is perpendicular to the photon rays:

$$\mathrm{d}S_{\perp} = -\frac{U^{\alpha}\,p^{\beta}\,\mathrm{d}^2S_{\alpha\beta}}{U^{\mu}\,p_{\mu}}\,. \tag{3.38}$$

The projection of an element of area, $\mathrm{d}S_{\perp}$ is defined by $\mathrm{d}^2S_{\alpha\beta}$, on a spatial slice of an observer with velocity U^{α} and it is perpendicular to the photon ray. In Special Kerr ingoing coordinates (Kerr-Schild form), the spatial infinity is brought to a finite value (to zero) and the element area $\mathrm{d}S$ is independent of the metric coefficients. Here, U^{α} is the four-velocity of an observer measuring the area $\mathrm{d}S_{\perp}$, and p^{β} is the four-momentum of the photon. The area $\mathrm{d}S_{\perp}$ associated to the same flux tube will be the same to all observers:

$$p^{\beta}\,\mathrm{d}^2S_{\alpha\beta} + p_{\alpha}\,\mathrm{d}S_{\perp} = 0\,, \quad \alpha = t,\, r,\, \theta,\, \varphi\,. \tag{3.39}$$

For $\alpha = t$ we have

$$\frac{\mathrm{d}S_{\perp}}{\mathrm{d}S} = \left|\frac{1}{g^{\theta\theta}}\frac{\mathrm{d}S_{\perp}}{\mathrm{d}^2S_{t\theta}}\right| = \left|-\frac{p_{\theta}}{p_t}\right| = \frac{r\mu_{\mathrm{e}}}{g}\,. \tag{3.40}$$

From eqs. (3.35), (3.36) and (3.40) the observed flux (density) per unit solid angle (Figure 3.3) becomes

$$N_{\mathrm{o}}^{\Omega}(E) \equiv \frac{\mathrm{d}n(E)}{\mathrm{d}t\,\mathrm{d}\Omega_{\mathrm{o}}} = N_0\int_{r_{\mathrm{in}}}^{r_{\mathrm{out}}}\mathrm{d}r\int_{\phi}^{\phi+\Delta\phi}\mathrm{d}\varphi\,N_{\mathrm{I}}(E/g)\,g\,l\,\mu_{\mathrm{e}}\,r, \tag{3.41}$$

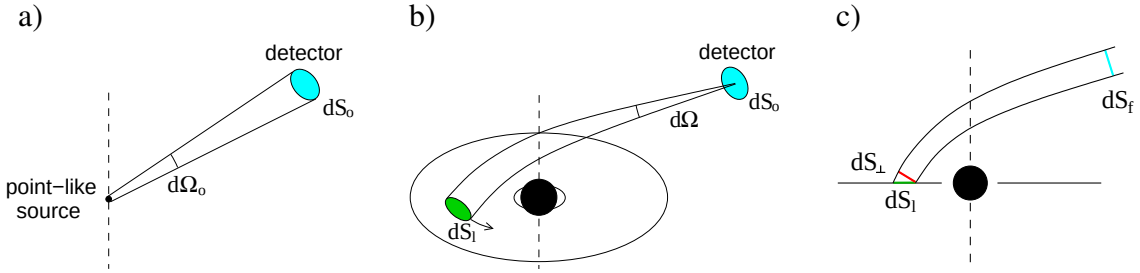

FIGURE 3.3: Approximations of solid angles and areas: a) the light source appears to the observer as point-like; b) the light rays received by the detector arriving from different parts of the disc (closer view); c) area of the light tube is changing as the a photon ray travels close to the black hole (the disc is edge on). Credit: M Dovciak, 2004

with N_0 the normalization constant and

$$l = \frac{\mathrm{d}S_\mathrm{f}}{\mathrm{d}S_\perp} \tag{3.42}$$

is the lensing factor in the limit $D \to \infty$ (keeping $D^2\mathrm{d}\Omega$ constant).

The integrated flux per energy bin, ΔE, becomes

$$\begin{aligned}\Delta N_\mathrm{o}^\Omega(E,\Delta E,t) &= \int_E^{E+\Delta E} \mathrm{d}\bar{E}\, N_\mathrm{o}^\Omega(\bar{E},t) = \\ &= N_0 \int_{r_\mathrm{in}}^{r_\mathrm{out}} \mathrm{d}r \int_\phi^{\phi+\Delta\phi} \mathrm{d}\varphi \int_{E/g}^{(E+\Delta E)/g} \mathrm{d}E_\mathrm{l}\, N_\mathrm{l}(E_\mathrm{l},r,\varphi,\mu_\mathrm{e},t-\Delta t)\, g^2\, l\, \mu_\mathrm{e}\, r\,,\end{aligned} \tag{3.43}$$

with Δt the relative time delay describing which photons arrive to the observer from different parts of the accretion disc. The transfer functions g, l, μ_e and Δt are pre-calculated and stored in FITS files. The transfer functions are generated for light rays emitted from the equatorial plane of the Kerr black hole and received by the observer located at infinity. The values of FITS functions for different spins of the black hole and inclination angles of the observer in Kerr ingoing coordinates are stored in each FITS file.

For a given local flux, we have $N_\mathrm{l}(E_\mathrm{l},r,\varphi,\mu_\mathrm{e},t-\Delta t)$. The observed flux $F_\mathrm{o}^\Omega(E)$ can be written as a function of the local flux $F_\mathrm{l}(E_\mathrm{l})$ in the disk:

$$F_\mathrm{o}^\Omega(E) = \int_{-\infty}^{\infty} \mathrm{d}E_\mathrm{l}\, F_\mathrm{l}(E_\mathrm{l})\, G(E,E_\mathrm{l}), \tag{3.44}$$

where

$$G(E,E_\mathrm{l}) = F_0 \int_{r_\mathrm{in}}^{r_\mathrm{out}} \mathrm{d}r\, R(r) \int_0^{2\pi} \mathrm{d}\varphi\, g^2\, l\, r\, \delta(E - gE_\mathrm{l}). \tag{3.45}$$

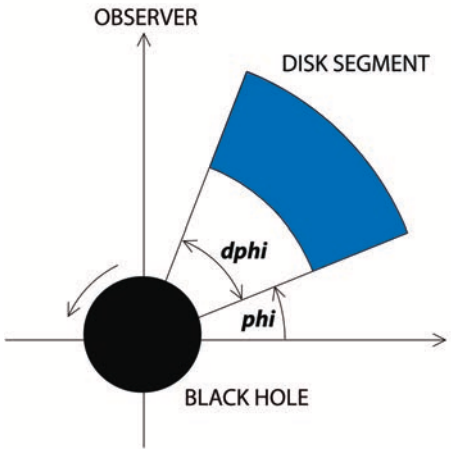

FIGURE 3.4: Segment of the thin disc from where the emission arises.

In this case, the integrated flux can be expressed in the following way:

$$\Delta F_{\rm o}^{\Omega}(E,\Delta E) \;=\; \int_{E}^{E+\Delta E} {\rm d}\bar{E}\, F_{\rm o}^{\Omega}(\bar{E}) \;=$$
$$= \int_{E}^{E+\Delta E} {\rm d}\bar{E}\, F_0 \int_{r_{\rm in}}^{r_{\rm out}} {\rm d}r\, R(r) \int_0^{2\pi} {\rm d}\varphi\, F_1(\bar{E}/g)\, g\, l\, r \int_{-\infty}^{\infty} {\rm d}E_1\, \delta(E_1 - \bar{E}/g) =$$
$$= F_0 \int_{r_{\rm in}}^{r_{\rm out}} {\rm d}r\, R(r) \int_{-\infty}^{\infty} {\rm d}E_1\, N_1(E_1) \int_{E/E_1}^{(E+\Delta E)/E_1} {\rm d}\bar{g}\, F(\bar{g})\,, \tag{3.46}$$

where we substituted $\bar{g} = \bar{E}/E_1$ and

$$F(\bar{g}) = \int_0^{2\pi} {\rm d}\varphi\, g^2\, l\, r\, \delta(\bar{g} - g)\,. \tag{3.47}$$

The function ${\rm d}F(\bar{g}) \equiv {\rm d}\bar{g}\, F(\bar{g})$ has been already pre-calculated and stored in separate files.

The main subroutine integrates the local emission parameters for unpolarized emission from the accretion disc near a rotating (Kerr) black hole characterized by the angular momentum a) for an observer with an inclination angle $\theta_{\rm o}$. The emission originates in the disk and the photon flux is computed at the observer's plane. Photons emitted in the vicinity of the Kerr black hole travel to the observer on null geodesics in curved spacetime and their light curves are computed using numerical integration over a solid angle subtended by the observer's plane.

The inner and outer radii are relative to the black hole horizon and, their minimum value is zero. The `ms` switch determines if we the emission originates below the marginally stable

orbit. If the value is zero and the disk inner radius is below this orbit, only the emission below the marginally stable orbit will be considered.

The `phi` and `dphi` parameters represent the axial sector of the disc from which emission comes as we can see in Figure 3.4. The `nrad` and `nphi` parameters determine the grid for numerical integration. If the `division` parameter is zero, the radial grid is equidistant; if it is one, the radial grid has an exponential form, with more points closer to the black hole.

3.6 Transfer functions

All special and general relativistic effects are stored in transfer functions that are computed backwards from the observer towards the black hole disk.

A number of functions (transfer functions) are necessary for the transfer of the local flux to infinity. Some functions are numerically calculated across the emitting region: (i) the energy shift affecting the photons or the gravitational and Doppler g-factor (ii) the gravitational lensing, (iii) the relative time-delay of the observed photon or the delay between different photons arriving from various regions of the emitting source. The time-delay factor is required here as the emission is not stationary (an orbiting blob).

The transfer functions are stored in the form of tables in a FITS (Flexible Image Transport System) file. The transfer of photons is computed from infinity and setting the initial radius $r_{\rm i} = 10^{11}$ to the disc by solving the equation of the geodesic. For this purpose the Bulirsch-Stoer method of integration was necessary.

These tables are calculated for the vacuum Kerr space-time and for a Keplerian co-rotating disc plus matter that is freely falling below the marginally stable orbit. The falling matter has the energy and angular momentum of the matter at the marginally stable orbit. It is possible to use different pre-calculated tables as long as they are stored in a specific FITS file. The ray-tracing method is associated with a radiation transfer routine that calculates the intrinsic continuum spectrum of the source.

The local emission from the area in the disk is time dependent therefore, we must take into account the relative delay with which photons from different parts of the disc may arrive to the observer.

An optically thick and geometrically thin flat disc has been assumed. Only null geodesics starting at the observer at infinity and ending at the equatorial plane of the black hole, with no crossing of the plane, is considered.

The transfer functions are necessary to transfer the local flux to the observer at infinity. The Kerr metric is used and the medium between the disc and the observer is assumed optically thin for wavelengths in which we are interested.

Special Kerr ingoing coordinates, non-singular at the horizon, with spatial infinity (in Kerr asymptotic limit) to a finite value (to zero), will be used. This allows the integration of the photon rays from a local area in the disc to a detector located at infinity. The code integrates the photon geodesics between a position inside the orbiting spot and an observer at infinity (by setting the initial radius at a distance where relativistic effects are negligible and the flux is not affected by the transfer functions). The transfer functions with a high precision even very close to the horizon of the black hole are therefore calculated. The Boyer-Lindquist azimuthal coordinate φ is transformed into Kerr coordinate φ_{K}, more precise for the interpolation between the disk values.

A number of transfer functions are directly dependent of the motion of the matter in the disc, assumed Keplerian above the marginally stable orbit r_{ms} and freely falling below it, where it has the same angular momentum as the matter which is on the marginally stable orbit.

Each transfer function except the lensing effect were pre-calculated analytically using the mapping of the impact parameters α and β to the disc coordinates r and φ_{K}.

We used 10^5 geodesic trajectories in the numerical simulation. The photon paths cover the region between the inner disc radius, close to the horizon to the disc outer radius of $r_{\mathrm{out}} \sim 1000$. The region that is closest to the horizon is most densely covered. The transfer functions on a non-regular grid over the disc are interpolated to a regular grid in r and φ_{K} coordinates using Delaunay triangulation.

In the next few subsections, we will address and define each transfer function used here: Gravitational shift, Doppler shift, Gravitational lensing and Relative time delay.

3.6.1 Gravitational and Doppler shifts

Light emitted from a moving emitting source is shifted in frequency as observed by a stationary observer:

$$\nu_0 = \gamma\nu_e(1 - \beta\cos\theta) \tag{3.48}$$

$$\tan\theta' = \frac{\sin\theta}{\gamma(\cos\theta - \beta)} \tag{3.49}$$

where ν_o and ν_e are the observed and emitted photon frequencies, β = v/c,$\gamma = \sqrt{(}1 - \beta^2)$, **v** is the relative velocity between the emission source and the observer, and the angles θ and θ' are between the 4-vectors in different inertial frames with respect to **v**. The first order in β and θ =0 gives the standard Doppler shift:

$$\nu_0 = \nu_e(1 - v/c) \tag{3.50}$$

which is a frequency shift in the direction perpendicular to the motion of the emitting source or the transverse Doppler effect. For $\theta = \pi/2$, we have

$$\nu_0 = \nu_e\gamma \tag{3.51}$$

Doppler distortion is a key feature of relativistic spectra exhibiting skewed and asymmetric and broadened light curve profiles, shifting the flux contribution from each radius to lower energy values. This effect is important only very close to the black hole.

The photons that originate within the disc change their energy due to the gravitational and Doppler shifts as they are are emitted by matter moving close to the source of strong gravitation. The cross-section of light tube will change as the photons rays propagate in the vacuum. We will see that such an effect is stronger for high inclinations of the observer and when the photons paths originating from behind the black hole are bent more. The bending effect also influences the area from which the photons arrive due to different emission angles. An aberration effect will be created by the motion of the disc matter. All these effects influence the intensity of light that the observer will measure.

Motion of matter in Keplerian rotation within the accretion disc is dominated by the gravitational potential of the black hole. Close to the black hole, the Keplerian velocity,

v_K becomes very large, reaching a significant fraction of the velocity of light. In the Locally Non-Rotating Frame (LNRF), i.e. the reference frame "rotating with the Black Hole" (Bardeen et al. 1972), the Keplerian velocity is:

$$v_K/c = \frac{r^2 - 2a\sqrt{r} + a^2}{(r^2 + a^2 - 2r)^{\frac{1}{2}}\,(r^{3/2} + a)}. \tag{3.52}$$

The accretion flow velocities can be very high near the event horizon, eventually reaching the speed of light and causing the frequency of the radiation of the infalling matter to be Doppler shifted and its intensity to be highly boosted. Just under $3GM/c^2$ the redshift starts dominating the light curve and almost no blueshift is present, the flux amplitude being highly suppressed. However, the gravitational potential near the event horizon is very strong, producing time dilation, which in turn will shift the radiation to lower frequencies. Time dilation will shift the light curves at earlier starting times, the photon arrival time being considerably modified for photons arriving from inner regions of the disk. A distortion of the light travel time and redshift contours from straight lines will occur near the black hole.

The transverse Doppler effect represents the nominal redshift or blueshift predicted by special relativity and it occurs when the emitter and receiver are at the point of closest approach.

Light aberration causes most of the photons to be emitted along the direction of motion. The Doppler effect changes the energy of the photons by red- or blue-shifting them. Time intervals as measured by clocks moving alongside the emitting object are different from those measured by an observer on Earth due to time dilation and photon arrival time effects. How all of these effects modify the brightness, or apparent luminosity, of a moving object is determined by the equation describing the relativistic Doppler effect (which is why relativistic beaming is also known as Doppler beaming).

The Keplerian velocity can be as high as almost half the speed of light, implying that the Doppler shift and boosting could be very significant. Doppler boosting is the brightening/dimming of the flux when the matter is approaching/receding. It is a Special Relativity aberration effect due to the fact that I_ν/ν^3 is a Lorentz invariant. As a result of light bending, geodesics of photons emitted in the far side of the disc are strongly curved making the disc appears bent towards the observer (see e.g. Luminet 1979, 1992).

Gravitational redshift in strong field potential produces remarkable distortions of the light curves if the rest frame feature is compared to its analogue in the observer's frame. The gravitational redshift decreases the energy of photons and accordingly their frequency while they propagate out of a gravitational potential. The deeper the potential the photon has to overcome, the higher the redshift. Hence this effect is especially relevant for massive and compact objects. This is true only for photons emitted from orbital radii exceeding the Schwarzschild radius, at which the redshift approaches infinity. Gravitational redshift shifts the spectral features and changes the shape of the light curve when compared to its analogue in the observers frame.

The g-factor is defined as the combined gravitational and Doppler shift and more explicitly as the ratio of the energy of a photon received by an observer at infinity to the local energy of the same photon emitted from the black hole disc

$$g = \frac{\nu_{\rm o}}{\nu_{\rm e}} = \frac{p_{{\rm o}\,t}}{p_{{\rm e}\,\mu}\,U^{\mu}} = -\frac{1}{p_{{\rm e}\,\mu}\,U^{\mu}}\,. \tag{3.53}$$

The frequencies $\nu_{\rm o}$ and $\nu_{\rm e}$ are the frequency of the observed and emitted photons, and U^{μ} represents the four-velocity of the matter within the accretion disc. For rotating black holes, the g-factor is defined as a function of the position within the disc and the emission angle $g = g\,(R, \varphi, \theta_e)$. For definition purposes only, we introduce the quantity $V_{\rm los}$, in order to introduce the transverse Doppler effect. For Keplerian orbital velocities we have, $V_{\rm los} = \sqrt{\frac{GM}{R}}\cos\varphi\sin\theta$.

In special relativistic approach, we have

$$g_{\rm STR} = \frac{1}{\gamma\left(1 - \frac{V_{\rm los}}{c}\right)}, \tag{3.54}$$

where $\gamma = \frac{1}{\sqrt{1-\frac{v^2}{c^2}}}$ is the Lorentz factor. The observed frequency is shifted even when the line-of-sight velocity is zero ($V_{\rm los} = 0$, "face-on" disc). Since $g_{\rm STR} = \gamma^{-1} < 1$ in this case, the frequency is shifted to lower energies. This effect is called the transverse Doppler shift.

In general relativity, the g-factor is defined in the geometrical optic approximation using the four-momentum of photons p_{μ} and the four-velocities u^{μ}. A g-factor of unity corresponds to un-shifted emission, while $g < 1$ indicates the redshifted emission and $g > 1$ the

blueshifted emission. We therefore have:

$$g = \frac{\left(p_\mu u^\mu\right)_{\rm obs}}{\left(p_\mu u^\mu\right)_{\rm em}}. \tag{3.55}$$

Using $u^\mu{}_{\rm obs} = [-1, 0, 0, 0]$ (four-velocity of the observer):

$$g = \frac{-(p_t)_{\rm obs}}{\left(p_\mu u^\mu\right)_{\rm em}}. \tag{3.56}$$

The frequency shift g and the emission angle $\theta_{\rm e}$ depend on the constants of motion:

$$g = \frac{C}{\mathcal{B} - r^{-3/2}\xi}, \quad \theta_{\rm e} = \arccos\frac{g\sqrt{\eta}}{r}, \tag{3.57}$$

where $\mathcal{B} = 1 + ar^{-3/2}$, $C = 1 - 3r^{-1} + 2ar^{-3/2}$; ξ and η are constants of motion using the common symmetries of the Kerr metric.

The higher intensity for the blue shifted photons will be caused by relativistic beaming, caused by the Lorentz invariance of I_ν/ν^3 along the photon bundle. Approaching the black hole, the spacetime curvature becomes more significant and the redshift grows rapidly whereas the g-factor approaches zero. It is important to mention that because of the asymptotical flatness of the Kerr spacetime, the spacetime curvature approaches zero at infinity. Therefore, there is no finite distance at which the gravitational redshift would vanish completely.

3.6.2 Gravitational lensing

The flux from a hot spot is periodically modulated on orbital timescales through gravitational lensing by the black hole. The shape of the disk itself is distorted because of gravitational lensing. The amount of deflection depends upon the mass distribution of the gravitational lens and the bend angle depends on the gradient of the gravitational potential. In a typical lensing situation, a photon is emitted from the source, approaches the black hole to a minimum distance and then escapes toward the observer. In some cases, the photon goes directly from the source to the observer moving away at all times from the black hole (see Figure 3.5). The lensing effect is derived from the integration of the equation of the geodesic deviation. The equation of the geodesic

$$\frac{{\rm D}p^\mu}{{\rm d}\lambda'} = \frac{{\rm d}p^\mu}{{\rm d}\lambda'} + \Gamma^\mu_{\sigma\tau} p^\sigma p^\tau, \quad \mu = \hat{t},\, \hat{u},\, \hat{\mu},\, \hat{\varphi} \tag{3.58}$$

and the equation of the geodesic deviation

$$\frac{\mathrm{d}^2 Y^{\mu}_{\mathrm{j}}}{\mathrm{d}\lambda'^2} + 2\Gamma^{\mu}_{\sigma\gamma} p^{\sigma} \frac{\mathrm{d}Y^{\gamma}_{\mathrm{j}}}{\mathrm{d}\lambda'} + \Gamma^{\mu}_{\sigma\tau,\gamma} p^{\sigma} p^{\tau} Y^{\gamma}_{\mathrm{j}} = 0\,, \quad \mu = \hat{t},\, \hat{u},\, \hat{\mu},\, \hat{\varphi}\,, \quad \mathrm{j} = 1,\, 2 \tag{3.59}$$

solutions in special Kerr ingoing coordinates $\hat{t}$, $\hat{u}$, $\hat{\mu}$, $\hat{\varphi}$ lead to computing the transfer functions over the accretion disc, where $p^{\mu} \equiv \frac{\mathrm{d}x^{\mu}}{\mathrm{d}\lambda'}$ is a four-momentum of light, λ' is an affine parameter for which the conserved energy $-p_t = 1$, Y^{μ}_{j} are two vectors characterizing the distance between nearby geodesics and $\Gamma^{\sigma}_{\mu\nu}$ are Christoffel symbols for the Kerr metric. In the initial point, the vectors are chosen to allow for the metric to be flat-space Minkowski at infinity, perpendicular to each other and to the four-momentum of light, space-like and have unit length.

The lensing effect is defined as the ratio of the cross-section $\mathrm{d}S_{\mathrm{f}}$ of the light tube at infinity to the cross-section $\mathrm{d}S_{\perp}$ of the light tube at the disc:

$$l = \frac{\mathrm{d}S_{\mathrm{f}}}{\mathrm{d}S_{\perp}} = \frac{1}{\sqrt{||Y_{\mathrm{e}1}||^2 ||Y_{\mathrm{e}2}||^2 - < Y_{\mathrm{e}1}, Y_{\mathrm{e}2} >^2}}\,. \tag{3.60}$$

where the magnitude of a four-vector is $||\ ||$ and the scalar product of two four-vectors is $<\ ,\ >$.

The four-vectors $Y_{\mathrm{e}1}$ and $Y_{\mathrm{e}2}$ are transported along the geodesic according to the equation of the geodesic deviation from infinity, space-like and perpendicular to each other and to the four-momentum of light. At infinity, the four-vectors are one. The cross section of the light tube is constant for all possible observers.

Stronger amplification occurs via gravitational lensing effect, if a precise geometrical alignment with the caustic position can be satisfied (e.g. Rauch and Blandford 1994; Bozza et al. 2005). The light rays emitted by a source are expected to be bent by the strong gravitational field, appearing at many different locations on the sky plane. In Figure 3.6, light rays starting from a source could orbit the black hole several times before reaching the observer generating an arbitrary number of Einstein rings. The analytical lens equations provide the position of multiple lensed images of the source together with the time of arrival of each image. Theoretically, infinitely higher order images can be formed. There is a constraint here, however. The higher order images should be exponentially suppressed in angular diameter and have increasingly longer light travel times compared to the original image.

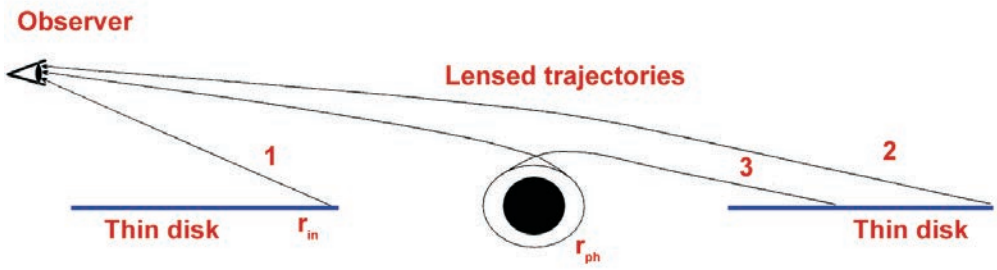

FIGURE 3.5: Photon trajectories coming from a thin accretion disk around a black hole at a high viewing angle. The trajectories passing the black hole in its very near vicinity are strongly lensed. The rays (1) are not very well gravitationally focussed, being in front of the black hole and closest to the observer. The rays (2) are strongly focussed as they come from behind the black hole and light will be bent as the ray passes the black hole. The rays (3) are both behind the black hole and closer to the black hole, therefore are affected the most by the lensing effect. These rays will produce higher order images because the photons orbit the black hole more times before they reach the observer.

The lensing effect magnifies the emission from some parts of the disc especially from behind the black hole from the observer's point of view in Kerr ingoing coordinates, becoming significant for observers at large inclination angles. Gravitational lensing effects on the intensity of the light are implicitly included in the generated light curve. If a region of the disk is magnified then it will cover more area in the sky plane, and thus will appear brighter than a non-magnified area. As the inclination angle also influences the amplitude of the light curve, we take into account that an inclined disk will cover less pixels in the sky plane than a face-on disk, where the number of pixels is roughly proportional to the inclination angle. The light bending effect will cause this euclidean proportionality to be only a rough approximation.

The gravitational lensing factor is proportional to the solid angle that a finite patch of emitting material subtends in the sky plane of the observer.

The lensing effect is calculated implicitly by the mapping of photon trajectories from the emitting region to the observer's sky plane. Lensing is manifested in the distortion of the disk relative to an image in flat space; regions of high amplification simply occupy more

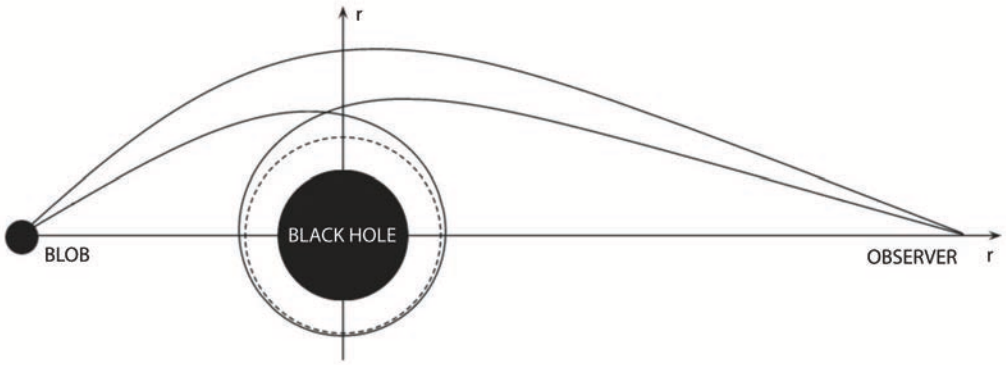

FIGURE 3.6: The observer located very far from the black hole observes two concentric Einstein rings formed by photons arriving at various times, measured with respect to the observers proper time. The two null geodesics that connect the blob and the observer have different light travel times. The dotted line represents the circular photon orbit.

pixels and thus appear magnified in the sense of geometric optics. The amplification factor for a given point on the disk is thus evaluated by mapping adjacent pixels to the disk surface.

The gravitational lensing and magnification of emission from the spot within the accretion disk is performed automatically by the geodesic integration of evenly spaced photon trajectories, stored in their respective transfer functions, so that high magnification will occur in regions where nearby points in the disk are projected to points with large separation in the image plane.

As the rays are deflected by the black hole, they tend to be focused on the far side, giving a strong magnification by mapping a large area in the image plane onto a small area of the source plane, using a higher density of lattice grid points.

To be able to estimate the effect of gravitational potential on the photons (and consequently the amplitude of the flux) coming from different parts of the disc, all three effects have to be taken into account: the g-factor, the emission angle μ_e and the gravitational lensing.

The gravitational lensing enhances the flux from the far side of the disc and magnifies the image of regions with velocity mostly tangential to the line of sight, without being strongly Doppler shifted. This fact boosts the light curve at g approaching unity.

Gravitational lensing causes significant magnification of the emission region when it is on the far side of the black hole, spreading the image of a single blob into an arc, much like galaxies are distorted by intervening matter in distant galaxy clusters.

3.6.3 Relative time delay

The relative time delay Δt is defined as the time elapsed between the emission of a photon from the accretion disc and the reception by a distant observer, in Boyer-Lindquist coordinates. This also includes a constant so that the delay is finite close to the black hole but not too close. If the equation of the geodesic is integrated in Kerr ingoing coordinates we are able to calculate the time delay in Kerr ingoing time coordinates $\Delta t_{\rm K}$.

The Boyer-Lindquist time is determined from $\Delta t_{\rm K}$ using:

$$\mathrm{d}t = \mathrm{d}t_{\rm K} - \left[1 + \frac{2r}{(r-r_+)(r-r_-)}\right]\mathrm{d}r\,, \tag{3.61}$$

with $r_\pm = 1 \pm \sqrt{1-a^2}$ the inner (−) and outer (+) horizon of the black hole. Let us integrate the equation and determine the time delay

$$\Delta t = \Delta t_{\rm K} - \left[r + \frac{2}{r_+ - r_-}\ln\frac{r-r_+}{r-r_-} + \ln\left[(r-r_+)(r-r_-)\right]\right] \quad \text{for } a < 1\,, \tag{3.62}$$

$$\Delta t = \Delta t_{\rm K} - \left[r - \frac{2}{r-1} + 2\ln(r-1)\right] \quad \text{for } a = 1\,. \tag{3.63}$$

The direction of integration is backwards in time from infinity to the disc.

3.7 Velocity of the emitter

In order to derive the 4-velocity of a plasma element in the disk, we need to derive the velocity components in spherical coordinates by projecting the orbital plane $x'y'$ (in $x'y'z'$ frame) of the emitter onto the equatorial plane xy (in xyz frame) of the black hole. The angular position of the each plasma element be $\varphi = \Omega t$, with t the coordinate time in the Kerr metric and the plasma particle's velocity components are

$$\mathbf{v}' = dx_{i'}/dt = v\,(-\sin\varphi, \cos\varphi, 0)\,, \tag{3.64}$$

where $v = r\Omega = r(a + \epsilon\sqrt{r^3/M})^{-1}$ and $\epsilon = +1$ is for prograde orbiting, $\epsilon = -1$ is for retrograde orbiting. In addition, we need to transform the velocity into the coordinate frame in which the z axis is aligned with the black hole spin. The y' axis coincides with the line of nodes and points at the ascending node. The xy plane is the equatorial plane which has a tilt angle β relative to the $x'y'$ plane. The projection of the z' axis on the xy plane has a twist angle γ relative to the x axis. We find the components v_i in the xyz coordinate basis using $v_i = T_{ij'}v_{j'}$, where

$$T_{ij'} = \begin{pmatrix} \cos\gamma\cos\beta & -\sin\gamma & -\cos\gamma\sin\beta \\ \sin\gamma\cos\beta & \cos\gamma & -\sin\lambda\sin\beta \\ \sin\beta & 0 & \cos\beta \end{pmatrix}, \tag{3.65}$$

from which we get

$$\begin{aligned} v_x &= v\,(-\cos\gamma\cos\beta\sin\varphi - \sin\gamma\cos\varphi) \\ v_y &= v\,(-\sin\gamma\cos\beta\sin\varphi + \cos\gamma\cos\varphi) \\ v_z &= v\,(-\sin\beta\sin\varphi)\ . \end{aligned} \tag{3.66}$$

In our calculations, we assume that the disk lies in the equatorial plane of the black hole, so that $\beta = 0$.

We calculate the velocity components in spherical coordinates by projecting the velocity $\mathbf{v}$ onto the spherical basis $\mathbf{e}_r$, $\mathbf{e}_\theta$, $\mathbf{e}_\phi$

$$\begin{aligned} v_r &= 0 \\ v_\theta &= v\,(-\cos\psi\cos\beta\sin\varphi\cos\theta + \sin\psi\cos\varphi\cos\theta + \sin\beta\sin\varphi\sin\theta) \\ v_\phi &= v\,(\sin\psi\cos\beta\sin\varphi + \cos\psi\cos\varphi)\ . \end{aligned} \tag{3.67}$$

where $\psi = \phi - \gamma$ is the azimuthal angle of the plasma element measured from the projection of the x' axis on the xy plane.

If we define τ as the proper time of the plasma element, we have

$$-d\tau^2 = ds^2 = -\Sigma\Delta A^{-1}dt^2 + \sin^2\theta A\Sigma^{-1}\,(d\phi - \omega dt)^2 + \Sigma\Delta^{-1}dr^2 + \Sigma d\theta^2\,, \tag{3.68}$$

and we divide both sides by dt^2

$$-\frac{d\tau^2}{dt^2} = -\Sigma\Delta A^{-1} + \sin^2\theta A\Sigma^{-1}\left(\dot{\phi} - \omega\right)^2 + \Sigma\dot{\theta}^2\,. \tag{3.69}$$

We can now write the 4-velocity of the plasma element:

$$\begin{aligned} u^0 &= \frac{dt}{d\tau} = \left(\Sigma\Delta A^{-1} - \sin^2\theta A\Sigma^{-1}\left(\dot{\phi}-\omega\right)^2 - \Sigma\dot{\theta}^2\right)^{-1/2} \\ u^r &= \frac{dr}{d\tau} = \frac{dr}{dt}\frac{dt}{d\tau} = \dot{r}u^0 = 0 \\ u^\theta &= \frac{d\theta}{d\tau} = \frac{d\theta}{dt}\frac{dt}{d\tau} = \dot{\theta}u^0 = u^0\frac{v_\theta}{r} \\ u^\phi &= \frac{d\phi}{d\tau} = \frac{d\phi}{dt}\frac{dt}{d\tau} = \dot{\phi}u^0 = u^0\frac{v_\phi}{r\sin\theta}\,. \end{aligned} \tag{3.70}$$

The radial component of the velocity is zero because of we assumed that the particle follows only Keplerian orbits.

The 4-velocity of the particle are defined by the Boyer-Lindquist coordinates. The expression for g is

$$g = \frac{E_{\rm obs}}{E_{\rm em}} = \frac{(u^\mu p_\mu)_{\rm obs}}{(u^\mu p_\mu)_{\rm em}} = (1+z)^{-1}\ . \tag{3.71}$$

The observer at rest at infinity has the 4-velocity p_μ=(-1, 0, 0, 0), thus in the numerator $(u^\mu p_\mu)_{\rm obs} = E$; while in the denominator

$$(u^\mu p_\mu)_{\rm em} = -Eu^0 \pm Eu^0\sqrt{\Theta}v_\theta/r + L_z u^0 v_\phi/\sin\theta\ , \tag{3.72}$$

therefore we have

$$g = \frac{1}{u^0(-1 \pm \sqrt{\Theta}v_\theta/r + \xi v_\phi/\sin\theta)}\ , \tag{3.73}$$

where the sign is given by the zenithal emitting direction.

4

Relativistic signatures in light curves

4.1 Introduction

Relativistic signatures in the light curve for continuum emission from a spot within the accretion disk of a black hole are here investigated using ray-tracing. We include all special and general relativistic effects when simulating the light curves observed at infinity. Firstly, the rapid Keplerian motion of the spot within the accretion disk causes both the Doppler frequency shift and Doppler boosting. Second, the strong gravitational field introduces gravitational redshift and lensing effects. There exist two types of peaks (Asaoka, 1989). The first one is a broad variation which is caused by Doppler effect. We call it the Doppler variation or the Doppler peak. The second one is a narrow higher peak which is caused by gravitational focusing. We will call it the lensing peak.

The light curves for an emission area in the disk are strongly dependent on Doppler

shift, gravitational redshift, lensing and time delay effects. The relative contribution of all these effects on the light curve is considered in the next sections. So far, hot spot model has been applied only to atomic line emission from AGNs. As the dominant radiation from a supermassive black hole is in the form of continuum emission, we only extract information from light curves from a continuum emitting blob in the disk.

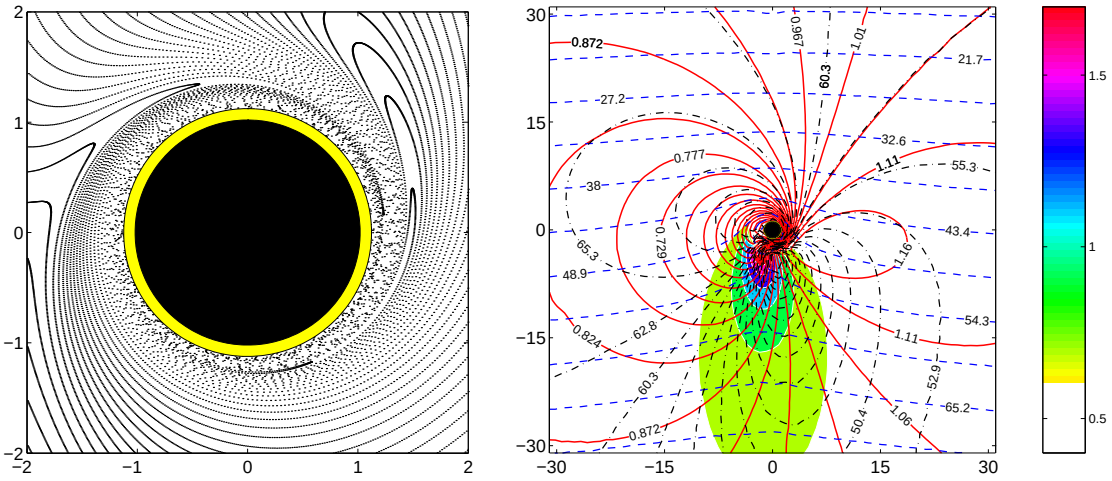

FIGURE 4.1: Relativistic effects on radiation from a blob near A Kerr black hole ($a = 0.998$). Photons come from different points of the equatorial plane. The Left panel shows the frame dragging of the photon trajectories. The observer is located at the top of the figure. In the Right panel, 4 sets of contours are plotted: (i) redshift function (solid lines); (ii) time delay (dashed); (iii) emission angle with respect to the local normal direction (dot-dashed); and (iv) light amplification due to gravitational lensing (different levels of shading). Credit: Karas, 2006

These signatures provide essential information about the nature of the spacetime geometry in vicinity of the event horizon. Consequently, if a flare is emitted close to the event horizon, it should exhibit a relativistic light curve affected by the spin (Reynolds & Fabian, 2008), gravitational redshift, gravitational lensing and other relativistic effects (Fabian et al., 1989; Laor, 1991) (see Figure 4.1). The event horizon is several times smaller if the black hole is rapidly spinning. General relativistic effects can then be very important.

A number of elements contribute to the observed variability of the emitting source:

* Doppler shift between the emitted and detected radiation that increase the intensity of

the rays originating at the approaching side of the source, and vice versa for the receding side. The effect tends to enlarge the light curve and to enhance the observed flux at its high-energy tail. The effect is expected to depend on the inclination angle of the observer. Doppler boosting effect becomes significant for high inclination angles.

* Gravitational redshift that affects mostly the photons coming from the inner parts of the source. This effect decreases the amplitude of the main peak in the light curve.

* Light-travel time that determines which photons are received at the same instant of time. Contours of constant time delay are deformed near the black hole. This effect influences the flux under suitable orientation angles.

* Gravitational lensing manifested in the distortion of the disk relative to an image in flat space. The effect enhances the flux from the far side of the source (the part of the source which is at the upper conjunction with the black hole). This tends to increase the observed flux in the light curve.

In this chapter, we consider a steady flat-spectrum continuum emission from a single orbiting blob of white light continuum emission spectrum. In the next chapter, we consider models that include intrinsic emission as well. The variation in flux from a blob without intrinsic variability arises from at least two fundamental processes. The first is the frequency shifting of photons from the Doppler effect as the blob orbits the black hole. The second is the flux amplification from gravitational lensing of photons by the black hole. The presence of these two effects, along with the flight time of photons to the observer, produces the light curve. The profile of the light curve is mainly due to the motion of the hot spot in a curved spacetime around the black hole. For a realistic model, other processes may be included, such as the occlusion of the photons by an optically thick accretion disk or by the surface of the black hole, a limb darkening effect, the tidal shredding of the orbiting material and many others. Here, we consider only the occlusion by the disk in the sense that we trace only the photons that are emitted from the side of the blob nearest the observer.

The importance of the relativistic effects for variability models has been discussed in various papers, but only for line emission (e.g. Abramowicz and Bao 1994; Xiong, Wiita and Bao 2000).

Because they are compact, the photon rays connecting the emitting spot and an observer

at infinity sample only a small portion of the spacetime around the black hole. Thus, the measured mass and spin are actually indicative of the spacetime in a small region. Observations of a hot spot at different orbital radii will consequently provide a way in which to measure the mass and spin at a number of distinct points near the black hole. These may then be compared to the general relativistic prediction that the spacetime is fully described by a mass and spin alone, thus providing an easy method to test the validity of Kerr metric.

4.2 Orbiting spot model

Motivated by the evidence of the observed periodicity in the NIR emission from Sgr A*, the simplest model for a flare is that of a transient over-dense bright compact region or a hot spot, orbiting inside an accretion flow and dominating the quiescent emission in the disk. The observed periodicities that suggest the presence of temporary clumps of matter in the accretion flow are not theoretically unexpected and may be common in the region near the ISCO, as strong inhomogeneities develop in the innermost regions of general relativistic magnetohydrodynamic simulations (De Villiers et al. 2003, Schnittman et al. 2006). Such a hot spot can be created by a flare, internal instabilities, stellar impacts or irregularities in the disk. Such a spot may also appear as the product of magnetic reconnection events or turbulent shocks within the accretion flow. The observed light curves contain significant information about the spacetime around the black hole.

There are a number of advantages to study these hot spots as opposed to the underlying quiescent accretion flow. Firstly, due to their compact, and essentially local nature, they are likely to be considerably simpler to model than the global structure of the accretion flow. As the hot spot is emitting only continuum radiation, the spectrum in the local frame can be written as a power law $I_c(\nu) \sim \nu^\alpha$, then the time-varying continuum signal I_ν from a spot that subtends a solid angle $\Delta\Omega$ on the observer's sky yields a flux of

$$\begin{aligned} F(t) &= \Delta\Omega(t-\Delta t)\int_{\nu_1}^{\nu_2} d\nu I_\nu(t-\Delta t) \\ &= \Delta\Omega(t-\Delta t)\int_{\nu_1}^{\nu_2} d\nu \left(\frac{\nu}{\nu_e}\right)^3 I_c(\nu_e) \\ &= C\Delta\Omega(t-\Delta t)[\mathcal{D}(t-\Delta t)]^{3-\alpha}\,, \end{aligned} \tag{4.1}$$

where $\mathcal{D} \equiv \nu/\nu_e$ is the redshift which is the same for all photons from the hotspot at a given time t; ν_1 and ν_2 give the detector bandwidth and ν_e is the photon frequency in the source frame. The constant of proportionality C in the last line of equations (4.1) depends only on the detector's bandwidth and the normalization of I_c (Bromley, Chen & Miller, 1997). With $\Delta\Omega(t)$ containing the information about amplification from gravitational lensing and $\mathcal{D}$ containing the variations in frequency shift, it is straightforward to interpret light curves in this case.

The observed flux at infinity will be time dependent and will take into account the time delay effect $t = t_o - \Delta t$ with Δt being the time delay with which the photons from different parts of the disc arrive at infinity at the same coordinate time. In our plots, zero time corresponds to the moment when the center of the spot was at the farthest point on its orbit with respect to the observer.

The hot spot model consists of a locally axially symmetric over-density of non-thermal electron bright region in circular and confined Keplerian orbital motion around the black hole. The hot spot model for continuum emission is characterized by the black hole mass, spin parameter, disk inclination angle, spot size, radial distance from the black hole, spectral index and frequency of the emitted light. The model produces a perfectly periodic light curve as a single hot spot orbits the black hole indefinitely.

We assume a stationary local emission and a dependence on the axial coordinate together with the prescribed dependencies on radius, spot size, spectral index and frequency:

$$F_1(r, \varphi, \nu, p, t - \Delta t) \equiv F_1(\nu, R(\beta, r) f(\nu, p). \tag{4.2}$$

The full expression of the local emission from the blob in the disk is dependent on the spot size, frequency and spectral index:

$$F_1(\nu) = \nu^{-\alpha} \exp\left[-\beta\,(\Delta r)^2\right] \text{ for } \beta\,(\Delta r)^2 < 4\,, \tag{4.3}$$

$$F_1(\nu) = 0 \quad \text{for} \quad \beta\,(\Delta r)^2 \geq 4\,. \tag{4.4}$$

Here β represents the size of the spot and $(\Delta r)^2 = r^2 + r_{\rm spot}^2 - 2\,r\,r_{\rm spot}\cos\left(\varphi - \varphi_{\rm spot}\right)$ with $r_{\rm spot}$ and $\varphi_{\rm spot}$ being polar coordinates of the spot.

Because we assume all points in the hot spot have the same 4-velocity as the geodesic

guiding trajectory, one must be careful not to use too large a spot or the point of emission $\mathbf{x}_{\rm em}$ can be spatially far enough away from the center $\mathbf{r}_{\rm spot}$ to render the inner product $p_\mu(\mathbf{r}_{\rm em})v^\mu(\mathbf{r}_{\rm spot})$ unphysical. One way to quantify the size of this physical region is through the use of Riemann normal coordinates, where the metric is locally flat and the Cartesian dot product is well behaved. The quadratic deviations from flat space scale according to the local curvature scale.

After the hot spot trajectory is tabulated as a function of coordinate time t, the ray-tracing map between the disk and the observer is used to construct a time-dependent light curve from the emission region. For each photon bundle intersection point there is a time delay $\Delta t_{i,j,k}$ (where i, j are the coordinate indices in the image plane and k is the latitude index in the disk) so for the observer time $t_{\rm obs}$, we first determine where the hot spot was at the coordinate time $(t_{\rm em})_{i,j,k} = t_{\rm obs} - \Delta t_{i,j,k}$. If the spot is close enough to the disk intersection point $(r, \theta, \phi)_{i,j,k}$, then the redshifted emission is added to the pixel spectrum $I_\nu(t_{\rm obs}, i, j)$.

The model produces a QPO signal associated with the Keplerian orbit of a hot spot of plasma at the last stable orbit. Orbital periods of 20 min are of significant importance for Sgr A* flare emission study, as they correspond to a quasi-periodic (QPO) signal, interpreted as the orbit of a spot at the last stable orbit of a Kerr black hole. It is also possible that such a hot spot may appear somewhere farther away from the ISCO, producing QPOs on longer timescales. While there is evidence for periodic modulations of 20 min, a major difficulty induced by the hot spot model is the lack of significant peaks in the periodograms, while performing robust statistical estimators, therefore no conclusive results in NIR regime (Do et al. 2008, Meyer et al. 2008). Additionally, some MHD simulations estimate that a hot spot could last less than an orbital time scale before it disappears.

A basic light curve of a simple hot spot can be seen in Figure 4.2. We have chosen an inclination angle, black hole spin and spot size in such a way that the relativistic effects are blended and merge into one single symmetric time dependent flux modulation. In the following sections we explore how the relativistic effects in light curves depend on these parameters.

The emission mechanism for the hot spot produces only periodic light curves. The peak broadening and the dampening of the resulting light curves were measured and compared for

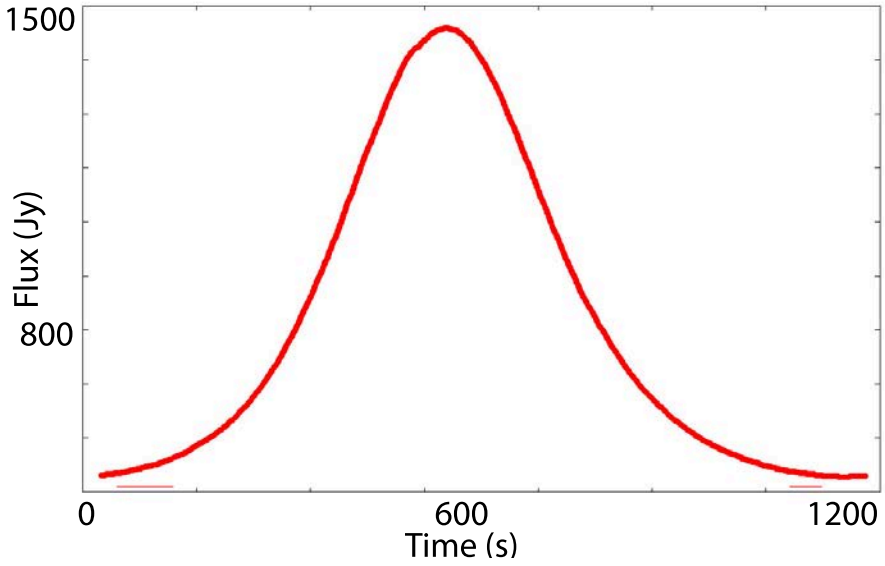

FIGURE 4.2: Light curve of a hot spot in a circular orbit around a Kerr black hole with spin $a/M = 0.3$ at the ISCO, viewed at the inclination of 60°. Flux is on the ordinate and proper time on the abscissa. The spot radius is $R_{\rm spot} = 1.5M$. The spot is moving at the $-\mathbf{e}_{\hat{\phi}}$ direction with $\phi(t = 0) = 180°$ and the observer at $\phi = 270°$.

different black hole spins, orbital radial position of the blob and disk inclination angles.

4.3 Light curve modelling

4.3.1 Gravitational and Doppler shift

Light curves are influenced and distorted by both gravitational redshift and Doppler effects. For emission originating from the inner disk region, the gravitational redshift signatures are strong, dominating over all other relativistic effects. The cause of smearing of the light curve is due to different flux contributions of the radiation. With decreasing distance from the event horizon, the g-factor starts to slowly deviate from the standard Doppler factor. We find that the emission from the inner regions within the disk around an extreme Kerr black hole are redshifted at all viewing inclination angles. We also find that this is contrary to the case of a Schwarzschild black hole, where there are regions on the inner disk boundary from which

the emission is highly blueshifted, at sufficiently high inclination angles.

Doppler shifting refers to both sides of the light curve, meaning that the emission from the approaching side will be blue shifted while that on the receding side will be red shifted. The length contraction along the line of motion beams the emission in that direction. Thus the blue shifted emission from the approaching side is also boosted in comparison to the red shifted emission, leading to a broadened and skewed light curve. An additional energy shift is provided by time dilation and also gravitational redshift which combine to broaden the light curve even further.

In the next sections we will refer to a ”blue peak” as the peak formed on the approaching side of the light curve and a ”red peak” on the receding side of the light curve.

Here we explore the relativistic effects, by showing how inclination angle of the observer affects the observed time dependent flux. Figure 4.3 shows light curves for a small spot on a circular orbit in the equatorial plane at a radial distance of $r_{\rm sp} = 6GM/c^2$, for various inclination angles. If the light curve is accurately determined, it places strict constraints on the disk inclination angle of the black hole. The light curve corresponds to two full orbital periods. The spot is moving towards the observer on the left side of the light curve, moving away on the right side.

At average inclination angles, the light curves show a blue peak that is still sharp and tall whereas the red tail is almost not present. For these angles, the redshift smears the light curve and is less noticeable as a separate peak distinct from the lensing peak, the light curve is broad and symmetric. The extensive red wing and a separate peak caused by the Doppler shifting of the photons starts to become noticeable at higher inclination angles as the light curve loses its symmetry. At higher inclination angles, the light curve becomes narrower because of the Doppler boosting and high lensing effect, the flux is highly amplified and the lensing peak becomes distinguishable. Also, because of the beaming effect, the photons arrival time to the observer’s plane is changed and the light curve is shifted towards earlier times. The beaming effect creates also a sharp look of the light curve on the left flank due to a shortened arrival time window of the beamed photons into the line of sight. For an extreme rotating black hole, the red peak is more defined as a second peak.

At low inclination angles, the light curve appears symmetric (see Figure 4.3, top left

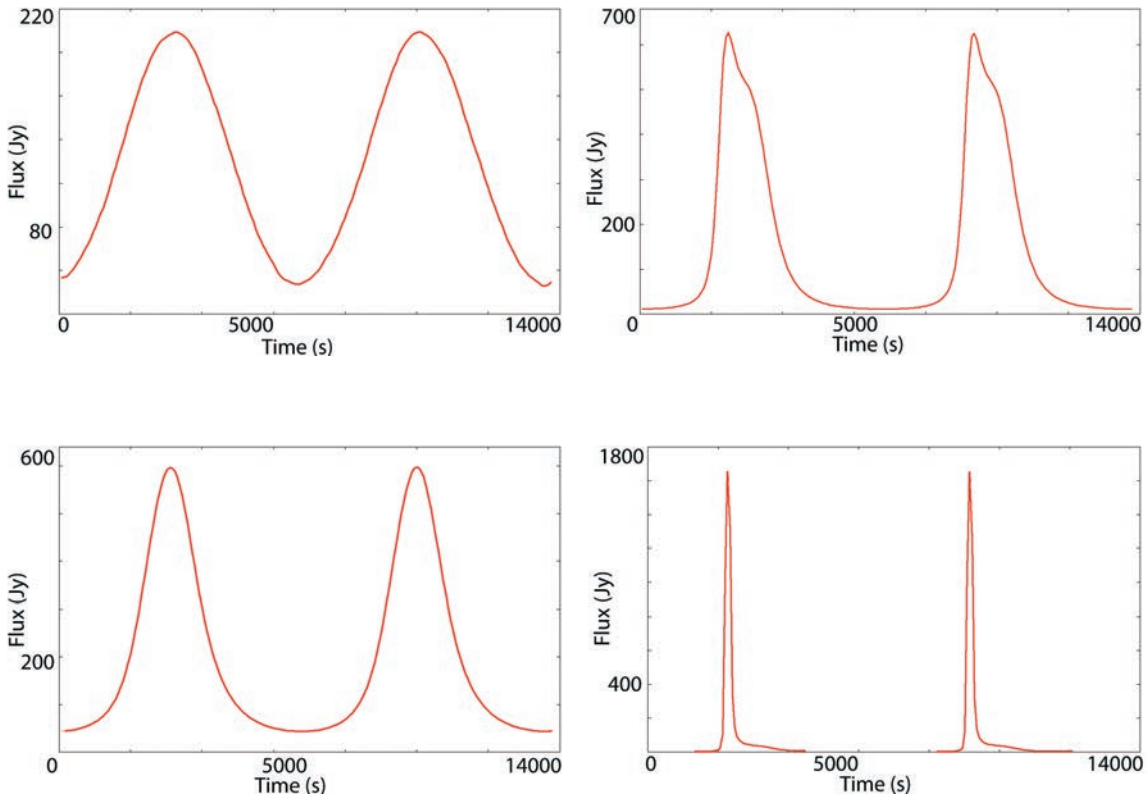

FIGURE 4.3: Light curves from a spot in a retrograde circular orbit in the equatorial plane of an extremely rotating black hole at a radial location of $r_{\rm sp} = 6GM/c^2$, for various inclination angles $\theta_{\rm o}$. The radius of the spot is $R_{\rm spot} = 0.5GM/c^2$. The first column shows light curves for $\theta_{\rm o} = 5^\circ$ (up) and $\theta_{\rm o} = 45^\circ$ (down). The second column shows light curves for $\theta_{\rm o} = 75^\circ$ (up) and $\theta_{\rm o} = 89^\circ$ (down). The initial orbital phase location of the spot is behind the black hole $\phi(t = 0) = -180^\circ$, the observer being located at $\phi = 0^\circ$.

panel) because the Doppler redshift smears the light curve, becoming significant relative to the boosting effect that takes over only at higher inclination angles. At low inclination angles, the profile of the light curve is almost triangular. Towards average inclination angles, the kurtosis of the light curve changes significantly because of a combination between the red peak and its tail and the narrow blue peak. This picture changes considerably as the inclination angle becomes higher and the light curve loses the symmetry.

For large inclination angles, the Doppler effect becomes more significant as the flux of a source moving with relativistic speed is strongly magnified or demagnified depending on

whether it is approaching or receding from the observer (relativistic beaming). The light curve is stretched as a function of the redshift effect. To conserve energy, as the curve is stretched, fewer photons are detected per second. The curve is stretched and disappears into the background as the redshift increases. The profile broadens and the flux is suppressed as the emitting spot is moved closer to the black hole.

For high inclination angles, both lensing and light bending effects play a significant role, however the dominating feature remains the blue peak associated with the maximum shift of energy because of the high magnification of the peak due to the lensing effect. A new peak of the maximum observed flux should arise, due to the lensing effect. The new peak is formed by photons arriving from another azimuth of the spot orbit. The secondary faint maximum is in the point where the effect of energy shift, lensing and time delay combine to produce the maximum amplification. However, the time delay and the g-factor vary rapidly across the region of the disc most affected by lensing. The two components of the g-factor remain entangled and can be separated only based on the dominating effect of gravitational redshift and Doppler shift for different parts of the orbit of the spot. The g-factor can either amplify or diminish the observed flux amplitude and the ratio between the components is distinct for different parts of the light curve. The ratio of the amplification produced by the two components is dependent on the orbital radius and the angular position of the spot. The diminishing effect happens for orbits in lower inclination disk angle due to the fact that the flare orbits very close to the black hole and gravitational redshift will prevail over the Doppler shift. Close to the black hole, where orbital velocities become relativistic, the beaming of the photons enhances the blue peak with respect to the red side, and the transverse Doppler effect shifts the profile to lower flux contributions. The relation is made complex by the time delays which can't be neglected, given the large velocities of the orbiting matter and the frame dragging effects near the black hole. As we approach the black hole and gravity becomes strong enough, gravitational redshift becomes important and the overall light curve is shifted towards lower frequencies, decreasing the final observed amplitude of the light curve. The disc inclination fixes the maximum flux magnification at which the emission can still be seen, especially because of the angular dependence of relativistic beaming and gravitational light bending effects.

A significant modulation results primarily from special relativistic aberration associated with the rapid orbital motion, as a strong function of radius and viewing angle. With increasing inclination, the radial velocity of the inner disc regions grows, and due to the aberration of light, the emitting area becomes increasingly bright, however the projected area on the line of sight decreases. The dependence upon viewing angle reaches a maximum when a great portion of the rays is incident along the orbital axis (however, due to gravitational lensing this doesn't occur when the orbit is face-on).

The light curve reveals all special relativistic effects such as the Doppler shift and beaming as the blob moves toward and then away from the observer. For a hot spot orbiting in the clockwise direction as seen from above ($v^{\phi} < 0$ with $\phi = 270°$ toward the observer), the point of maximum blue shift actually occurs at a point where $\phi > 0$ because of the gravitational lensing of the light, beamed in the forward direction of the emitter and then bent toward the observer by the black hole. Gravitational lensing also causes significant magnification of the emission region when it is on the far side of the black hole, spreading the image into an arc or even an Einstein ring for $i \approx 90°$.

There are two types of Doppler effect. The longitudinal Doppler shift considers the simpler case of a source moving directly towards the observer or away from the observer along a straight line. The transverse Doppler effect, on the other hand, considers what is observed when the observer is placed in a direction perpendicular to the direction of the spot motion. We distinguish between the time an event occurs in the observer's frame and the time when the observer sees it occur. The code calculates the time it takes for the light to travel from the flare event to the observer. The observer will see some of the particles from within the spot arriving at earlier times, as they are beamed relativistically into the direction of motion, as they reach a great percent of the speed of light. This effect happens only closer to the ISCO and it is not related to the gravitational potential but only to the relativistic velocities of the particles. Some particles will arrive earlier in time by taking a shortcut to the observer instead of waiting for the spot to come around and move towards the observer. The effect is combined with the gravitational lensing effect that elongates the observed emitter and several photons from the observed arc or filament could actually come earlier that the expected arrival time as they are apparently located further from the observer

than the flare itself. Some of the photons in the arc will also come from different phase angle, behind the black hole and they will be further lensed.

The strength of the Doppler shift depends on the line-of-sight velocity. This effect is the strongest at the closest orbit to the black hole where the orbital velocity is maximal. By measuring the redshift, the spin of the black hole can also be calculated. For stable orbits, the maximal redshift occurs at the marginally stable orbit. On the other hand, the maximal blueshift effect occurs farther from the black hole due to the gravitational redshift, and its location depends on the inclination angle. For lower inclinations, the Doppler effect becomes much weaker and it overcomes the gravitational redshift at a farther orbital radius. Sufficiently far from the event horizon, the two regions of blueshift and redshift are separated by to the signature of rotation and the direction of the line-of-sight velocity towards the observer. The frequency shift decreases with the orbital radius as the orbital velocity decreases. For a flare located within a disk viewed at any other inclination than face-on, substantial Doppler boosting is present, causing the disk of the black hole to appear asymmetric with a bright (or dim) approaching (or receding) side. For nearly edge-on viewing, the boosting effect dominates the appearance of the accretion disk. As the observer approaches edge-on angle with the disk, the light curve is sharply peaked by the combination between the beaming of the flare as it moves towards the observer and the gravitational lensing as the flare moves behind the black hole.

As expected from the Doppler shift and relativistic beaming, the approaching portion of the spot orbit (left-hand side of the light curve) appears considerably brighter than the receding portion of the spot orbit (right-hand side of the light curve). In general, the most energetic photons largely come from the inner portion of the disc, where the linear speed of accreted matter is comparable to the speed of light. The net effect of Doppler broadening is a net blueshift of the light curve, as a larger amount of the flux comes from the blueshifted regions than from the redshifted regions.

While the redshift at smaller radii reduces the energy of all emitted photons equally, special relativistic beaming causes the observer to see a larger number of blueshifted photons (through the invariance of I_ν/ν^3), increasing the flux contributions in the light curve. At high inclination angles ($\gtrsim 70^\circ$) the beaming factor dominates, giving larger values of the flux at

smaller radial locations, while at lower inclinations ($\lesssim 70°$) the gravitational redshift wins out and reduces the flux contribution in the light curve.

The comparable influences of the transverse Doppler effect and gravitational redshifting shifts the flux contributions towards lower energies, respectively lower frequencies.

A face-on orientation of the disk, i = 0 will completely suppress the longitudinal Doppler effect because there is no relative emitter motion along the line of sight. However, we still take into account the transverse Doppler effect although this is important only for relativistic speeds of the emitter.

When the spot is located at lower orbital radii within the disk, i.e. closer to the black hole, it orbits faster, and the light curve peaks at much lower flux values as it gets close to the ISCO. Due to the time dilation effect and earlier arrival time of the photons from the source, the light curve will be shifted at earlier times. If the emission is produced at larger distances from the black hole, the emitting material is rotating slower and therefore the light curve becomes broader.

For large inner radii, the most significant differences in shape are seen for high values of the inclination angle while the red tail and the Doppler peak are more distinguishable. The slight increase in flux at the lowest energies is due to the increased Doppler shift. The high energy, blueward extent of the light curve is a strong function of the inclination of the disk. The blue extent of the light curve is almost entirely a function of the inclination, thereby providing a robust way to measure the inclination of the disk. On the other hand, the redward extent of the light curve is a sensitive function of the orbital radius of the spot and the spin of the black hole.

The intensity is varied by the special relativistic beaming of photons emitted toward and away from the observer. Smaller contributions to the intensity modulation also come from the transverse (”second-order”) Doppler shift and from the gravitational lensing of the far side of the accretion disk. As the spot approaches the black hole, the relativistic beaming of photons towards the observer is enhanced, as the velocity of the emitter is higher at smaller orbital radii. Therefore, the relativistic beaming enhances the emission for smaller radii, giving larger amplitude fluctuations for high inclinations. Near the black hole, where the orbital velocities of matter become relativistic, special relativistic beaming enhances the blue

peak of the light curve for any orbital radius. The beaming effects compensates for the signal demagnifying caused by redshift, close to the black hole, as more photons get captured by the event horizon.

For large inclination angles (i.e., when the disk is almost "edge-on"), the beaming serves to compensate for the intensity decrease due to the gravitational redshift. As a result, the two major relativistic effects counter each other and the intensity modulation becomes higher. The emission model shows greater emission at small radii and, thus, higher amplitude variations for larger inclinations of the disk.

Gravitational redshift causes an additional suppression in flux so that close to the black hole the emission from a medium to highly inclined ring is asymmetric and skewed. The ray tracing simulations confirm the predictions based on theory. The gravitational redshift decays with increasing distance. The blue peak is very narrow and bright, while the red one is wider and much fainter. Besides, the gravitational redshift causes further deformations of the light curve by smearing the blue emission into a red one. The redshift approaches $z- > 0$, i.e. that $g- > 1$, at infinity. The combined g-factor affects the light curve showing that the rotation of the black hole becomes visible only in its vicinity ($r \lesssim 10$). Close to the event horizon, the g-factor decreases down to zero due to the gravitational redshift effect, whereas far from the center the Doppler shift is dominant. Very far away from the black hole, the matter of the disc rotates slowly, thefore the g-factor becomes one (see Figure 4.4). The gravitational redshift becomes infinite on the event horizon ($g = 0$). The onset of gravitational redshift can be tested observationally with sufficient spectral resolution. In general, gravitational redshift is an indicator of black hole mass and spin as well as for the inclination angle of the accretion disk. According to the asymptotical flatness of the Kerr metric, there is no finite distance at which the gravitational redshift vanishes completely.

The emission from the flare originates from a radius r in the disc and it is affected by a different redshift amount depending on the observer inclination. As we discuss only continuum emission, the g-factor (gravitational and Doppler combined) signatures can be found only from the light curve itself. Unfortunately, there is not sufficient precision on the highly shifted and damped red wing of a light curve, but the information is more helpful if the emission originates close enough to the event horizon.

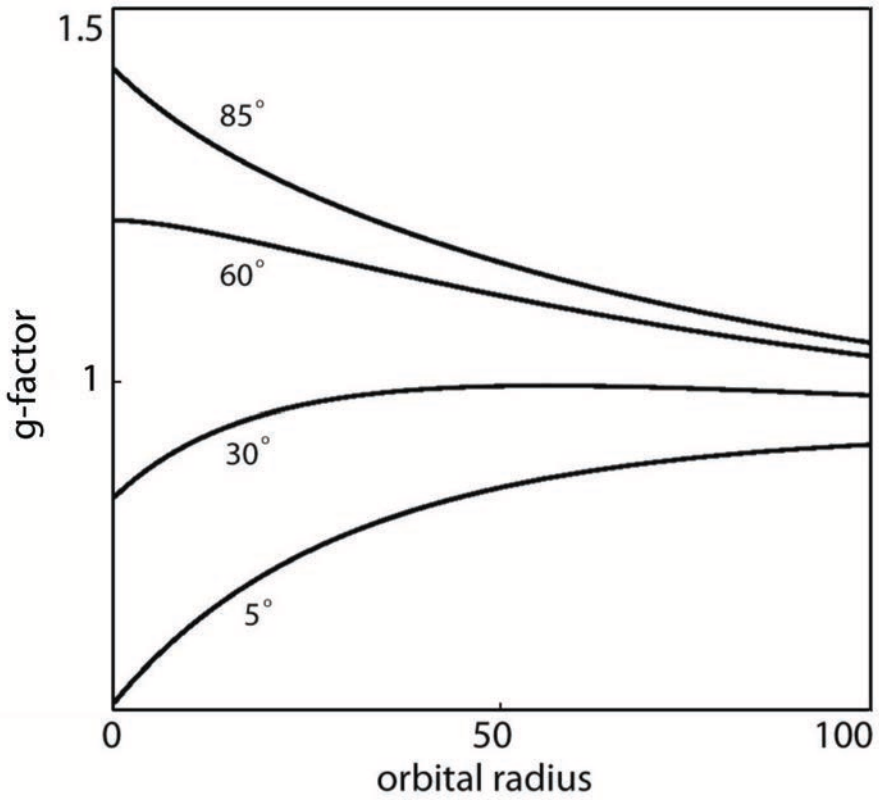

FIGURE 4.4: The g-factor as a function of the radius, for various inclination angles. for a Kerr black hole with $a = 0.998\,M$

The magnitude of the frequency shift g depends on the effects of gravitational redshift and Doppler shift. Near the black hole, the gravitational redshift is much stronger than the Doppler shift, resulting in a loss of brightness that can be observed in plotted light curves, close to ISCO. We find that the gravitational redshift decreases with distance to the black hole and decays more rapidly for Kerr black holes, compared to Schwarzschild case, by modelling light curves for orbital radii between ISCO and 100 Schwarzschild radii (see Figure 4.5).

Additionally to the increased gravitational redshift for higher spin parameters, the orbital velocity increases, in turn increasing the relativistic beaming and blueshift as the spot moves towards the observer, causing the light curve to become sharply peaked. The typical maximum redshift occurs when $\phi \approx 160°$ and the maximum blueshift occurs when $\phi \approx -45°$. The blueshift extent could reach positive orbital phase values, towards $\phi \approx -20°$, if the emission is highly lensed at a high inclination angle of the disk. A simulated time-dependent energy spectrum or spectrogram is shown in Figure 4.6, for a spot of $R_{\rm spot} = 0.5M$ orbiting at the

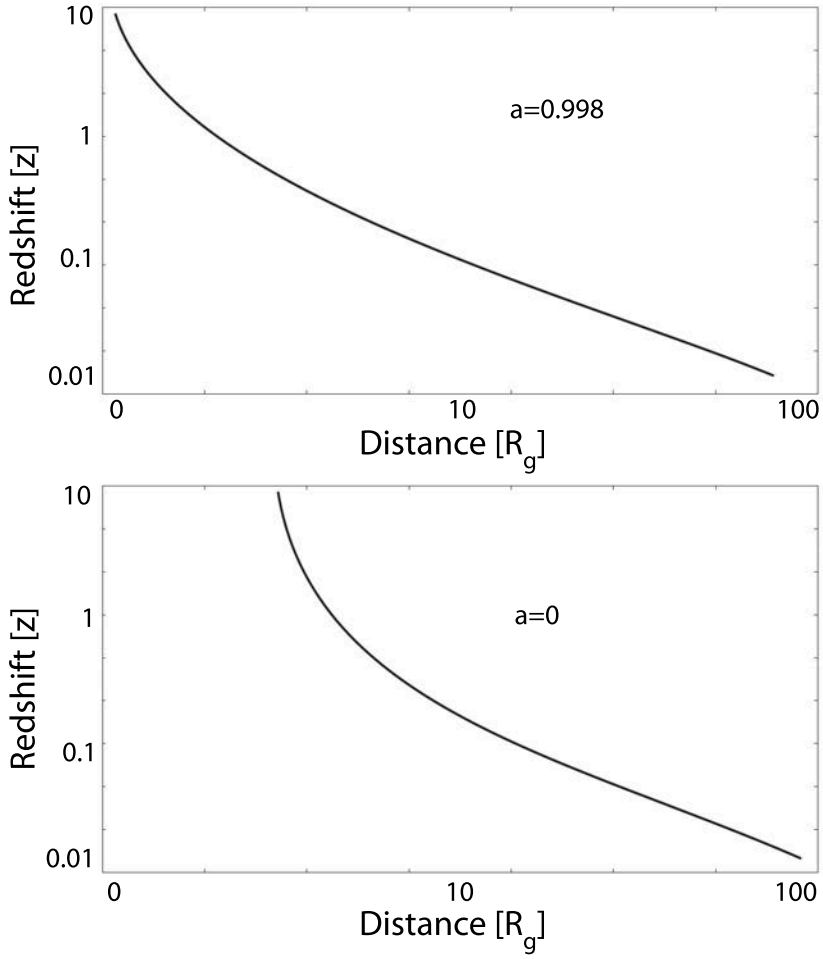

FIGURE 4.5: Gravitational redshift z decay with the increasing distance to the black hole. The top figure shows the redshift for an extreme Kerr black hole, $a = 0.998\,M$ and the bottom figure shows the Schwarzschild case.

inclination of 60° and black hole spin $a/M = 0.7$. The orbital period is 13 min. The horizontal axis measures proper time in the observer's frame, with $t = 0$ corresponding to the time at which the spot is moving away from the observer ($\phi = 180°$). The point of maximum redshift occurs closer to $\phi = 160°$ due to gravitational bending of the emitted light.

Due mainly to the Doppler effect, we found an average of about 15 percent in dampening of the observed flux amplitude for an average inclination angle. The amplitude of the observed flux variation will significantly depend on the inclination angle. The gravitational amplification factor is proportional to the solid angle that a finite patch of emitting material

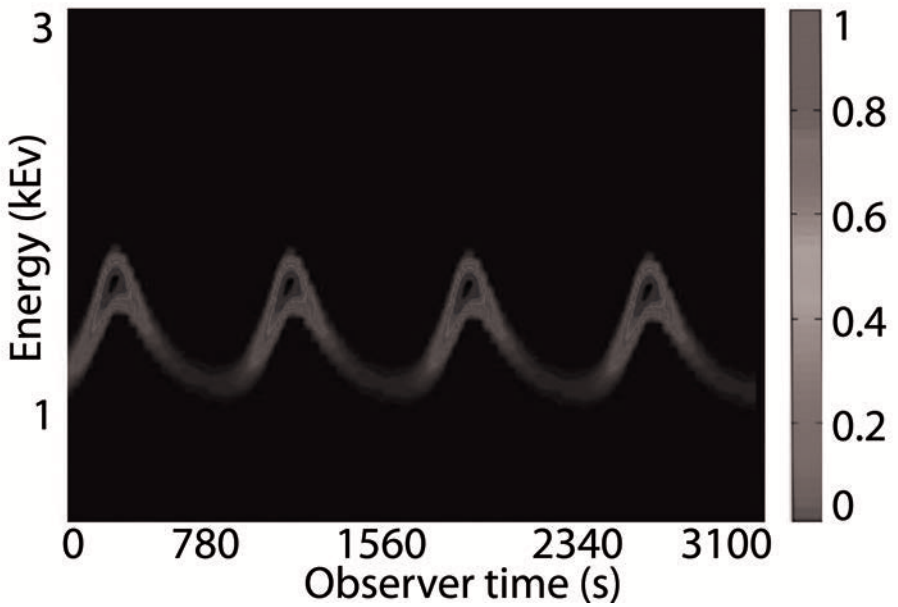

FIGURE 4.6: Spectrogram of a hot spot in a circular orbit (for an iron line with E = 6.4 keV). Energy is on the ordinate and proper time on the abscissa. The spot radius is $R_{\rm spot} = 0.5M$ and it orbits a Kerr black hole with spin parameter $a/M = 0.7$ at the ISCO, viewed at an inclination of 60°. The orbital period is 13 min. The spot is moving at the $-\mathbf{e}_{\hat{\phi}}$ direction with $\phi(t = 0) = 180°$ and the observer at $\phi = 270°$. The maximum redshift occurs when $\phi \approx 160°$ and the maximum blueshift occurs when $\phi \approx 20°$.

subtends in the sky plane of the observer.

In the extreme Kerr case, the disc extends down to $1.235R_g$ far closer to the event horizon than in the Schwarzschild case, introducing a greater complexity to the geodesic paths.

Stronger gravitational lensing effects are seen, especially for high inclination images. Photons from the far side of the disc pass close to the black hole, so the light curve is strongly distorted. Because the area of the emission is magnified, the contribution to the observed flux should be large. However, the low inclination light curves are also affected by light bending effect, though they are not magnified by gravitational lensing.

The orbital speeds within the inner $10R_g$reach a considerable fraction of the speed of light. Beaming, aberration, and the light bending affect the emitted photons significantly in

this region. Less energetic photons come from the outer parts where the motion slows down and the relativistic effects are of diminished importance. Individual rays experience unequal time lags for purely geometrical reasons, and other relativistic effects occur in the very vicinity of the black hole and are relevant for the source variability, namely, lensing and Doppler boosting. In the case of long life flares in the disc, there is, indeed, a substantial contribution to the variability caused by the orbital motion (Abramowicz et al. 1991; Mangalam, Wiita 1993).

We find a complicated interplay of geometrical effects originating from the high curvature and rotation of the spacetime, with the aberration effects which result from the orbital motion of emitting matter. All these need to be taken into account when determining the expected light curves.

4.3.2 Gravitational lensing

The lensing effect due to the gravitational focusing of the light generates the global maximum flux of the light curve which occurs when the observer and the flare (at a retarded time) are located in the opposite direction with respect to the black hole. Gravitational focusing effect dominates at high inclination angles. We find that strong gravitational lensing can cause high amplitude modulations in the light curves, even for a relatively small flare.

The gravitational amplification factor is proportional to the solid angle that a finite region of emitting material subtends in the sky plane of the observer. Regions of high amplification occupy more pixels and thus appear magnified in the sense of geometric optics.

The photons emitted at the far side of the observer are collimated and their flux is focussed in such a way that it is strengthened by the gravitational lensing. Photons emitted at the near side of the observer are being diverged and the resulting flux is weakened. The effect at the far side of the black hole is stronger as the light becomes more collimated while passing by the near vicinity of the black hole. The effect of aberration makes the apparent solid angle narrower, focussing some of the photons while the spot is moving towards the observer. The focussing effect is weaker and the solid angle is much larger when the spot is moving away from the observer.

As we know, two peaks may appear in the light curve, in one orbital period, caused by the gravitational focusing of the photons (the lensing peak) and the signatures caused by the Doppler shift and aberration. When the emitter moves towards the observer, the aberration effect causes the apparent solid angle of emission to become narrower. If the orbital period is smaller, the gravitational focussing effect lasts for a shorter time window and the lensing peak allocates a smaller portion within the light curve, the Doppler shift effect and aberration becoming dominant as we get closer to the black hole. The ratio between the peak and trough of the light curve is larger for smaller orbital radii. As we get nearer the black hole and the orbital radius becomes smaller, all other effects become dominant over the lensing effect and there are no remaining photons creating a positive trough in the light curve. For closer orbits, between two orbital periods, the flux (trough) is zero, the lensing effect becoming insignificant. In this way, the ratio peak/trough becomes larger for smaller orbits. The lensing effect has its largest amplification contribution for the inclination angle of around 85°, whereas for low inclinations under 30° its effect can be neglected.

Gravitational lensing is significant at edge-on viewing directions, where the spot, the black hole, and the observer are (nearly) lined up. For inclinations of 85°, the peak of the light curve occurs when the spot passes behind the black hole, at 180°. At average inclinations angles the Doppler shift effect is dominant. In contrast to the Newtonian regime, the maximum (minimum) relativistic Doppler shift does not occur when the spot is approaching (receding from) the observer at maximum velocity but it rather happens at the phase of about 225°, respectively at 45°.

The magnification varies significantly with the orbital radius (see Figure 4.7) and the inclination of the orbit relative to the line of sight. The strongest magnification is obtained for orbits which pass directly behind the black hole. In principle, some photon rays coming from the close vicinity of the black hole and from behind the black hole don't reach the observer directly and they have to orbit the black hole more than one time in order to reach the observer, especially at large inclination angles. In our calculations, rays are not allowed to pass through the plane defined by zero inclination angle, so we do not see multiple images of sources behind the black hole. However, for sufficiently large inclinations and spin parameters, single points from the spot in the equatorial plane can be mapped to different regions of

the image plane, creating multiple images of certain regions of the spot.

The photon rays are not isochronal, as they have different propagation times, therefore different arrival times. The final light curve contains lensing information from an apparent extended source, as photons apparently don't originate from the same region in the disk but rather originate from an extended source, much like an arc or annulus formed by the apparent extended image of the spot. Their arrival time will definitely be earlier than the expected arrival time for photons coming directly from the spot. The lensing arc effect can be seen in Figure 4.8 where the flux amplitude never drops to zero between consecutive orbits, showing the presence of a number of photons at every phase angle, even when the spot should be totally eclipsed by the black hole itself. In our case, for orbits very close to the ISCO, the photons that arrive earlier at the observer are produced, besides the lensing effect, by a pure special relativistic effect of beaming the light into the direction of sight. The two effects could be theoretically disentangled (not a task here) in the light curve by calculating the arrival time of the photons from the geometry of light deflection (including the Shapiro time delays) and from the transverse Doppler special relativistic effect.

The light curves plotted for high inclination angle reveal an additional feature: Small faint spiky second peaks appear in the light curve (see Figure 4.9). The extra peaks are generated by photons emitted from the far side of the disk, therefore we have a manifestation of gravitational lensing. The occurrence of Einstein rings and multiple high order images can be observed in the substructure of the light curve. This phenomenon develops when the the observer and the emitting source are aligned, with the black hole between them. In Figure 3.6 we have shown that the observer may observe two concentric Einstein rings, formed by photons arriving at different times at infinity. Light rays starting from the blob could orbit the black hole several times before reaching the observer which could yield to an arbitrary number of concentric rings. This effect should also diminish the brightness from images formed by photons moving on longer paths.

The peak flux originates from the development an Einstein ring (including multiple images), an apparent ring-shaped image of the spot with the black hole in its center. It occurs when the light source, the black hole and the observer are aligned (and the black hole is in between). Due to the finite extension of the source, conditions for an Einstein ring are

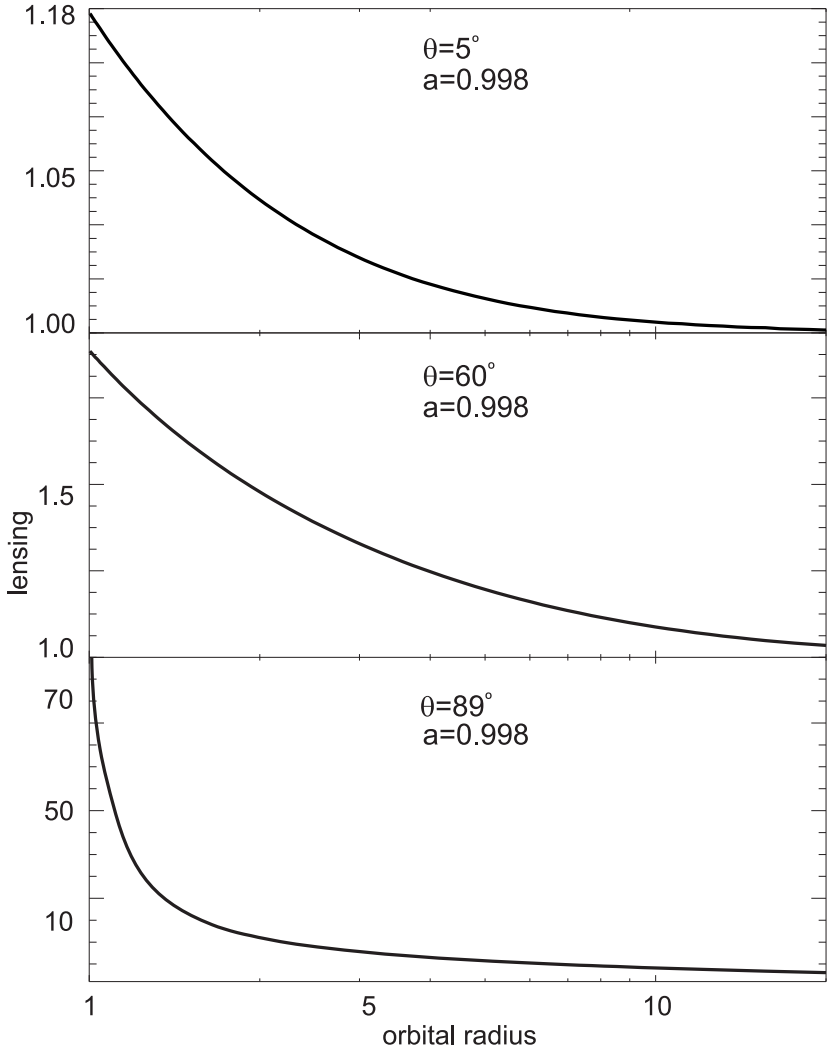

FIGURE 4.7: Lensing of an orbiting spot as dependent on the orbital radius

fulfilled in a finite but small range of inclinations.

As the emitting source has a finite size, the sought conditions for developing an Einstein ring are found in a very small range of disk inclinations. We don't use the direct 90° case but close values to this inclination. Further multiple higher order Einstein rings can develop, if the photons will keep orbiting the black hole. Narrow spikes appear in the light curve (Figure 4.8).

A secondary Einstein ring flux spike appears when the hot spot passes in front of the black hole. We then receive photons from the far side of the spot, which have orbited the black hole once. In fact it occurs a bit later, since one has to consider the finite speed of

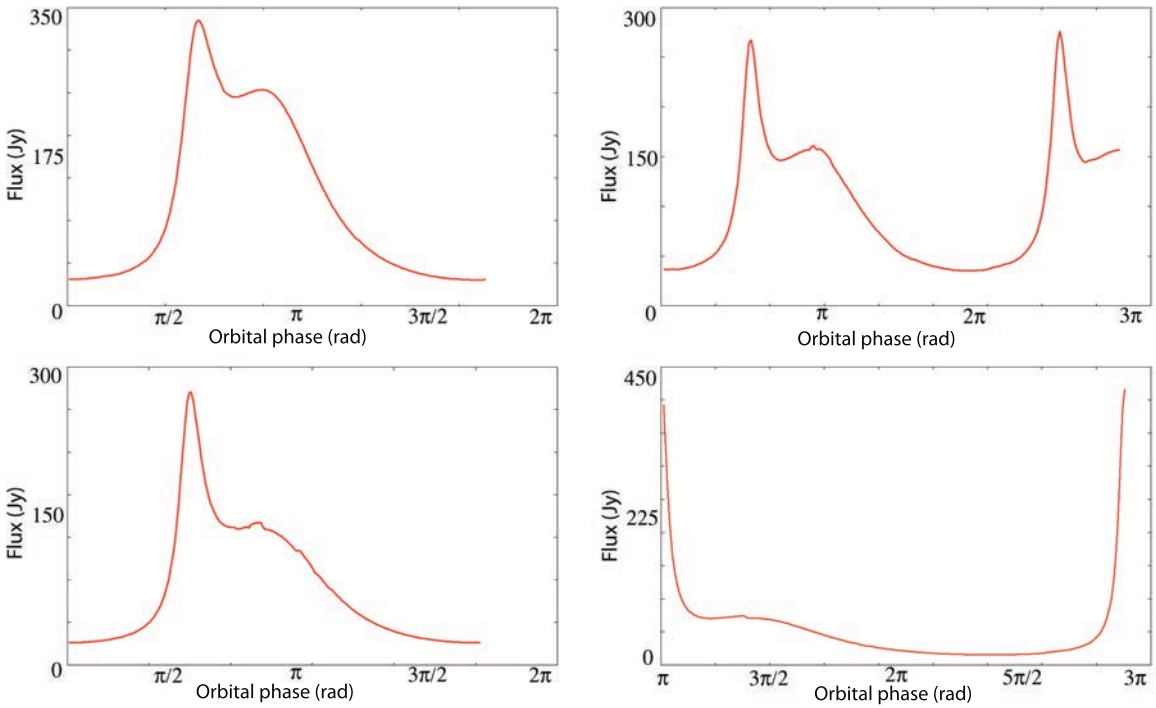

FIGURE 4.8: Light curves as functions of the orbital phase, for a spot orbiting a black hole with $a/M = 0.9987$, for different inclination angles and large orbital radii. The first column shows a spot located at $r_{sp} = 15GM/c^2$ at $\theta_o = 75°$ (top) and located at $r_{sp} = 20GM/c^2$ at $\theta_o = 79°$ (bottom). The second column shows a spot at $r_{sp} = 30GM/c^2$ at $\theta_o = 79°$ (top) and an obscured spot at $r_{sp} = 30GM/c^2$ at $\theta_o = 85°$ (bottom). The initial orbital phase is shifted with 180°.

the photons when orbiting the black hole. These peaks appear in our plots, in the receding redshifted side of the light curve. They are a lot fainter than the ones caused by the primary Einstein ring (see Figure 4.9).

Only photons from the far side of the black hole will reach the observer. These photons have only orbited the black hole once. For disk inclinations close to 90°, the spot will exhibit a light curve containing an essential characteristic: on the approaching side, before the expected peak, created by a combination of gravitational lensing and Doppler boosting, a second peak will also emerge from the Einstein ring formed by the gravitational focusing effect.

At slightly lower inclinations we no longer expect Einstein rings, but still multiple images

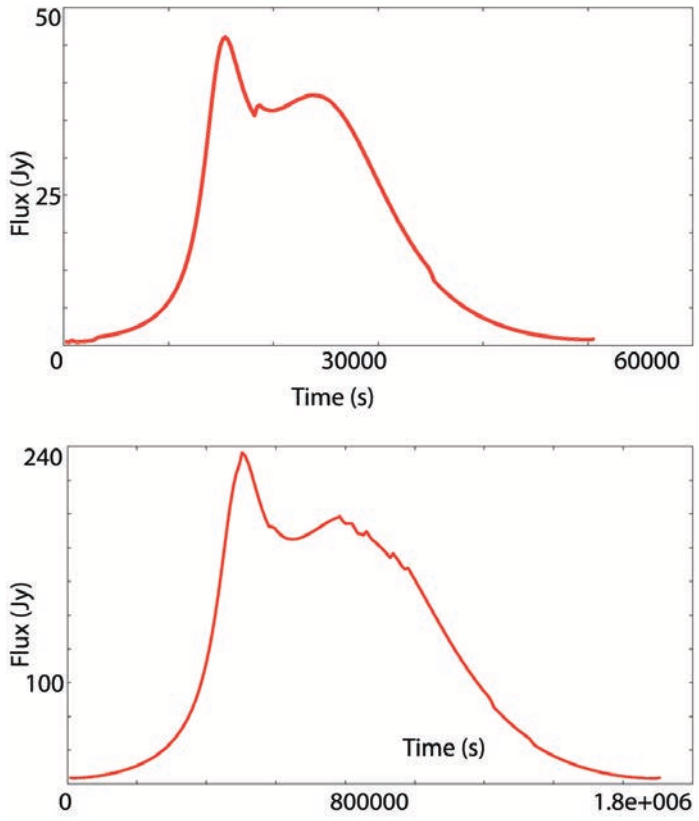

FIGURE 4.9: Light curves for a spot orbiting (retrograde) a black hole with $a/M = 0.9987$, at $\theta_o = 75°$ for a spot of radius $R_{spot} = 0.2GM/c^2$, located at $r_{sp} = 20GM/c^2$ (Top) and $R_{spot} = 0.5GM/c^2$, at $r_{sp} = 30GM/c^2$ (bottom.

of the spot. Obviously, their effects on the light curves are marginal. Distinct spikes appear in the structure of the light curve. Comparing the occurrence of these spikes with the occurrence of the sub-peaks in the light curves, we can ascertain that they appear at the same orbital phase. These can again be associated with the Einstein rings. A second cusp emerges on the approaching side. At lower inclinations no Einstein ring is formed, but multiple high order images of the flare can still be present but very faint. However, a deviation in the symmetry of the light curve is caused by the multiple images of the flare.

Light curves corresponding to flares over 70° inclination to the observer will exhibit a signature in the main peak of the light curve. This distortion or cusp in the light curve suggests the existence of a secondary image. The small apparent size of the flare will prevent

the secondary image from making a good impression in the light curve. The cusp in the light curve is more prominent for higher inclination angles.

Along with the special relativistic beaming of the emitted radiation, we find that strong gravitational lensing can cause high amplitude modulations in the light curves. For a rapidly rotating black hole, we found a difference in the lensing signature between prograde and retrograde orbits, which is detailed in the next section.

4.3.3 Black hole spin signatures

We consider spin signatures in the light curves for a localized emitter in the form of bright, continuum emitting blob on a circular orbit around the black hole. Such an object produces a time varying signal that can reveal valuable information about the black hole spin. We only look here for simple indicators of the spin in the light curve structure, not infer the spin parameter at this time. We will later attempt to calculate the Sgr A* black hole spin, taking into consideration some other aspects that complement these initial findings.

We consider light curves of emission as a function of time for co-rotating spots in extreme Kerr and Schwarzschild spacetimes. The light curve from a hot spot shows differences between the two, although these too are pronounced only at large inclination angles. Material drawn close to a black hole is likely to carry some angular momentum, hence the formation of the accretion disk seems inevitable. The dominant radiation is in the form of continuum emission, which has been the subject of intensive analysis over last few years.

We initially consider the orbital period of the spot for different black hole spins in Figure 4.10. We find that for prograde rotation, as long as we know the mass of the black hole, we can obtain a lower limit of the spin parameter, for emission presumably originating near to the ISCO, fact that we find useful later, when we estimate Sgr A* black hole spin.

The radiation originating from the innermost part of the disk shows different dependence on the inclination angle than the emission of the outer parts. To demonstrate this, we assumed that the disk surface is radiating uniformly in the local frame co-rotating with the accretion disk. Depending on radial distance to the black hole and the orientation angle to observer, the emission is influenced by Doppler effect, gravitational redshift and beaming to a different

extent. If we compare the flare emission for an extreme Kerr black hole with that for an infinitely slow rotating (using Kerr metric) or non-rotating (using Schwarzschild metric) black hole, we are be able to find differences in most relativistic signatures in the light curves. These include the height and location of the Doppler peak, the depth of the trough, the the amplification from gravitational lensing, the redshift tail and the bend found on the blue side of the trough when the inner radius is very small. We also explore the relation between various spin dependent features that produce visible signatures in the light curves. Individual rays experience unequal time lags, for purely geometrical reasons and for relativistic time dilation. The final signal is smeared by relativistic effects that become dominant in the close vicinity of the black hole and are relevant for the light curve and the variability of the source.

The differences between the Kerr and Schwarzschild cases are not strongly evident for small inclination angles θ and large radiii ($r_e \gtrsim 6R_g$), but are enhanced with increasing θ and decreasing r_e. Without any highly distinctive features such as multiple peaks, perhaps these differences can be exploited only if the angle of inclination can be determined independently.

The light curve from a single flare shows differences between two black hole spins, although they are pronounced only at large inclination angles. To establish the differences between rotating and non-rotating regimes for Keplerian orbits, we compare light curves from a flare at the same orbital radius for different spins. As Schwarzschild case keeps the ISCO well far out, we choose to compare slowly rotating black holes (a=0.3) values with extremely rotating black holes, to keep ISCO slightly lower than $6R_g$. One way of enhancing these relativistic effects is to allow the disk to extend closer to the black hole, which is possible when the black hole is rotating.

The differences between the Kerr and Schwarzschild cases are expected to be quite small. However, the shape of the light curve is slightly different because in the Kerr metric material exists in stable orbits below $\sim 6R_g$. This material contributes only a small fraction of the total flux in the light curve, so the differences are not pronounced. The detection of frame dragging by identifying emission from this material is very difficult, requiring very low flux measurement errors. The analysis of light curves from a spot about a Kerr black hole are considered for possible signatures of the frame-dragging effect.

When the inclination angle is small ($i < 60°$), the former Doppler variation dominates.

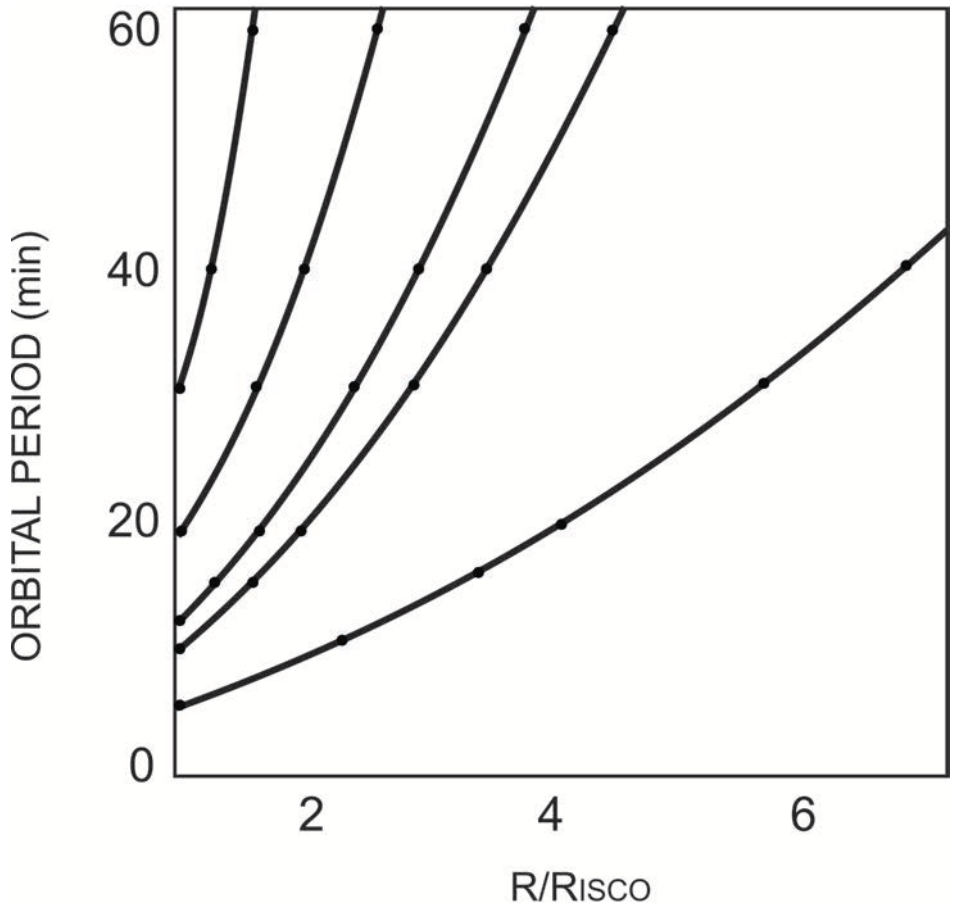

FIGURE 4.10: Orbital period (in minutes) of a spot in circular orbit around a black hole of mass $4.31x10^6 M_\odot$ with spin parameter of 0 (top left), 0.5, 0.7, 0.8 and 1 (bottom), as a function of the orbital radius in units of the ISCO radius.

When the inclination angle is large ($i > 80°$), the lensing peak is prominent. The light curves of a spot orbiting in a Keplerian disk are periodic with typically two peaks, originating from gravitational focusing and Doppler boosting, respectively. If the flare is created at a sufficiently large radius and spirals towards the center, multiple peaks appear with different peak heights and intervals. The peak height decreases quickly as the spot infalls. However, the peak interval maintains its periodicity with the rotation period. Generally the red tail provide the information about the spin of the black hole, while the high peak about the inclination angle.

There are quantitative differences in the magnification similar to those seen when the spin is varied. Higher black hole spin parameters will tend to demagnify the emitting source

slightly. For higher black hole spins, stable circular orbits extend closer to the horizon. Placing the orbits at the ISCO will result in an increase in the maximum magnification and a reduced orbital period. Circular particle orbits around a black hole are only stable outside the radius of marginal stability. Within this radius, it is normally assumed that the material plunges ballistically into the black hole. The location of ISCO depends on the black hole spin, decreasing from $6R_g$ for a static Schwarzschild black hole (a/m = 0) to $1.235R_g$ for prograde orbits around a maximally spinning Kerr black hole (a/m = 0.998). The retrograde ISCO orbit moves out considerably. Thus the inner edge of a Keplerian accretion disk will be at ISCO. The degree of redshifting is an indication of how close the emitting region extends to the black hole. Sharp features will be mostly smeared as a result of the Doppler and other relativistic effects.

The dependence on disk inclination is very strong, whereas the dependence on spin is less substantial. We illustrate this in Figure 4.11, where we plot the dependence of the ratio between the peak and trough of the light curve on the inclination angle at various spin parameters. The dependence on inclination is strong, with only a weak dependence on the spin parameter. For a non-spinning black hole, the dependence is steep, whereas for spinning black holes, as the spin increases, the same ratio values shift towards higher inclination angles, flattening the curve at the same time.

Due to the strong gravitational redshift in the inner regions, the observed intensity is reduced by a significant factor of $\nu_{\rm obs}^3/\nu_{\rm em}^3$, resulting in a weak dependence on spin, assuming uniform emission (no limb darkening law).

As the sign of a is defined with respect to the angular momentum of the accretion disk, negative values imply retrograde orbits and larger values of $R_{\rm ISCO}$. If we obtain the inclination of the disk independently, theoretically the spin can be inferred from the light curve broadening. It can be seen that the black hole spin especially affects the red wing and that this wing is more extended towards lower energies for higher values of the spin. At the same time, the light curve becomes wider and its red peak brighter.

Figure 4.12 demonstrates that the differences between the Kerr and Schwarzschild spacetimes can be noticeable. However, the distinction is less evident at small inclination angles and at large orbital radii.

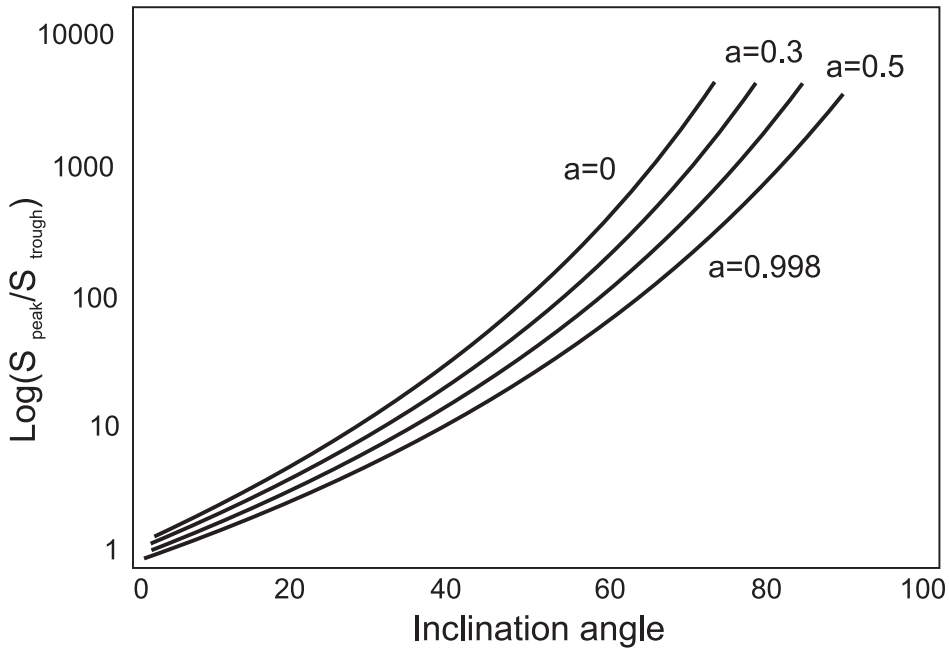

FIGURE 4.11: Change of the ratio of peak to trough observed flux with inclination angle for different black hole spins. The spot is located at an orbital radius of $r_{\rm sp} = 5GM/c^2$. The spot radius is $R_{\rm spot} = 0.5GM/c^2$.

A rotating black hole transfers its angular momentum to the accreting matter via frame dragging, and as a consequence, the marginally stable circular orbit decreases considerably. The location of ISCO depends on the black hole spin, decreasing from $6R_g$ for a static black hole to $1.235R_g$ for prograde orbits around a maximally spinning black hole.

As the spin increases, the ISCO moves closer to the horizon, increasing the circular velocities of particles on the ISCO and thus the Doppler shift effect on the light curve. Figure 4.12 demonstrates this by showing a slightly broadening of the light curve for higher spin parameters.

The Figure 4.13 shows light curves for two different black hole spin values. A static black hole will have light curves that peak slightly later and at higher maximum values of the flux. However, the primary distinction between different spins is likely to be the variation in the radius of the ISCO, and therefore the orbital period. The spin is directly related to the location of the disk's inner edge. As the spin of the black hole increases, an evident increase in the orbital velocity of matter leads to an enhancement of the relativistic beaming, shifting

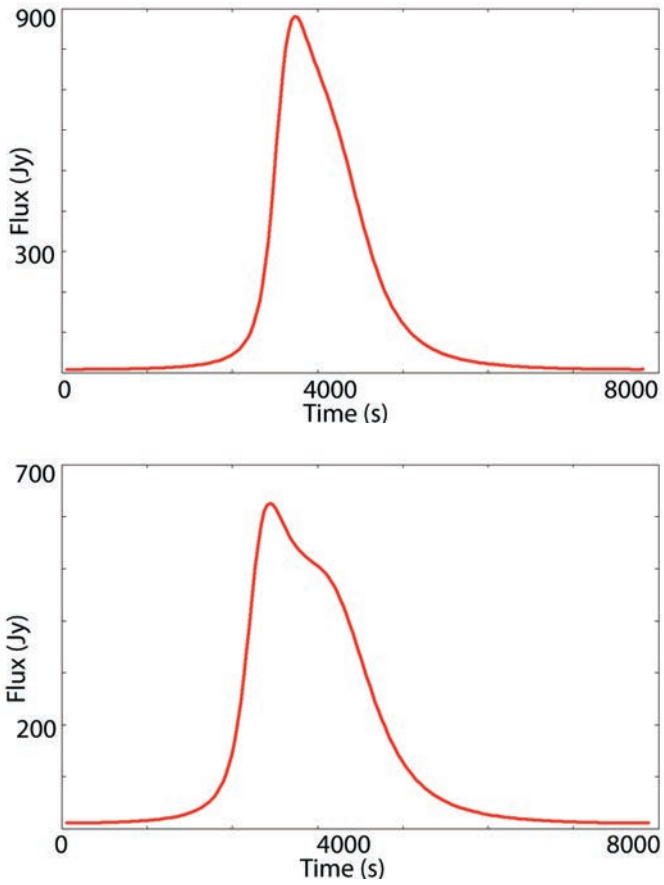

FIGURE 4.12: Light curves for a continuum emitting spot located at $r_{sp} = 6GM/c^2$ and $\theta_o = 75°$, for two black hole spins (retrograde motion). The spot radius is $R_{spot} = 0.5GM/c^2$. The top figure shows the case $a/M = 0$ and the bottom one shows the case $a/M = 0.9987$. The orbital phase is $\phi(t = 0) = -180°$, with the observer at $\phi = 0°$.

the peak of the light curve towards the approaching side (left hand), as the photons arrive earlier at the observer (see Figure 4.12). Earlier arrival times shifts the light curve on the time axis, even for large orbital radii, far enough from the black hole. The Doppler peak starts to become significant for high spinning black holes, even for average inclination angles. As the photons are dragged into the direction of motion by the spacetime itself, they leave quicker, so that the Doppler peak becomes significant. This is actually an apparent Doppler increase, as it mainly due to the Lense-Thirring effect on the redward flank of the light curve. As the receding side brings flux contributions, the light curve is smeared and therefore for higher black hole spins, the flux peaks at much lower values. For the extreme rotating Kerr case, we

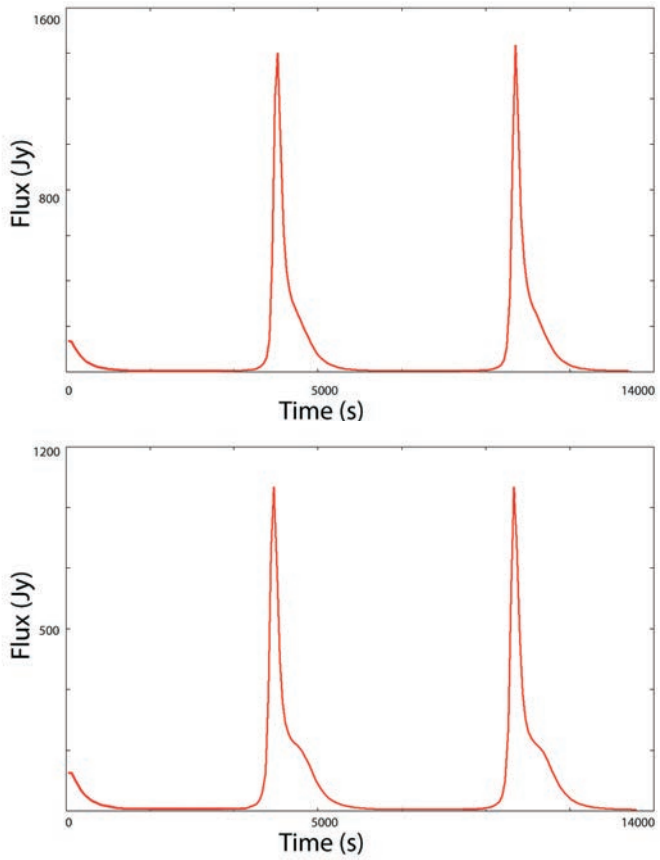

FIGURE 4.13: As in Figure 4.12 but at an inclination angle $\theta_o = 85°$, for two black hole spins. The top figure shows the case $a/M = 0$. The bottom figure shows the case $a/M = 0.9987$. The initial orbital phase of the spot is in front of the black hole $\phi(t = 0) = 180°$, with the observer at $\phi = 0°$.

will have light curves that peak much earlier, at lower values of the flux, with a clear second peak caused by the frame dragging (see Figure 4.13). The presence of this frame dragging signature can be used as a measure of the spin of the black hole, even at average inclination angles of the accretion disk.

We isolate the transverse Doppler and frame dragging effects acting on the photons that, in this case will arrive earlier at the observer (see Figure 4.14). Light received by the observer is emitted earlier, the photons being beamed into the direction of the motion. We can't accurately compare the two cases of a slow rotating and fast rotating black hole, as the ISCO for two black holes of a different spin parameter are actually placed at a different radial

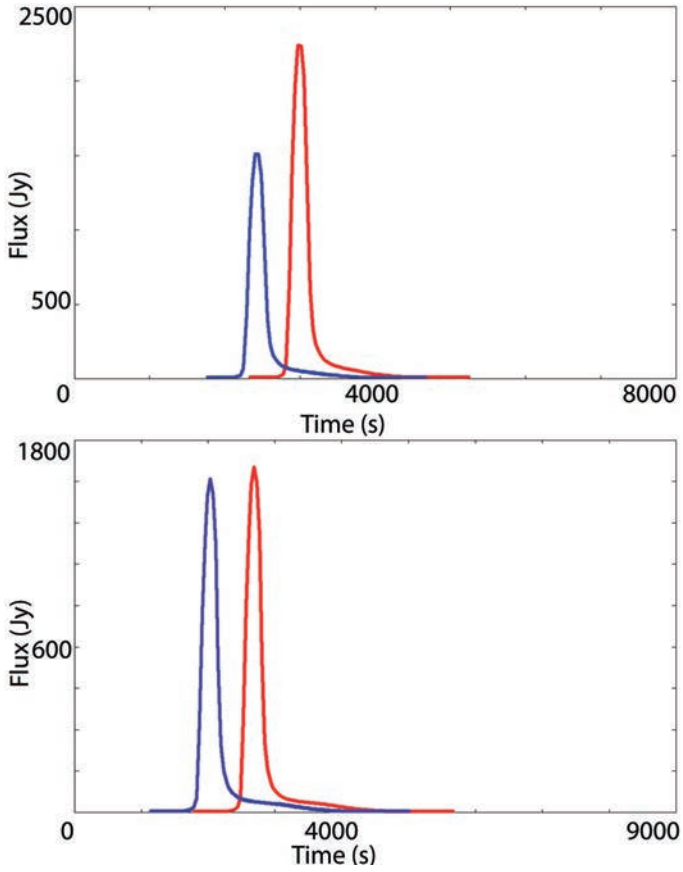

FIGURE 4.14: Light curves for a spot located at $r_{sp} = 5GM/c^2$ and $\theta_o = 89°$, for two black hole spins. The radius of the spot is $R_{spot} = 0.5GM/c^2$. The top figure shows the case $a/M = 0.3$ and the bottom one shows the case $a/M = 0.9987$. The orbital phase is $\phi(t = 0) = -180°$, with the observer at $\phi = 0°$. Prograde (blue) and retrograde (red) rotation is assumed.

location. We only show the qualitative evidence of each relativistic signature in the light curves.

The spin affects mainly the receding wing of the light curve. The Doppler peak appears brighter and the light curve shows a more extended and slightly broader profile, for higher values of the spin. (see Figure 4.15).

The second (”red”) peak is brighter in the case of highly rotating black holes, however it is also more embedded into the first (”blue”) peak wing and therefore less separable from it. In the retrograde case, the frame-dragging will act in opposition to the disk angular

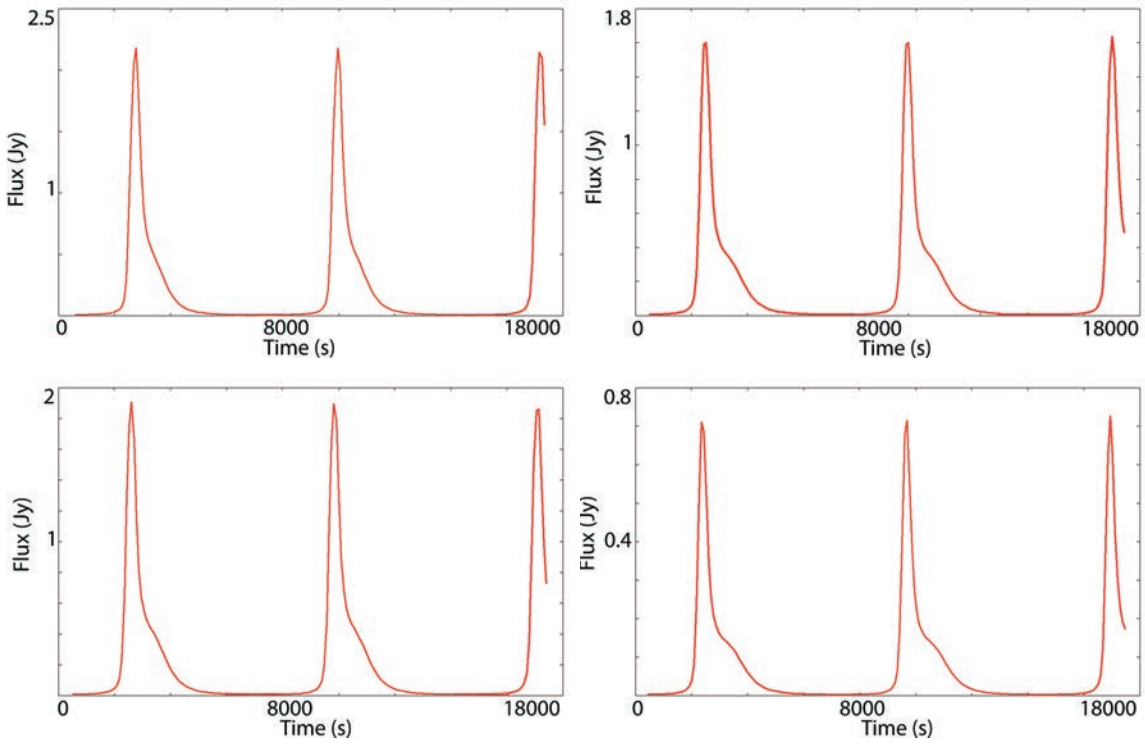

FIGURE 4.15: As in Figure 4.12 but at the inclination $\theta_o = 85°$, for various spins. The spot radius is $R_{spot} = 0.1GM/c^2$. The first column shows a spot orbiting a black hole with $a/M = 0$ and $a/M = 0.5$. The second column shows a spot orbiting a black hole of $a/M = 0.8$ and $a/M = 0.9987$.

momentum, causing orbits to plunge farther out. In the prograde case, the frame-dragging will rotationally support the orbits close to the black hole. The retrograde light curve shows a stronger Doppler boosting therefore a stronger signal compared with a strong dampened redshifted prograde light curve (see Figure 4.16).

The changes in the light curve in the presence of the black hole spin explicitly depend on whether the motion of the light ray is in the direction, or opposite to the spin. Compared to the Schwarzschild case, the bending angle is greater for direct orbits, and smaller for retrograde orbits.

In addition, for higher spins, the effect is more pronounced resulting in tighter winding of direct orbits with respect to the axis of rotation, and a higher degree of unwinding of retrograde orbits. A direct consequence of this effect combined with the time delay caused

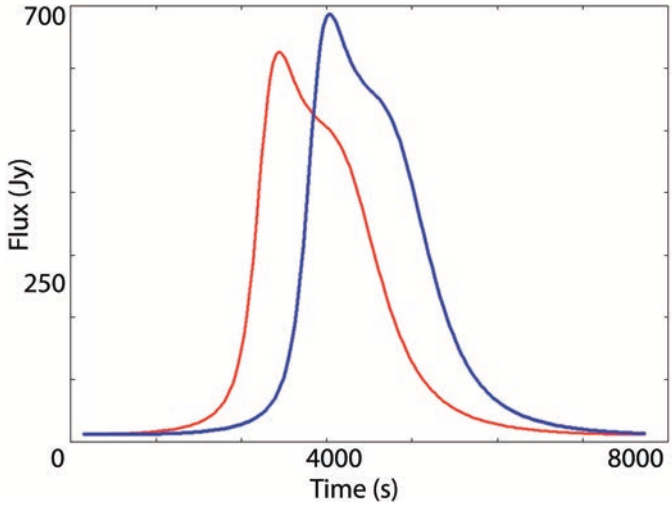

FIGURE 4.16: As in Figure 4.12, bottom, for prograde and retrograde motion and $a/M = 0.9987$. The spot is located at an orbital radius of $r_{\rm sp} = 6.5GM/c^2$. The radius of the spot is $R_{\rm spot} = 0.5GM/c^2$. The red light curve shows a spot in prograde rotation. The blue light curve shows a spot in retrograde rotation. Radius is in units of GM/c^2. The initial orbital phase location of the spot is behind the black hole $\phi(t = 0) = -180°$.

by Lense-Thirring effect is a shift of the light curve at later times for retrograde orbits. The best chance of detecting the frame dragging effect is to search for stable Keplerian orbits at radii below or close to the limit of $6R_g$ imposed in a Schwarzschild metric (Laor 1991). We find that the differences between the Kerr and Schwarzschild cases are generally not so strong beyond $10R_g$. The dragging of inertial frames is the strongest at the equator, and in this case, it cancels out the retrograde motion of the photons. Away from the equator, the dragging becomes weaker and so the orbit regains its retrograde character. Particles on retrograde orbits require larger absolute values of the specific angular momentum to remain out of the black hole than particles on prograde orbits. Frame dragging approaches zero on the axis of rotation and it is maximum at the equator.

Because the most significant influence of the relativistic effects is visible in the close vicinity of the black hole, the relativistic effects are more pronounced for highly rotating black holes (Figure 4.13). If the black hole rotates with extreme spin $a = 0.998M$, the inner radius $r_{\rm in}$ for the accretion disk is only $1.23R_g$. The gravitational redshift and the

light bending become more significant here. Some photon trajectories which are initially retrograde could be forced to turn back to become prograde due to the frame dragging. In this case, the red tail is rather long and extended, while the blue tail ends very abruptly, although cut off quite sharply for high inclinations (see Figure 4.16). However, the light curve contains contributions to the flux mainly from the outer region of the disk ($r > 10R_g$), where the frame dragging effect is much smaller. The retrograde orbiting of the spot reduces the contribution from the innermost parts of the accretion disk so that the red and blue tails become slimmer.

For a retrograde black hole, the emission becomes greater with decreasing angular momentum of the black hole. The peak is observed earlier for a faster rotating black hole (see Figure 4.16), as the photons are dragged into the direction of motion and more dragged photons come at an earlier time than in the case of a slow rotating black hole. In the prograde case, the peak is still observed earlier because of the frame dragging effect being stronger for a fast spinning black hole but in this case, the peak flux increases for a faster rotating black hole. Since the marginally stable orbit is smaller for a higher angular momentum of the black hole, the hardening effect of the spectrum is more significant in Kerr regime than in Schwarzschild case.

For a rapidly spinning black hole, there is a difference in the lensing signature of prograde and retrograde orbits, keeping in mind that the retrograde ISCO moves considerably farther out in the disk. The differences between the magnification for prograde and retrograde light curves are small in comparison to those associated with the variations of the orbital parameters. The light curves from a spot in retrograde rotation show a few differences that can be interpreted through frame dragging effect and beaming of the photons in the direction of motion. The light curve for a flare in retrograde motion appears to be delayed, as the photons are turned around in the direction of the black hole spin, being ”dragged” be the spacetime to follow prograde orbits. We notice this time delay at every inclination angle, the signature being more significant at higher spins of the black hole, where frame dragging effects are the strongest. The second signature in the retrograde orbits is a special relativistic effect due to the ”beaming” of the photons while they are boosted into the direction of the black hole spin. For rapidly spinning black holes there is a difference in the lensing signature of prograde

and retrograde orbits. There are quantitative differences in the peak flux similar to those seen when the spin is varied (higher black hole spin tends to demagnify the flux peak). The combination between lensing and beaming effects participate to a slight increase of the peak flux in the retrograde case (see Figure 4.14). Aside from its influence on the ISCO radius, the black hole spin has only small impact on the shape of the light curves. For this reason it is almost impossible to deduce the spin parameter from the light curves alone.

4.4 Light curve properties and substructure

The shape of the light curve is determined by various physical parameters: the black hole angular momentum and the inclination angle of the disk to the observers line of sight. The profile of a light curve from a spot in a circular orbit has a characteristic double-peaked shape with a longer tail on the red extent, a narrow peak to the gravitational lensing and a broad Doppler peak where this becomes significant (see Figure 4.16). The final light curve is the composite of the two peaks representing light emitted when the source is approaching or receding relative to the observer. The emission from the black hole is beamed into the direction of motion, making the blue peak much brighter than the red one (see Figure 4.3). We find that the blue wing is quite sensitive to the inclination angle, compared to the red wing.

Relativistic effects, particularly for a maximally rotating Kerr case, significantly affect the shape of the light curve, especially from the inner disk when viewed at large inclination angles. At medium and high inclination angles, the differences between light curves still persist. The most important one is the redshift due to the gravitational potential at small orbital radii. The light curve for a spot around a rotating black hole has a unique shape which may be fit to real data to determine the orbital parameters. At high inclination angles the light curve characteristics can help to distinguish the extreme Kerr and Schwarzschild spacetimes (Figure 4.13). Without any highly significant features, these differences can be exploited only if either the angle of inclination or the spin can be determined independently.

We display light curves for a spot model for spot radii (see Figure 4.17) and inclinations of the disk. Decreasing the spot radius leads to narrower, higher peaks in the light curve.

This fact is due to the increasing spot velocity leading to stronger relativistic Doppler and beaming effects. The same changes are produced by increasing the inclination of the disk, since this increases the line of sight velocity of the spot. In our used parameter range, the changes in inclination exhibit the sought relativistic effects more strongly than the changes in the orbital radius. When comparing light curves for different blob sizes and orbital radii, one of the first notable features in the profile is the double peak aspect which is mostly determined by the physical and geometrical parameters at a relatively large distance from the inner most stable orbit.

The flare time scale and the flux/trough ratio are good indicatives of the orbital radius and inclination angle of the disk. We find a symmetry breaking between the approaching part and the receding part of the orbit. Doppler beaming as well as the light focusing contribute to variations of the observed flux, especially at high view angles when the orbit is seen almost edge-on. The Doppler boosting effect is off phase with respect to the light focusing effect, roughly by 0.25 of the full orbit at the corresponding radius (Figure 4.3). This de-phasing depends on the black hole spin and on the inclination through the finite light-travel time from different parts of the orbit towards the observer. The finite light travel time affects the resulting signal and causes an additional enhancement of the observed flux, especially in the case of an extremely rotating black hole. Although the light time delay arises as an immediate consequence of the finite speed of light, the interplay with the light bending and focusing effect is complicated, being interconnected in a rather complex manner.

We find that the size of the spot can be a significant parameter that contributes to the shape of the light curve, as well as the amplitude of the observed flux at infinity, as we can see in Figure 4.17. The effect of gravitational lensing requires a fine tuned geometrical arrangement, which occurs with only a low probability in practical observations.

The competition between the relativistic beaming effect and gravitational redshift is very interesting. In Figure 4.18 we see that the beaming effect on the incoming photons causes a magnification of the observed flux as we locate the spot closer to the black hole reaching a maximum at about $r_{\rm sp} = 3GM/c^2$. However, within this limit, as we get closer to the black hole, the flux diminishes rapidly due to strong gravitational redshift. The degree of redshifting is an indication of how close the emitting region extends to the black hole. Near

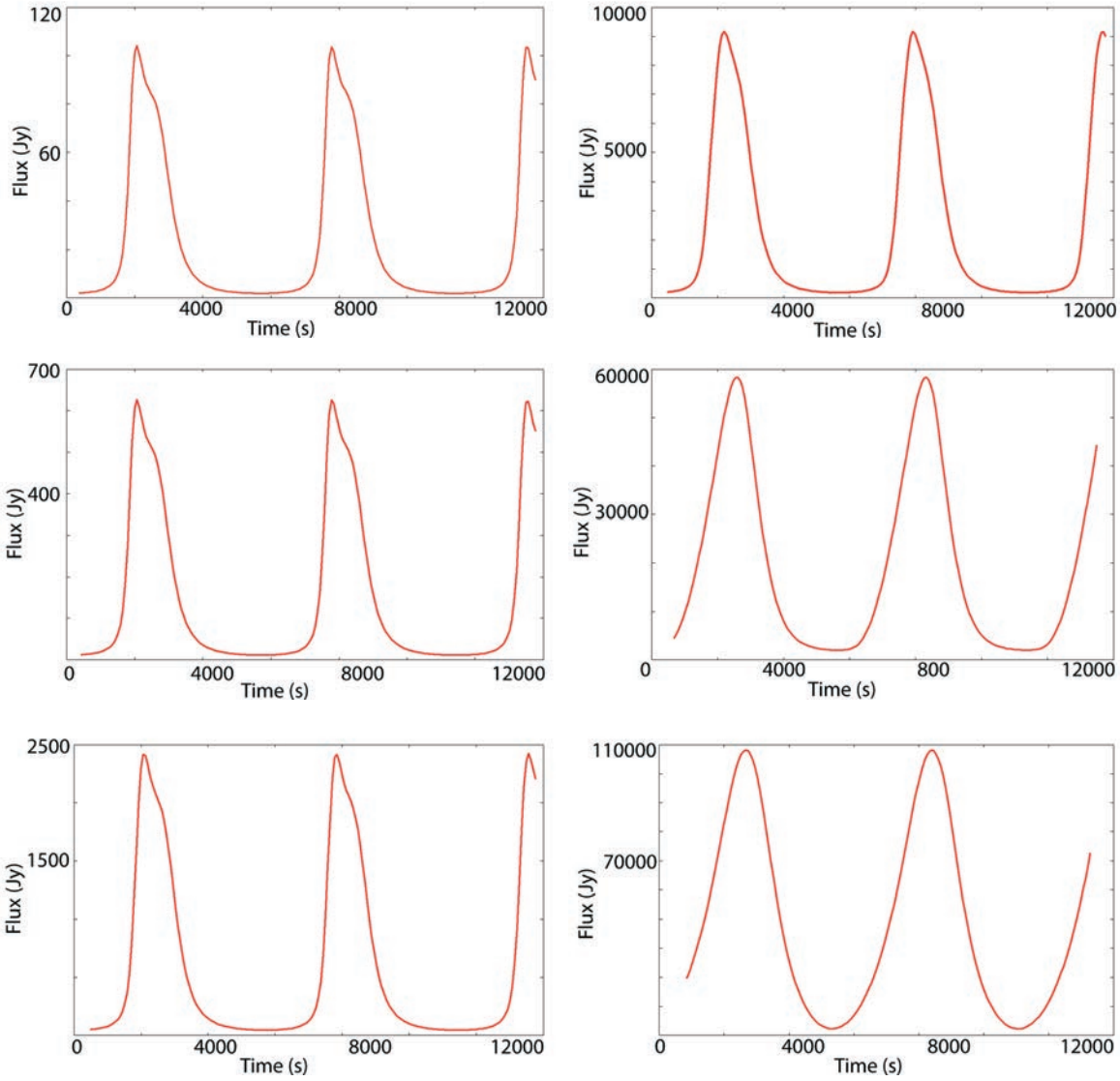

FIGURE 4.17: As in Figure 4.12, bottom but for various sizes of the spot and $a/M = 0.9987$. The first column shows a spot of radius $R_{\rm spot} = 0.2GM/c^2$, $R_{\rm spot} = 0.5GM/c^2$ and $R_{\rm spot} = 1GM/c^2$. The second column shows a spot of radius $R_{\rm spot} = 2GM/c^2$, $R_{\rm spot} = 6.3GM/c^2$ and $R_{\rm spot} = 10GM/c^2$.

the black hole, where the orbital velocities are relativistic, the beaming effect enhances the blue peak of light curve. The extent of the broadening is determined by both Doppler and gravitational shifts. However, the total shift is always towards the red as the latter effect always overwhelms the former. At large distances to the black hole the light curves are not dominated by gravitational redshift. These effects are shown by simulating light curves at

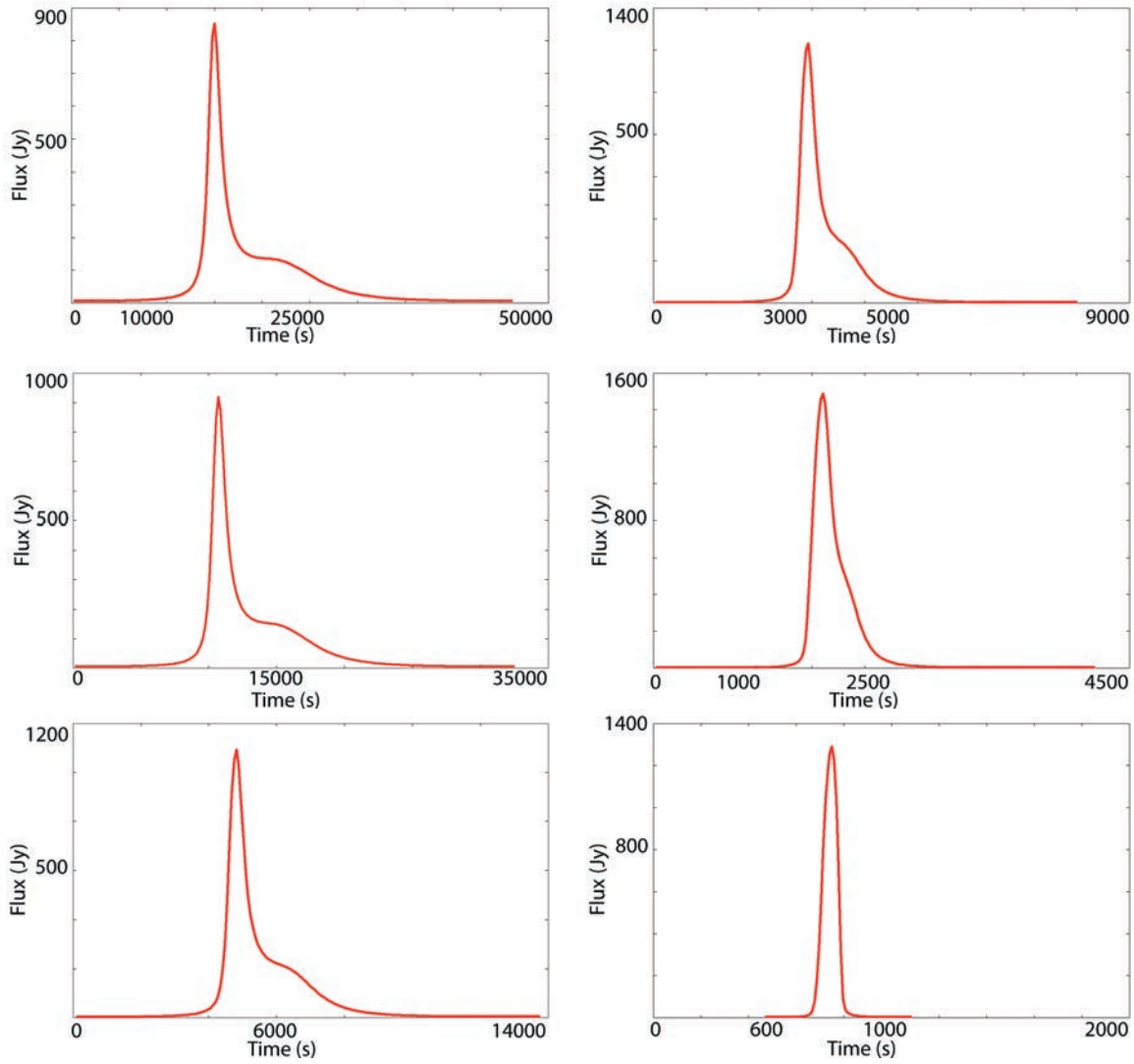

Figure 4.18: As in Figure 4.12, bottom but at the inclination $\theta_o = 85°$, for various radial locations and $a/M = 0.9987$. The first column shows a spot located at $r_{sp} = 9GM/c^2$, $r_{sp} = 8GM/c^2$ and $r_{sp} = 6GM/c^2$. The second column shows a spot located at $r_{sp} = 5GM/c^2$, $r_{sp} = 4GM/c^2$ and $r_{sp} = 3GM/c^2$.

larger inclination angles. The only way to have significantly redshifted flux is for the source of emission to move quite close to the innermost stable orbit of the black hole. Unfortunately, for a static black hole, the ISCO is located too far from the black hole to observe any strong signatures. The principal difference between these two spacetime geometries is the location of the innermost stable orbit (and hence the inner edge of the emission).

The photons are also experiencing a slowing down of time or gravitational time dilation, relative to an observer located outside the gravitational field. The observer will see that any physical events and clocks appear to run slower. As the object approaches the event horizon, the time dilation would approach infinity, the local time would appear to be stopped. As seen by a distant observer, the local time associated with an object plunging into the black hole appears to slow down, approaching but never actually reaching the event horizon. Combined with this effect, the object appears redder and dimmer, because of the extreme gravitational redshift. Eventually, the plunging object becomes so dim that it can no longer be seen, at a point just before it reaches the event horizon.

Light curve distortion by strong gravity, i.e. very skewed and asymmetric profiles (see Figure 4.19) occur at smaller orbital radii. There are several differences in the asymmetry of light curves. In particular, there is a dependence on inclination angle: the asymmetry strengthens as the inclination increases. This is due to the emission from high accretion disks becoming amplified by relativistic Doppler beaming. The amplitude of the light curve changes due to the combined effect of gravitational lensing, rotation and Doppler shift. In addition, the light curve becomes asymmetric (Fukue 1987).

The light curves have distinctive skewed, double-peaked profiles which reflect the Doppler and gravitational shifts associated with emitting material in a strongly curved spacetime (see Figure 4.19).

The delay amplification plays a significant role in enhancing the local flux. From the observer point of view, the flare spends more time in certain parts of the orbit than in the others and therefore less photons per unit observers time are detected. In Kerr regime, the flare orbits with a higher velocity being closer to the black hole and the delay amplification is more significant. The effect of rotation becomes visible only close to the black hole.

The symmetry of the light curve is regained when the spot is located closer to the black hole, because of a lack of lensing effect in the area. We can see that there are no remaining photons that make up a positive trough in the light curve, showing an elongated filament or Einstein ring around the black hole. In this way, the flux is never null, where lensing effect is acting, like in the middle figure, at around $r_{\rm sp} = 6GM/c^2$. The gravitational lensing effect will also break the symmetry of the light curve, at a high inclination angle. In the

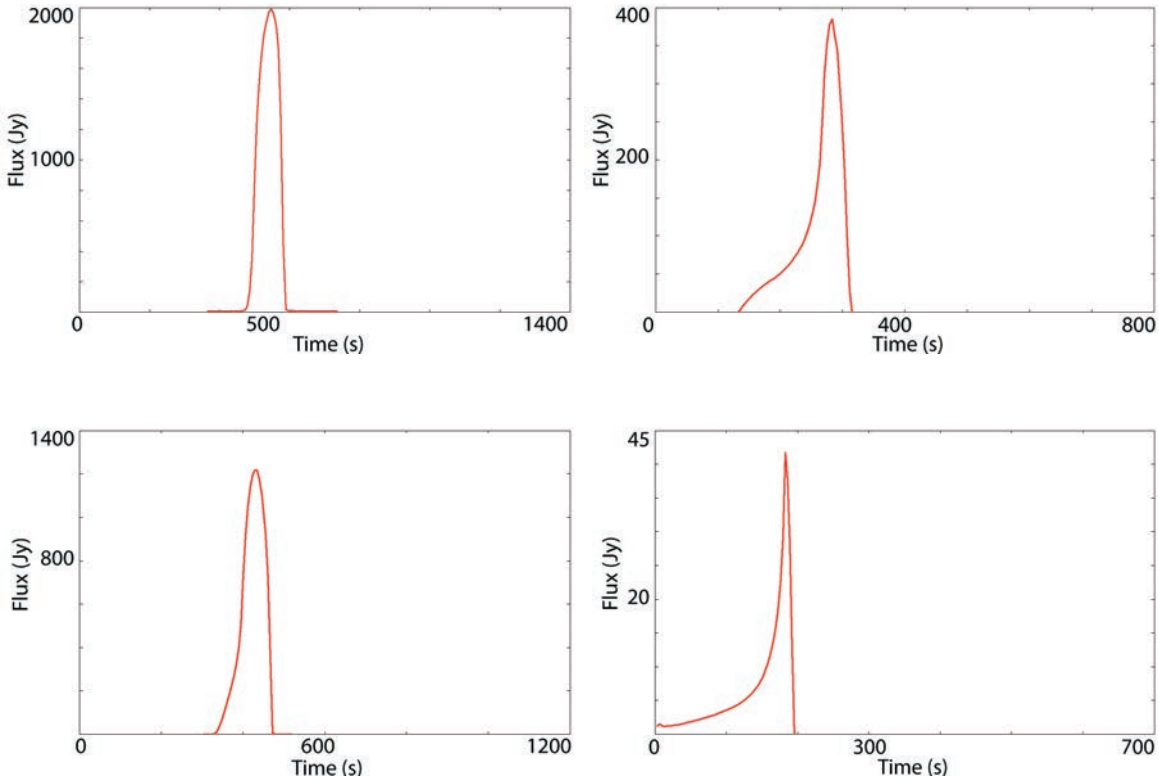

FIGURE 4.19: As in Figure 4.12, bottom but at $\theta_o = 85°$, for $a/M = 0.9987$ and for four radial locations, close to the ISCO. The double-peak profile is lost because of the redshift. The first column shows a spot located at $r_{sp} = 2.7GM/c^2$ and $r_{sp} = 2.5GM/c^2$. The second column shows a spot located at $r_{sp} = 2.2GM/c^2$ and $r_{sp} = 2GM/c^2$.

bottom figure, the lensing effect is much smaller, the flux actually becoming zero between two consecutive orbits. No elongation or ring effect is formed in this case and the light curve keeps its symmetry. The blueshift peak is dominant and the light curve actually gains in amplitude because of the boosting of the light. The gravitational redshift will counter-balance and compensate for the amplification caused by the lensing effects, generating a final loss in the observed brightness. The observed periodicity depends on the relation between the longest and the shortest photon geodesics that connect the spot with the distant observer at a given time in the observer's frame. Going towards larger inclination angles, the shape of the light curve changes and it becomes more symmetric, with an exception for the phase of 180°, when the spot passes behind the black hole. The closest symmetry is reached between 45° and 60°. For larger angles, the flux decreases rapidly and the light curve becomes much

flatter. We included photon energy shifts due to Doppler and general relativity effects, as well as light bending and the time delays that influence the observed light curve.

The relativistic light curve exhibits a dependence for many physical parameters. The energy of the blue peak is mainly dictated by the inclination of the observer line of sight with respect to the accretion disc axis. The difference in the redshift or blueshift is mainly a result of the difference in the position of the ISCO. While the magnification varies with the orbital radius, it is a stronger indicator of the inclination of the orbit relative to the line of sight (not to be confused with orbits lying out of the equatorial plane of a Kerr black hole). Placing the orbit at the ISCO results in a reduced orbital period and a strong redshifted demagnified flux amplitude. By increasing the orbital radius (with spin and inclination fixed), the dominant factor is the gravitational redshift rather than the relativistic beaming. On the other hand, the latter becomes important for large inclinations.

Time delays can significantly influence the observed flare duration and the light curve profile. The general transfer function together with the time delay amplification tell us how much the local flux from the flare is amplified when observed from infinity. Both functions depend on the location of the emitting source within the accretion disc. Consequently, we need to know where the flare is located at the time when an observed photon was emitted from the disk, in other words, we need a time dependent emission law. If the spot is moving in the local frame with a constant velocity, the observer at infinity sees that the flare changes its velocity, due to different time delays with which the emitted photons are observed. For larger inclinations, the overall amplification has a higher maximum in Kerr regime, because of a larger lensing effect, Doppler shift and delay amplification, whereas for lower inclination angles it is diminished because of a smaller gravitational shift. The contribution of each component to the transfer function is present in the light curve profile.

In our modelling, we assume that the inner edge of the disk is located at the marginally stable orbit and exclude all photons which cross the surface of the disk and therefore are recaptured. We can see in Figure 4.20 the effect of eclipsing the light curve from the spot by the outer regions of the disc, resulting in a narrower profile of the light curve. In the approximation where the height of the accretion disk is much smaller than the radius of the disk, if the disk is opaque, the effect of eclipsing the light curve of a spot by the disk itself

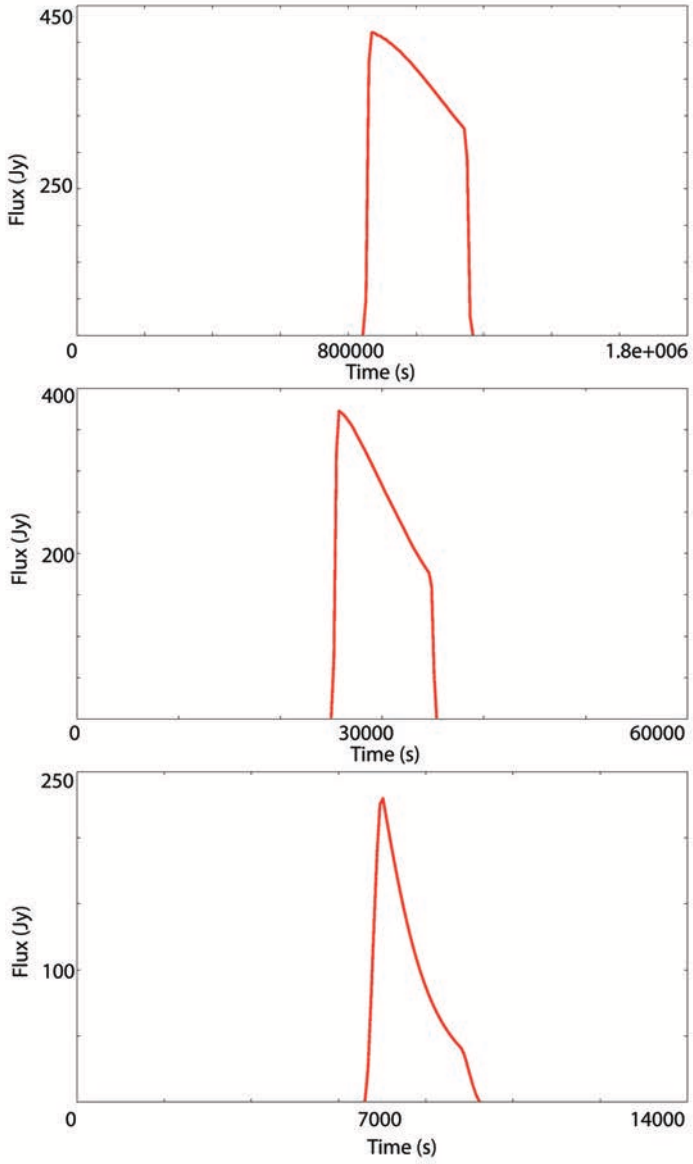

FIGURE 4.20: Light curves for an eclipsed spot orbiting a black hole of $a/M = 0.998$, testing the effect of the outer regions of the disc. The spot located at $r_{\rm sp} = 30GM/c^2$ at $\theta_{\rm o} = 45°$ and azimuthal inclination $\phi_{\rm o} = 70°$ (top). In the middle the spot is located at $r_{\rm sp} = 20GM/c^2$ ($r_{\rm in} = 2GM/c^2$ and $r_{\rm out} = 50GM/c^2$) at $\theta_{\rm o} = 60°$ and azimuth $\phi_{\rm o} = 80°$. In the bottom figure the spot is located at $r_{\rm sp} = 6GM/c^2$ ($r_{\rm in} = 2GM/c^2$ and $r_{\rm out} = 20GM/c^2$) at $\theta_{\rm o} = 80°$ and $\phi_{\rm o} = 80°$.

is interesting. As we can see, the shape of the light curve relies strongly on the geometry of the disk, apart from the inclination angle of the disk. The eclipsed light curves could be used to determine the geometry of the accretion disk itself, as the light curves produced in this way contain sharp peaks and plateaus that are specific only to orbits nearly in the equatorial plane.

We find that most of the significant observable relativistic effects are obtained only for high inclination angles. The shape of the light curve is far from symmetric when the relativistic effects are strong. The Doppler shift and the gravitational lensing generate sharp features within the light curve if the viewing angle is large enough. Within the redshift factor, both Doppler shift and gravitational shift determine the strength of the emission, the g-factor being dominated by the Doppler effect, whereas the gravitational shift effect is less intense. The shape of the light curve becomes more sinusoidal when the orbital radius is large enough and the disk is nearly face-on. The gravitational lensing is most sensitive to the inclination angle, especially for a disk inclined nearly edge-on.

The characteristic peak of the light curve is determined by the interplay between the Doppler shift and gravitational lensing. The lensing part induces the maximum at the center, whereas the Doppler shift determines the characteristic edge of the light curve. The light curve has a hump and a peak in one single orbital period, the peak results from the lensing effect when the flare is behind the black hole and the hump comes from the Doppler effect when the flare moves towards to observer. The Doppler effect is suppressed with increasing strength of the lensing effect. Contrary to the Schwarzschild black hole, a spot orbiting a Kerr black hole close to the ISCO can be eclipsed even for average inclination angles. For a flare orbiting an extremely rotating black hole, two peaks are present in the light curve, if the disk is seen nearly edge-on. The main peak occurs when the spot is just behind the black hole, as a result of the gravitational focussing. The second peak occurs at around 270° and it is a result of the Doppler shift, effect that is dominant for disks seen nearly face-on.

As the inclination angle increases, the brightness is significantly amplified, due to the special relativistic beaming which will focus the radiation toward the observer, increasing the relative flux contributions from the emitting blob. As the spin of the black hole increases, the ISCO moves towards the horizon and the velocity of a photon near the ISCO will increase,

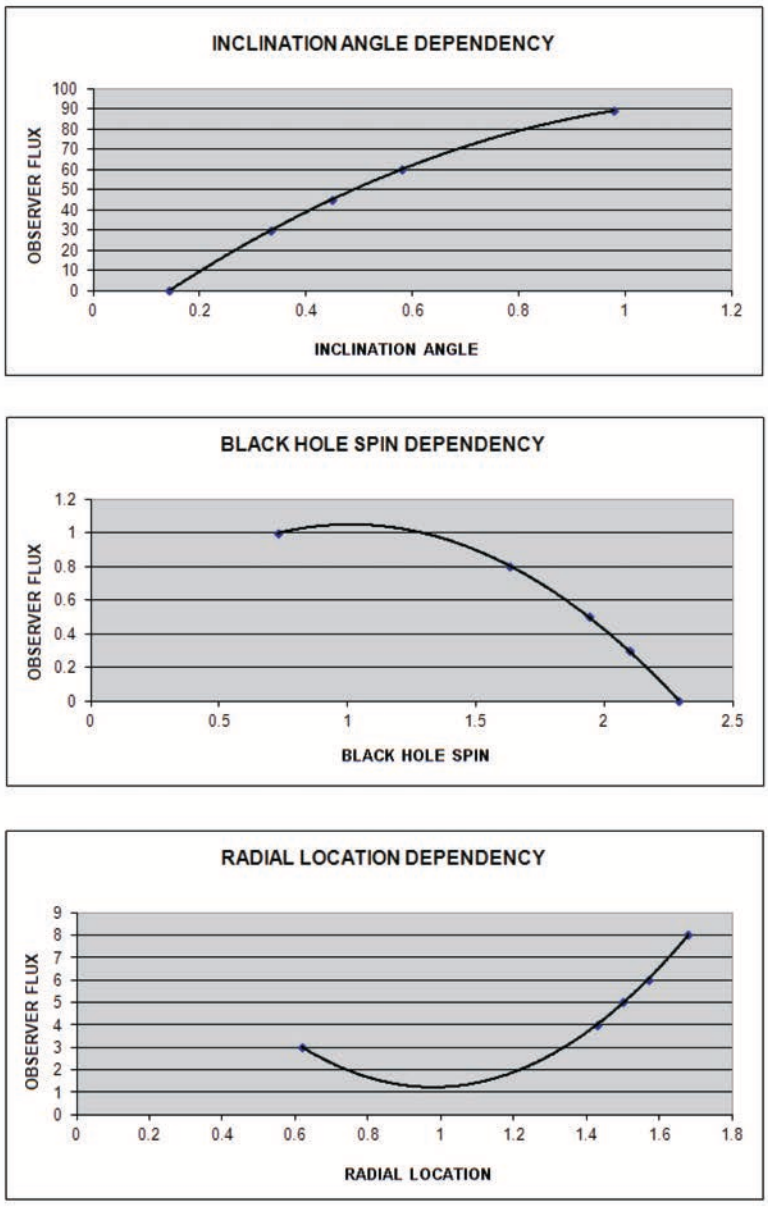

FIGURE 4.21: The observed flux for various disk angles for a black hole of $a/M = 0.9987$(Top). The spot ($R_{\rm spot} = 0.5GM/c^2$) is located at $r_{\rm sp} = 6.5GM/c^2$. The observed flux for different spin parameters (Middle), for a spot located at $r_{\rm sp} = 6GM/c^2$, and $\theta_{\rm o} = 30°$. The observed flux for various orbital locations for a black hole with $a/M = 0.9987$(Bottom) and $\theta_{\rm o} = 30°$.

together with the gravitational lensing. This fact should cause a considerable magnification of the flux contributions from the flare. However, this is not the case, as we can see in

Figure 4.21 (middle). The reason for this is the increasing gravitational redshift as the spot is located closer to the event horizon and under stronger gravitational potential. The phase lag of the blueshift peak with respect to the initial angular phase of the spot is also amplified for smaller values of ISCO, producing asymmetric light curves. This lensing effect becomes more significant for higher inclinations as the black hole and the emitting region approach collinearity with the observer, producing an Einstein ring as $i \rightarrow 90^{\circ}$. This adds up to the the special relativistic beaming as the light curve peaks over a broader phase of the orbital period due to lensing. Therefore the dependence on inclination for a Kerr light curve is smaller than that for the Schwarzschild geometry. For example, in Figure 4.11 we show the dependence of the ratio between the peak and trough of the light curve on the inclination angle for various spins. However, if the spot is rotating in a retrograde motion with respect to the black hole spin, the ISCO moves away from the horizon (e.g. $R_{\rm ISCO}$ = 8.97M for a/M=-0.99) and this way reverses the effect, leading into a stronger dependence on inclination.

The effect of light bending is most important in the high energetic parts of the observed spectrum. Photons at these high energies originate close to the central black hole, and hence their trajectories are most affected by the light bending effect. Depending on the viewing angle, this can enhance the observed flux, if the light bending effects are not neglected.

The peak of the light curve is given by the maximum flux due to both special relativistic beaming and the magnification caused by the gravitational lensing onto emission from the far side of the black hole. The lensing effect produces an intermediate peak from the gravitational magnification of light moving transverse to the observer line of sight (Beckwith & Done 2004; Schnittman & Rezzolla 2005). This peak is most pronounced at very high inclinations where lensing is more important. At high inclination angles, the shape of the light curve (for a continuum emitting spot) can serve to distinguish the extreme Kerr and Schwarzschild geometries, even at radii near $6R_g$. Lensing effect causes magnification of the main peak of the light curve and a different ratio between the peak and the trough of the light curve. When the lensing effect is not significant, at low inclination angles (see Figure 4.3), the Doppler shift raises the trough between consecutive peaks of the flux and dampens the overall shape of the light curve.

Due in large part to these relativistic effects, the amplitude of the light curve is primarily

sensitive to the inclination angle which affects not only the total observed intensity, but also significantly changes the shape of the relativistic light curve. Close to the black hole, the light curve loses its shoulders, the kurtosis becoming flatter as the spot gets near the ISCO. For large radial orbital locations, if the flare is locate far away from the ISCO, the kurtosis becomes thinner. The photons arrive earlier at the observer, as the light is beamed into the direction of motion, therefore the light curve is shifted to earlier times, as we can see in Figure 4.19. Close to the ISCO, the light curve exhibits a very long tail on the left (approaching) side caused by a number of photons being beamed at very early times, as in Figure 4.3).

As the inclination increases, the matter moves towards and away from the observer with higher velocity, narrowing the light curve. Near the limit of $\rightarrow 90°$, while the greater beaming helps narrowing the light curve, gravitational magnification amplifies the contribution of a small region of the emission region. At smaller inclination angles, relativistic beaming plays a significantly smaller role, so the gravitational redshift dominates the flux contributions in the light curve at small spin and radius, broadening the entire light curve and giving it symmetry (see Figure 4.3). We find the most symmetrical profiles at about 45°. The nearly face-on projection also gives a much smaller range of redshift, corresponding to smaller values of energies.

The shape of the light curve changes as a function of radial location or distance from central black hole. When the emitter is located at lower radii within the accretion disk, i.e. closer to the central black hole, the light curve is broader and the profile is more asymmetric. If the emission is originating at larger distances from the black hole, the red peak becomes brighter and profile narrower and more symmetric. We show how the peak flux changes with the orbital location of the spot (see Figure 4.22).

The effect of black hole rotation becomes prominent for almost extreme values of the black hole spin. The differences between $a = 0$ and $a = 0.5$ are found to be relatively small. We find that presence of frame dragging is not notable if the inner radial location of the spot is $\sim 5R_g$ or above; for example the profile from a Kerr black hole from the radius of $r_i = 5.5R_g$ is similar to the Schwarzschild case with close to the minimum stable orbit of $6R_g$.(see Figure 4.14). This result gives hope that black hole rotation may be detected but only if there is a blob emitting region that comes well below $6R_g$. The prominent features

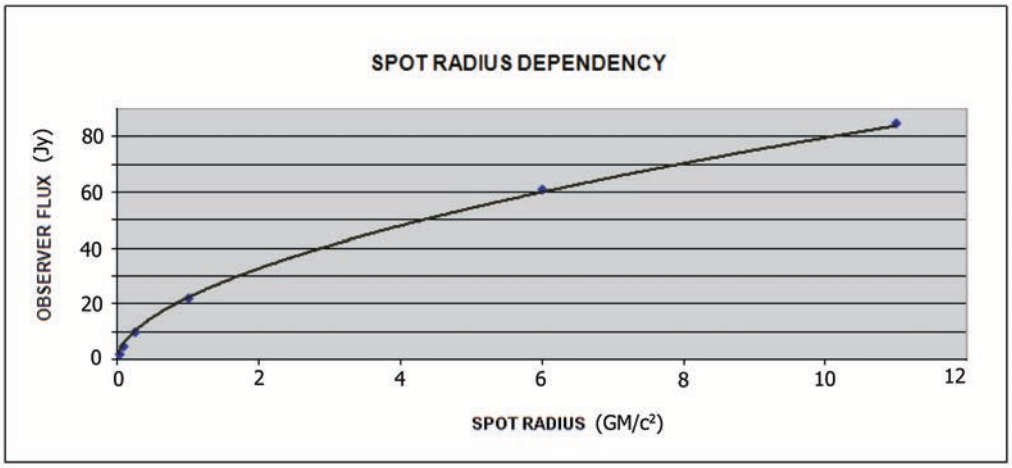

FIGURE 4.22: The peak flux for different orbital locations of a spot orbiting an extreme spinning black hole of $a/M = 0.9987$. The spot is viewed from $\theta_o = 75°$.

in the profiles include the height and location of the peaks, the depth of the trough, and the kink found on the blue side of the trough when the radial location is above several R_g.

We also find a large difference in the orbital phase of the maximum emission between the extreme regime, $a \to 1$, in contrast to the static case, $a \to 0$. The reason is that for large black hole spins, the time delay and the effect of frame dragging on photons emitted behind the black hole are quite prominent, as we can see in Figure 4.14. For very high inclination angles, most of the flux actually comes from the far side of the disc, due to very strong light bending. The light curve is sensitive to the inclination angle of the observer. For low inclination angles, the profile tends to be a single broad peak with the same endpoints of the red and blue tails, and almost all of the photons are redshifted due to strong gravitational redshift and weak Doppler blueshift. The lensing effect is also not very significant and doesn't contribute with a considerable magnification to the peak of the light curve.

All these investigations indicate that the light curves are a helpful tool for studying the properties of the supermassive black holes (such as the inclination angle of the disk and the black hole spin), spacetime geometry in their vicinity, the accretion physics, probing the effects of strong gravitational fields, and testing the predictions of General Relativity. In the next chapter, we include the effects of intrinsic variability and apply our model to Sgr A*.

5

Modelling Sgr A* flare variability

5.1 Variability of Sgr A*

Sgr A* is strongly variable in the X-ray and near-infrared wavelength bands (Baganoff et al. 2001, 2003, Eckart et al. 2004, 2006a, Porquet et al. 2003, Goldwurm et al. 2003, Genzel et al. 2003b, Ghez et al. 2004, Eisenhauer et al. 2005, Belanger et al. 2006, and Yusef-Zadeh et al. 2006a). The X-ray and infrared flares occur almost simultaneously, with no significant or visible time delays (within 3 minutes). The strong flares in the submillimeter band show structure at very small angular scales (Doeleman et al. 2008) leading us to the hypothesis that the innermost regions of the accretion disk are strongly variable.

Sgr A* is continuously variable showing low-level emission above 5 mJy known as flaring state and low level emission as the quiescent state. At low-level average flux, the variability in NIR follows a log-normal distribution (Dodds-Eden et al., 2010). The low-level

emission above 5 mJy was identified (Schdel et al., 2006) as the flaring emission state and the low-level emission below 5 mJy represents the quiescent state, with minimum 0.5 mJy flux due to faint stellar components. Flares with more than 5 mJy of variability are rare, about two per year. The quiescent emission seems to show variability with four NIR flux peaks and only one X-ray flux peak per day. At high flux values, above 5 mJy, the flux distribution seems to flatten, most likely caused by sporadic flare events superposed onto the quiescent emission.

Sgr A* variability shows more significant activity (larger amplitudes, shorter time scales) at shorter wavelengths. The flares are most likely generated by high energy processes occurring within a few Schwarzschild radii of the event horizon. The flares occur several times a day and typically last for about 60-100 min. During a flare, the luminosity increases by a factor of up to 100 in X-rays (Baganoff et al. 2001; Porquet et al. 2003; Eckart et al. 2004) and rises by factors up to 20 during a single flare infrared event in K-band. The infrared flares occur on average $\sim$ 4 times per day (30-40% of the observing time). The X-ray flares seem short with high amplitude outbursts. A strong X-ray flare followed by three other moderate flares can be observed once a day.

Superimposed on the hour-scale flares, another type of shorter timescale variations were noticed in the NIR regime, quasi-periodic oscillations (QPOs). Sgr A* exhibits flaring in the NIR a few times daily, with 30-40 minute flare durations and peak flux amplitudes starting from 30 mJy (see Genzel et al. 2003; Eckart et al. 2006b; Yusef-Zadeh et al. 2006, 2009; Do et al. 2009). Evidence for a quasi-periodic signal of about 17-22 mins, together with a short variability timescale, down to only a few minutes, suggests that the origin of the variability must be a compact emission region located near the ISCO of the black hole. The cause of these flares is not clear but the general consent is that they might be caused by synchrotron or synchrotron self-Compton emission in the inner 10 Schwarzschild radii (Eckart et al. 2006a; Gillessen et al. 2006). The flares are most likely synchrotron emission from a high energy electron populations, accelerated by magnetic events within the accretion disk, cooling by synchrotron losses. The 30-40 minute flare duration is in agreement with the electron synchrotron cooling timescale. The amplitude of a typical IR flare increases by a factor of about 5 while the X-ray amplitude increases by 1 or 2 orders of magnitude.

The reported variability observed at mm/cm wavelengths(Zhao et al. 2003; Miyazaki et al. 2004) is smaller than at X-ray/IR wavelengths, with a variability timescale between days and weeks.

The NIR/X-ray variability may be associated to the variability at radio through sub-millimeter regime exhibiting variations on time scales from hours to years (e.g. Bower et al. 2002, Herrnstein et al. 2004, Zhao et al. 2003, 2004, Markoff, Bower & Falcke 2007, Markoff, Nowak & Wilms 2005, Mauerhan et al. 2005).

As the NIR emission is highly polarized, it is most likely synchrotron radiation from a NIR transient population of ~GeV accelerated electrons. The particle acceleration mechanism responsible for the NIR flares is not yet understood. The process may be related to acceleration in weak shocks (e.g. Yuan et al. 2003), magnetic reconnection events in a disc corona (e.g. Yuan et al. 2004) or acceleration by a spectrum of plasma waves associated with the dissipation of magnetically-driven turbulence (Liu et al. 2004; 2006a,b). The position of these flares was found to coincide with the dynamical center of some stellar orbits.

Multi-wavelength observations also show evidence of delayed mm and sub-mm emission of about 100 minutes after NIR/X-ray flares (Kunneriath et al., 2010). Subflares within timescales of 15-25 minutes occur in IR regime. In the near-IR (NIR), the flare emission is optically thin synchrotron, whereas at longer wavelengths (submillimeter, millimeter and centimeter), the flaring activity is due to optically thick synchrotron emission. The exact frequency corresponding to the transition from optically thick to thin emission is not yet known. In radio wavelengths, Sgr A* appears to be a permanent and resolved source. Hour-scale variability has been observed at 2 and 3 mm (Miyazaki, Mauerhan). Yusef-Zadeh recorded delayed flares at 7 mm and 13 mm, with time lags of 20–40 min between the flux peaks. At centimeter wavelengths, periods of 57 and 106 days were recorded and claimed as an orbital period by Townes and Zhao (Townes et al. 1999;. Zhao et al. 2001), later disproved by Macquart (Macquart Bower. 2006). The flux variations of Sgr A* could be explained in either a disk or jet model (Eckart et al. 2006ab, 2008a) or as a in relation to an underlying red-noise process (Do et al. 2008, Meyer et al. 2008). Coordinated observations (Eckart et al., 2008, Yusef-Zadeh et al, 2006, Marrone et al. 2007) have shown evidence that the sub-millimeter/mm flares always seem to follow the largest event observed

at NIR/X-ray wavelengths with an approximate delay of ~1.5±0.5 hours. We will adopt as a working hypothesis that the flares at millimeter wavelengths are interconnected to the earlier IR flare event and therefore have the same origin. However, the relationship between the sub-mm/mm and NIR/X-ray emission remains quite unclear due to the very limited simultaneous time coverage between the radio, IR and X-ray telescopes (Yusef-Zadeh et al. 2009).

Figure 5.1 displays the broadband spectral energy distribution of Sgr A*. The peak lies in the sub-millimeter band and it is presumed to be the dividing line between optically thin emission at higher frequencies and the optically thick emission at lower frequencies (Zylka et al. 1995; Falcke et al. 1998). This submillimeter bump could be the signature of a very compact synchrotron emitting region with a size of a few Schwarzschild radii (Falcke 1996; Falcke et al. 1998). The change in spectral index and the association between NIR and X-ray flares could be indications of the different nature of the high flux near-infrared emission from Sgr A*.

In the sub-mm and radio, long term variability (on a 100 days timescale, e.g. Zhao et al., 2001) occurs together with moderate short term variations (on hourly timescales, e.g. Bower et al., 2002) a possible effect of modifications within the accretion flow. The optical depth seems to also be an important factor in softening the observed short term variability (see Goldston et al. 2005). Simultaneous near-IR and sub-mm observations exhibit two near-IR flares of 20–35 min lifetime within a 850 μm flare with a duration of about two hours (Yusef-Zadeh et al. 2006a). The first near-IR flare is simultaneous with the submm flare but the second flare comes delayed by 160 minutes after the submm flare. If we assume that near-IR and submm flares are in some way related to each other, the evident conclusion is that both near-IR and sub-mm flares are generated by the same synchrotron emitting electrons. It is possible that the sub-mm flare could be correlated simultaneously with the second near-IR flare, or it could be caused by the first near-IR flare with the observed 160 minutes time lag. The time delay between the near-IR and sub-mm flares leads us to the possible conclusion that the synchrotron emission in the emission region is initially optically thick in sub-mm bands and it becomes optically thin during the adiabatic expansion of the plasma (van der Laan 1966). This is a common phenomenon observed in micro-quasars (e.g. Ueda et al. 2002).

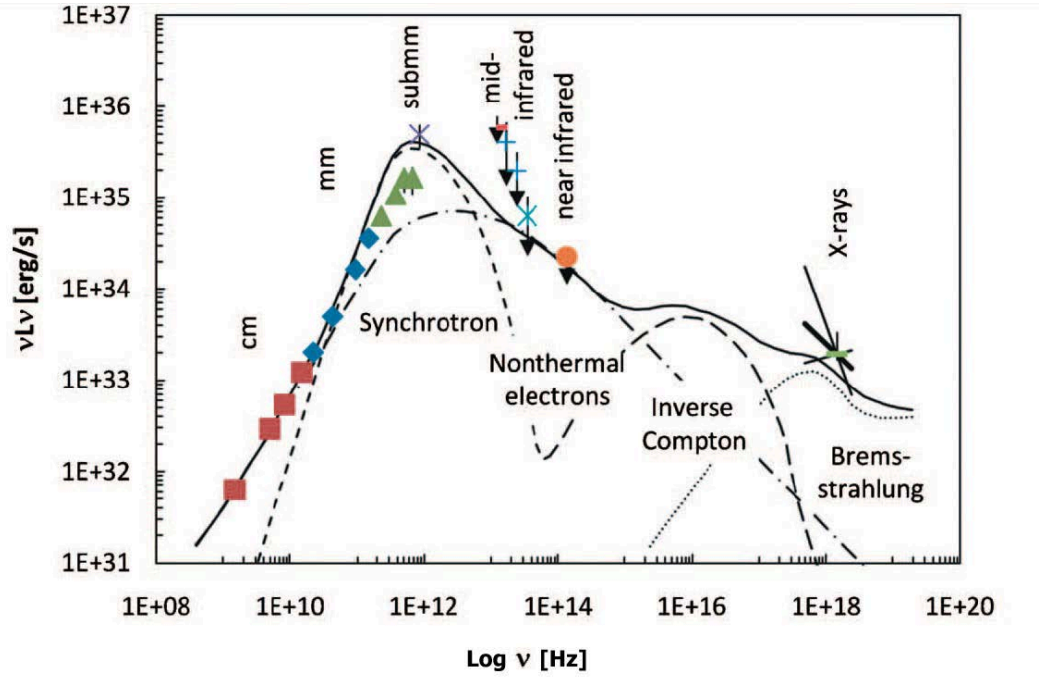

FIGURE 5.1: Spectral energy distribution of the emission from Sgr A* from Genzel et al. (2010). Below 86 GHz, the spectrum follows a power law and above it, the sub-mm bump. The curve peaks then steeply drops towards infrared band. The quiescent X-ray emission is thermal bremsstrahlung. Over-plotted is a quiescent emission model (Yuan et al. 2003): the radio spectrum is produced by synchrotron emission of thermal electrons (short-dashed line). The secondary maximum comes from inverse Compton upscattering of synchrotron thermal electrons.

Most of the previous models that explain the variability of Sgr A* have focussed only on the NIR and X-ray flaring activity (Baganoff et al. 2003, Eckart et al. 2004, 2006; Yusef-Zadeh et al. 2006a; Hornstein et al. 2007) where the the IR flaring is generated through synchrotron emission from a transient electron population of electrons in a magnetic field, while the x-rays are produced by synchrotron from higher energy electrons or inverse Compton scattering of transient electrons (synchrotron-self-Compton) or the sub-mm environment. We could say that the infrared wavelength is a very important component of the spectrum of Sgr A* flare emission. The flare may be firstly produced in infrared band and followed by submm and radio emission with a delayed peak flux with respect to the peak in IR band. In

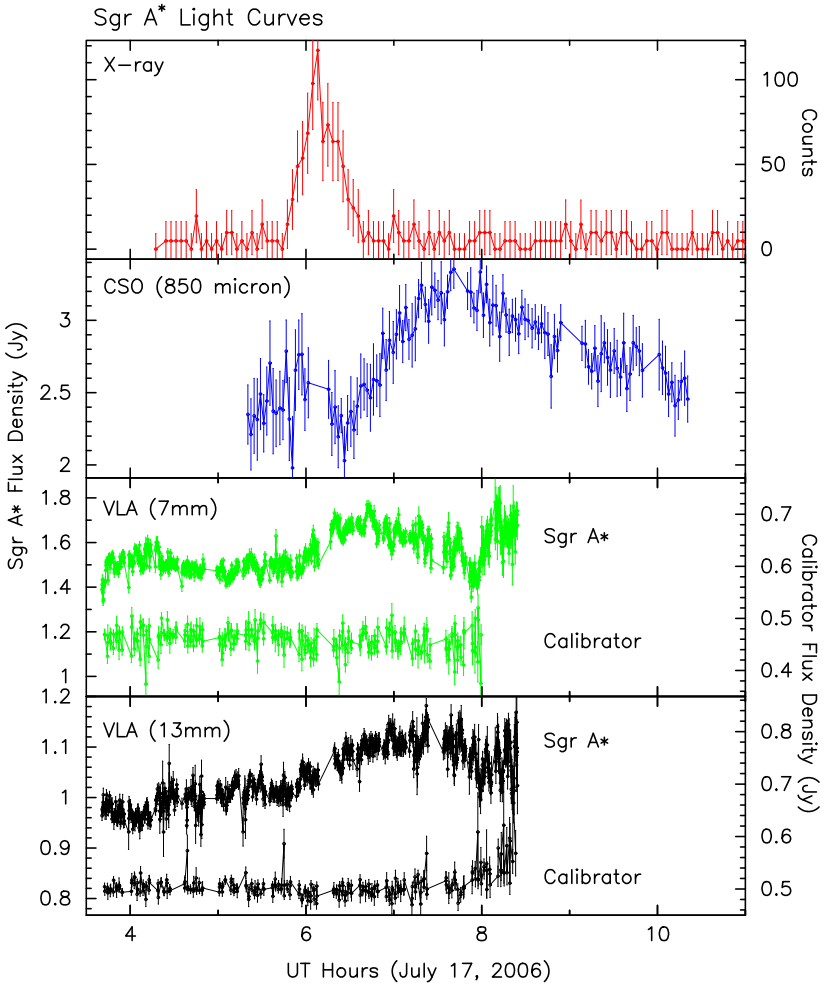

FIGURE 5.2: Sgr A* light curves from 2006 July 17 using , CSO and VLA data. The X-ray (2-8 keV), submm (850 μm) and radio (7 and 13 mm) data are binned every 207 seconds, 20 minutes and 9 seconds (from top to bottom). Credit: Yusef-Zadeh et. al. 2008

this expanding plasmon scenario, the flare at a particular frequency is formed by the adiabatic expansion of an initially optically thick plasma blob of synchrotron emitting relativistic electrons. The model can offer an accurate understanding of the nature of the observed time lags in the Sgr A* flare emission in the optically thick regime. Nonetheless, the relationship between IR and radio/submm flare emission is not yet well understood. Previous studies have been limited in analyzing time dependent constraining parameters of the observed flares due to a considerable lack of complementary observations (Eckart et al. 2004, 2006c; Yusef-Zadeh et al. 2006b). Consequently study is often restricted to information extracted from an

individual flare (Marrone et al. 2008). Although there have been various emission models aiming to explain the nature of flaring activity, only recently time-dependent modelling has been considered (Chan et al. 2009; Dexter, Agol, Fragile 2009; Maitra et al. 2009).

Two possible main scenarios have been so far considered: hot plasma within the disk or expanding plasma ejected near ISCO. Broadband campaigns found evidence that X-ray/NIR flares are actually accompanied by time delayed radio emission (Yusef-Zadeh et al. 2006a; Eckart et al. 2006a). These events were interpreted as originating from an expanding plasmon in orbital motion in the vicinity of the black hole, the source of optically thin and thick synchrotron emission with the flux peak depending on frequency (van der Laan 1966).

Simultaneous observations in multi-wavelength bands have been found very useful in differentiating between different emission models of Sgr A* in its quiescent state and studying the Sgr A* estimated low accretion rate. Existing simultaneous observations studying the correlation of the variability in various wavelength bands is very limited. Several scenarios were proposed for the origin of the Sgr A* flaring:

A Star-disk interactions far away from the black hole, at about 10^2–$10^4 \boldsymbol{R}_s$. This concept can't justify the observed synchrotron emission and the quasi-periodic emission on timescales of a minutes. The observed disk size in radio($r_{\rm disk} \lesssim 1\ AU$) is actually in conflict with the idea of stable stars on inward orbits (Nayakshin et.al., 2003).

B An increase in the accretion rate caused by the infall of clumps of plasma, fast and non-linearly merged onto the disk, developing into strong Rossby vortices, due to Rossby wave instability (Tagger and Melia, 2006; Falanga et al., 2008). The emission originates from material in the inner few Schwarzschild radii. The instability increases rapidly over several orbital periods, causing the clump of material to accrete close to the inner edge of the accretion disk. The material forms a symmetrical spiral structure, caused by a wave-like rotation in the disk. The emitting plasma generates quasi-periodic oscillations, not of a Keplerian origin, with the rate close to the orbital period. Because the orbits are not Keplerian, the black hole spin can't be constrained based on the periodic timescale.

C Sudden heating of electrons by magnetic reconnection in a permanent jet (Falcke and

Markoff, 2000). The short-term variability seen in lightcurves could be caused by very dense blobs ejected at a pseudo-frequency, on dynamical timescale of the disk. If a blob of plasma passes through the reconnection node with velocities of a fraction of c, the blobs could exhibit short-term proper motion within the accretion disk.

D Synchrotron emission from electrons accelerated close to the black hole, by intense shockwaves, turbulent processes, magnetic reconnections and weak shocks in the accretion disk. Observational data seems to agree with this idea. The plasma becomes confined into a small area within the accretion disk (Gillessen et al., 2006) or a plasma blob of highly accelerated electrons in a broken power-law distribution ($n_e \approx 10^5$ cm^{-3} γ^{-3} in the NIR). Even though the plasma moves with high velocities (about half the speed of light), there is no expectation of long-term proper motion, on timescales of more than one orbital period.

The strong variability at shorter wavelengths and the correlation between light curves in submm, NIR and X-ray bands provide evidence that the emission is produced in the close surroundings of the black hole. As a result, properties of the black hole and of the variable emission as well as the accretion mechanisms in the close proximity of the event horizon can be studied at these wavelengths.

5.2 A plasma blob close to the event horizon

Multi-wavelength monitoring of Sgr A* flaring activity confirms the presence of embedded structures within the disk on size scales commensurate with the innermost accretion region, matching size scales that are derived from observed light curves within a broad range of wavelengths.

Motivated by the evidence of quasi-periodic enhanced emission within Sgr A* accretion flow (see Genzel et al. 2003, Eckart et al. 2004, 2006, Meyer et al. 2006), the simplest model for a flare is that of a transient orbiting bright spot that would dominate the entire emission. A confirmed periodic signal from a flare could be very helpful with constraining the flaring nature and serving as evidence for strong general relativistic effects around SgrA*.

We explore here a few of the observational signatures for an orbiting spot within the accretion disk around Sgr A*.

5.2.1 Orbital periodicity in Sgr A* light curves

Sgr A* exhibits strong flares in the NIR and X-ray, implying that the innermost parts of the accreting region is strongly variable. Various observations show a periodic variability varying between around 20 min and around 40 min (Genzel et al. 2003; Dodds-Eden et al. 2010). These pseudo-periodicities are interpreted as the period of an orbiting hot spot.

The measurement of orbital periodicity has the potential to place a lower limit on the black hole spin parameter (see Genzel et al. 2003; Broderick Loeb 2005; Meyer et al. 2006). There is evidence for a 17±3 minute periodic modulation in NIR and X-ray bands (Genzel et al.2003b, Eckart et al. 2006b, Meyer et al. 2006ab, Belanger et al. 2006, Aschenbach et al. 2004ab). The 17-22 mins periodicities were observed clearly only in a few cases, raising doubts about their orbital origin, but Eckart et al. (2006b) found that the QPOs are present in NIR polarized light, while still not visible in the total observed flux. In this way, it is possible that the QPOs, while invisible in the total flux, could indeed be present in all NIR flares. As the orbital period at the last stable orbit of a Schwarzschild black hole is much longer than 20 min, this periodicity is the closest evidence for Kerr metric around Sgr A*.

A fruitful characteristic of the model is a weak dependence on the spin parameter. Most models that aim to produce QPO signals include either Keplerian orbits of hot spots at ISCO (Meyer et al., 2006; Trippe et al., 2007) or models with rotational instabilities in the accretion flow (Falanga et al., 2007). The orbit is stable only for radii larger than the ISCO and consequently it is dependent on the spin parameter. A lower limit of the orbital timescale is here imposed by the spin of the black hole. For example, Sgr A* dynamical timescale lies between 27.3 min for a Schwarzschild black hole with $a = 0$ and 3.7 min for an extreme black hole with $a = 1$, assuming prograde orbits, $a > 0$. However, a flare could actually form at radial locations larger than the ISCO.

Assuming that the detected periodic signal origin is orbital, for the co-rotating ISCO, Genzel (Genzel et.al., 2003) derives a lower limit of the spin parameter of $a = 0.52$, whereas

based on disk oscillation model, Aschenbach (Aschenbach, 2007) found $a = 0.996$ and Kato found $a = 0.4$ (Kato et.al. 2009). Assuming the shortest period claimed to date, 13 ± 2 min, the Sgr A* spin parameter becomes $a > 0.70$.

For the flare from 2002, 3 October, Belanger et al. derived the orbital period of 22.2 min. Belanger also found the presence of a 22.2 min period in the X-ray flaring event from 2004 August 31 using simultaneous XMM-Newton and HST data (see Yusef-Zadeh et al. 2006, Belanger et al. 2005 and Belanger et al. 2006). A bright flare was simultaneously observed in NIR and X-ray on 2007, April 4 (Dodd-Eden et al. 2009, Porquet et al. 2008). The NIR power spectrum shows quasi-periodic variations of about 23 min.

Assuming the orbital period to be close to the NIR observed periodicity, of about 22 minutes, it is possible that only one of the peaks of the light curve to contribute to the orbital period of the flare and the other peak to be caused by the intrinsic variability of the flare. From the observed X-ray flare, assuming that only one of the peaks, in this case, the second peak, is responsible for the orbital periodicity and corresponds to the lensing peak, we notice a number of important features: the presence of another peak that could correspond to the intrinsic flare and a third smaller peak on the right side of the flare, which most likely corresponds to the Doppler blueshift effect on the approaching side of the orbit. We will be discussing this matter in detail a little bit later in the chapter.

5.2.2 Plunging blob model

Both NIR and X-ray observations provide evidence for a blob orbiting very close to the ISCO, on a non-keplerian unstable orbit, falling in towards the ISCO on the last portion of the accretion disk. We use a simple in-falling flare in a plunging orbit within the ISCO. The light curve for a in-falling flare that models the 2005 X-ray light curve, can be seen in Figure 5.3. The quasi-periodicity refers to the average period of a detected signal with periodic features, while there is still a possible evolution from longer to shorter periods, leading to successively broader peaks.

We model the time evolution of such an emitting compact source in plunging orbit around the black hole, with successive smaller orbital periods while the flux distribution decreases,

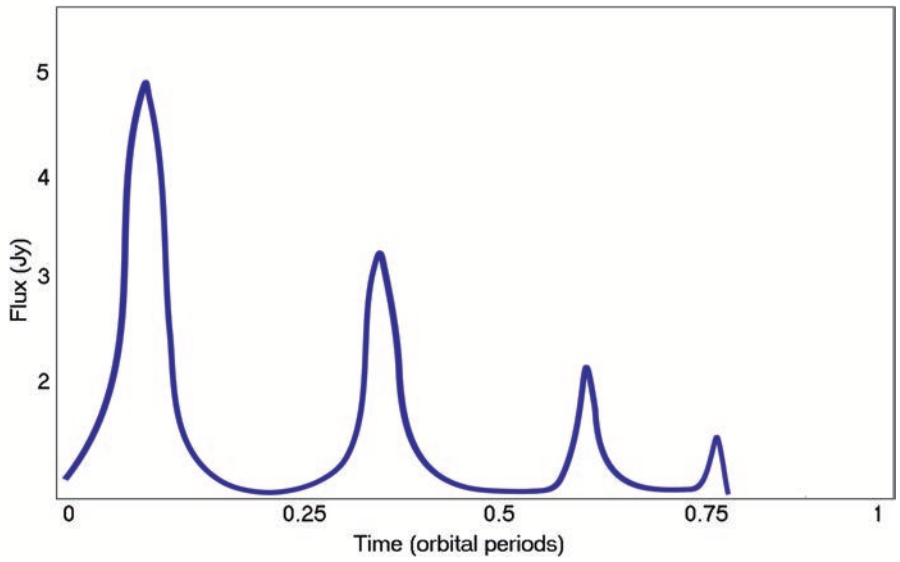

FIGURE 5.3: Relativistic light curve from a initially located at $r_{\rm sp} = 0.93GM/c^2$ falling into the event horizon of an extremely rotating black hole, at a viewing angle $\theta_{\rm o} = 75°$. The radius of the spot is $R_{\rm spot} = 0.5GM/c^2$. The orbital period decreases monotonically with time.

as the blob approaches the event horizon.

However, we don't eliminate the possibility to have plunging orbits for orbital radii larger than ISCO, due to a possible evolution detected by Belanger in X-ray from longer to shorter orbital periods. The evolution of the orbital period as a function of time was considered, as it is expected from the in-spiraling motion on a plunging orbit close to the ISCO, as seen in Figure 5.4.

The period of $\sim$ 17–23 minutes corresponds to orbital radii of 0.73–0.94 $r_{\rm ISCO}$ below the ISCO ($r_{\rm ISCO} = 3R_s = 6GM/c^2$) for a Schwarzschild black hole. The X-ray flare is modelled using a continuously decreasing orbital period of the orbiting material. The magnetic reconnection event could be interpreted as a sudden drop in magnetic field in an inner region of the disk, occurring every 20 min, on the natural dynamical timescale. Magnetic reconnection events are expected to occur near the ISCO, accompanied by sudden heating of the inner regions of the accretion flow due to magnetic dissipation.

The flare emission may be produced by a hot, magnetized Keplerian flow of clumping matter (Yuan et al. 2004; Kato et al. 2009), in in-spiralling orbital motion very close to the

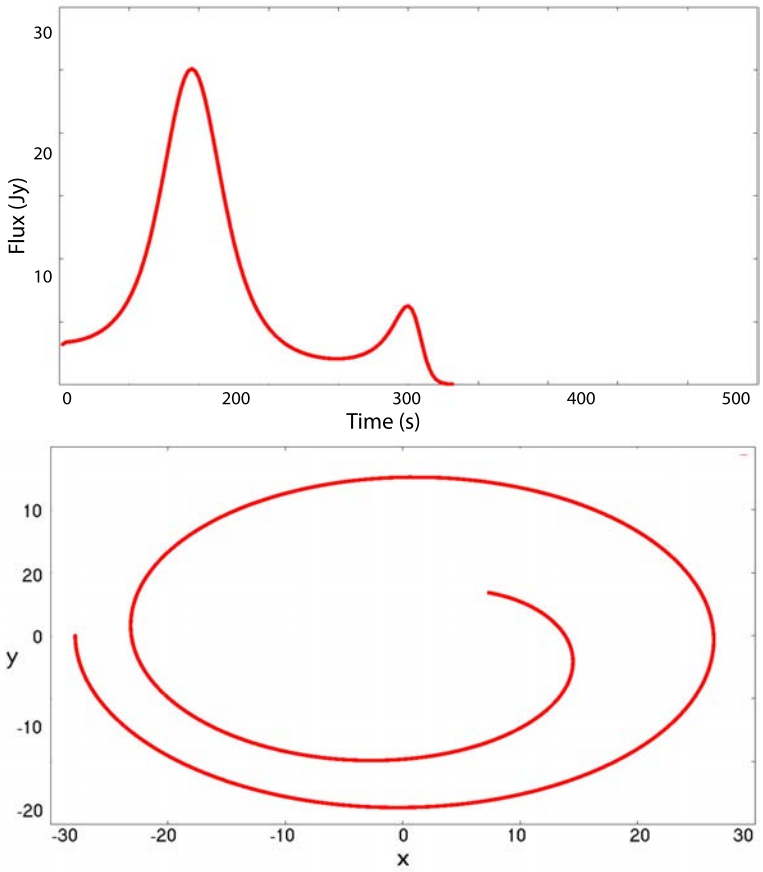

FIGURE 5.4: Relativistic light curve from a blob initially located at $r_{sp} = 0.85GM/c^2$ falling into the event horizon an extremely rotating black hole, at $\theta_o = 60°$. The radius of the spot is $R_{spot} = 0.2GM/c^2$. (Top) Trajectory in the equatorial plane of the same flare. (Bottom)

ISCO and the stress edge of the accretion disk (Krolik and Hawley, 2002). The flare observed emission may be directly associated here with a monotonically decreasing orbital period. The decrease of the period would suggest the temporal evolution of an compact source that moves inwards across the ISCO of the black hole. The orbit is no longer Keplerian due to the presence of a radial velocity component. The X-ray flare lifetime is shorter than the NIR flare counterpart. When simultaneously detected, the X-ray flare could be most likely related to the flare infrared counterpart. The similar morphology of the sub-structure in the light curves suggests the same population of highly energetic electrons that trigger the flare emission. As the X-ray and near-IR emission could be coupled, we may expect very strong similarities in the lightcurves.

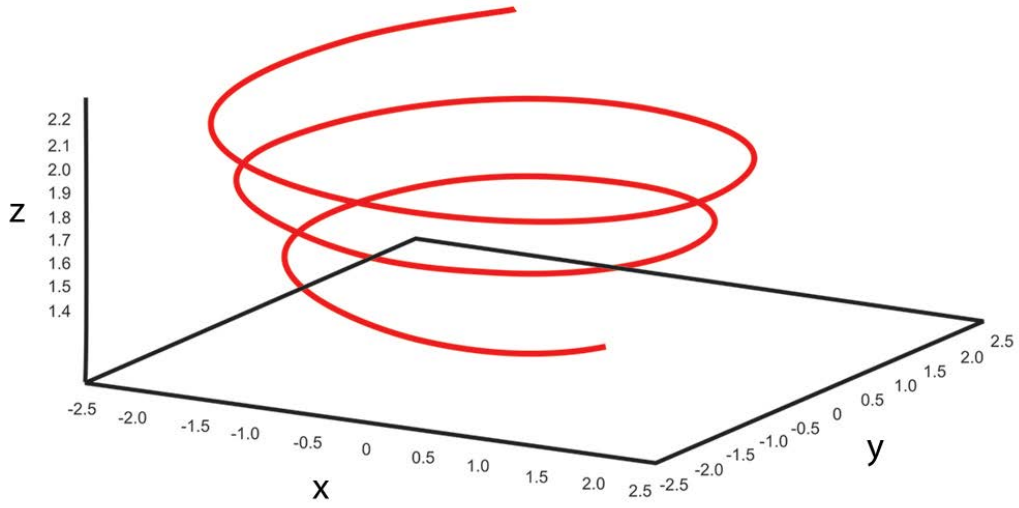

FIGURE 5.5: Plunging trajectory blob initially located at $r_{sp} = 0.93GM/c^2$ on an unstable non-keplerian orbit, falling into the event horizon of Kerr black hole with $a/M = 0.9987$, at a viewing angle $\theta_o = 75°$. The radius of the spot is $R_{spot} = 0.5GM/c^2$.

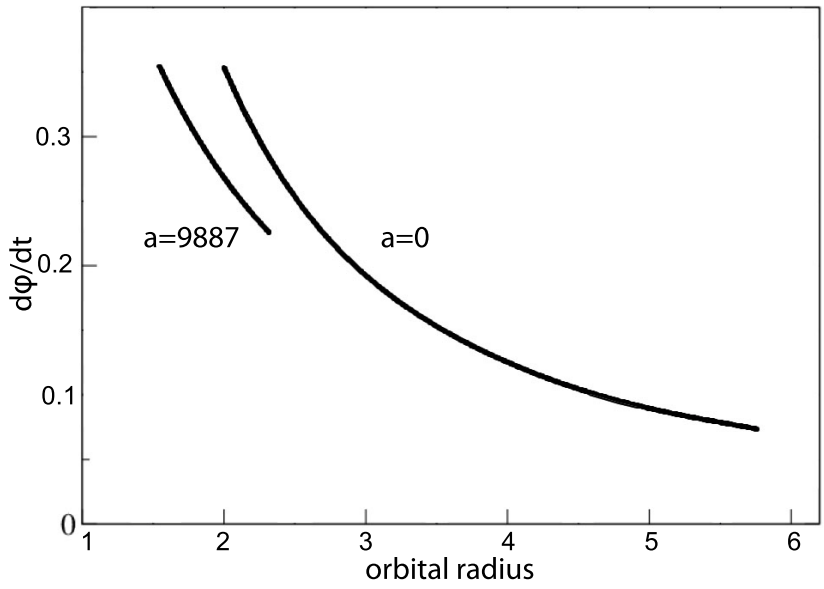

FIGURE 5.6: The angular velocity evolution during the plunge of the blob from ISCO towards the event horizon, for an extremely rotating black hole and for a Schwarzschild black hole.

The trajectory of a particle in Kerr metric in Boyer-Lindquist coordinates approaching the event horizon at $x = x_{\rm h}$ follows a plunging trajectory, quasi-periodically "winding up" with the angular velocity $\Omega_\varphi \rightarrow \Omega_{\rm h}$. coming close to the angular velocity of the black hole horizon $\Omega_{\rm h}$, where

$$\Omega_{\rm h} = \frac{d\varphi}{dt}\Big|_{x\rightarrow x_{\rm h}} = \frac{a}{2(1+\sqrt{1-a^2})}. \tag{5.1}$$

Figure 5.5 shows the plunging trajectory of a flare with the angular velocity $\Omega_\varphi \rightarrow \Omega_{\rm h}$, located between the event horizon and the ISCO, quasi-periodically infalling into the black hole and approaching the event horizon at the southern hemisphere. The dependence of the angular velocity on the orbital radius, for a plunging particle or photon from the ISCO into the event horizon is shown in Figure 5.6. We show both Schwarzschild and Kerr black hole cases. The angular velocity of black hole event horizon Ω_φ may be imprinted to the QPO variable signal from the black hole. However the NIR and X-ray Sgr A observations are limited to 1-2 hours flare event durations. Due to this short duration, the QPO periodicity is still open to argument. However, the QPOs are only seen at the flaring time and most likely occur near the ISCO (Genzel et al. (2003); Aschenbach et al. (2004); Eckart et al. (2006); Belanger et al. (2006)). The blob approaches the event horizon and it is viewed by the observer as a relativistically beamed and boosted forward emission that is repeated quasi-periodically with a frequency very close to $\nu_{\rm h} = \Omega_{\rm h}/2\pi$. An oscillation with the angular frequency $\Omega_{\rm h}$ from (5.1) could be a proper observational signature for the spin of the black hole and may be related to the QPOs of non-equatorial bound orbits in the accretion flow.

5.3 Relativistic modelling of Sgr A* NIR variability

Typically, a NIR flare lasts for 100-140 min, which is much longer than the synchrotron cooling time for a plausible magnetic field strength in the inner regions of the accretion disk, close to the ISCO (Dodds-Eden et al, 2010). Therefore the production of the synchrotron emission should require sustained injection of highly energetic electrons throughout the life-time of the flare.

In order to understand the time dependent NIR emission we use a simple non-thermal

electron acceleration picture to explain the broad NIR flare. Possible processes responsible for the non-thermal component (turbulent acceleration, reconnection, weak shocks) can accelerate electrons to very high energies.

Most NIR flares show obvious sub-structural characteristics in the light curves (Genzel et al., 2003b). Using relativistic modelling of an orbiting hot region around a Kerr black hole, close to the ISCO, we are able to fit typical NIR flares at several timescales in the light curve. We have previously discussed a particular periodic substructure of the order of 15-20 minutes which we associate with the orbital timescale of matter at the ISCO. A detailed analysis of this flaring substructure, based on relativistic suborbital assumptions, will lead us to confirm the orbital origin of the signal and therefore calculate the black hole spin. A very similar sub-structural periodic modulation on the same characteristic timescale between 15-25 minutes has been recorded in several NIR flares (Genzel et al., 2003b; Meyer et al., 2006; Eckart et al., 2006c; Trippe et al., 2007; Do et al., 2009a).

We propose a simple time-dependent model of the NIR flares, using the hot spot picture. We consider light curves in continuum emission as a function of time for a prograde hot spot in Kerr and Schwarzschild geometries. We neglect all structure of the accretion disk and the dynamics of the outflow and focus only on the information that can be extracted from continuum profiles and time-varying signals from a flare within the accretion disk.

We assume the emitter to be an isotropic source (extended segment in the disk but point-like source as seen from the observer's location) of stationary emission within the disc plane. Here, the hot spot emission, while only stationary, is still computed in proper time, allowing direct comparison with existing data. The source is located in the equatorial plane, following a circular orbit close to the ISCO. The trajectories of emitted photons are integrated through the Kerr metric to a infinitely distant observer to construct time dependent light curves of the emission region.

Our model for Sgr A* is an optically thin, geometrically thick accretion flow around a rotating black hole with the orientation of the black hole spin and the accretion disk rotational axis aligned. In our modelling we assume that the flares from Sgr A* are caused only by plasma on Keplerian orbits around the black hole and that the period recorded in the light curves represents a signature of the orbit itself. The flare is caused by a temporary local event

close to the ISCO. The cause of the flare event could be magnetic reconnection processes in the disk, stochastic acceleration of electrons or Magneto Rotational Instabilities (MRI) inside the plasma.

We propose that the emission comes from a blob formed within the disk, gets injected for a limited time with high energy electrons from the disk. If the electron distribution is high enough, a slow expansion process may be triggered. The dominant energy loss mechanism is synchrotron cooling. The electrons obey a simple power law with the exponential cut-off are injected into the synchrotron blob for a limited time interval.

We apply a simple injection model to the observed light curves for the simultaneous NIR/X-ray Sgr A* flare from 2007, April 4, (Dodds-Eden et al. 2009; Porquet et al. 2008; Trap et al. 2009; Yusef-Zadeh et al. 2009). The April 4, 2007 flare, observed with NACO (VLT) and XMM-Newton shows light curves obtained simultaneously at NIR and X-ray wavelengths, providing the opportunity to study the particle acceleration and cooling processes in the disk.

The 2007 April 4 L-band light curve shows significant sub-structure on a timescales of 20 minutes, previously found in Ks-band flares (see Figure 5.7). (Genzel et al., 2003b; Eckart et al., 2006b; Trippe et al., 2007). The presence of this type of sub-structure is a common feature of IR flares. Our model explains two outstanding features in the NIR flaring: the broadness of the NIR light curve and the sub-structure in the NIR lightcurve.

The near-IR flaring of Sgr A* is due to optically thin synchrotron emission from a transient population of particles from within $\sim$ 10 Schwarzschild radii of the center (e.g., Genzel et al. 2003; Eckart et al. 2006; Gillessen et al. 2006; Yusef-Zadeh et al. 2006).

The single component synchrotron models, with the standard particle distribution $dN(\gamma) \propto \gamma^{-p}\, d\gamma$) seem to be problematic (see discussion in Dodds-Eden et al. 2009, Trap et al. 2011) as the particles that are required to produce the X-ray flare have shorter cooling times than a typical X-ray flare duration. A continuous injection process seems to not be able to sustain the same power-law index p at both all energies, in order to replenish the population of the flare. Such a simple power-law particle distribution can't maintain the same power-law index p at all energies.

If the emission originates near the ISCO, the escape time calculated for a black hole mass

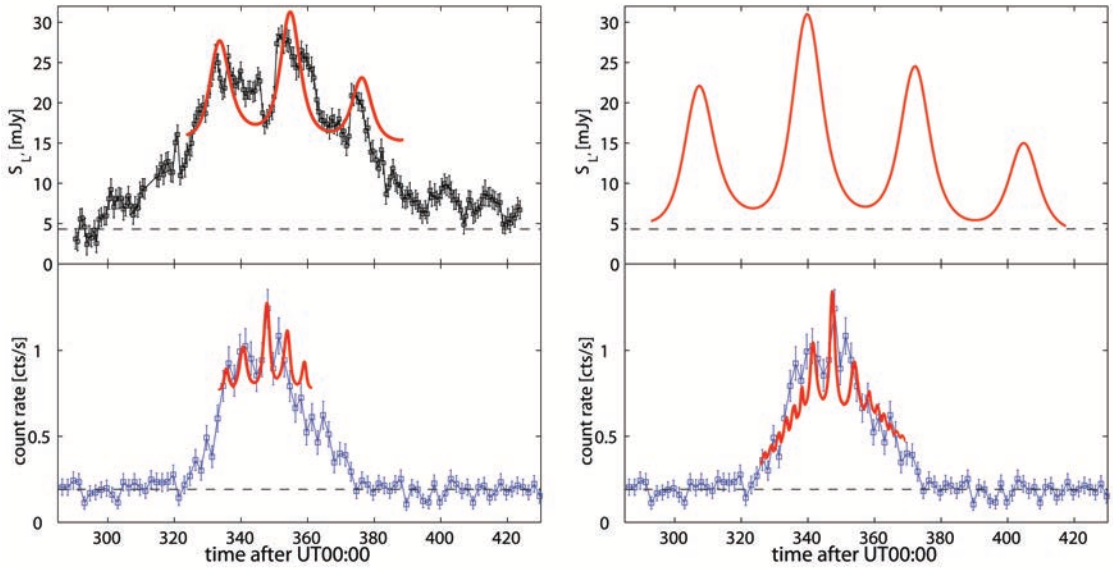

Figure 5.7: (Left) IR (L'-band) and X-ray lightcurves from the April 4, 2007 and (right) the theoretical modelling results of the IR flare

$4 \times 10^6\ M_\odot$ is:

$$\tau_{esc} \sim 3\frac{6GM}{c^3} \approx 6 \text{ min} , \tag{5.2}$$

The cooling break occurs at the frequency above the NIR and below the X-ray, for a magnetic field of the order 20-30 G that is required to produce the quiescent emission.

$$\nu_b \approx \left(2 \times 10^{14} \text{ Hz}\right)\left(\frac{B}{30 \text{ G}}\right)^{-3} , \tag{5.3}$$

To model a non-thermal process we assume a constant injection of particles following a power-law distribution. In this model the injection duration is connected to the broad flare timescale. We use the data of the 2007, April 4 IR/X-ray flare given in Porquet et al. (2008) and Dodds-Eden et al. (2009). The values of the chosen parameters are determined from the SED of IR and X-ray light curves, at the same time endorsing the picture of an initially synchrotron blob that starts to expand at a later time. The model and parameters used are detailed below. The flare timescale is fixed by the injection time of non-thermal electrons, directly connected to the electron acceleration process. The magnetic field is assumed to be constant. The injection duration is directly connected to the flare timescale. In a purely

phenomenological way, we assume that the relativistic particle distribution that generates the NIR/X-ray flare has the form:

$$dN(\gamma) = N_0 \begin{cases} 0, & \text{if} \gamma < \gamma_{\min} , \\ K\gamma^{-p} \exp(-\gamma/\gamma_{\max}), & \text{if} \gamma \geq \gamma_{\min} , \end{cases} \quad (5.4)$$

where K, p, $\gamma_{\min}$, and $\gamma_{\max}$ are parameters. The parameter γ is the electron Lorentz factor. We define $q(\gamma)$ as the injection rate per unit volume and unit interval of γ. The parameter $\gamma_{\max}$ is assumed time dependent. The duration of the injection process is $t_{\rm inj}$. The normalization factor, K, can be defined by assuming the value of the injection rate per unit volume:

$$q_{\rm inj} = \int_{\gamma_{\min}}^{\infty} q(\gamma) d\gamma. \quad (5.5)$$

The model parameters involved are R, $q_{\rm inj}$, p, $\gamma_{\min}$, $\gamma_{\max}$ and $t_{\rm inj}$. The blob gets injected with $q_{\rm inj}$ constant for $t < t_{\rm inj}$, decreasing as $q_{\rm inj} \propto \exp[-(t - t_{\rm inj})/(0.25 t_{\rm inj})]$ for $t > t_{\rm inj}$. The initial parameters are $\gamma_{\min} = 2$, $p = 1.3$ and $t_{\rm inj} = 8R/c$. The parameter $\gamma_{\max}$ is linearly increasing. The theoretical light curves superimposed over the IR and X-Ray observations (Figure 5.7) include full relativistic modelling, including gravitational lensing and Doppler beaming effects. The synchrotron cooling time would be on the timescale of hours for a typical magnetic field strength in the accretion flow.

The parameter $\gamma_{\max}$ increases linearly with time. For $t < t_{\rm inj}$, the number density of electrons will increase due to the injection process. For $t > t_{\rm inj}$, the injection rate will decrease exponentially in time. The synchrotron cooling will cause the decrease in number of higher energetic electrons. Both NIR and X-ray emissions are produced by synchrotron radiation. The maximum value of the synchrotron energy flux per unit frequency, νF_ν should appear between the IR and X-rays bands.

The initial blob is a very small hot spot of insignificant small number of particles and can be considered empty at $t = 0$.

A large number of non-thermal electrons start to be injected for $t > 0$. If $\gamma_{\max}$ would have a fixed value, the particles should be injected almost instantly at $t = 0$ and the light curve should rise very steeply, which is not the case in NIR. This is the reason we assume that $\gamma_{\max}$ increases linearly with time, in order to obtain a slow rise of the light curve. The injection

rate decreases linearly after $t = t_{\rm inj}$. The parameter $\gamma_{\rm max}$ increases from $q_{\rm inj} = 500$ to 5×10^4 between $t = 0$ and $t_{\rm inj}$.

We assume $q(\gamma) \propto \exp[-(t - t_{\rm inj})/(\xi t_{\rm inj})]$ for $t > t_{\rm inj}$. The parameter $\gamma_{\rm max}$ is constant for $t > t_{\rm inj}$.

During the steady phase of the blob, of a constant size, the duration of the flare is independently chosen, as strictly dependent on magnetic field, injection timescale of non-thermal electrons or other factors strictly dependent on how the blob was formed within the disk (through magnetic reconnection, shock acceleration or ejected from the inner edge or near the inner edge of the accretion flow). These parameters will be included in further modelling of the light curves and they are not part of the current work. Shock acceleration in the disk or magnetic reconnection processes could generate non-thermal electrons.

The NIR broad flare rising is produced by a combination between the heating of the electrons and the injection of new accelerated particles in the blob, whereas the decay is produced by the radiative cooling through synchrotron emission. Once heated, the particles start cooling producing an exponential cutoff in the infrared light curve with a cutoff frequency decreasing in time.

The emission at a given frequency ν is dominated by electrons with Lorentz factor $\gamma_e = \sqrt{\nu/\nu_B}$, where ν_B is the electron cyclotron frequency and the cooling time of the flare observed at ν is

$$\tau_{\rm c} \simeq 10^2 \left(\frac{\nu}{10^3 GHz}\right)^{-1/2} \left(\frac{B}{30G}\right)^{-3/2} \; min. \tag{5.6}$$

The synchrotron cooling process may also account here for the observed variable spectral index, requiring magnetic fields of about $20 - 30$ G. We find that for a magnetic field $B = 20$ G, the synchrotron cooling time is $\tau_{\rm c}$=16 min (for $B = 5$ G, $\tau_{\rm c}$=128 min, for $B = 8$ G, $\tau_{\rm c}$=63 min, for $B = 10$ G, $\tau_{\rm c}$=45 min, for $B = 15$ G, $\tau_{\rm c}$=25 min).

For accretion disk models with $\dot{M} \approx 10^{-8}\, M_\odot$/yr (see Agol, 2000) a magnetic field of $B \approx 30$ G is required at a orbital radius of $3.5\, R_{\rm S}$. The synchrotron cooling time of electrons that emit radiation of $\lambda = 2\, \lambda_2\, \mu$m for $B = 30\, B_{30}$ G is

$$t_{\rm cool} \approx 8\, B_{30}^{-3/2}\, \lambda_2^{1/2} \,{\rm min}\ . \tag{5.7}$$

we notice that the cooling time is very similar to the orbital timescale.

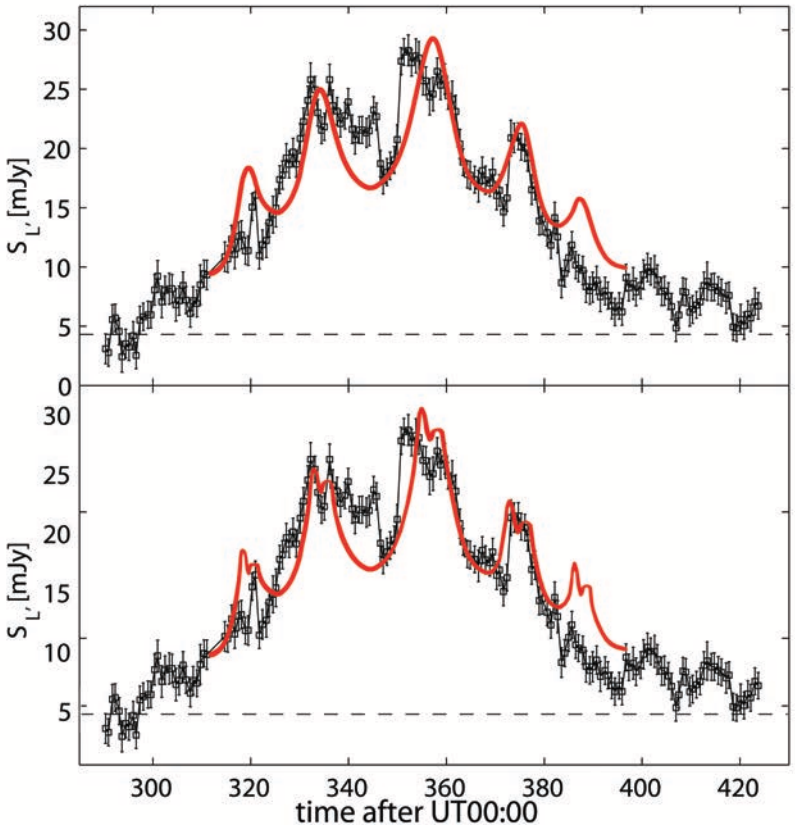

FIGURE 5.8: (Top) Light curve of a blob orbiting an extremely spinning black hole. The blob of radius $R_{\rm spot} = 0.5GM/c^2$ is located at $r_{\rm sp} = 6GM/c^2$ The initial parameters are $B = 20$ G, $\gamma_{\rm min} = 2$, $p = 1.3$ and $t_{\rm inj} = 8R/c$. The model fits the IR (L'-band) April 4, 2007 data. (Bottom) Light curves fitting the 2007 flare with suborbital relativistic effects.

The NIR flare observed in L' band (3.80 μm) (2007, April 4) that lasted for about 100 minutes exhibits sub-structural variations on the known timescale of $\sim$ 20 minutes. In Figure 5.8 we model light curves of a blob with radius $R_{\rm spot} = 0.5GM/c^2$ that is located at $r_{\rm sp} = 6GM/c^2$ from the black hole. The black hole has the spin parameter $a/M = 0.998$.

Most NIR flare characteristics, employing various timescales, are shown in Figure 5.8. Both light curves are modelled as a steady (constant size) synchrotron blob with $p = 1.3$, placed in a magnetic field $B = 20$ G, and injected with new electrons with $\gamma_{\rm min} = 2$ that increases from $q_{\rm inj} = 500$ to 5×10^4 between $t = 0$ and $t_{\rm inj}$. The difference between the top and bottom pictures is that the first figure considers only the lensing effect, whereas the second

picture assumes both Doppler beaming and gravitational lensing effects, producing a clear sub-peak structure within the orbital timescale. The X-ray flare brightness is directly dependent on $\gamma_{\max}$ and $t_{\rm inj}$ because the X-ray electrons are highly energetic and their cooling time is very short. When the injection rate of the electrons begins to decrease, the X-ray flux will start to decline rapidly. The NIR electrons have a longer cooling time than the X-ray emitting electrons. In order to understand the NIR broad flare, there must be continuous injection of relativistic electrons considering the 100-150 minutes cooling lifetime electrons emitting synchrotron radiation. We expect that the accretion flow is injecting electrons into the low magnetized inner plasma. We make assumptions about variability at various timescale levels and build up the final picture for both NIR and radio wavelength regimes employing all three steps: sub-orbital, orbital and super-orbital. We find sub-structural variations with characteristic timescales of 17-25 minutes that conform the observed quasi-periodicity found in both NIR and X-Ray on a regular basis. If we assume multiple orbits of the same synchrotron emitting blob, we obtain theoretical light curves that closely simulate the broad NIR flares of Sgr A*, as we can see in Figure 5.9.

We describe the 2007, April 4 light curve using three superimposed components:

(1) an overall modulation with a total span of 100 min, i.e. around five ISCO orbital periods of a Kerr black hole, that models the broad NIR flare using an injection model. The flare duration is partially determined by the injection timescale of the non-thermal electrons. The flare decay is caused by the radiative cooling process after the initial injection of the non-thermal electrons has finished.

(2) the broad modulation could trigger the formation of an expanding plasmon at the same timescale, visible at optically thick wavelengths through the presence of 2-2.5 hours flares with optical depth effects and time lags between peaks at different frequencies.

(3) a smaller periodic modulation, of orbital origin, varying over about one orbital period. We find that the periodic sub-structure observed in the NIR light curves being caused by a combination between gravitational lensing and relativistic beaming on the approaching side of the orbit.

The NIR and the X-ray lightcurves are relatively symmetric and peak simultaneously, (up to five minutes lags), with NIR rise and decay times slower than the X-ray flares.

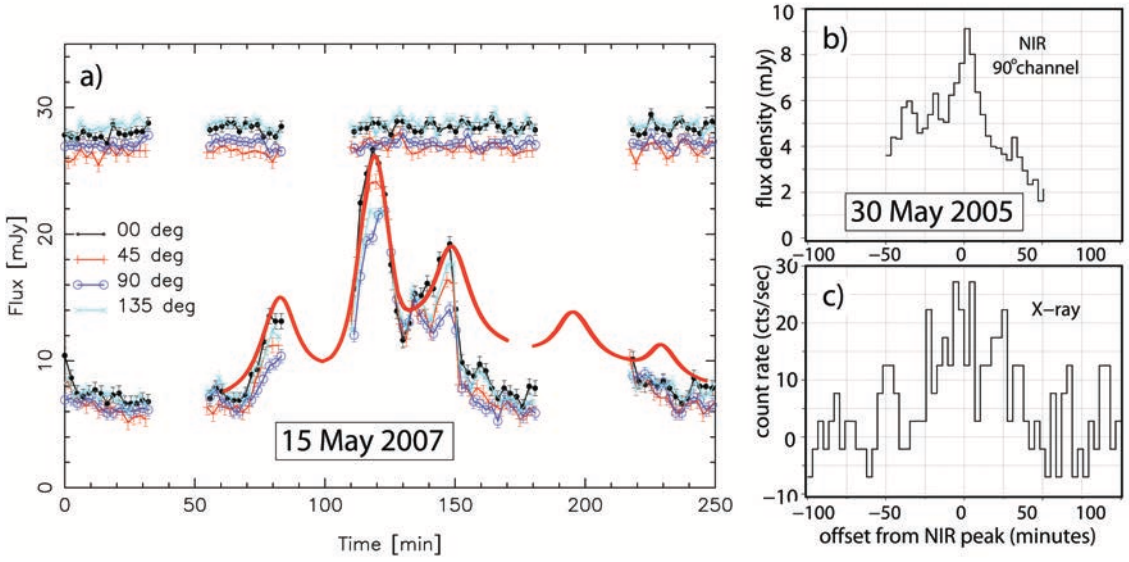

FIGURE 5.9: **a):** A bright infrared flare of Sgr A* observed with NACO/VLT on 2007, 15 May and the model light curve (red) of the IR flare. The polarimetric channels have different colors. The light curve of a constant star, S2, is also shown. **b) and c):**The NIR (top) and X-ray (bottom) data for the Sgr A* flare observed on 2005, 30 May. The X-ray data are corrected for quiescent emission. The NIR peak occurred at 02:56:00 UT ±3 minutes, within about 7 minutes of the X-ray peak.

Our simulations suggest, independent of the emission mechanism, that the observed X-ray/NIR flare involve the same population of electrons, responsible for both NIR and X-ray flare emission. However, in all detected NIR flares with X-ray counterparts, there is no evidence for time lag between the flare peaks, confirming the hypothesis that both NIR and X-ray emission are optically thin.

The model predicts that X-ray and NIR flux peaks will occur simultaneously, as they are both optically thin during the expansion, fact consistent with most simultaneous X-ray and NIR campaigns. However, in 2012, Yusef-Zadeh et al. (2012) found evidence that the X-ray emission actually lags the NIR peak by a few to tens of minutes.

In this case, while a NIR event would occur within the inner regions of the accretion flow, the X-ray flares would be caused by inverse Compton scattering of infrared photons by the thermal electrons from the accretion flow, at a greater radius, producing time delays in the

light curves (Yusef-Zadeh et al. 2009; Wardle 2011).

The inverse Compton scenario or the upscattering of NIR photons by 10 MeV electrons in the accretion disk (Yusef-Zadeh et al. 2006, 2009) is not ruled out either.

The X-ray emission mechanism was associated with transient accelerated electron populations arising through self-synchrotron-Compton (SSC), inverse Compton (ICS) and synchrotron emission (Markoff et al. 2001; Liu Melia 2002; Yuan et al. 2004; Yusef-Zadeh et al. 2006a; Eckart et al. 2009; Marrone et al. 2008; Dodds-Eden et al. 2009).

In the inverse Compton scenario, sub-mm photons arising from the quiescent flux are upscattered by transient electron populations that produce the IR flares (Yusef-Zadeh et al. 2006a). In a second scenario, NIR photons that are emitted during the flare event are upscattered by the mildly relativistic electrons which are also responsible for the quiescent radio/sub-mm emission (Yusef-Zadeh at al. 2006a, 2008, 2009).

While it is settled that the NIR flares are due to synchrotron emission of transiently heated electrons, we have to take into account the fact that the emission should be definitely affected by the orbital dynamics, injection and synchrotron cooling process at the same time.

We suggest that the NIR variability is caused by a combination between transient heating processes with subsequent synchrotron cooling, injection of new electrons and orbital dynamics providing relativistic signatures in the light curve.

The main broad flare is based on an initial population of heated electrons. The broad NIR flare of 100 minutes duration is most likely due to synchrotron cooling while new accelerated electrons are injected into the blob. Relativistic beaming together with gravitational lensing effect near the event horizon are the most likely source of substructural flux modulation in the NIR emission.

In the last section of this chapter, we propose a connection between the NIR activity and the flaring at higher frequencies

5.4 Modelling of Sgr A* radio flaring

5.4.1 The adiabatic expanding plasmon model

The hot spot scenario analysed in the previous section expects that the flares are hot spots orbiting within few Schwarzschild radii of the black hole (Broderick Loeb 2006) where Doppler boosting, redshift and other relativistic effects become significant. The model doesn't predict any time delay between the peaks of flare emissions at different wavelengths. However, existent observations show time delay between the peaks of NIR/X-ray and sub-millimeter flares (Yusef-Zadeh et al. 2008; Marrone et al. 2008; Eckart et al. 2009). The observed variability could actually be linked to relativistic emission originating from a single or even multiple spots at different orbital radii within the accretion disk close to the last stable orbit. We analyse light curves from an expanding plasmon in orbit around a Kerr black hole, taking into account all special and general relativistic effects. The combination between our theoretical relativistic amplification light curves and a simple plasmon mechanism provide a good time dependent flare emission model.

Yusef-Zadeh et al. (2006a) proposed that the evolution of radio wavelength flares could be explained in an expanding synchrotron plasmon model (Shklovskii 1960; Pauliny-Toth Kellermann 1966), following the original formulation of van der Laan (1966). A schematic picture of the expanding blob is shown in Figure 5.10. The adiabatic cooling of electrons in the plasmon and the flux-conserving diminution of the magnetic field are the main characteristics of the model, causing a non-radiative decrease in the synchrotron observed flux. The plasmon model predicts lower amplitude and time delayed flare peaks at successively longer wavelengths, with a change in the spectral index from optically thick to thin before and after the flare peak at any wavelength.

One of the motivations of this Thesis is the relativistic analysis and application of the plasmon model to Sgr A* based on the recent observing campaigns in multiple bands. To understand the nature of the Sgr A*s flaring activity, we use the plasmon model of van der Laan (1966) and analyze the light curves of the flare emission at various wavelengths. In this model, the flaring at a particular frequency is caused by the adiabatic expansion of an initially optically thick bubble of synchrotron emitting relativistic electrons. The Sgr A*

flare emissions in radio, sub-millimeter and millimeter regimes vary on hourly time scales (Marrone et al. 2007; Miyazaki et al. 2006; Maurehan et al. 2005; Yusef-Zadeh et al. 2006). The model of a synchrotron emitting blob of electrons that cool down via adiabatic expansion processes could explain the time lag between various flux peaks at several wavelengths as well as the asymmetric shape of the light curves. We use Yusef-Zadeh et al. (2006) model to analyse Sgr A* light curves that exhibit time lags in radio, sub-millimeter and millimeter. The derived lifetime of the radio flares show evidence that the cooling process could be due to adiabatic expansion, suggesting that the flare activity is caused by an expanding plasma blob (Yusef-Zadeh et al. 2006) rather than a hot spot. Light curve analysis of radio data at 7mm show a lifetime of a radio flare of about two hours, similar to the lifetime of flares in sub-mm regime (Yusef-Zadeh et al. 2006; Marrone et al. 2006). The peak frequency of emission (the initial optically thin near-IR flare) shifts towards lower frequencies (sub-millimeter, millimeter and then radio) as a self-absorbed synchrotron source that expands adiabatically. Rather than synchrotron cooling, the adiabatic cooling is associated with the expansion process of a relativistic emitting plasma source and is the likely cause for the decline of the flare.

The rise of the observed flux is caused by the increase of the blob's surface area in the optically thick regime. The turn over happens when the magnetic field decreases enough to cause the switch to the optically thin regime. While the magnetic field drops, the blob will expand because of the adiabatic cooling. The emission in mm and sub-mm is dominated by synchrotron emission from a compact expanding blob of relativistic electrons with the energy spectrum $n(E) \propto E^{-p}$. The model assumes a plasmon is surrounded by a magnetic field, B. The particle density and spectrum and magnetic field strength are assumed to be uniform. Following van der Laan (1966), we assume a uniformly expanding blob of relativistic electrons with a power-law energy spectrum, $n(E) \propto E^{-p}$, threaded by a magnetic field that declines as R^{-2}, and of energy and density that decline as R^{-1} and R^{-3}, respectively, as a result of expansion of the blob. If R_0, S_0 and τ_0 are the size, flux density, and optical depth of the source at the peak frequency (ν_0) of the synchrotron spectrum, the optical depth and flux density at a given frequency ν scale can be calculated as follows. The original van der Laan model assumed a different coefficient of τ_0 as the expression refers to the optical depth

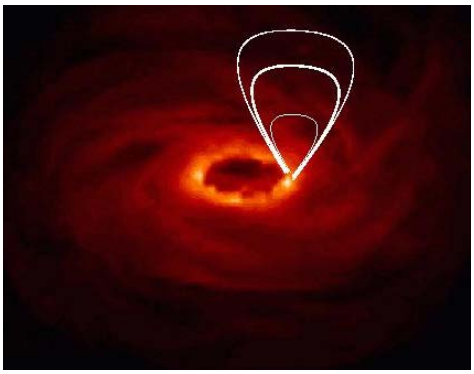

FIGURE 5.10: Diagram of a blob expanding away from the accretion disk, superimposed on an MHD simulation of the synchrotron emission from the central 16R$_s$ (from Goldston, Quataert Igumenshchev, 2006). The bright area is located near the ISCO. Credit: Yusef-Zadeh et al., 2006

corresponding to the maximum in the spectrum at some instant ($\partial_\nu S(\nu, t) = 0$) rather than the maximum in the light curve at a particular frequency ($\partial_t S(\nu, t) = 0$). The blob emits an initial synchrotron spectrum depicted by two connected power-laws. The initial synchrotron self-absorption frequency ν_0 is dependent on the magnetic field B $\nu_0[\propto \{R_0\, k_\mathrm{e}\}^{2/(p+4)} B^{(p+2)/(p+4)},]$. The flux reaches its maximal value, F_0, at the ν_0 frequency. Below this value, for $\nu < \nu_0$, the spectrum is optically thick ($F_\nu \propto \nu^{5/2}$).

For larger frequency values $\nu > \nu_0$, the spectrum is optically thin ($F_\nu \propto \nu^{(1-p)/2}$) and will break exponentially at a frequency proportional to $\mathrm{E}^2_{\mathrm{max}} B$.

For a specific frequency the light curve requires one additional parameter to a standard Gaussian form (the particle index p and the expansion speed v). The existing observed light curves at other frequencies, including the measured time delays can match a best fit Gaussian model without any additional parameters.

The observable parameters for a light curve at a reference frequency ν_0 are and the background level, the time and magnitude of the peak flux (t_0, and S_0), the particle index p and expansion speed in units of R_0 per unit time, controlling the asymmetry and width of the flare, respectively. The background value of the quiescent flux is the most uncertain parameter, as it can vary over the lifetime of a single flare.

The synchrotron flux from the plasmon is

$$S_\nu(R) = S_0 \left(\frac{\nu}{\nu_0}\right)^{2.5} \left(\frac{R}{R_0}\right)^3 \frac{1-\exp(-\tau)}{1-\exp(-\tau_0)} \tag{5.8}$$

where $R(t)$ is its radius, p is the index of the relativistic particle energy spectrum ($n(E) \propto E^{-p}$), and the optical depth

$$\tau = \tau_0 \left(\frac{\nu}{\nu_0}\right)^{-(p+4)/2} \left(\frac{R}{R_0}\right)^{-(2p+3)} \tag{5.9}$$

The critical optical depth at the maximum of the light curve at a any frequency,τ_0 satisfies the following:

$$e^{\tau_0} - (2p/3+1)\tau_0 - 1 = 0 \tag{5.10}$$

where ν_0 is the frequency corresponding to the $R = R_0$ condition. We employ Yusef-Zadeh et al.(2006) model, that uses a different coefficient of τ_0 than van der Laan's $(p+4)/5$ because the expression refers to the optical depth corresponding to the maximum in the spectrum at some instant ($\partial_\nu S(\nu,t) = 0$) rather than the maximum in the light curve at a particular frequency ($\partial_t S(\nu,t) = 0$). Here τ_0 ranges from 1 to 1.9 while p ranges from 1 to 3 (Yusef-Zadeh et al. 2006b). Given the particle energy spectral index p and the peak flux S_0 for a light curve at a reference frequency ν_0, the adiabatically expanding plasmon model predicts the variation of flux density at other frequencies.

Recent observations found time delays in the optically thick emission in radio, mm and submm which remain consistent with the model of a synchrotron blob optically thick in these bands. The plasma is embedded within the accretion disk or it could remove itself from the disk as the expansion is more pronounced at other wavelengths that exhibit time delays with respect to the initial IR flare. As the expansion gets noticeable, the flux will start peaking and declining at each frequency once the plasma becomes optically thin. Firstly it happens at high frequencies and later at longer wavelengths.

The particle index p determines the critical optical depth τ_0. The value of the peak flux S_0 determines the initial radius R_0 via $S_0 = \pi R_0^2/d^2 \times (1-\exp(-\tau_0))$ where d is the distance to the Galactic center (see Yusef-Zadeh et al. 2008). In this way, the expansion speed can be expressed in real physical units. The magnetic field and the electron density can be calculated

from the optical depth and the size of the emitting source, assuming equipartition between the magnetic field and relativistic electrons (we assume $E_{min} = 1$ MeV and $E_{max} = 100$ MeV).

To obtain numerical values, we assume that a typical flare with flux 1 mJy is produced by a population of relativistic electrons in equipartition with the magnetic field. The population is confined to a blob characterized by the initial size R_0.

Assuming that $R \propto t$, a model for $R(t)$ is necessary here to map the blob expansion to time or more explicitly, the dependence on radius to time: we adopt a linear expansion model at constant speed v, so that $R = R_0 + v\,(t - t_0)$ where t_0 is the time of the peak flux at the reference frequency ν_0.

We assume a power-law spectrum (E^{-p}) and use $p = 1$–2 in our numerical simulations to study the asymmetry of the produced theoretical light curves.

The frequency at which the light curve peaks can be written

$$\nu_p = \nu_0 \left(\frac{R}{R_0}\right)^{-(4p+6)/(p+4)} , \tag{5.11}$$

with the peak flux

$$S_p = S_0 \left(\frac{\nu_p}{\nu_0}\right)^{(7p+3)/(4p+6)} = \left(\frac{R}{R_0}\right)^{-(7p+3)/(p+4)} . \tag{5.12}$$

The spectral index α of the peak fluxes ($S_p \propto \nu_p^{\alpha}$) is weakly dependent on the particle index p, ranging from 1.21 to 1.55 while p runs from 2 to 8.

For a given particle spectral index p and peak flux density S_0 at a reference frequency ν_0, the model predicts the variation in flux density at any other frequency as a function of the expansion factor (R/R_0). Figure 5.11 shows the dependence of the flux density on the expansion factor (R/R_0). The flare emission (radio and millimeter) is plotted as as a function of the size of the expanding blob. The curves assume a particle energy spectrum of $\propto E^{-3}$ and an initial blob size of $4R_s$, where R_s is the Schwarzschild radius.

At times $t > t_0$, if we increase the turnover frequency ν_0 or the initial plasmon size R_0 the light curve will shift its decaying flank to later times. The only problem here is that decreasing the spectral index $\alpha_{\rm synch}$, the light curve will also shift at later times, which makes it difficult to constrain the other parameters. A potential issue is that if the initial phase angle of the blob changes, we will obtain the same effect but for all light curve not just its decaying flank.

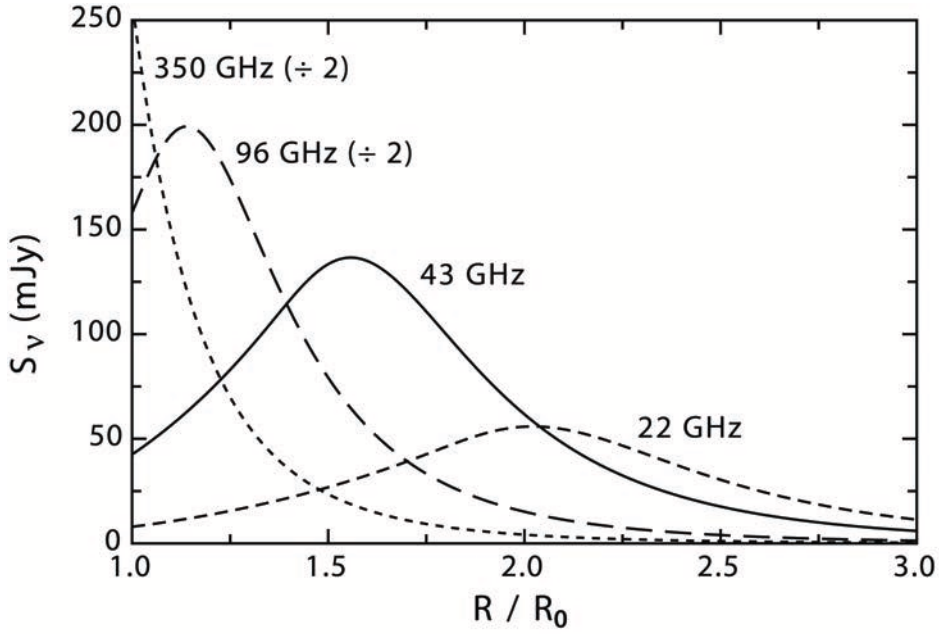

FIGURE 5.11: Light curves of synchrotron emission at four frequencies for an expanding blob. The near-IR peak flux is 1 mJy and R=4R_s. Credit: Yusef-Zadeh et al. 2006

Another constraining parameter that needs to be corroborated is the adiabatic expansion velocity of the plasma. We find that if the expansion velocity v_{exp} is increased, this will shift the light curve peak to earlier times. We also find that the initial size of the blob together with expansion velocity both determine the lifetime of the emitting source or the total flare duration. At very high expansion speeds, the spot dies very quickly and the short timespan would include a much smaller number of orbits. The initial size of the blob also determines the peak flux of the flare.

Firstly, we plot light curves at different frequencies for a blob that does not expand (see Figure 5.12). The adiabatic expansion model makes the prediction that the NIR and X-ray emission are expected to be simultaneous and therefore optically thin whereas the optical depth effects start to become significant only at lower frequencies, where a time delay is expected between the peak fluxes. To find evidence, various simultaneous data were obtained, leading to a temporal correlation of light curves in different wavelength bands, for each day of observation. There is evidence in this data that the Sgr A* flux constantly changes and that there is low-level flare activity in most of the frequency bands. We study the light curves

and the effect on the curve shape of using various expansion speeds of the plasma as well as several initial radii of the blob. If the blob doesn't expand, the light curves for different frequencies show that for a specific initial size, the accelerated particles produce simultaneous, rather than delayed flares, as we can see in Figure 5.12. The time delay is, on the other hand, dependent on the spectral index value. The plots show that if the blob is kept with a constant size and the expansion is not present, the light curves will always be simultaneous, showing no time delay between the peaks. This picture will still show frequency dependent curves with different values for the peak flux as the emission is still synchrotron whereas the stationary hot spot model will exhibit no frequency dependency at all. For different frequencies, the light curves will be identical.

The remaining parameters are the particle spectral index (p) and the initial blob radius (R_0). It is important to note that if we vary the particle spectral index p or the initial radius of the blob R_0, at the same frequency we obtain simultaneous light curves with no time delay, as we can see in Figure 5.13. The time lag between the peaks of the light curves will appear only as an effect of the adiabatic expansion process for successive lower frequencies. The decaying flank can be shifted toward later times by: the turnover frequency ν_0, by increasing the initial source size R_0, by lowering the spectral index or by lowering the peak flux density S_0 in the light curve. The flux declines monotonically as the blob is expanding. In the thin part of the spectrum, the flux initially increases with the initial source size at a constant optical depth, then it decreases because the blob starts to expand and the optical depth starts to decrease as well, causing a drop in the flux. The adiabatic expansion process implies a slower decay rate and longer flare timescales at lower frequencies. We plot light curves for various initial blob sizes, various optical depth values and different expansion velocities of the plasma. We find that the flare lifetime is determined by the frequency, the initial source size and the expansion speed of the plasma. The peak flux of the flare is determined by the blob size as well. As we see in the plots, the expansion speed is an important factor that controls the flare duration.

In this case, the shorter variability timescales, between about 10 and 30 minutes would be dominated by the orbital motion timescales. (about $\sim$ 20 minutes in average at the innermost stable orbit for Sgr A*). The orbital motion in the near proximity of a black hole is important

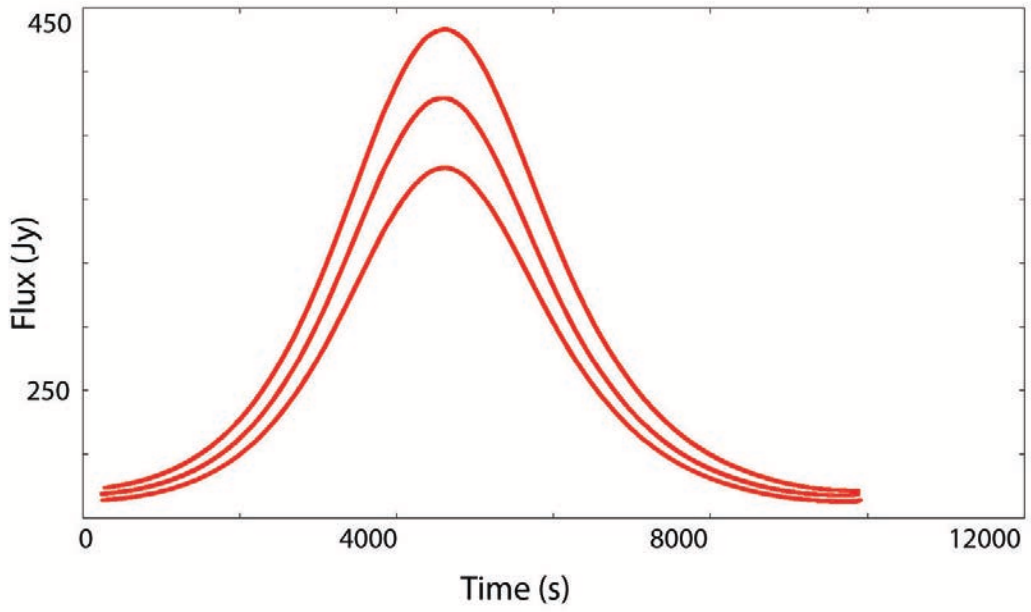

Figure 5.12: Theoretical relativistic light curves of a blob that doesn't expand, showing no time delay for different frequencies

as it is helpful in estimating the black hole parameters(mass, spin and disk inclination).

In Figure 5.14 or Figure 5.15, we plot light curves at 3 different frequencies of a blob that expands during multiple orbital periods.

We notice the interplay between the relativistic behaviour of the orbital motion together with the broad envelope of the expansion process. We interpret the radio flaring emission in terms of the plasmon model by assuming the adiabatically expansion of a plasma blob. The flaring activity is dominated by synchrotron emission arriving from a compact expanding self-absorbed blob of relativistic electrons.

Flares produced at a specific frequency originate in the process of adiabatic expansion of a blob of synchrotron emitting relativistic electrons. The plasmon is initially optically thick. The variability is frequency dependent in this case. The time lags between multiple flux peaks at several frequencies are explained via adiabatic expansion of synchrotron emitting plasma that cools down and decays after the initial flaring event.

The increase of the plasmon surface area while it still remains optically thick will cause the initial rise of the flux in the light curve. As the blob gradually becomes optically thin

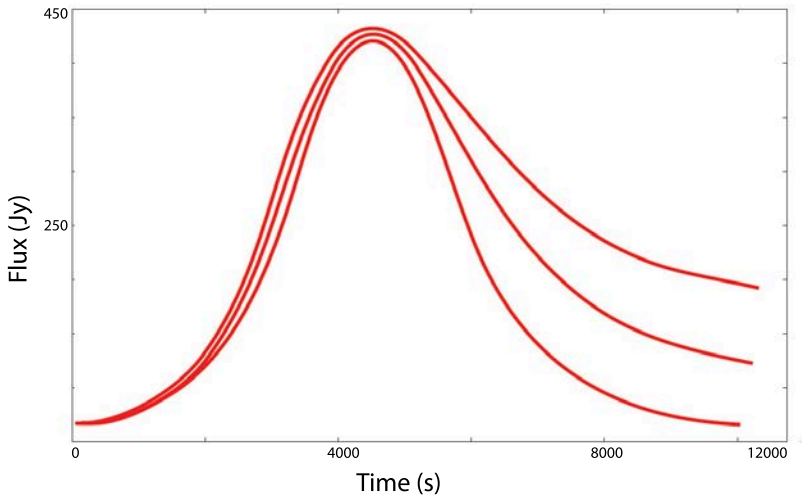

FIGURE 5.13: Theoretical relativistic light curves for a blob expanding with the velocity v=0.01c shown for different *p*, the index of the relativistic particle energy spectrum p=2, p=2.5, p=3 (bottom)

while the magnetic field diminishes, the light curve will turn over and the flux will start to decay.

The amplitude and timescale vary with the relativistic particle energy distribution, the expanding velocity and the size of the plasmon. If the blob lasts for multiple orbits and the timescale of the flaring is much smaller than the orbital period, at different frequencies, the plots will show a decay or rise, like in Figure 5.14 or Figure 5.15. We will discuss this issue more in detail in the next chapter.

Any simultaneous light curves for different two or multiple frequencies provide a good matching test of the existing non-relativistic plasmon model. In this case, matching realistic light curves require a relativistic approach, as the emission comes from the close vicinity of the event horizon.

As long as the time scales for the intrinsic flare variability and the orbital period amplification are not too close, therefore they are not interfering with each other, on a dynamical time scale, we can use light curves for an expanding plasmon at a very large orbital period. This approximation would be sufficient to describe the variation in flux of the expanding blob, while the lensing amplification together with any other relativistic effects would be

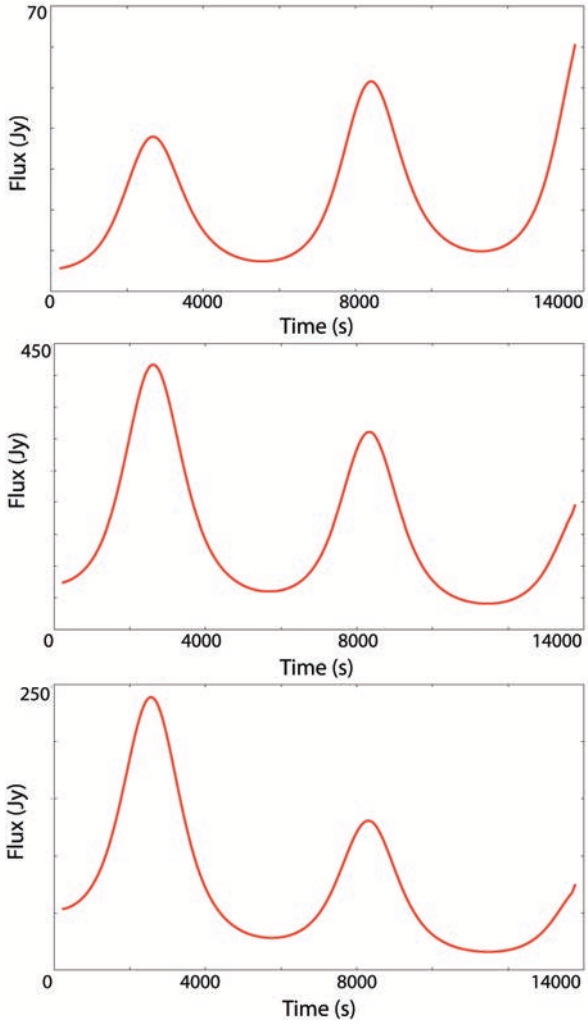

Figure 5.14: Relativistic light curves of an expanding blob with the orbital period T=75min, p=3, v=0.02c at 3 different frequencies

ignored.

We can see that there are two important time scales involved here. The only reason we would ignore these effects here is if the time scale of the two variability time scales taken into account would be too far from each other.

The timescale of the flare will be longer at lower frequencies and will exhibit a slower decay rate, because of the expansion process. Therefore, the flare time scale will be longer at lower frequencies. As we can see, the constraining model parameters are complementary and participate partially to the full picture of the light curve. Let us not forget that some relativistic effects, especially boosting and redshift bring a significant contribution here, leaving

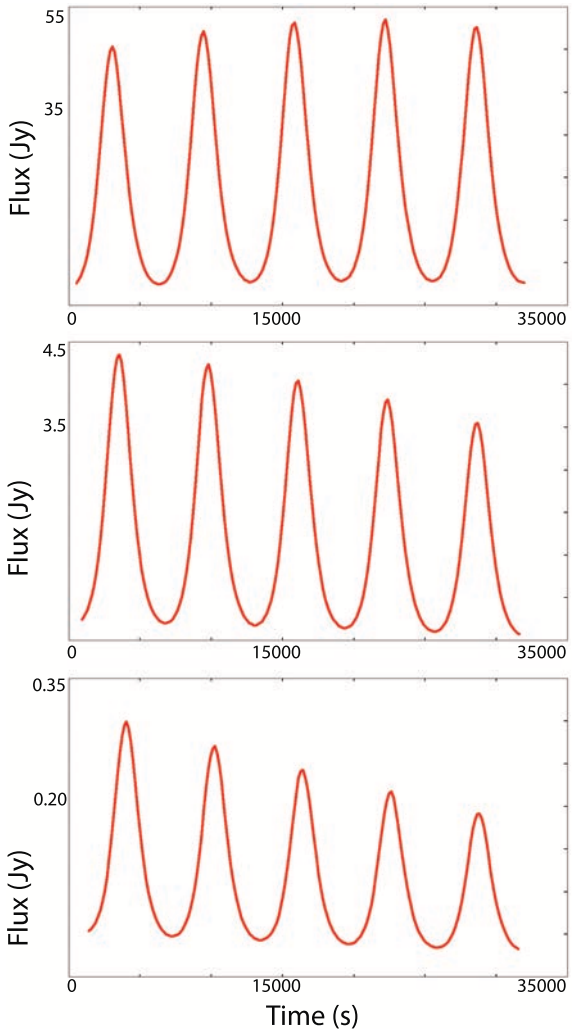

FIGURE 5.15: Relativistic light curves of an expanding blob with the orbital period T=105min at 3 frequencies for v=0.005c, p=2.5

space for interpretation of the final features of the observed flare.

The position and width of the flare peaks is also dependent on $v_{\rm exp}$ and R_0 values. We also have to take into consideration different values of the spectral index $\alpha_{\rm synch}$ to be able to match the observed flux densities.

The initial blob size R_0 and the spectral index of the particles p are both strongly constrained by the combination of measurements at frequencies that are initially optically thin ($\nu > \nu_0$) and optically thick ($\nu < \nu_0$). The initial flux at a given frequency above ν_0 is always dependent on the original near-IR flux due to the the particle spectral index constraints. However, it is not dependent on the blob size.

The plasmon size affects only the peak flux in light curves at any frequencies below ν_0 by determining the initial optical depth. The light curve rises initially is because of the increase of the blob's surface while it is optically thick.

As the plasma becomes optically thin, the light curve turns over because of the decrease of the magnetic field, the adiabatic cooling of the particles, and a decrease of the column density.

The adiabatic picture postulates simultaneous emission that produces a flare and declines at optically thin high frequencies and produces successive delayed flaring at optically thick lower frequencies.

We assume that for $t \leq t_0$, the optical depth of the plasmon equals its frequency dependent initial value τ_ν at $R = R_0$. In the optically thin part of the spectrum the flux initially increases with the plasmon size at a constant τ_ν and then decreases due to the diminishing optical depth as a consequence of the blob expansion.

For $t > t_0$ the decaying flank of the light curve shifts towards later times at the turnover frequency ν_0. The time delay between light curves is also noticed if the initial plasmon size R_0 is increased. Furthermore, by lowering the spectral index or the peak flux density S_0, the curve will also exhibit delayed arrival.

On the other hand, by increasing the adiabatic expansion velocity v_{exp}, the peak of the light curve will shift to earlier times. Adiabatic expansion causes also a slower decay rate and a longer flare timescale at lower frequencies.

Of course, we assume the values of other physical parameters of the spot model and the expanding plasmon model, like: the energy range of relativistic particles, the particle spectral index and the quiescent flux density.

We notice that the expansion speed is an important factor in differentiating between various light curves, as we can see in Figure 5.16. An increase of the expansion speed will shift the peak flux of the light curve to earlier times. A change in the expansion velocity will have as a result a change in the shape of the light curve. A blob that expands at a higher rate will exhibit a narrower light curve and a peak flux shifter at a slightly earlier time.

As the initial blob size and the particle index determine the peak flux of the light curve, he flare lifetime will depend on the expansion velocity of the plasma (see Figure 5.17).

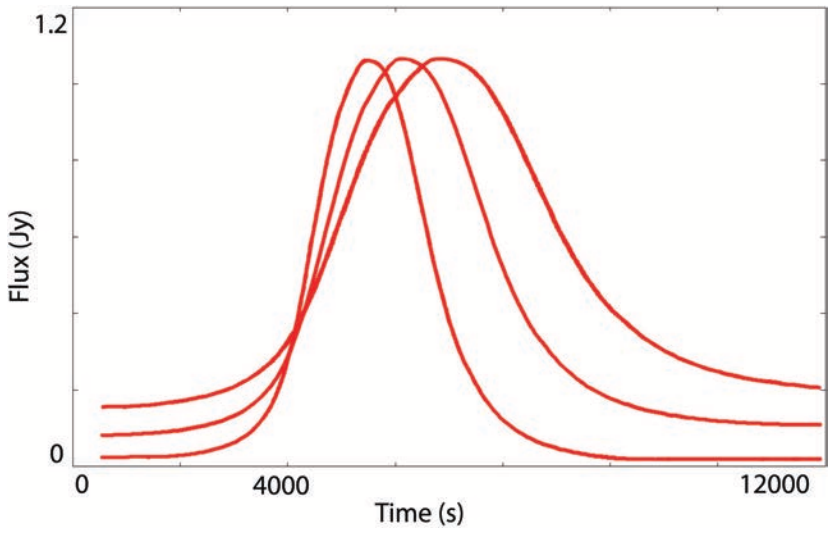

FIGURE 5.16: Theoretical relativistic light curves with p=2.5 for different expansion velocities: v=0.02c, v=0.005c and v=0.002c(the latest peak)

Consequently, there is a small time delay cause by the expansion velocity of the plasma.

The emission at a specific frequency peaks as the blob becomes optically thin at that particular frequency, which means that the blob size determines the peak flux of the flare.

We also conclude that the expansion velocity determines the flare duration. This is evident in the modelled light curves for different expansion speeds of the blob.

The estimated expansion speed of the plasma is a few percent of c, the plasma itself may be bound to Sgr A* or be embedded in the base of a jet (Maitra et al. 2009; Yusef-Zadeh et al. 2009). In this scenario, the contributions of the flares to the structure functions at 7 and 13 mm should be related to one another.

The initial increase in flux density is caused by the increase of the blob size while it is still optically thick. If the initial size of the blob is larger, the light curve will peak at a higher value. Consequently, the flux amplitude is dependent on the initial blob size, as we can see in Figure 5.18. Another interesting fact is that a larger initial size of the spot R_0 means a greater emitting surface, keeping the expanding plasma optically thick for a longer period. Hence, a longer time delay.

Our current theoretical modelling confirms the main picture of an expanding synchrotron emitting plasma blob matching several observations in radio with strong evidence of time

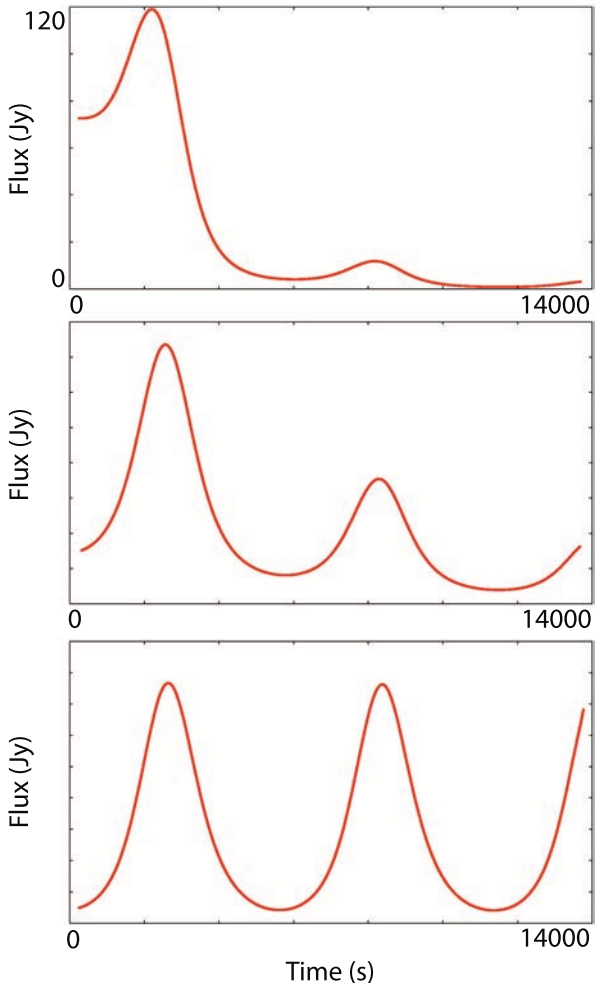

Figure 5.17: Theoretical relativistic light curves for an adiabatically expanding blob at the same frequency for various expansion velocities: v=0.5c, v=0.1c and v=0.005c

lags between the peaks of flare emission. The existing observational data shows time delays that match the phenomenological model of a uniformly expanding plasma blob from Sgr A*.

As we deal with a pure phenomenological model, we don't need to use best fitting model but only simple reasonable matches between our relativistic theoretical plots and the observed light curves. The study of the plasmon behaviour will help us understand the origin of the emission from Sgr A*. The flare durations and time lags modelled for optically thick flare emission are found to be consistent with the existing observations.

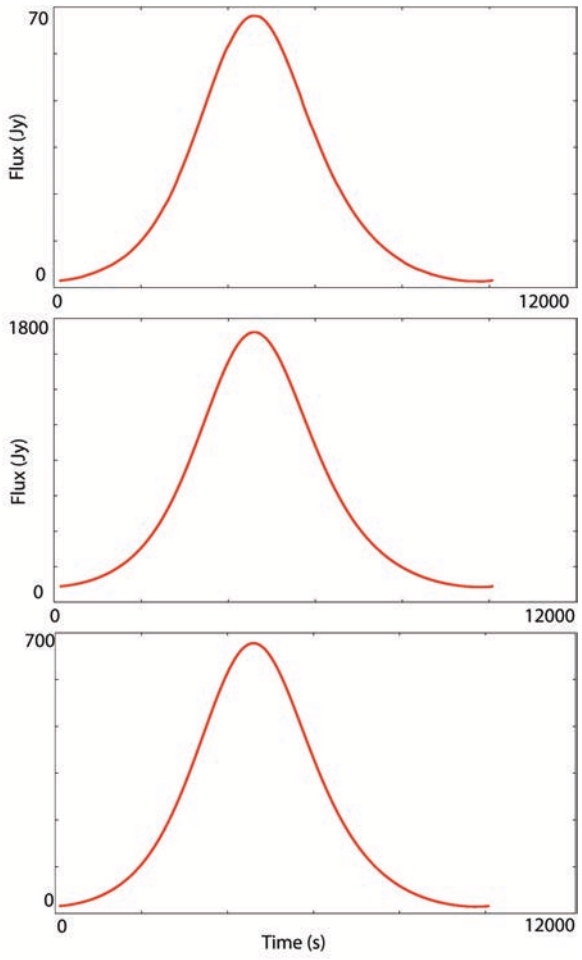

FIGURE 5.18: Theoretical relativistic light curves with p=1.5, vexp=0.01c for different initial blob sizes R=0.2Rs (lowest flux peak), R=1Rs, R=2Rs

5.4.2 Modelling the radio light curves

The adiabatic expansion of a synchrotron emitting blob based on the plasmon model explains the overall characteristics of the observed flaring activity in multiple frequency regimes. Here we test the plasmon model's applicability by including the relativistic effects on the light curves.

The model developed here will mainly account for the main flare structure and the sub-flare structure in optically thick regime by including optical depth changes and strong relativistic signatures. The amplitude modulations in the light curve are determined in this case by two different factors: the flaring modulation, caused by the intrinsic change in brightness

and the relativistic modulation, mainly caused by lensing and Doppler effects. We refer to these as the flaring component and the relativistic component in the light curve, respectively.

We compare the light curves to the existing observations. We find that the simulated profiles obtained in the context of the model of an adiabatic expanding plasmon, match very well the shapes of the light curves, the relative flux of the peak emissions and the peak time lags between successive frequencies from current observations. The substructure of the flares is here explained through relativistic effects. The observed flare durations and time delays in optically thick emission are found consistent with the proposed phenomenological model. The orbital motion of the plasma bubble introduces variability on 20 min average timescales with possible shorter timescale relativistic modulations, due to lensing and Doppler effects. Note that the suborbital relativistic flux peaks don't exhibit visible time delays between different frequencies.

The frequencies of interest for the plasmon model are below 350 GHz for which the emission is optically thick and the synchrotron cooling time of the particles is longer than the flare lifetime. The adiabatic expansion phase does not account for the initial energization of the electrons as the flare is optically thick and the synchrotron cooling time of the particles is longer than the flare lifetime. Therefore, the synchrotron cooling process is not included in this picture. We will later consider the possible connection to NIR band.

We focus on data of two overlapping Sgr A* flares at 43 GHz (7mm) and 22 GHz (13mm) on 2005, February 10 and 11. The emission is variable on hourly time scales with the 22 GHz peak delayed with respect to the 43 GHz peak (Yusef-Zadeh et al. 2006b).

For a specified particle spectral index p and initial blob size R_0, the observed delay (for example a delay of $\sim$ 30 minutes between 22 and 43 GHz frequency regimes) would allow us to infer that the source expands at a specific rate of R_0/hr or $\approx 0.02\,c$.

In Figure 5.19, we model Sgr A* light curves at 22 GHz and 43 GHz from 2005, finding a maximum 10% increase in amplitude with reference to the average quiescent level. The 22 GHz emission lags the flare at 43 GHz by $\sim$ 20 minutes (see Yusef-Zadeh et al. 2006b). We look for time delays between various flares at several successively longer wavelengths and simulate time lags between other wavelength bands, comparing with observations from VLA , CSO and Chandra.

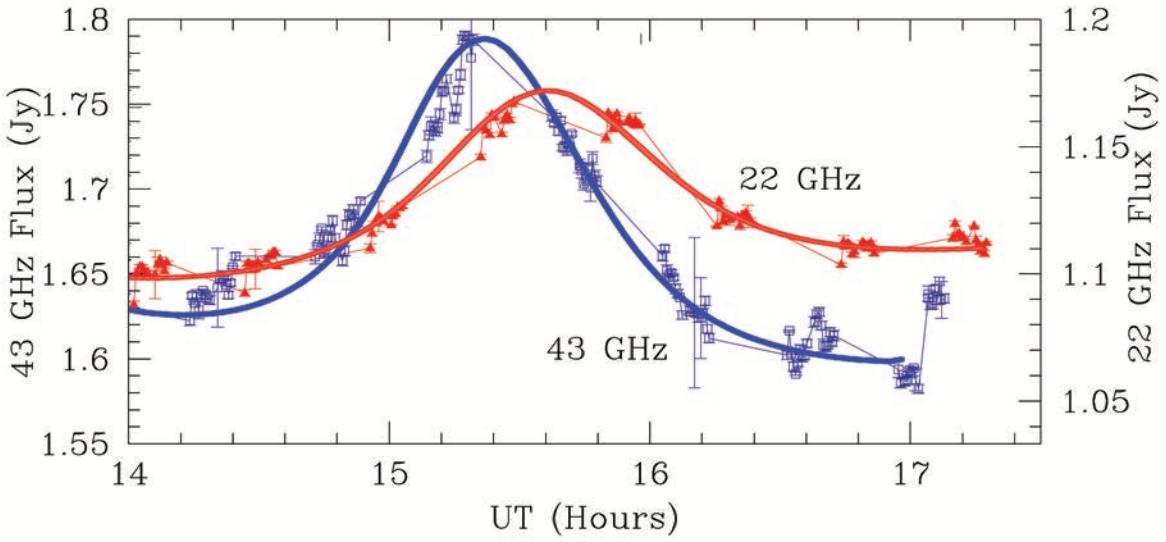

FIGURE 5.19: The light curve of Sgr A* at 43 and 22 GHz with a 30s sampling time and and the theoretical relativistic light curves at two different frequencies for an expanding blob of plasma with R=1R_s, superimposed over the data.

The two hour radio light curves show an increase of flux of about 7% at 43 GHz (λ=7mm) and 4.5% at 22 GHz (λ=13mm), when compared to the quiescent flux. The rise and fall time scale is about 1.5 – 2 hours, very similar to the flare measured time scale in sub-mm and mm wavelengths (Yusef-Zadeh et al. 2006; Mauerhan et al. 2005; Eckart et al. 2006). Monitoring of various observations at 43 GHz also show a 2-4 hour time scale (Roberts et al. 2006).

As we are interested also in the shape of the light curves, the plots showing evidence of sensitivity of the decaying part of the light curves to the spectrum as the magnetic field diminishes and therefore the synchrotron energy at a reference frequency increases with time.

The plasmon model predicts that both particle spectral index p and initial blob size R_0 are strongly constrained by the successive frequencies that are initially optically thin ($\nu > \nu_0$) and optically thick ($\nu < \nu_0$). The initial flux at frequencies above ν_0 was found to match the near-IR flux and it is constrained by the particle spectral index without any dependence on the blob size. For small values of p, the peak flux declines very rapidly. Considering the plasmon being initially optically thick for a particular frequency, the spectral index for any peak flux

will slowly decrease for an increasing p. The particle index p is always quite sensitive to α and consequently it is difficult to be obtained from existing observations. Of course, we can also conclude that α is weakly dependent on the particle index p, assisting with the prediction of the plasmon model. The source size constrains the peak flux in light curves at frequencies below ν_0 by determining the initial optical depth. Simultaneous monitoring at various successive frequencies would eventually allow us to constrain and estimate the parameters of the source on a flare-by-flare basis.

By modelling the flare emission using the adiabatic expansion of a synchrotron source we are able to constrain optically thin spectral index values $\alpha_{\rm synch}$, adiabatic expansion velocities $v_{\rm exp}$, the initial blob size R_0, the cutoff frequency $\nu_{\rm obs}$ and the flux density $S_{\rm max,obs}$ of the synchrotron source. Theoretically, if the initial plasmon parameters (orbital parameters, size, optical depth and spectral index) are known, then the spin of the black hole may be determined. Because the photon rays are compact, their trajectories connect the spot and the observer at infinity only through a small portion of the spacetime around the black hole. Thus, the known mass of the black hole together with the estimated spin could be actually good indicatives of the spacetime in a small region. Observations of multiple spots, using both hot spot and adiabatically expanding plasmon models, at different orbital radial locations, therefore various orbital periods, will consequently provide a good method to measure the black hole spin at a number of distinct locations near the black hole. These findings could be then compared to the no hair theorem for Kerr metric predicting that the spacetime around the black hole would be fully described only by the mass and spin alone. Such a result would provide a good method to quantitatively test the Kerr metric itself.

By minimizing the number of free parameters we are able to constrain a significant number of features in the observed light curves. Unfortunately, the model parameters are not all independent, e.g., the width and peak of a light curve signatures depend to a varying extent on all parameters $S_{\rm max}$, $\alpha_{\rm synch}$, R_0, and $\nu_{\rm max}$.

The parameters that influence the properties of delayed emission are the initial size of the emitting source (before the expansion starts) and the expansion speed. The initial size of the blob shouldn't modify the NIR/X-ray light curves, as they are optically thin and the emission depends only on the total number of accelerated particles, not on the initial size of

the blob or the electron density. Nonetheless, at lower frequencies, emission could become self-absorbed and will therefore introduce the dependence on the initial blob size.

The time delay is clear evidence that the 2 hours flare does not represent a signature of the orbital period. These light curves don't show strong evident sub-structure of the flare, but such features are present in observations of other flares, such as observed on 2007, April 4 (see Figure 5.8). The measurements at 43 and 22 GHz are interleaved and therefore is some uncertainty as to the exact value of the peak flux density at 43 GHz, considering that there is missing data around the peak flux, bearing a lot of uncertainty in regards to a single peak or a two peak structure.

In order to provide a better picture on the flaring activity in radio wavelengths, we use Figure 5.20 which is an explicit developed model of the first simple expanding plasmon scenario, but this time including general relativistic effects due to periodic orbital motion. The first figure showed modelling of the adiabatic expansion of the blob without any assumption about the orbital motion. The plasmon expands during 5 orbital periods and exhibits time delays of 20-25 minutes between each corresponding peak, due to a main time lag between the broad light curve at 43 GHz with a duration of approx. 2 hours and the light curve at 22 GHz with a duration of approx. 2.5 hours. The ratios between peak fluxes at different frequencies corrected with all relativistic effects closely match the peak flux ratios and time delays from simultaneous observations of Sgr A* at several frequencies. More accurate observational data and a better sampling time might reveal a more detailed and discriminating substructure of the flare, providing information about the orbital motion of the blob.

As a last step in our modelling of radio light curves, we introduce various relativistic effects at sub-orbital level and take into account a relatively small size of the source. We previously found that the flaring seems to occur at small orbital radii in the inner accretion flow, most likely near the ISCO. Consequently, relativistic effects play a significant factor in affecting the variability of the emitting source. We will find that both gravitational lensing and relativistic beaming near the event horizon are sources of significant magnification of the amplitude of the sub-orbital modulations. Figure 5.21 includes both Doppler beaming and gravitational lensing effects visible for each orbit of the expanding blob. During the expansion process, the plasmon modulates its flux amplitude during each orbit, due to

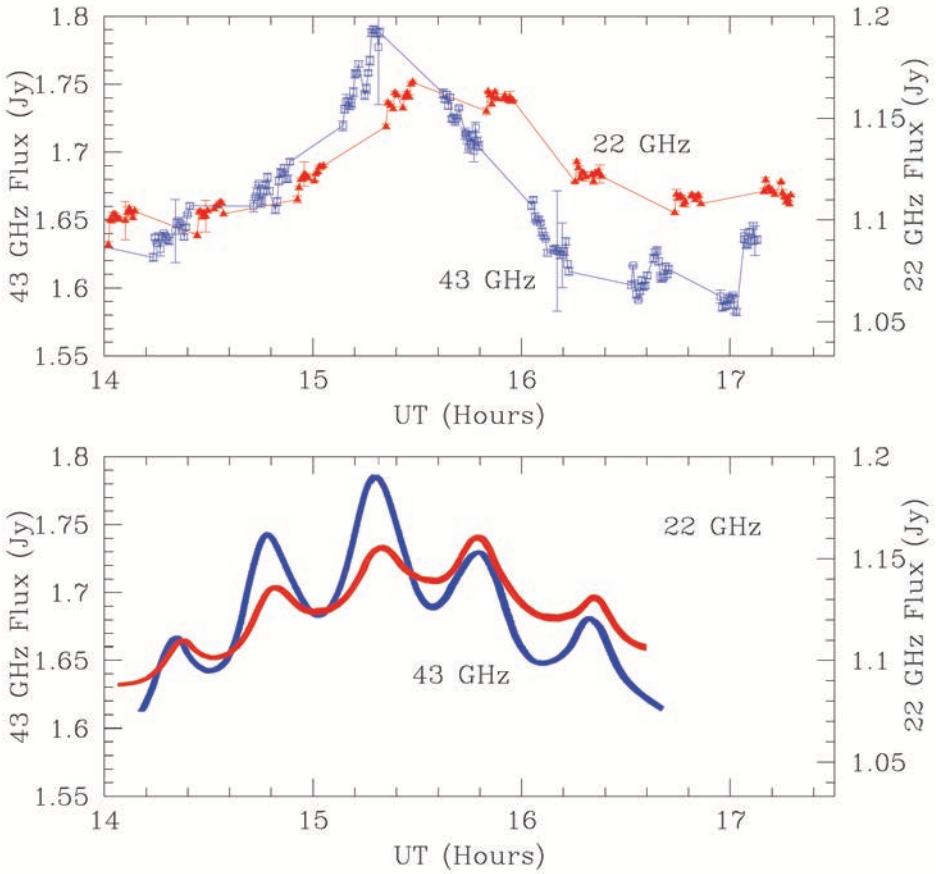

Figure 5.20: (Top) The light curve of Sgr A* at 43 and 22 GHz with a 30s sampling time and (Bottom) Theoretical relativistic light curves at two frequencies for a plasmon with R=1R_s. Gravitational lensing has been suppressed

Doppler effects and gravitational focussing factor. A double peak structure becomes visible at a sub-orbital level, under the 20 minutes average duration of an orbital period. Further radio observations with better sampling are necessary in order to confirm the presence of relativistic multi-peak flare structure (both lensing and Doppler effects).

The sub-flares are due to a single flaring event caused by a an adiabatically expanding blob on an orbit around the black hole and secondly, by several relativistic effects. Both events are being modulated and simulated on the same timescale. The blending between the two underlying events will account for the complete broad overall flare. Relativistic effects like beaming and lensing will also imprint on the intrinsic emitted radiation. Looking

for genuine flaring events and separating them from orbital motion flux modulation is our main task here. The interplay between the two components is obviously dependent on the timescale of each event.

The model matches the existing shapes of the light curve profiles and the time delay between various frequencies. The derived emission source size, density and magnetic field strength are all in agreement with the predicted parameters by accretion models.

Matching theoretical relativistic light curves with simultaneous observed light curves of Sgr A* at various frequencies and performing a quantitative analysis of the findings, allowing us to determine the peak fluxes and time lags is an excellent method to test the plasmon model's applicability and recipe for probing various flaring features and measurement of any flare parameters. The most important result remains the analysis and constrain of all special and general relativistic effects in the context of realistic matching observed light curves. Due to the proximity of the black hole event horizon, general and special relativistic effects imprint on the synchrotron radiation of such inhomogeneities. All the model parameters have to be corroborated with constraining information from black hole and geometry parameters like initial radial location, initial azimuthal angles, observed inclination angle of the disk, orbital period and the spin parameter of the black hole. The analysis of relativistic radio light curves is important to understand the nature of Sgr A* flare activity and confirm the model of an expanding synchrotron source.

5.4.3 Expansion speed estimates

The radio flaring activity, including the observed time lags can be understood through the expansion of a plasma blob within the accretion disk. By simulating light curves for blobs of various initial sizes and considering the maximum flare length between 2–3 hours, we find expansion velocities which are in agreement with the derived values from Yusef-Zadeh et al. (2008) The expansion velocities predicted by our model are lower than the orbital velocity derived by previous authors for the hot spot model, not allowing the plasma to escape from the inner regions close to the ISCO. For a 30 minute time delay, the plasmon doubles its initial size in about one hour. However, the sound speed for a relativistic plasma and the

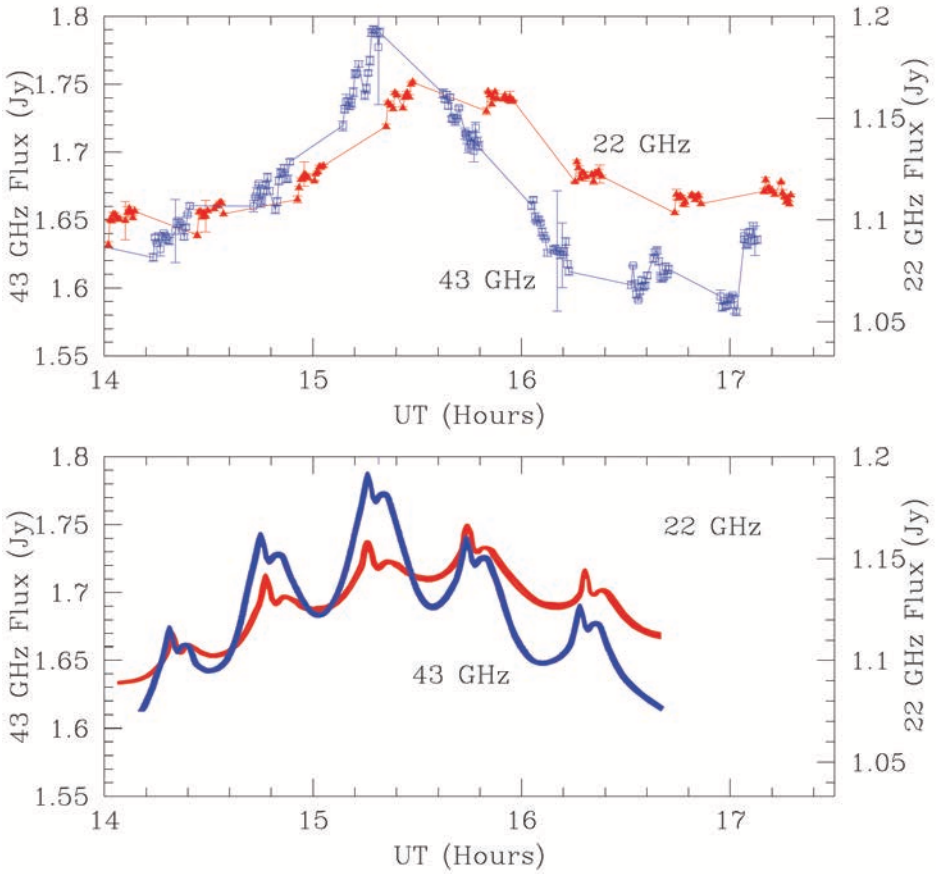

FIGURE 5.21: (Top) The light curve of Sgr A* at 43 and 22 GHz with a 30s sampling time and (Bottom) Relativistic light curves (includes lensing and beaming effects) at 2 frequencies for a plasmon with R=1R_s.

escape speed from the black hole should be on the order of $\sim 0.5c$ average velocity.

We model the sub-mm and radio flare from 2006 July 17 and the radio flare from 2005 February 10 and 2006 February 10. We compare with the model fitting of the data from Yusef-Zadeh at. al. 2008 and find similar expansion velocities for the plasmon. The sub-mm theoretical light curve from 2006 July 17 (Figure 5.22, a) looks asymmetric and shows a slow decay. For a particle spectral index p=1, we derived the expansion speed of v = 0.0028c corresponding to a magnetic field of B = 76 G. As the synchrotron cooling time for particles emitting at 350 GHz is about 45 minutes,it is possible that the decay of the light curve might be affected by it. There is evidence for time delay between X-rays and 850 μm

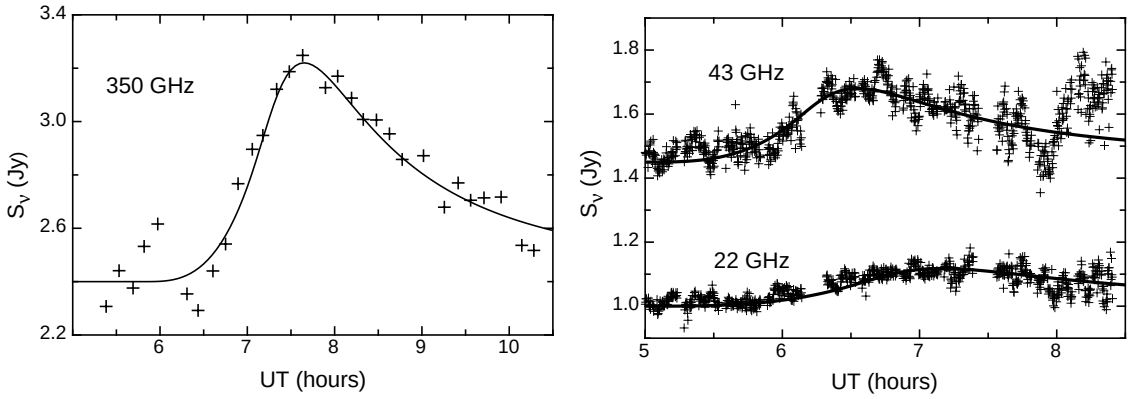

FIGURE 5.22: **(a) Left** The solid line is a sub-mm light curve fitting on 2006 July 17 at 350 GHz. The fit only uses the bright flare and not to the weak flare peaking around 6h UT. **(b) Right** Light curves at 43 and 22 GHz fitted simultaneously for the 2006 July 17 data. Credit: Yusef-Zadeh et. al. 2008

emission suggesting that the optically thin near-IR/X-ray emission leads the optically thick sub-mm and radio flaring by about 2-3 hours. This delay confirms the simultaneous near-IR and sub-mm 2004 observations showing a sub-mm flare being delayed by 160 minutes after the initial near-IR flare (Yusef-Zadeh et al. 2006a).

The radio light curves at 43 GHz and 22 GHz from 2006 July 17 are modelled and for a particle spectral index of p=1, we find an expansion speed of v = 0.12c corresponding to magnetic field of 11 G as we see in Figure 5.23,b.

The existing 340 GHz light curves of Sgr A* (Eckart et al. 2006a) show that a highly accelerated expansion of the blob is a very unlikely event. A highly accelerated or decelerated expansion would cause a sharp drop or rise in the light curve, which is not the case. From our theoretical light curves, plotted for various expansion velocities, we can deduce that a low expansion velocity would firstly show high flare flux levels for a few hours after the initial event. A change to a higher expansion velocity would show a sudden drop of the light curve. These kind of light curve profiles don't seem to match any existing Sgr A* data. In the same way, a strongly decelerated flare would exhibit a fast drop to low flux density values.

If we want to make any assumptions about the expansion velocity, some considerations about the magnetic field have to be considered. The expansion velocity could be derived from the assumption of magnetic tangled fields, as a result of the turbulence during the adiabatic

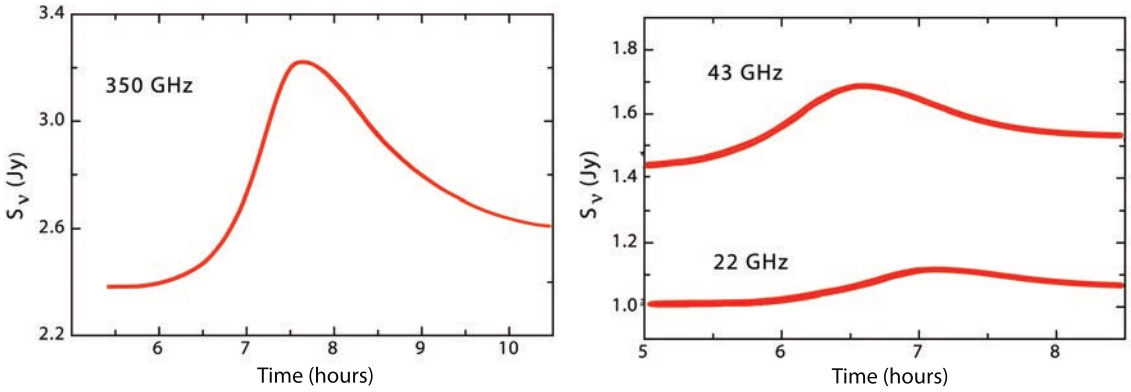

Figure 5.23: **(a) Left** The theoretical light curve fitting the sub-mm 2006 July 17 flare at 350 GHz. **(b) Right** Theoretical Light curves at 43 and 22 GHz fitted simultaneously for the 2006 July 17 flare. The data is shown in Figure 5.22

expansion process (van der Laan, 1966). If the expansion happens along with an outflow, therefore within a partially aligned field, the expansion can be prevented from developing perpendicular to the field lines. The source will remain more confined and we would have significantly lower values of the expansion velocity.

The adiabatic expansion of a blob within the accretion disk that also assumes shearing due to differential rotation could actually explain the low values of the expansion velocities. However, the blob can have a bulk velocity much higher or lower than the expansion velocity and could therefore affect the final expansion speed of the plasma. We don't include any shearing mechanism in the model and in this chapter, for the current purposes here, we don't limit our assumptions about expansion velocities. In the next chapter, these assumptions become an important factor as we seek to confine all existing parameters to realistic ones, to be able to match accurately the Sgr A* data.

It has been suggested that the lifetime of the NIR and sub-mm flares could imply that the flaring is caused by an outflow (Yusef-Zadeh et al. 2006a), persuading several authors to look for time delays in radio bands. The Sgr A* light curves at 7 and 13mm (VLA, 2005) are still the most representative existing data to be investigated for this purpose and used to confirm the adiabatically expanding model. The curves show a 5-10% increase of flux amplitude for both frequencies with respect to the quiescent level. The 13 mm flare lags the 7mm one

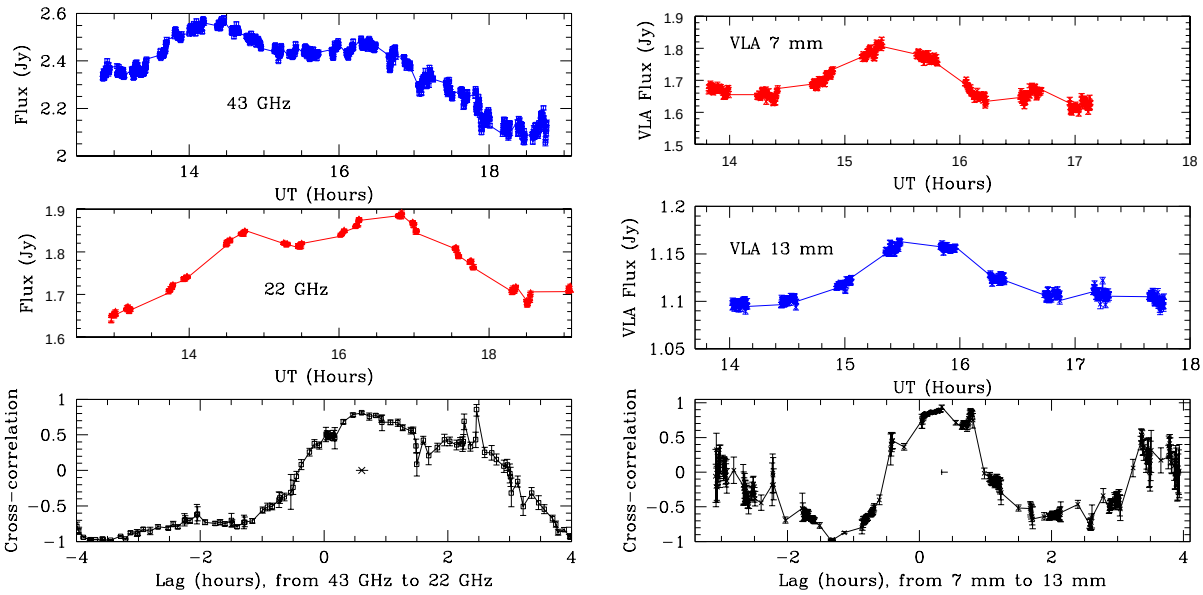

FIGURE 5.24: **(a) Left** Light curves of 7mm (43 GHz) and 13 mm (22 GHz) emission from 2006 February 10 data and their cross correlation (bottom). The 13 mm data indicate a time delay of 20.4±6.8 minutes with respect to 7 mm emission. **(b) Right** Same as (a) except the data is taken from 2005 February 10. The time delay is about 30±12 minutes. Credit: Yusef-Zadeh et. al. 2008

by ∼ 20 minutes (Yusef-Zadeh et al. 2006b). The peak near-IR frequency shifts toward lower frequencies (sub-millimeter, millimeter and then radio) and confirms the picture of a self-absorbed synchrotron blob that expands adiabatically (van der Laan 1966). A model of an intrinsically faint accretion disk dominated by red noise with emission assumed from a bright orbiting spot in conjunction with a short jet was also proposed (Eckart et al. 2006b, Meyer et al. 2006ab, 2007). The model was analyzed using the brightest flares from SgrA* with high signal to noise light curves from multi-wavelength observations.

For the light curve from 2006 February 10, shown in Figure 5.24, a, we find for a particle energy index p=1 we find the expansion speed of v=0.012, with B=11 G.

The light curves from 2005 February 10 at 43 and 22 GHz are both modelled in Figure 5.25, a and derive the physical parameters of the flare. For a particle index of p=1.5, we find the expansion velocity of v=0.018c corresponding to a magnetic field of B=12 G.

We confirm that the time delay measured from theoretical light curves is consistent with

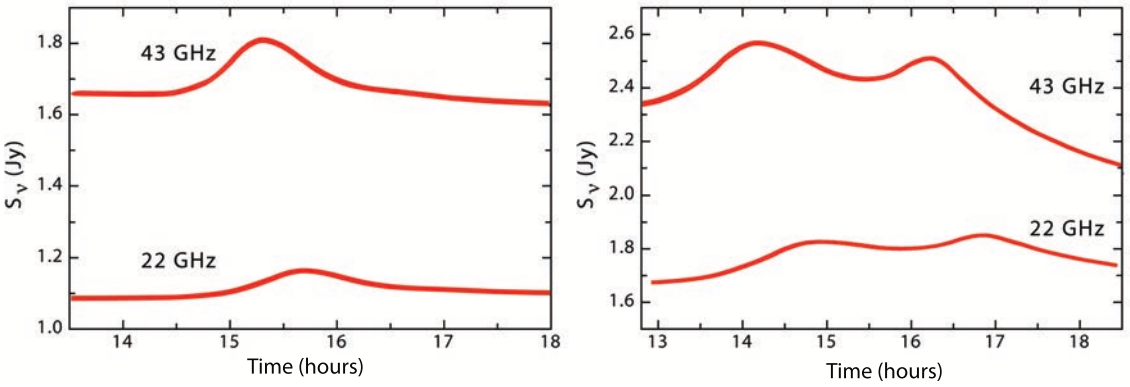

Figure 5.25: **(a) Left** Theoretical light curves of the flare at 43 and 22 GHz fitted simultaneously. The data is from 2005 February 10. **(b) Right** Theoretical light curves of two overlapping flares at 43 and 22 GHz fitted simultaneously. The data is from 2006 February. The data is shown in Figure 5.24

the picture of an adiabatic expansion of a self-absorbed source. We find that the expansion velocities are smaller than 0.1c.

The inclusion of an adiabatic expansion component requires expansion velocities below the canonical sound speed 0.5c. As the blob diameter is assumed to be in the range of several R_s, it may well be located at 10 or even more R_s. The blob may be in this case embedded in the outer layers of an accretion flow where it would be mildly over-pressured with respect to the neighbouring material.

Our model infers low adiabatic expansion velocities for the flares of SgrA*. We used expansion velocity values of ~0.002 c, ~0.005 c, ~0.009 c up to ~0.5 c close to the range of velocities of v_{exp}=0.003-0.1c values given by Yusef-Zadeh et al. (2008). The required expansion velocity value is lower than the typical inferred orbital velocity of the standard orbiting hot spot model (Eckart et al. 2006b, 2008ab, Meyer et al. 2006ab, 2007, 2008, Trippe et al. 2007). Therefore, the observed sub-mm/mm flare emission can be interpreted as a slow expanding blob within the accretion disk around SgrA*.

The expansion time scale would be comparable to the buoyancy or orbital time scale. We find that the emitting blob is located much closer to the black hole (within $5R_s$), but expanding more slowly than expected at these orbital radii, leading us to make assumptions about the surrounding environment.

The blob may be slowed down by the bulk mass of plasma where the blob is embedded. If there is a bulk motion that slows down the blob, this fact should be also present in the time delays in the observed light curves. If the bulk motion is lower than the expansion velocity of the blob, we should be able to see slightly longer time delays between light curves at successive frequencies, than the predicted time delays for a simple plasmon expanding in vacuum. The plasmon would cool slower than the expected values from the adiabatic plasmon model.

One interesting way to see this plasmon being dragged backwards and slowed down by the bulk material would be assuming a retrograde motion for the blob, while the bulk material is moving together with all accretion flow in a prograde direction with reference to the black hole spin. We make these assumptions about the environment where the plasmon is embedded but further evidence has to be provided by future simultaneous frequency campaigns. A model for the dynamical evolution of the blob could probe the properties of the accretion flow itself together with the feeding processes of Sgr A*.

We are able to impose limitations on the expanding velocities of the expanding plasmon. The simulated decay rates of both NIR/radio flares suggest a non-radiative cooling process, such as adiabatic expansion that explains the flaring activity in these wavelengths.

The modelling of these light curves results in low expansion speeds, lower than 0.2c. We find expansion velocities in radio frequencies of the order of v_{exp}=0.003-0.2c, in agreement with the findings of Yusef-Zadeh et al. The expansion velocities have lower values than the expected relativistic supersonic speeds for orbital velocities near the ISCO.

5.4.4 Contribution to time delays from orbital motion of a plasmon

The key motivation of our model is to find relativistic signatures in Sgr A* light curves using the adiabatic expansion model of the intrinsic flaring to account for delayed peaks and focus on features that are signatures of relativistic orbital motion. We find that the predicted time lags slightly differ from the observed delays. We interpret this discrepancy as a relativistic signature, produced by orbital motion, blending with the evolution of the intrinsic flux and shifting the timing of the observed peak. As long as we can compare our theoretical values of

time delays derived from the plasmon model, with the observed time lags in multiple bands, the peaks that don't exhibit delays could be considered as signatures of gravitational lensing and/or Doppler boosting on orbital timescale. For simplicity, we assume here that the flares produced on 20 min timescale arise in matter on Keplerian orbits around the black hole.

If the separation between two observation frequencies is too large, the task of relating them phenomenologically and understand the possible connection between the time lags at different frequencies can become a non-trivial and confusing job.

A robust measurement of the time lags should be only taken between light curves simultaneously observed at relatively small frequency ratios. In our modelling, we use small frequency ratios, mostly 1:2 or 1:3 between two theoretical light curves, in order to examine time delays in radio variability.

The numerical findings are found consistent with the observed time lags between the two consecutive flare peaks at optically thin radio frequencies and higher optically thin frequencies.

Here we use other pair of flares, at 84 GHz and 43 GHz to calculate the time lag and match to the NMA observed light curves. Using the plasmon model, we obtain predicted time lags that are shorter than the observed time delays between the same used frequencies. The observed time delay between light curves at 84 GHz and 43 GHz is 1 hour, whereas the predicted time lags are 18.75 at p=2, 19.25 min at $p = 3$ and 19.03 min at $p = 2.5$. Previously, Myiazaki et al. performed NMA simultaneous observations of flux densities at 90 and 102 GHz in order to detect the time delays between these frequencies (Myiazaki et al., 2013). The time lag predicted by the expansion model was not detected during this epoch.

The observed time lag between 146 GHz and 134 GHz $\Delta t_{146\text{-}134}$ is 3 min, whereas the predicted values of the time delay are 1.77 min for $p = 3$, 1.67 min for $p = 2$ and 1.72 min for $p = 2.5$.

Another interesting fact is that the predicted time lags and the observed time delays are on the same timescale, with very close values, suggesting that we may indeed have a number of different consecutive flares, with individual additive time lags, blended with relativistic information and ultimately exhibiting a longer time delay of the composite broader flare.

The lack of time lags in this case could be understood through blending of the intrinsic

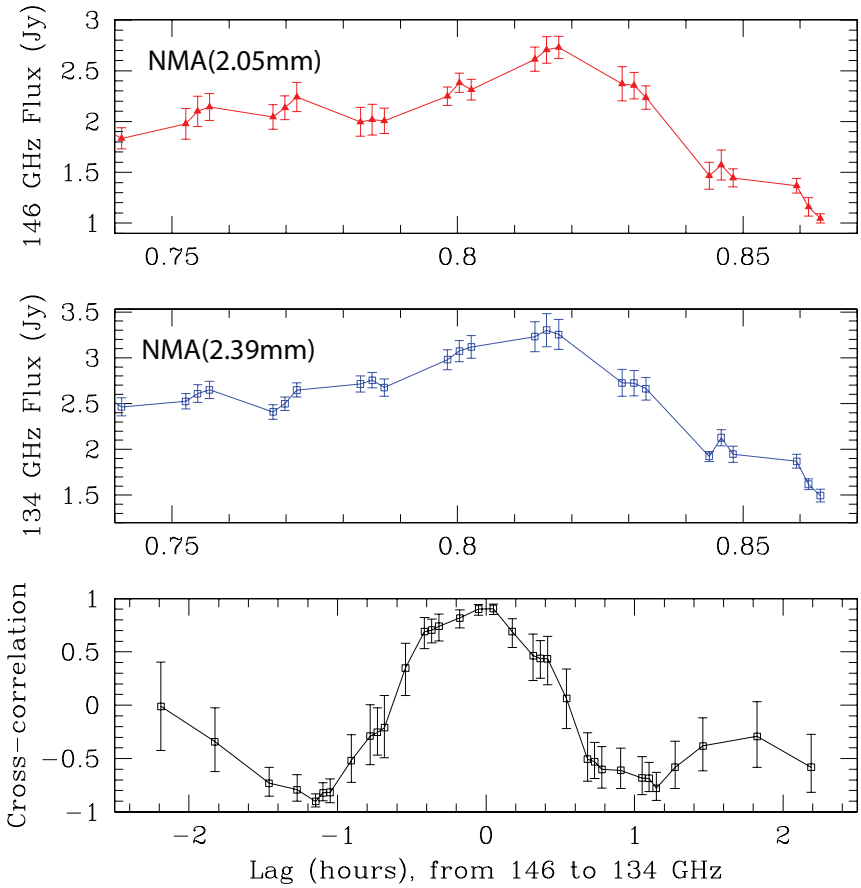

FIGURE 5.26: Simultaneous light curves measured with the NMA at 146 GHz and 134 GHz on 2007, April 4, respectively. The cross correlation plot shows $3^{+3.4}_{-8.0}$ minutes time delay. Credit: Yusef-Zadeh et. al. 2009

flaring emission with relativistic signature peaks. Contrariwise, two or more consecutive neighbouring flares (from more than one individual blob) could be blended with lensing effects and exhibit a broader flare formed from multiple peaks. In this case, the observed time lag could be actually longer than the predicted time lag of an individual expanding plasmon. This fact could be significant to understanding the relativistic signature peaks occurring on same timescales with an individual flare. Following Myiazaki et al., the flux peaks at the frequency:

$$\nu_p = \nu_0 \left(\frac{R}{R_0} \right)^{1/A}, \tag{5.13}$$

with $A = -(p+4)/(4p+6)$ and p the index of the relativistic electron energy spectrum

[$n(E) \propto E^{-p}$]. The plasmon expands linearly with a constant expansion speed, v_{exp}.

$$R - R_0 = v_{exp}(t - t_0), \tag{5.14}$$

with $t - t_0$ the lifetime of the plasmon. The lifetime of the blob is frequency dependent:

$$t - t_0 = \left[\left(\frac{\nu_p}{\nu_0}\right)^A - 1\right] \frac{R_0}{v_{exp}}. \tag{5.15}$$

From here, we can derive the time lag between any two observing frequencies:

$$\Delta t_{146\text{-}134}\ (\text{min}) = \left[\frac{146\ \text{GHz}^{\,A} - 134\ \text{GHz}^{\,A}}{43\ \text{GHz}^{\,A} - 22\ \text{GHz}^{\,A}}\right] \times \Delta T_{43\text{-}22}\ (\text{min}), \tag{5.16}$$

with $\Delta T_{43\text{-}22}$ the time lag between two known frequencies: we use the time lag between 43 and 22 GHz in minutes.

If the time delay $\Delta T_{43\text{-}22}$ is set as 25 min, the time delay $\Delta t_{146\text{-}134}$ is expected to be 1.67 min at $p = 2$ and 1.77 min at $p = 3$, whereas the NMA observations show a 3 min time delay between the two light curves. Figure 5.26 shows light curves measured simultaneously with the NMA at 146 GHz and 134 GHz on 2007, April 4, respectively. The peak flux at 146 GHz will arrive around 3 min later than the peak at 134 GHz.

In the same way, we calculated the time lag between the light curves at 84 GHz and 43 GHz:

$$\Delta t_{84\text{-}43}\ (\text{min}) = \left[\frac{84\ \text{GHz}^{\,A} - 43\ \text{GHz}^{\,A}}{43\ \text{GHz}^{\,A} - 22\ \text{GHz}^{\,A}}\right] \times \Delta T_{43\text{-}22}\ (\text{min}), \tag{5.17}$$

When the time delay between two flares is already known, the time delay between two desired frequencies can be also calculated. We find a predicted time delay of 18.75 min for p=2, 19.03 min for p=2.5 and 19.25 for p=3 between the light curves at 84 GHz and 43 GHz, whereas the observed time delay is 62 min. In the same way, we calculated a time delay of 1.67 min for p=2, 1.72 for p=2.5 and 1.77 for p=3 between light curves at 146 GHz and 134 GHz, while the observed time delay is slightly longer: 3 minutes.

For modelling purposes, we use the Figure 5.21 that shows five orbits of an expanding blob, containing both lensing and Doppler beaming signatures. The relativistic orbital modulations corresponding to 43 GHz and 22 GHz are almost aligned (simultaneous) whereas the broad 2.5 hour flare show a 25 minutes time lag between the light curves at both frequencies.

Depending on the initial phase where the blob starts orbiting the black hole, the lensing and beaming peaks are formed in a different part of the light curve. The existing simulation is generated using a blob that starts orbiting at the far side of the black hole, producing a first lensed flux and a secondary beamed flux of the first lensed image. The flux ratios between the lensing modulation and the beamed peak can also vary, depending on the orbital phase and inclination angle of the observer.

In order to find the time lag between the two light curves, some information about the orbital motion of the blob is necessary. The peaks of the two light curves at 43 GHz and 22 GHz can be slightly shifted by a different phase location of the lensing/beaming peak or the flux ratio between these two peaks (it is possible that the beamed secondary flux to produce a a higher peak in the light curve).

The task of locating the peak in the 22 GHz delayed flare, is not a straightforward job and it is dependent on the orbital parameters. A small difference between the estimated delay (between the 43 GHz and 22 GHz flare peaks) and the observed time lag can here be understood in the context of a relative location of the peak, dictated by relativistic modulations at sub-orbital level. The blending between the neighbouring individual orbital modulations may also shift the peak of the flare at earlier or later times.

As we don't aim for a quantitative analysis of the light curves, but only present a possible scenario that may explain, in a relativistic context, some discrepancies found in the observed time lags at multiple radio wavelengths. The simple expanding plasmon model predicts a large number of radio/mm data but not all of it.

We only suggest here that the predicted time lags are not always in agreement with the data, because of possible relativistic tampering with the light curve. The presence of outlier peaks that are not necessarily produced by a change in optical depth, but of relativistic origin, will ultimately interfere with the expanding plasmon theoretical fits. This conclusion is a first step in introducing (in the next section) a novel composite model containing relativistic, hot spot and expanding plasmon components. This picture may also account for observations where no time lags between radio flares were detected as in the case of the flares at 90 GHz and 102 GHz (see Miyazaki at. al. 2013). This model opens up extremely interesting perspectives, including a potential estimate of the spin of the black hole. The method reinforces

and corroborates the findings of quasi-periodic emission in X-ray and NIR, confirming that the periods observed in the light curves could be a signature of the orbit and not an effect of the intrinsic flux modulations occurring in the accretion flow due to magnetic field variations, injection of new particles or disk instabilities.

5.5 A composite relativistic model for Sgr A* variability

5.5.1 Timescale setup

The key concept here is that different time scales are present in Sgr A* variability. Firstly, orbital motion of the spot around the black hole produces modulation of the light curve by lensing and Doppler relativistic effects. The second time scale is the timescale of variability in the intrinsic flare. The flux modulation is caused here by the increasing brightness of the flare due to e.g. a variation in the magnetic field, a disk instability, a particle injection process or expansion. The matter can become very confusing when one considers all of the various timescales in which Sgr A* shows variability.

Intermediate timescales, from a few minutes to several hours probe the dynamical evolution of the accretion flow on timescales from less than an orbit to multiple orbits. As the internal variability timescale appears to be of order the orbital timescale, relativistic effects could become a significant factor in understanding the Sgr A* flare emission.

A flowchart that outlines the modelling process is shown in Figure 5.27. It identifies the orbital timescale and the flaring timescale as the initial factors that subsequently determine the presence of relativistic signatures within a light curve. The flare lifetime is dependent the expansion velocity of the plasma and the initial size of the blob. The flare can be formed and evolve on any time scale and our flowchart considers time scales, smaller or larger than the dynamical orbital scale. In our light curve modelling, we take into account and discuss the different time scales and are not restricted to a single period.

The flowchart is a tool for seeking for relativistic signatures, while we take into account both delayed light curves and flares that exhibit time lags. This tool leads us to the conclusion that if the two timescales are not close to each other, we can't discern between orbital

relativistic modulations and intrinsic flaring. Fortunately, this is most likely not a realistic picture anyway, as the expansion velocities of the plasma that cause intrinsic brightness modulations, are on the same timescale with the orbital motion of the plasmon around the black hole. This only means that there are chances for us to find relativistic signatures and orbital periodic signals amongst light curves that also exhibit time lags as evidence for expansion of the plasma. If we find for a possible orbital periodic signal in X-ray, for example that can be confirmed by close findings in infrared, a good validation of these results would be the evidence for the same periodic signal in mm/sub-mm wavelengths. If we separate the time delayed peaks from genuine candidates for orbital modulations, we are presented with the possibility to speculate that the 22-30 min patterns observed in radio are indeed orbital signatures. This phenomenological construct is based on the assumption that the plasmon expands on the orbital timescale.

We show on the chart that in all cases where we could have both of the timescales almost equal, we have the opportunity to search for general relativistic signatures. The presence of delayed peaks is crucial here, as these modulations are not candidates for lensing and/or Doppler boost signatures. In view of the current available observations at hand, our model can constrain the orbital period, using the plasmon model as a tool for finding candidate peaks for measuring the orbital period.

Our presentation is developed around the timescales that are required to understand the full picture of the flaring behaviour. We introduce the expansion timescale, the delay timescale between spot or plasmon formation and the onset of expansion, the flare timescale, the flare lifetime timescale, the cooling timescale, the injection/escape timescale (see Table 5.1).

Because of the various timescales we introduced, such as the cooling, injection, expansion, etc., further modelling of the synchrotron steady (not expanding) blob would be necessary in order to study the flaring characteristics in more detail, using radiative transfer constraints. The problem of the hot spot surviving for multiple orbits is strictly dependent on the cooling process. In the case of an expanding plasmon, the constraining parameters are already implemented, with the aim to obtain the existing time lags between observed light curves at various wavelengths.

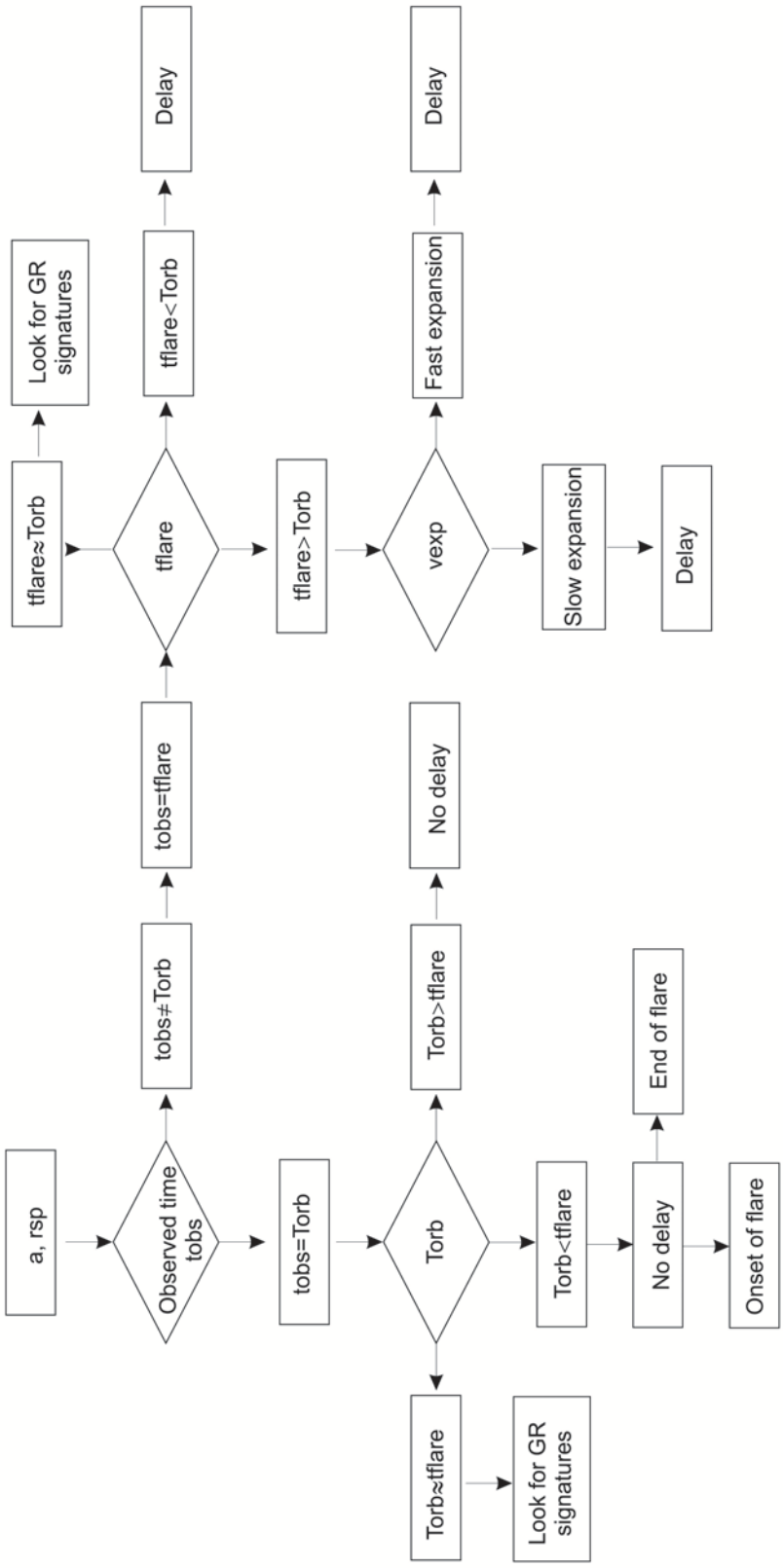

FIGURE 5.27: Flow diagram showing possible choices of the time scale of a light curve

Timescales used in the model:	Range
Orbital period	P
Flaring	$1P - 100P$
Expansion	$0.1P - 100P$
Phase displacement	$0.1P - 10P$
Injection	$0.5P - 100P$
Synchrotron cooling	$0.1P - 10P$

TABLE 5.1: Timescales used in our flare model.

5.5.2 Relativistic substructure of the light curve

The shape of the light curve holds information about the parameters of the black hole and the orbital motion. Nevertheless, some of these parameters, like lensing and Doppler shifts, leave their strongest signatures only on particular portions of the light curve. We search for relativistic signatures in Sgr A* light curves at sub-orbital scale. As we take into consideration all special and general relativistic effects, we are able to isolate each particular imprint in the light curve and separate it from other time-dependent flare characteristics that might affect the shape and sub-structure of the light curve.

We focus on the time dependent behaviour of the relativistic signatures, in particular the sub-flare structure in a light curve. As part of the modelling, we find that the flaring structure is partially caused by relativistic modulations exhibiting separate amplification peaks in the light curve. A sub-orbital relativistic picture is here assumed, considering that most relativistic effects may have a substantial influence on the observed emission from Sgr A* and should be taken into account when analysing the nature of Sgr A* flaring.

The properties of the light curve can be understood by analysing the different contributions of the flux, determined by the spin of the black hole, the geometry parameters, the size of the blob, the emissivity mechanism and the inclination angle. Using the current observational data, we make predictions based on our modelling setup, to provide constraints on Sgr A* flare emission. The unique parameters necessary to model the light curve are shown in the Table 5.2 and will be discussed later in this section.

Parameters:	Intrinsic peak		Relativistic peak
Rise time	$-1.5P - 1.5P$		-
Decay time	$1.25P - 1.0P$		-
Flux ratio	1-6	/	1
Phase displacement	-		$0.25 - 0.75C$

TABLE 5.2: Model parameters used in our flare simulations where P is the orbital period and $C = 2\pi r$ the circumference of the blob orbit.The maximum brightness is half time between the rise time and the decay time of the flare, for the intrinsic flux.

Some X-ray light curves show a double peaked bright flare in phase with the NIR brightest double peaked flares. The amplitude of the X-ray and NIR peaks are not equal but the basic skeleton of both light curves seem very similar. There is also a similar morphology between the radio and X-ray flares and the sub-structure of the light curves that will be analysed later.

Repeated patterns of 20 minute cycles in both IR and X-ray bands could be attributed to a hot spot orbiting the black hole, with an average orbital motion of 20 min. Most light curves contain several cycles of this average orbital period. The interesting fact here is that the period of $17 - 22$ min, already accepted as orbital origin, corresponds to the expected magnetic field of about 30 G, derived from the observed spectral index. It is quite possible, in this case, that the cooling of the hot electrons actually happens on the orbital dynamical scale and, while newly electrons are injected into the blob, the emitting source will continue to survive for a number of orbits, producing a number of superposed flares of about $17-22$ min. The evident question is: is this $17 - 22$ min periodic signal only an orbital signature of the emitting source, caused by Doppler beaming/boosting or gravitational lensing effects? Alternatively, is there another process (injection, heating, magnetic field fluctuation) that would interfere with the relativistic modulations at an orbital timescale?

Several bright X-ray flares exhibit a multi-peak substructure that could arise from a combined intrinsic flaring with relativistic effects that independently modulate the observed emission. The two or three peak sub-flare structure leads to a relativistic interpretation of an

approx. 20–22 min period, close to the QPO periodic signals previously found in NIR and X-ray wavelengths. The model for the sub-structure of the flare strengthens the previous claims for periodicity (including radio wavelengths) and subsequently suggests a correlation or common origin of the emission in X-ray and the NIR flare activity. Previously, the X-ray flare emission has been modelled as inverse Compton, self-synchrotron-Compton, or synchrotron emission. A possible X-ray scenario is the acceleration of highly energetic electrons that are responsible at the same time for the IR flaring. The main ideas that have been proposed are the up-scattering of sub-mm photons (Markoff et al. 2001, Yusef-Zadeh at al. 2006, 2008) or synchrotron self-Compton processes (Eckart et al. 2006a) as the emission originated either from the high energy tail of the accelerated electrons (Yuan et al. 2003, Dodds-Eden et al. (2009) or from NIR electrons (Eckart et al. 2006a). Yusef-Zadeh et.al. (2012) proposed that the X-ray flare emission is produced through the interaction of the quiescent and flaring components. The strong X-ray counterparts to NIR flaring that originate within the inner disk show no significant time delays, while the events in the outer disk will exhibit lower energy, broad and delayed X-ray flares.

The light curve is dominated by a first peak occurring when the spot is close to the primary caustic behind the black hole. This peak is followed by a secondary peak, depending on the spot distance, caused by the Doppler effect (see Figure 4.18).

A basic starting hypothesis is the presence of intrinsic flux signatures of the flare at orbital scale during the dynamic motion of the blob around the black hole, with a possible magnetic origin in the near vicinity of the ISCO.

The $\sim$ 20 minutes average timescale is comparable to the orbital timescale T near the ISCO:

$$T \doteq 110 \left(r^{3/2} + a_\star\right) \frac{M}{4.1 \cdot 10^6 M_\odot} \text{ [sec]}, \tag{5.18}$$

with $a_\star$ the spin parameter ($-1 \leq a_\star \leq 1$), and r is a orbital radius within the equatorial plane, in units of gravitational radius $r_g \equiv GM/c^2$. Any modulations under this scale are possible candidates for relativistic signatures and/or intrinsic variable emission of the flare.

For simplicity, at first we assume that the flaring period and the orbital period are equal, which means that a flare forms at the initial phase in the orbit and dies within one or multiple orbits. The relativistic orbital motion could generate separated peaks in the light curve. The

lensing peak and the flare peak wouldn't necessary coincide. The same concept applies to Doppler boosting effects. The search for relativistic signatures becomes a genuine search for orbital periodicity. If we choose this timescale to be almost equal to the dynamical timescale of the orbital motion, the blob may circle the black hole for more or less than an orbit but close to one orbit. The case of multiple peak scenario can happen especially if the timescale for the intrinsic flaring and the timescale of the orbital period are very close to each other. The magnitude of the relativistic flux modulation will increase with the emitting source inclination and will reach a maximum for the edge-on view.

As the synchrotron cooling occurs on scales close to the orbital timescale, it is plausible that the blob gets injected and starts cooling transiently on orbital scales. The blob is still able to survive for several orbits until the cooling process is finished and the initial event that triggered the injection process has completely stopped. While the $\approx$ 20 minutes scale suggests an orbital origin of the emission, close to the ISCO, additional components such as injection, synchrotron cooling and adiabatic expansion processes might contribute to the flare variability.

This fact is expected if an instability in the disk generates on a dynamical orbital timescale, a periodic injection into the blob, of new heated electrons. As the blob moves around the black hole, it cools down and while the cooling process is not finished yet, the blob gets injected on the next orbital period with more electrons, producing another 20 min flare, during one orbit. We assume the same relativistic particle distribution law that generates the intrinsic flaring as in 5.3, earlier in this thesis. In modelling the broad NIR flares, we assumed that the orbiting blob is gaining new accelerated particles, over multiple orbits. However, here the injection and cooling occur during one single orbital period. The blob gets fed with hot electrons every orbit. This recurrent re-charging process can cause the blob to survive for a number of orbits, until the injection process stops, together with the initial event that generated the continuous feeding of the blob with new particles.

Although the signature for the spin of the black hole together with the special relativistic beaming and the formation of high order multiple images generated by lensing effects seem

to be quite marginal in the light curves, they shouldn't be ignored at all. The current numerical resources are not sufficient to reproduce all relativistic effects in a realistic way and reveal accurately high order general relativistic images. Future simultaneous multi-wavelength campaigns and photometric measurements should provide more evidence and accurate data to be used for current studies of the temporal evolution of the expanding plasma in orbits close to the ISCO.

Apart from lensing/Doppler peaks, some of the observed substructures visible in X-ray/NIR/radio could be most likely caused by relativistic beaming on the approaching side of the blob orbit around the black hole.

The X-ray flare from Figure 5.28 and exhibits a clear 3-peak sub-flare morphology. The three peaks could be caused by gravitational lensing and Doppler boosting effects of the emission arriving from a blob that is injected with new electrons during one single orbital period. The middle peak corresponds to the gravitational lensing signature, whereas the last peak is generated by the transverse Doppler effect.

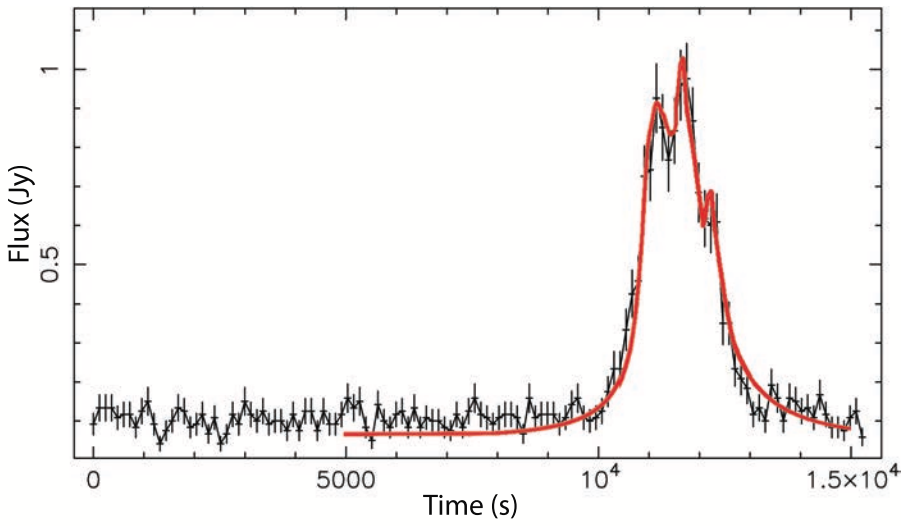

FIGURE 5.28: Theoretical modelling of the X-ray light curve from 2002 October 3 observation.

The spectral index of the flare emission alters the shape of the light curve. This modulation of the flux gets combined with the relativistic signatures and further leads to significant

changes in the light curve. A modification of the observing range of frequencies used, therefore of the Spectral energy distribution (SED) of the emission is also crucial in understanding the shape of the light curve. The Doppler effect will shift the emitted radiation, ultimately leading us to actually observe different parts of the SED every moment in time. When the flare is approaching the observer, the emission becomes blue-shifted. If the emission behaves as a red or blue SED, the emission that reaches the observer will be higher or lower, respectively. A red SED with $\alpha < 0$ will brighten the emission on the approaching part and therefore will increase the beaming signatures whereas on the receding side, the emission will be dimmed. A flare following a blue SED, with $\alpha > 0$ will have the opposite behaviour. The flux will not be modified in any way by the Doppler shifting, if the SED is white or $\alpha = 0$.

Due to the Doppler effect, the observed flux will relate to a different rest frame frequency for different orbital phases. A curved spectrum is expected from a synchrotron model. If the source spectrum is curved, the flux distribution and the spectral index seem to be correlated. The flux from the brightest part has a rest frequency with a larger spectral index than the dimmer flux from shorter wavelengths. The light curve peak rises with decreasing spectral index. If we assume an overall blue SED, the observed flare emission on the approaching side will become very diminished so that a secondary lensed image of the flare will be exposed. The flux should be higher than the flux of the primary image for a very short time. If we assume an overall blue SED, the original flux peak will become very narrow and will increase in brightness. In this way, the secondary peak will arise slightly before the flare actually arrives on the approaching side. The multiple image lensing effect is stronger if the flare has a red SED, because the flux of the first image will get diminished more substantially on the receding side. The flux of the secondary lensed image will be more substantially amplified on the approaching side. The light curve in the case of a blue SED flare looks more symmetric and shows less relativistic signatures.

If the flare orbits in the anticlockwise direction, the point of maximum blue shift occurs just before the flare reaches the closest point to the observer $\phi = 0$ as the gravitational lensing gets beamed in the forward direction of the emitter and is also bent towards the observer at the same time. Gravitational lensing causes strong magnification of the emission region

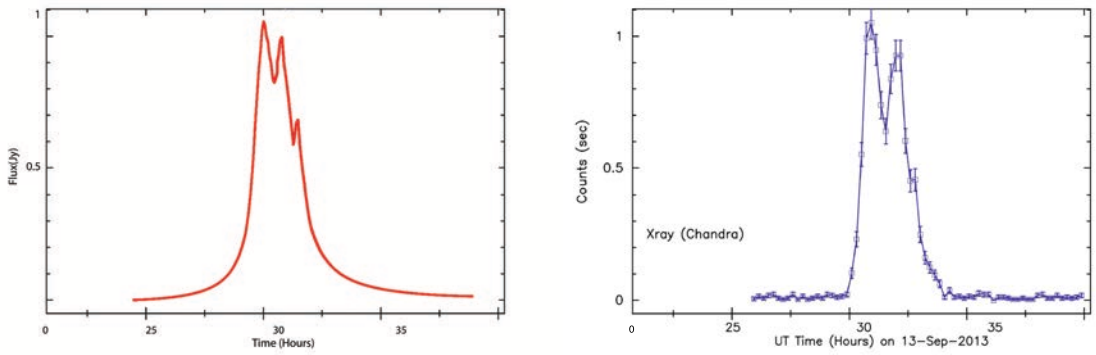

FIGURE 5.29: An X-ray light curve observed in September 2013 (Yusef-Zadeh et al.) consistent with a theoretical relativistic light curve (right) of a compact hot spot orbiting a Kerr black hole with spin $a = 0.3$, for $\theta_o = 75°$. The blob is located at $r_{sp} = 4.5GM/c^2$ and it is injected with particles during one orbital period. The three peaks of the simulated flare represent the intrinsic flare peak, the lensing peak and the Doppler blueshift on the approaching side on the latest part of the light curve.

when the flare is located on the far side of the black hole, and spreads its primary image into an extended arc. Due to the relativistic Doppler shift and beaming effects, the approaching portion of the blob orbit will appear much brighter than the receding portion. The modelling of the X-ray flare observed in September 2013 (Figure 5.29) shows a 3-peak sub-structure of the light curve: a first intrinsic flare peak, caused by the injection of fresh particles, the gravitational lensing peak and the transverse Doppler effect on the approaching side of the disk. The same model was applied to the similar light curve of the October 26, 2000 X-ray flare (Figure 5.30) but with a smaller number of particles that get injected into the blob, exhibiting a lower amplitude peak than the flux modulation generated by the gravitational lensing effect. The presence of the Doppler transverse effect is evident in all discussed X-ray light curves.

As long as the sub-flare characteristics are caused by relativistic signatures, a strong similarity in the sub-structure of the NIR and the X-ray light curves is expected, together with the same flux ratios in beaming or lensing signatures. It is also possible that the new particles that get injected might exhibit a different behaviour in X-ray and NIR. If the new injected electrons are seen in X-ray, cooling rapidly, the same particles might cool much

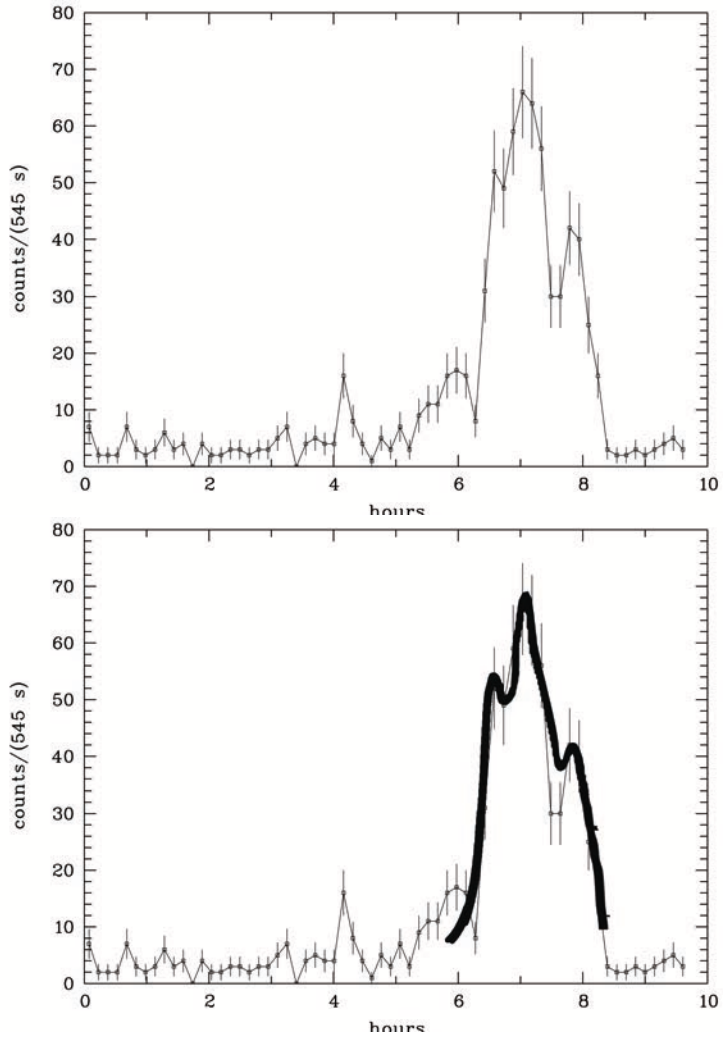

FIGURE 5.30: **(a) Left** ACIS-I light curves of the Chandra observation of October 26, 2000. **(b) Right** Theoretical light curve fitting the October 26, 2000 X-ray flare.

slower as part of a bulk motion observed in NIR. The same effect on the light curve as the injection could be generated by changes in electron acceleration or variations in the magnetic field.

Our analysis makes predictions on possible future measurements of Sgr A* emission and requires accurate data for revealing theoretical signatures modelled by our light curves. The asymmetric structure present in the observed light curves may be caused by relativistic effects, showing evidence of clumping flaring material present on scales within a few tens of Schwarzschild radii from the black hole.

We look for similarities, patterns and recurrent ratios in the observed light curves at

various wavelengths. The search for a patterned sub-structure in the flares is motivated by our intention to understand the origin of the Sgr A* variability. We find that the flare events occur quite close to the ISCO and provide strong constraints and a significant insight into the nature of the inner accretion flow. The existing rapid modulations in the flare emission favours such a picture. We interpret the sub-flares of 20 minutes average duration, superimposed on the wide flare, as being due to orbital relativistic signatures of synchrotron emission from a blob that orbits the central SMBH. The intrinsic blob emission could be due to transiently heated and accelerated electrons. The variations in the sub-flare amplitude together with the time separation between the peaks can be explained using such a model. Different variations are possible for stronger modulation of the blob brightness or starting phase of the expansion process. We will also apply this sub-orbital relativistic picture to the modelling of NIR and radio light curves. Our sub-orbital picture accounts for the different short timescale variability in NIR and X-ray bands. Additional future simultaneous observations at different frequencies become necessity, in order to confirm the predictions of our modelling.

5.5.3 Relativistic modelling of NIR and radio flares

The motivation of the work here is to develop a model that explains the multi-peak sub-flare structure in Sgr A* light curves. Subsequently, the model is expected to offer a possible explanation for Sgr A* variability in multi-wavelength bands. As we know, all relativistic effects become important close to the inner edge of the accretion flow, making significant contributions to the full shape of the lightcurve itself. We consider all relativistic effects from a localized emitter in the form of bright, continuum emitting hot spot in orbit around the black hole. Such a bright region produces a time-varying signal that can reveal valuable information about the environment of a black hole.

We are looking for relativistic signatures in the light curves and subsequently we take into account all relativistic effects. We target periodic signatures in the light curves and consequently possible links between changes in the peak flux and light curves. In order to provide a realistic picture, we consider Doppler beaming, multiple high order images, gravitational lensing effects and Doppler shifts. We find that in each flare the sub-flares are

generated by flux density contributions of a single blob in orbital motion around the black hole and eventually eliminate the multiple blob hypothesis.

The light curve could be the result of a single flare that dominates the emission for a few orbital periods. The modulations in flux could be also caused by a number of different spots with individual lifetimes that are shorter than one orbital period close to the last stable orbit. If a blob would expand within the disk or cause a short outflow above the accretion disk, the quasi-periodic emission is smeared out. It is possible, in this way, to not be detected at lower observing frequencies.

By assuming that the observed flux variations could be dominated by the orbital motion of the emitting source, the timescale therefore the orbital period is determined by the orbital radial location of the source and the black hole angular momentum. On the other hand, the magnitude (amplification) of the flux variations increases with the spot inclination reaching its maximum for the edge-on view. The light curves for the orbiting expanding plasmon model are calculated under the assumption that the blob remains confined, i.e. to first order preserved in strength and extent, for several orbital periods.

We analyse the relativistic signatures for emission from a small blob in prograde orbit close to the ISCO and produce theoretical relativistic light curves containing both relativistic effects and intrinsic emission with sub-flare characteristics. Combined with the special and general relativistic effects, we are able to place strong constraints on the possible size of the blob, luminosity, orbital period, expansion speed (for an expanding plasmon) and black hole parameters (disk inclination angle and spin). The discrimination between different types of peaks that can appear in an observed light curve, gives us the opportunity to diagnose the nature of the emission and, depending on the relationship between the two timescales (which one is longer/shorter), to constrain a number of plasmon parameters (like expansion velocity of the plasma, optical depth), orbital parameters (the orbital period being the imperative one) and ultimately, the spin of the black hole. We show that the flare emission can be described by the simple combination of a synchrotron spot model followed by an adiabatic expansion of the source components, with intrinsic flaring ocurring on orbital timescale, where relativistic effects could equally count for multiple peak substructure in the light curve.

For multiple frequency modelling of an expanding plasmon within the disk, the particle

spectral index and the expansion speed v parameters are introduced. The observables for a typical light curve at a frequency ν_0 are the timing t_0 of the flux, the magnitude of the peak flux, S_0, the particle index p and the expansion speed in units of R_0 per unit time, causing the asymmetry and width of the flare in the light curve, together with the background level or the quiescent flux that can slowly vary over the course of the flare.

The emitting source is fixed by the index p which determines τ_0. The minimum and maximum energy values are assumed to be E_{min} = 1 MeV and E_{max} = 100 MeV. We also assume equipartition between the average magnetic field and total relativistic electron energy. The magnetic field and electron density are calculated from the optical depth and size of the emitting region.

Our model assumes that the both radio and NIR emission is synchrotron emission from relativistic accelerated electrons moving close to the ISCO. The radio broad flare produced by the plasmon emission is an effect of the optical depth, whereas the NIR flare is caused by the heating and acceleration of electrons.

A blob of plasma of initial radius R_0, filled with relativistic electrons, remains constant in size for a specific time and starts to expand at time t_0. The number density n_e is uniform. To model the plasmon, we picture the electrons distributed in an energy power-law ($dn_e/dE = k_e E^{-p}$, $E_{min} \leqslant E \leqslant E_{max}$). The blob is surrounded by a magnetic field B.

For illustration purposes, we consider various scenarios of an expanding blob orbiting the black hole, starting to expand before t=0. The light curve starts with the blob already expanding and peaks, due to a maximum flux in the intrinsic emissivity of the plasmon, before the source passes behind the black hole. The gravitational lensing peak, combined with the Doppler boosting peak appear later as a second modulation in the light curve, with less than a quarter of an orbit phase difference. It is possible for the blob to not expand from the beginning of the orbit and this fact will introduce the phase displacement. The blob may expand during one single orbit or close to one orbit, which will create multiple peak structures in the light curve, at a sub-orbital scale, or expand over multiple orbital periods. The sub-orbital scale, the shortest scale that we use in our model is going to be employed again, when we assume a plasmon expanding on orbital timescale. The flux modulation caused by the optical depth due to the expansion process, can be disentangled from the rest

of the sub-peak structure caused by orbital relativistic modulation.

The phase displacement timescale relates to the delay between the appearance of a steady orbiting blob and the moment when the blob starts expanding. The phase displacement is important to locate and identify the sub-peaks in the light curve. We use the terms "expansion timescale" to refer to the adiabatic expansion of the plasmon, and "flare timescale" to refer to the full lifetime of a flaring event.

Before the flare starts to modulate its internal flux, it is possible to orbit the black hole a number of times, producing, on the same time scale, a lensed image just after it passes the far side of the black hole. If we assume a simple orbiting hot spot, the cooling time of the flare might constrain the blob to complete no more than one single orbit. The hypothesis of a hot spot combined with an expanding synchrotron blob is eliminated if the blob doesn't last sufficiently long enough to orbit the black hole more than once and generate multiple peak structures in the light curve. The constraint is here imposed by the orbital period.

To apply the plasmon model, we have two constraints that should be taken into consideration: the plasmon lifetime is determined by the cooling process and the expansion velocity determines the flare duration. We also have to consider that the number of particles within the blob is not necessarily constant at all times and there could be an injection of particles at a specific time, especially if we need a longer cooling time of the blob (if the blob has to last for a longer time) or contrariwise, a loss of particles escaping from the accretion disk in a jet or wind. In both cases, we could deal here with a change (increase or decrease) in the intrinsic flux of the flare. The expansion of the blob brings different time delays for the radiation from different parts of the spot so the onset and the fading of the flare emission are slightly different for an expanding plasmon instead of a steady spot. There is still an additional constraint that has to be taken into account: the size of the flare itself. We plot light curves for different sizes of a spot around an extreme black hole and find that, as expected, for a very large size of the flare, most of the distinguishable relativistic signatures are lost and the amplitude of the flux is highly amplified. As long as we keep the source size within $1GM/c^2$ (we get the best effects for a source of $0.2GM/c^2$), we can expect that the relativistic imprints on the light curve would be easily detected and isolated.

For Sgr A*, the orbital time scale close to ISCO is between 3.7 min and 27 min for

orbits around extremely rotating and non-rotating black holes, respectively. The viability of a model that combines a hot spot with an expanding blob requires that the synchrotron cooling time scale to be larger than the orbital period, for the hot spot to last long enough to introduce the plasmon scenario as well.

The fact that a single component adiabatic expansion model cannot account for the observed sub-mm/mm light curves, the considerable spread in source parameters (brightness, size, spectral index, sub-mm turnover frequency) as well as the presence of a long term variability (on scales of more than one or a few days) indicate a low level activity in addition to the presence of repeated individual bright flares. A two phase model, consisting of an initially steady synchrotron blob and an expanding plasmon is necessary here. The peaks generated by the expansion process are expected to exhibit time delays in the light curves, whereas the rest of the peaks shouldn't show any time lags. As the initial steady blob gets injected with new electrons, we should be able to see a large broad change in brightness (set by the injection timescale). The injection timescale should be very close to the new adiabatic cooling timescale of the plasmon newly formed. We already found (5.3) that the broad NIR timescale of 100-140 min can be modelled as a slow injection of fresh particles into the blob. The blob starts expanding on the same timescale, a fact confirmed by observed light curves in radio wavelengths.

We should be able to see two peaks, one caused by a lensing effect from a previous orbit of a synchrotron blob and a later peak caused by the intrinsic variability of the expanding flare.

We introduce a new parameter: the brightness ratio between the intrinsic flux of the confined spherical emission blob region and the peak flux created by the extended arc independently formed by lensing and boosting effects. Another parameter introduced in the model is the phase displacement between the phase where the plasmon peaks and the phase where the relativistic modulation reaches its maximum flux, caused by the steady blob or by the plasmon itself. While the brightness ratio parameter doesn't affect the orbital period measurement in any way, the phase displacement between the peaks does.

The arrangement of the source components in the phase disk, on the orbit, provides a set amount of lensing amplification and Doppler boosting relative to the second component

of intrinsic emissivity. We try different arrangements in the disk, at different relative phase displacements and different brightness ratios between the two components.

Motivated by the fact that some of the existing observational data show evidence for a spot evolution within the relativistic disk and the existing light curves exhibit flaring sub-structure, we assume in our model two types of amplification component, showing separated peaks in the light curve: relativistic amplification and intrinsic brightness of the flare. We further assume the flare starting to expand (after orbiting the black hole for a set time, with constant brightness) at a specific orbital phase in the accretion disk, which we can freely choose, as a new constraining parameter of the model.

For each of these set positions within the orbit, the flux density distribution within the disk can be take different values. This means that we can have an intrinsic flare of a higher or lower amplification than the peak formed by relativistic boosting or gravitational lensing effects. Different orbital phase shifts between the positions of the flare within the disk will result in different time displacements between the peaks within the light curve. The peaks are distinct and separated at various time intervals in the light curve, depending on how close the intrinsic flux will reach its maximum relatively to the lensing/Doppler modulation. The Doppler redshift only makes a small contribution of smoothing the light curve together with the effect of broadening the receding wing of the light curve. Figures 5.31, 5.32, 5.33 and 5.34 show simulations of such expanding blobs, with distinct locations of the maximum intrinsic flux in the orbit, affecting the sub-structure of the light curve in a different way. All Figures show peaks caused by expansion, lensing and Doppler shift occurring at distinct orbital phases. The order of the peaks and their significance is detailed beneath each Figure.

The model assumes two separate scenarios:

A The first scenario assumes a compact hot spot or a flare of constant flux and size orbiting the black hole on a keplerian orbit, on a dynamical time scale close to the orbital period. After a set time, due to an energetic event, like the injection of new particles, an instability in the disk or a fluctuation in the magnetic field, the blob starts expanding. The heating/cooling process has its own life cycle and it can be characterized by a rise time and a decay time of the flare. The three components of the model are the orbiting

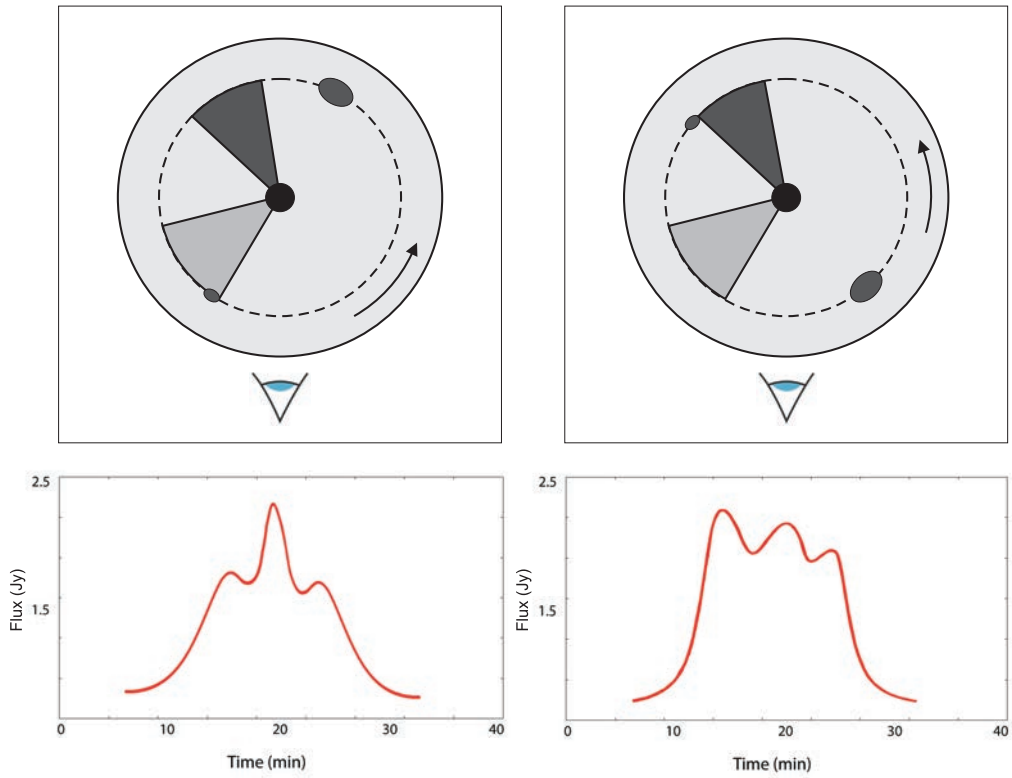

FIGURE 5.31: (Left) Diagram of an expanding plasmon orbiting a rotating extreme black hole (Top) and the light curve (Bottom). The diagram shows a dark lensing area and a light shade Doppler boosting area. The small spot shows where the plasmon starts to expand, whereas the larger spot shows the maximum intrinsic peak flux. The light curve shows (in order, from left to right) a peak caused by expansion (i), lensing (l) and Doppler boosting (b) for $i < l$ and $l > b$.(Right) Diagram and light curve for $i > l$ and $l > b$.

spot phase, the expansion phase and the relativistic effects that generate independent orbital motion modulations in the observed flux. The model can be applied to multiple wavelength bands, comprising both hot spot model and the expanding plasmon models. In this way the model covers both simultaneous and time delayed light curves. The lensing and Doppler blueshift effects, associated with orbital motion, could be produced by the expanding blob or by a hot spot not yet expanding.

B The second scenario proposes an adiabatically expanding plasma blob that starts expanding from the beginning. The flux modulates intrinsically and in general peaks at

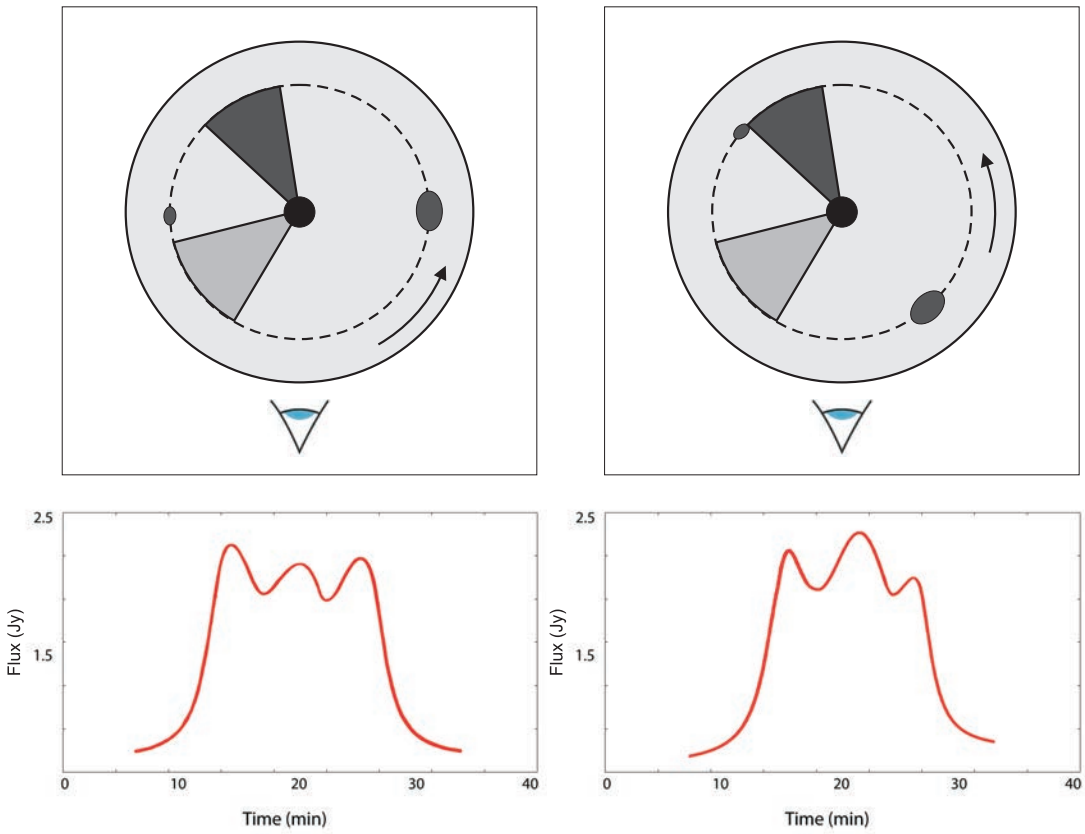

FIGURE 5.32: (Left column) As in Figure 5.31, for $i > l$ and $l < b$. (Right column) Diagram and the light curve for $i < l$ and $l > b$.

a different phase within the orbit than the orbital modulation.

The flare peaks and just after it passes behind the black hole, the lensing peak is also formed, at only a few minutes difference from the first peak. The blueshift peak is formed on the approaching side as the flare is almost reaching the closest location to the observer. Figure 5.35 shows flares produced by different initial size blobs, showing various intensities of the intrinsic flux, blending with neighbouring peaks formed by relativistic signatures. The model is based on the primary assumption that the two time scales (intrinsic and orbital) are close to each other. For simplicity reasons, we assumed the two timescales being almost equal and seek various types of peaks in the light curve, due to both expansion and relativistic effects. In Figure 5.36, we illustrate the different timescales used in the modelling.

The timescale of about 20 minutes, assumed to be the orbital period, suggests orbital

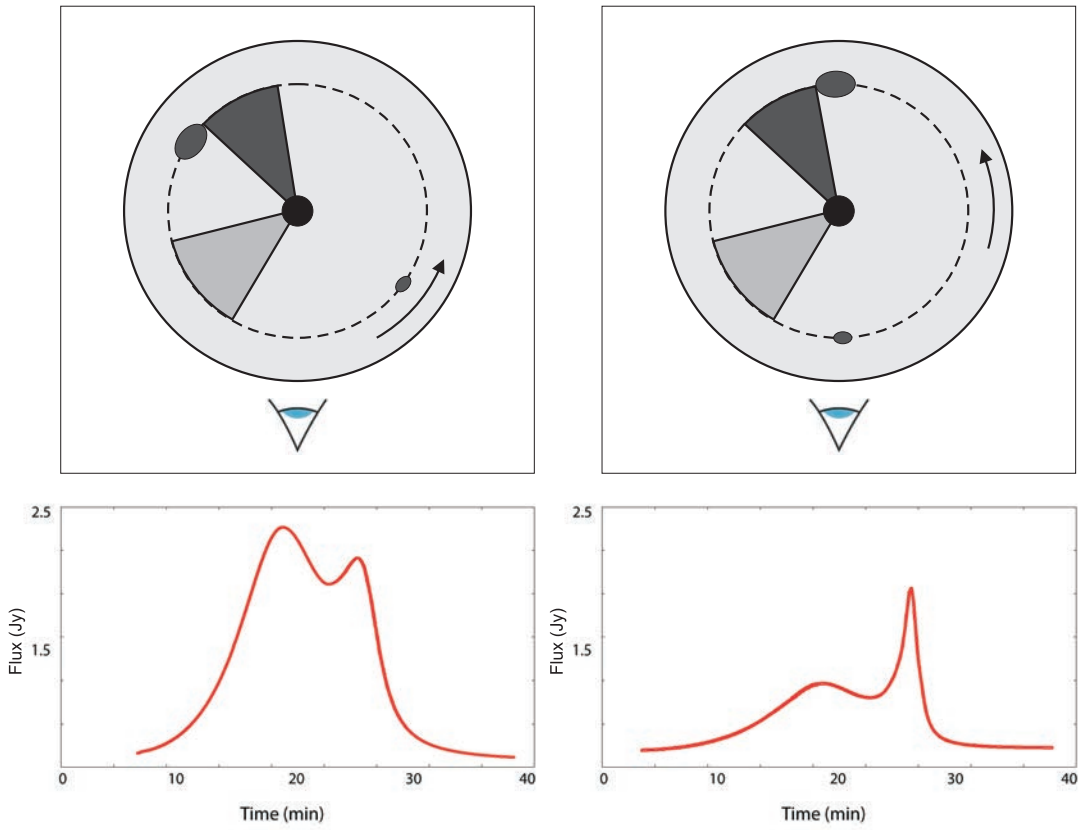

FIGURE 5.33: (Left column) As in Figure 5.31. In this case, there are only two peaks in the light curve $i+l > b$. (Right column) Diagram and the light curve for the two peak case where $i + l < b$.

motion very close to the ISCO. This timescale can be also found in X-Ray and radio wavelengths, endorsing the fact that indeed it describes orbital motion. Any radiation produced propagates through strongly curved space-time. By the time we include multiple images, Doppler shifts, beaming effect, gravitational lensing, we attempt to eliminate the 20 minute period as being produced by the flux variation of the flare. The model predicts that this period, if it has an orbital origin, will not generate any time lag when observing/simulating the same flare at a different frequency. In the model, the presence of a time lag provides evidence of intrinsic flaring caused by the expansion of a self-absorbed source. The similarity between the flare timescales in NIR and the mm/sub-mm suggests that the energy loss processes are not dominated by radiative cooling but adiabatic expansion.

We argue that the entire X-ray/NIR flare is delayed towards sub-mm/radio frequencies

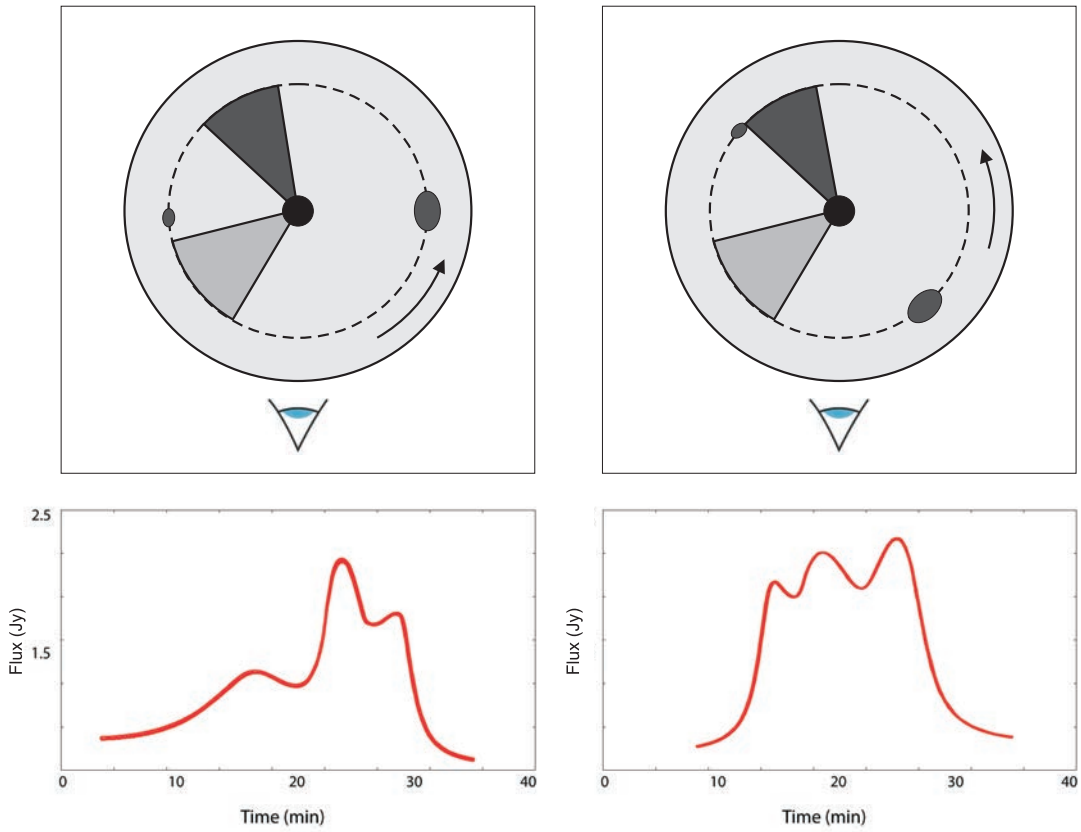

FIGURE 5.34: As in Figure 5.31 for $i < l$ and $l > b$. (Right column) Diagram and the light curve for the case $i < l$ and $l < b$.

but some characteristics in the substructure of the flare remain preserved: the brightness ratio between the sub-flare characteristic flux peaks is conserved, together with the phase ratio (or phase displacement, on the blob orbit) between the individual sub-flare peaks. We notice both features when we stretch the NIR or X-ray flares to match the radio light curve and obtain similar brightness ratios and time ratios. The typical duration of a broad NIR flare is 100-140 min whereas the radio flare lasts about 1-2 hours. The stretching of the NIR light curve can be seen as a simulated expansion of a compact blob initially observed in NIR and being followed by the expansion of a plasmon emitting at radio wavelengths. The stretching factor applied to NIR flare was selected to match the radio light curve, keeping the ratio of the observed durations.

Both plasmon model and the orbiting spot model are considered as possible scenarios in

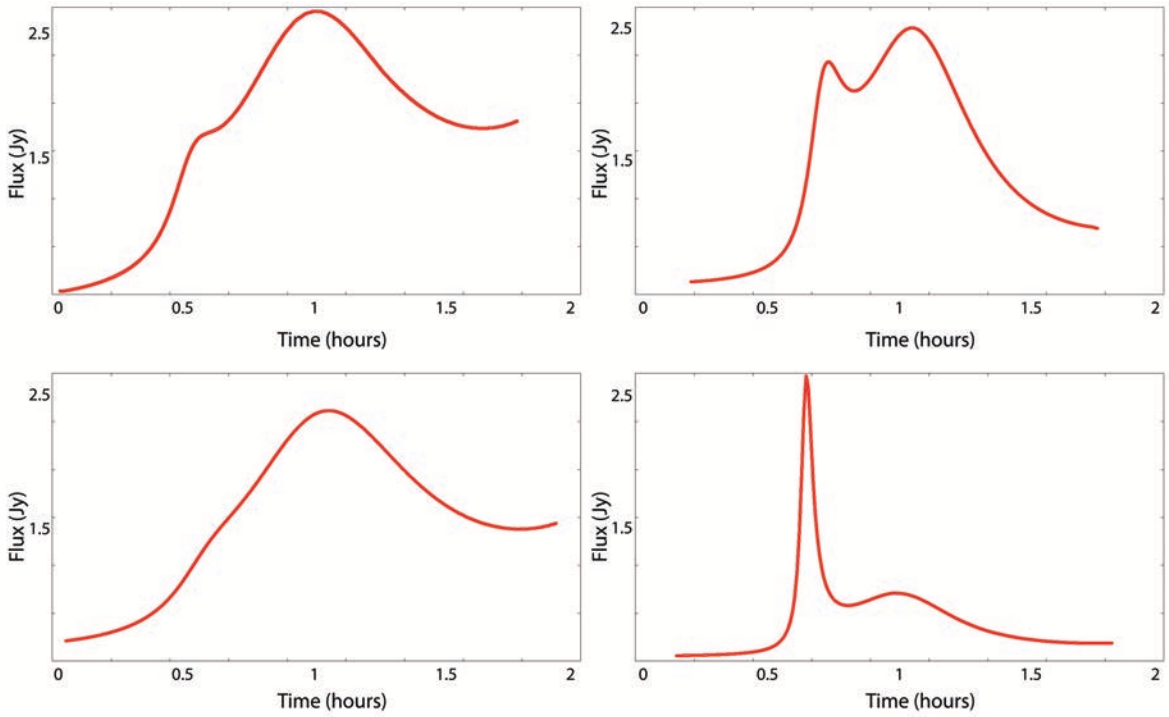

FIGURE 5.35: Theoretical modelling of a flare that expands during one and a half orbit. The flare starts expanding before the starting phase of the light curve. In all cases, the flare peaks before is passes behind the black hole. The first peak (in order, from left to right) is formed by the intrinsic emission of the plasmon. The second peak is caused by the lensing/Doppler effect. The flare brightness is different in each panel. The flare timescale is close to the orbital timescale

the model, while the time lag between different observing frequencies can help distinguish between them. The adiabatic expansion process, combined with all relativistic effects and the possibility to have a constant size hot spot orbiting the black hole, before the expansion starts, can explain the overall characteristics of the flare emission in multiple wavelengths. The time delays found are consistent with the adiabatic expansion of a self-absorbed source. If we consider these features through the prism of our model, the peak that is delayed (the main large flare structure) is not a candidate for an orbital motion event, whereas the sub-flare peaks seem to represent characteristics that reminisce the common relativistic signatures

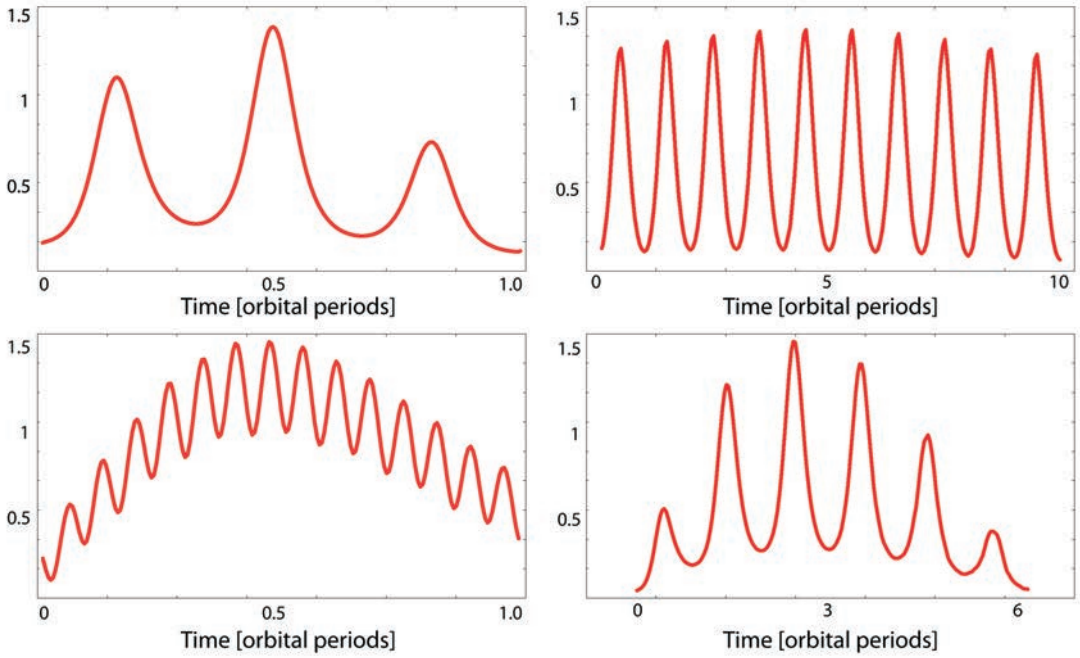

FIGURE 5.36: (Left, top) Modelling of a single blob with variable intrinsic emission, superposed over a broad orbital light curve. The intrinsic variability timescale is shorter than the orbital timescale.(Left, bottom) Modelling of orbiting multiple blobs that last a fraction of the orbit, superposed over a broad orbital light curve. (Right) Modelling of a blob that expands during multiple orbits (top), respectively 6 orbits (bottom). The expansion and cooling timescales are longer than the orbital timescale. The broad light curve is given by the blob expansion.

within the amplification light curve of a blob in orbital motion around the black hole (lensing and Doppler effects). We shifted and stretched the light curve in order to display more prominently the substructure of the flare and the ratios we are interested in. A close comparison between the 43 GHz flare and the NIR light curve clearly suggests that the two emissions are closely related with each other. A similar shift/stretch was also used by Yusef-Zadeh et. al. on the same flare to suggest the time delay between light curves at the two frequencies and show the duration of flare as it evolves in time.

We carried out the time-shift and time-stretch operations, obtaining a zero time lag between radio and X-ray data and same substructure (patterns and flux ratios) of the light

curves, in order to propose a strong correlation between the flares. The stretched light curves contain most characteristics and substructure features as their counterpart, suggesting a common origin of the two events.

Continuous hourly timescale radio variability hinders the identification of the relevant matching radio flare counterparts for the NIR light curves. Figure 5.37 shows composite VLA, VLT, HST and XMM light curves from 2007, April 4. The radio flare recorded between 10h and 15h UT is a possible matching delayed counterpart of the NIR/X-ray flare. The main morphology of the flares exhibit a rise in the flux amplitude, with a number of smaller peaks, followed by a flattening of the emission. The stretched light curve exhibits similar features with the radio light curve, including the relative flux ratio between the 3 peaks in the flare, as we can see in Figure 5.38. The observed emission at 43 GHz is the time delayed matching flare with respect the NIR/X-ray flare. The similar features seem to conserve when changing from an optically thin regime (X-ray/NIR) to the optically thick radio band. The most interesting fact here is that we notice the same 3 peak substructure in the flare in several occasions: both X-ray light curve from 2002 October 3 and the September 2013 X-ray flare exhibit 2 bright peaks and a third peak of much smaller amplitude, which we argue to be caused by Doppler blueshift effect on the approaching side of the blob orbit. The flare observed during the 2006 July 17 campaign shows also very similar characteristics to the other multiple peak X-ray light curves.

The model explains the sub-flare structure for NIR emission, showing that in the X-ray band, the substructure of the flare has a very similar shape and when stretched, the X-ray flare seems to overlap the NIR flare, showing very similar patters of close durations and flux ratios between the sub-peaks. We show the overlaid X-ray and infrared flares in Figure 5.37. We assume that the synchrotron emission from transiently accelerated particles can explain the NIR lightcurves. The NIR and X-ray flares provide enough evidence of strong correlation between the two types of emission with no visible time delay. A strong NIR/X-ray flare was detected on 2007, April 4 exhibiting a main peak at 5.9h UT with a duration of about two hours in NIR.

The NIR/X-ray emission from 2007, April 4 can be used here to relate the optically thin emission with the flaring at radio wavelengths. An optically thin NIR flare with a shorter

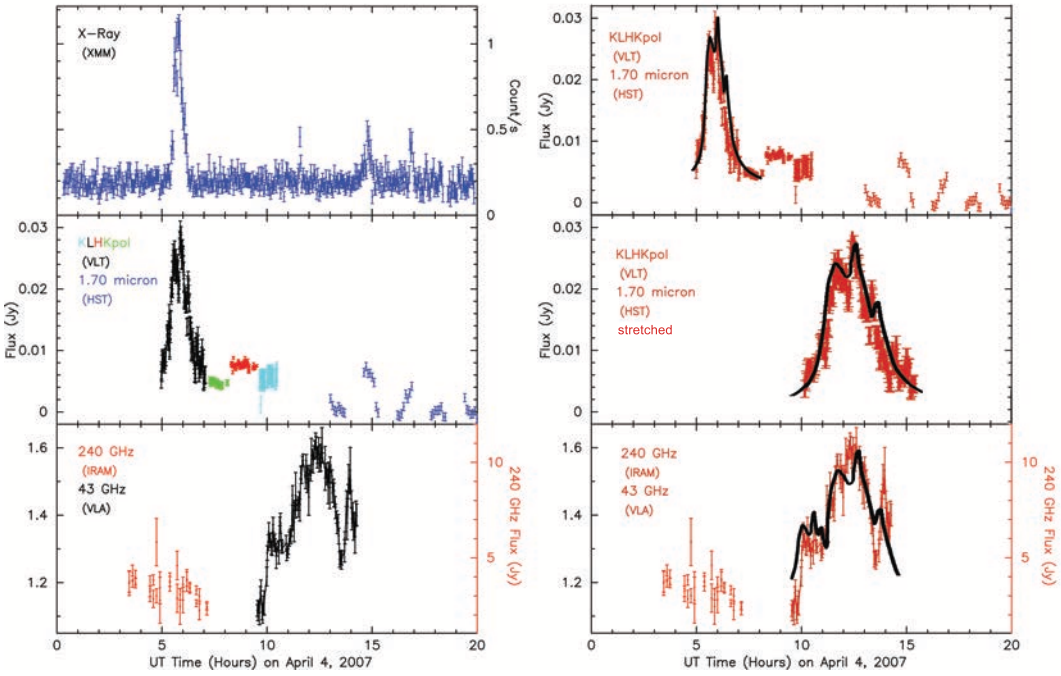

FIGURE 5.37: (Left) Sgr A* light curves from 2007, April 4 obtained with XMM in X-rays (top), VLT and HST in NIR (middle) and IRAM-30m and VLA at 240 GHz and 43 GHz (bottom). The NIR light curves are shown in red, K_s and K_s-polarization mode in green and blue, L' in black, and NICMOS of HST in blue. In the bottom panel, red and black colors show the 240 and 43 GHz light curves. (Right) The top panel shows the NIR light curve and the modelled light curve superimposed, the middle panel shows the NIR light curve shifted by 6 hours, stretched by a factor of 2.5. Superimposed it is the simulated light curve. The bottom panel shows the 43 GHz light curve with the superimposed simulated light curve.

lifetime is expected to have a radio counterpart shifted later in time with a longer lifetime. As there is (almost) no time delay between the NIR and X-ray flares, it is possible to consider a radio counterpart for an X-ray light curve. In Figure 5.38, the stretched NIR light curve seems to have most characteristics and sub-structure shape features of the radio flare, suggesting a strong correlation between the two events. In Figure 5.39,the X-ray light curve was stretched by a factor of 3.5 and shifted by 5.25 hours, to match the NIR light curve.

The duration of a flare at 22 GHz is about 2.5 hours and at 43 GHz is about 2 hours. If from the opacity law we extrapolate a light curve corresponding to NIR wavelengths, we

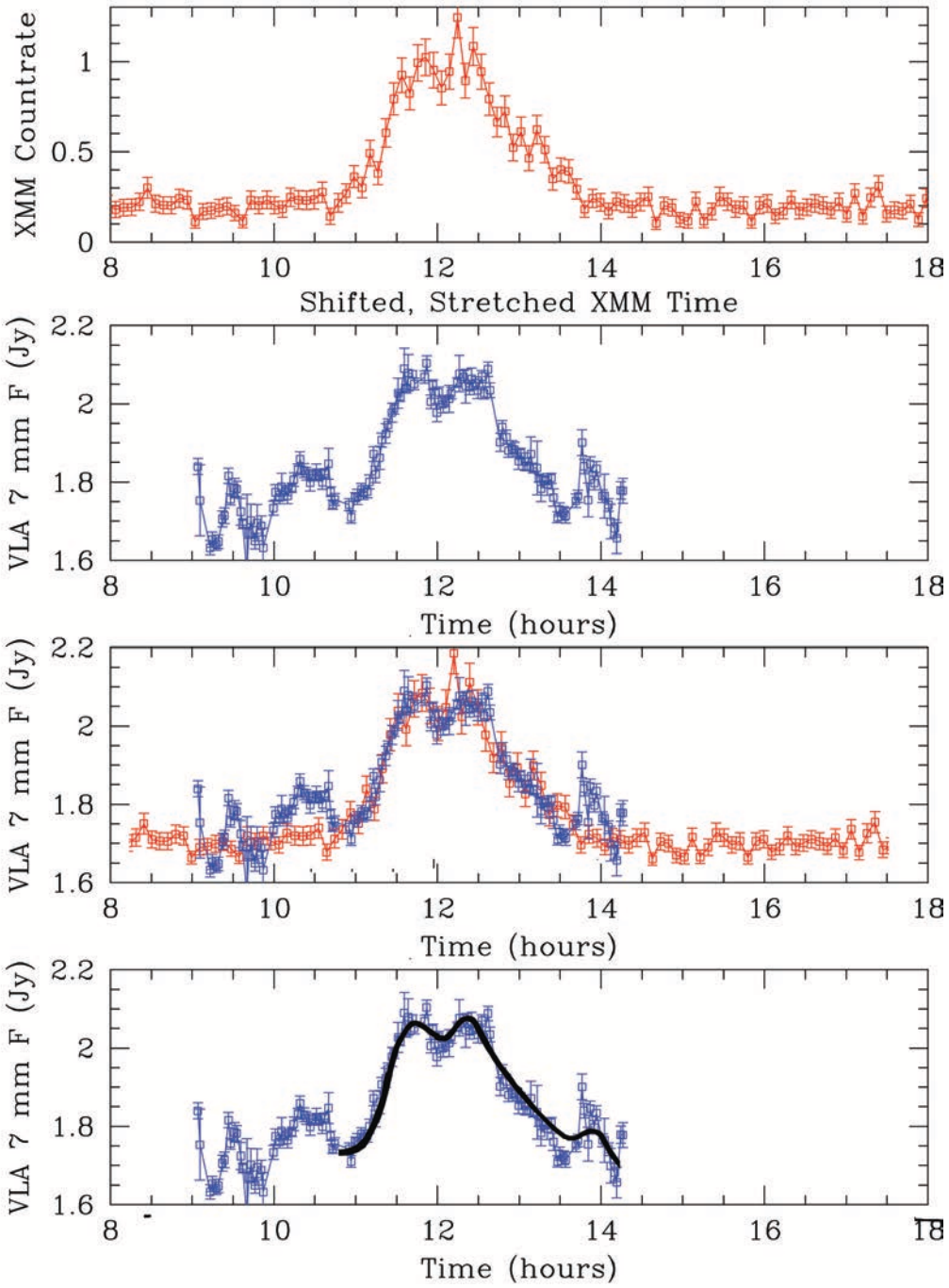

FIGURE 5.38: The top picture shows the XMM data from 2007, April 4, the second panel shows the VLA flare at 43 GHz. The X-ray light curve is shifted by 6 hours and stretched by a factor of 2.5. The two bottom panels show an overlap between the two light curves and the theoretical modelling of the VLA flare.

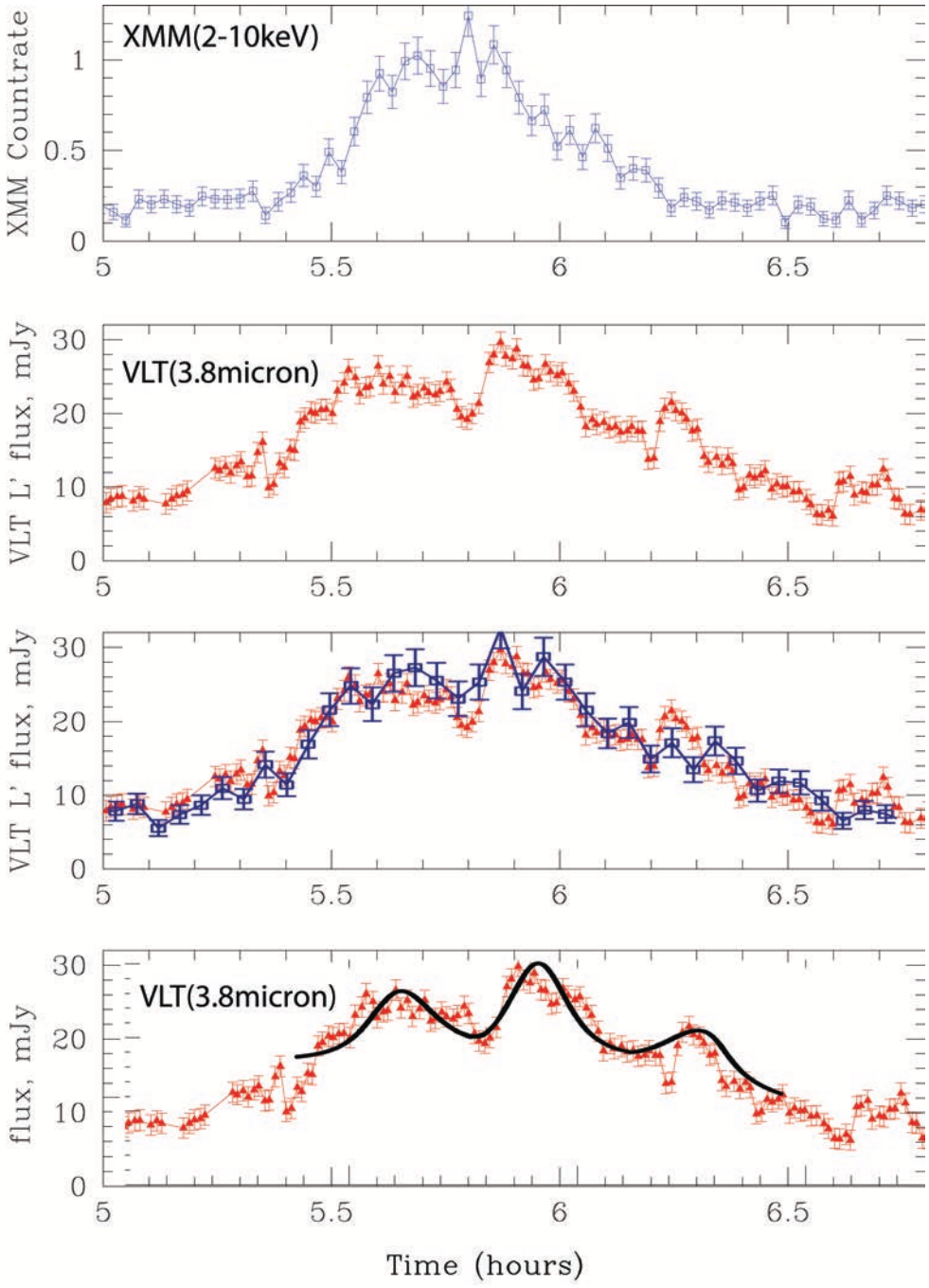

FIGURE 5.39: The top and middle plots show the X-ray and NIR light curves taken on 2007, April 4. The X-ray light curve was shifted by 5.25 hours and stretched by a factor of 3.5. The bottom panel shows the first X-ray light curve that has been stretched and superimposed over the second NIR light curve.

obtain a flare that lasts about 1.5 hours, which confirms many NIR observed flares with durations of about 120-140 min. The broad radio flare shows clear time lags when simulated and observed at different frequencies. The change in flux is controlled by the changing optical depth of the intrinsic emission of the self-absorbed plasmon. As the broad NIR flare is optically thin, we must eliminate that the change in flux is dependent on the optical depth. Consequently, we assume that the broad NIR 100-140 minutes average duration flare is generated by the injection of new particles in the blob. As new accelerated electrons are included in the blob, the flux amplitude slowly increases and eventually the blob starts expanding on the same timescale, beginning to show time lags at lower frequencies. In NIR, the cooling is radiative via synchrotron emission, causing the flux distribution to vary on timescales of 100-140 minutes, whereas during the expansion, the cooling is done only through adiabatic processes.

A number of flare scenarios or sub-models contribute to our final picture:

(1) the extended synchrotron spot model (synchrotron steady blob and expanding plasmon)

(2) the particle injection model (multi-orbital scale)

(3) the sub-orbital relativistic model (includes expansion)

If we assume a connection between the NIR flare and the radio event, based on close timescales of the observed broad light curves and close patterns of the flare sub-structure in both NIR and X-Ray, we can extrapolate the existence of the same orbital peaks, as found in NIR and X-ray. This hypothesis can be applied to the 22 GHZ and 42 GHz flaring and assume a sub-structure with orbital origin (see Figure 5.21). We propose 5 orbital periods, as the 2007 NIR flare shows 5 orbital periods during a 100-120 minutes time window. By extrapolating to a 2 hours 43 GHz and a 2.5 hours 22 GHz light curves, we can easily assume that the plasmon may orbit the black hole 5 times, before it dies. We re-model the light curves at 22 GHz and 43 GHz with orbital dynamics and find that the time delays between orbital modulations at successive frequencies should be approx 20-25 minutes, which is the main time lag observed between the broad light curves at 22 GHz and 43 GHz. Consequently, the time lags between the orbital peaks are related to the broad adiabatic expansion process that occurs during the 5 orbital periods.

The final scenario assumes that the NIR flaring is caused by synchrotron radiation of non-thermal electrons that are injected in the blob. This event triggers the formation of a plasmon that starts expanding adiabatically, exhibiting time delayed flares on close timescale to the NIR broad light curve associated with the injection and the synchrotron cooling processes.

This picture explains some properties of the structure and substructure of light curves in both NIR and radio:

(1) the time delays between the IR flares and the radio flares.

(2) the broad NIR flare timescale of 100-140 minutes.

(3) the radio flare timescale of 2-2.5 hours.

(4) the 20 minutes average quasi-periodic modulation, identified with the orbital period.

(5) the sub-orbital modulations with variations due to beaming and lensing effects

The average range of expansion velocities as measured from the theoretical relativistic NIR and radio flares show expansion of plasma between 0.003c and 0.1c. These values confirm the expansion velocities calculated from observed VLBI radio and infrared flares. Such a low velocity might suggest that the plasma is not escaping the accretion flow. Our expanding plasmon light curves show slow expansion velocities that are required to produce the time delayed flares, also much smaller than the escape speed near the ISCO. A second suggestion is that the plasma is part of a large bulk motion (see Marrone et al. 2008 and Yusef-Zadeh et al. 2008). The adiabatically expanding plasmon should be part of a bulk motion larger than v_{exp}, contributing to the accretion flow of the disk or a jet or to the formation of a corona. On the other hand, shearing processes caused by differential rotation within the disk can also explain these low speed values (see Eckart et al. (2008a) and Zamaninasab et al.).

In order to construct a full realistic model of the flaring activity in NIR/radio bands, we follow a number of steps:

(1) separate all relativistic effects at sub-orbital level

(2) assume the 20 min average periodicity as orbital origin

(3) assume an injection event that triggers the formation of an expanding plasmon

(4) assume the observed time lags at radio wavelengths to be caused by adiabatic expansion

Our first hypothesis considered a synchrotron spot orbiting the black hole, possibly multiple times, that starts expanding on a dynamical time scale close to the orbital period.

In the second scenario, we assumed a plasma blob, completing one or more than one orbit that starts expanding from the beginning but at a later time that we pick randomly at different phases, it will start modifying its intensity. The flare, in our example simulations, starts at four different phases in the orbit.

A recording of the same time separation between two peaks, assumed to be the orbital period, at different frequencies (for example between NIR and mm) may discard these modulations as being produced by an intrinsic flaring event. However, there is little evidence to support the premise that a blob would survive so long in a region where shearing is supposed to be quite strong. A second complementary constraint is that the peaks recorded at one frequency and delayed at a different frequency, can't be caused by simple orbital motion. Therefore, we can consider these delayed peaks as a possible origin of the intrinsic flaring mechanism. These factors are significant constraints when searching for orbital periods or dealing with intrinsic or relativistic flux modulations that could fully or partially contribute to the light curve amplification. Such constraints can be imposed to help with the confinement of the flare at a specific orbital radius, which is also determined by the orbital period as recorded in the light curve.

If we find non-delayed peaks in a light curve, it is very possible that their origin is purely relativistic due to a constant or variable size blob orbiting the black hole and cooling down via synchrotron or adiabatic processes. If we assume that the cooling of the blob is adiabatic, the non-delayed peak might be caused only by relativistic modulations. When blended with relativistic signatures on the same natural timescale, some peaks might show shorter or longer time delays than the predicted values. The adiabatic expansion can explain the time lags between the NIR/X-ray and radio peaks. The presence of time lags in radio has lead us to the idea of using the plasmon model as a method (or part of a method, more exactly) to seek for relativistic signatures and orbital periodicity, together with deriving the spin, by searching and discarding the delayed peaks as candidates for orbital/relativistic signatures and use only the non-delayed peaks as possible orbital modulations.

The brightness ratio as well as the relative phase ratio between these peaks seem to confirm our picture, as long as we consider that we are dealing with a blob that expands on the orbital timescale during one single orbit. The superimposed simulated light curves are obtained by using a plasmon that expands on a dynamical timescale (0.5 up to 1.5 orbits) experiencing the predicted relativistic modulations during the orbital motion.

Depending on the initial size of the blob and the expansion velocity of the plasma, we obtain different relative flux ratios between the two main sub-flare peaks. In the same way, depending on the initial location of the blob (or, more strictly, the initial orbital phase where the blob starts to expand –this is the case when we consider an initial orbiting blob of constant size that starts expanding later in the orbit), the flare will peak earlier or later and the orbital phase between the intrinsic peak flux and the lensing/boosting peak will be different.

If new particles are still produced or injected in the plasmon, the time delays at successive frequencies should be larger in the observed light curves than the predicted time delays for a simple plasmon expanding in vacuum. Such a hypothesis would confirm the previously found time delays, slightly longer than the theoretical calculated timelags from the plasmon model.

We find at least two pairs of radio frequencies where the observed time delays are larger than the predicted values. We can assume in this case that new electrons are still injected into the blob while expanding. For pairs of frequencies with observed time delays close to the predicted plasmon model values, we can safely assume that no new particles are injected into the plasmon. The accretion flow builds up during a process that could take between 100-150 min. A rapidly synchrotron cooling spot with an additional extended injection process component can solve the long duration of 100 minutes flaring time. In the absence of continued injection of high energetic particles, the cooling process will begin suppressing the high energy part of the particle distribution function, generating a cutoff in the NIR spectrum.

If the blob is able to persist for multiple orbits, it must not expand significantly and the expansion velocity should be quite small. The flare timescale for NIR flares, close to the expansion timescale (which can't be applied to NIR because of a lack of optical depth effects in this wavelength) has a duration comparable to the orbital timescale (about 5 times longer). It is unlikely that such a hot spot could survive for several orbits and a very reasonable

solution is to assume here a separate process of production or injection of new particles in the blob, helping the blob to last for multiple orbits. In the same way, a separate mechanism had be invoked for the periodic broad flare in radio wavelengths, if the observed expansion time is longer that the time derived for an expanding blob.

We also consider a second case of a blob that is expanding in more or less than one full orbit. The blob might expand in one and a half orbits, two orbits or half an orbit, for example.

The two scenarios are covered here: in one case, the blob starts expanding around the black hole at least one orbit before it starts modifying its internal flux and optical depth; in the second scenario, the blob starts expanding from the beginning, scenario only covering the mm/sub-mm case. The relativistic modulation is caused here by the optically-thick expanding blob in orbital motion. There is not additional relativistic signature that might be produced by a non-expanding hot spot.

We have in this case a flare that starts expanding from the moment we start our light curve or before we plot the light curve, for example the closest point to the observer, $\phi = 0$ but the expansion velocity of the plasmon will constrain the flare lifetime to not be exactly equal to one single orbit but below one orbit or multiple orbits.

The relativistic effect could be caused by the blob that is still optically thick and not yet changing its optical depth or by the flare already in full expansion and modulating its internal flux. We obtain multiple peak structures as long as during one single epoch, we may observe both components: relativistic effects caused by the orbital motion around the black hole and the flare flux modulation produced by the expansion process. The optical depth of the blob will start changing from the moment it starts expanding.

It is also possible, however, that during a NIR/X-Ray flare the blob to undergo expansion. In this case, the adiabatic cooling is insignificant and dominated by radiative cooling processes, with no visible time lags between the light curves. However, in the optically thin regime we can make an assumption about the intrinsic emission of the flare, following for example, a flux normal distribution, without any assumptions regarding the optical depth of the flare. The blob changes size and its intrinsic emission becomes variable due to a different number of accelerated electrons in the blob. The only effects we may see in the light curve are the relativistic modulations during the orbital motion and the flare variability caused by

an intrinsic variation in number of particles in the blob.

The two model components line up on the far side of the black hole, on opposite phase locations relative to the centre. A relative brightness minimum in the light curve is created between the two peaks (or three peaks, if the Doppler peak is visibly separated from the lensing peak) of different emission origin. Figure 5.40 shows a blob that starts expanding half way through the orbit, while the total duration of the flare is one entire orbit. The first peak is caused by the relativistic orbital dynamics of a synchrotron steady blob, whereas the second peak corresponds to the intrinsic flux modulation of the expanding plasmon.

As expected, the last peak exhibits time lags when reproduced at a different frequency. In this case, we doubled the first frequency, to be able to simulate the difference between flux peaks at 22 GHz and 43 GHz frequencies. In Figure 5.41 we show the extreme case when the blob starts expanding after one orbit and lasts for another orbit.

The total duration of the flare is two orbital periods, first orbit of a single steady blob and the second orbit of an expanding plasmon. The time delay between the two peaks corresponding to the maximum intrinsic flux modulation of the plasmon is about 20 minutes, as observed between the light curves at 22 GHz and 43 GHz.

In order to estimate the expansion velocity of the plasma, we found necessary to employ a plasmon that expands during two orbital periods. The flare lifetime in Figure 5.42 is a total of 3 orbital periods, with the first orbit as a steady blob and the last two orbits as an expanding plasmon. The first and the second plots show evidence for a time lag between the plasmon peaks at two frequencies, 42 GHz and 22 Hz, whereas the last picture still shows the light curves at 22 GHz but for a plasmon that expands much faster than the first one. The middle figure corresponds to a plasma velocity of $v = 0.09$, whereas the bottom figure corresponds to $v = 0.4$.

We can notice the different decay rate for each of the expansion velocities. In the case of a fast expanding blob, the flare duration is shorter and decays more rapidly, as we can see in the bottom light curve from Figure 5.42.

In the first scenario, we assumed an expanding blob completing a number of orbits before it starts changing in intensity. We proposed that the cooling process could be due to

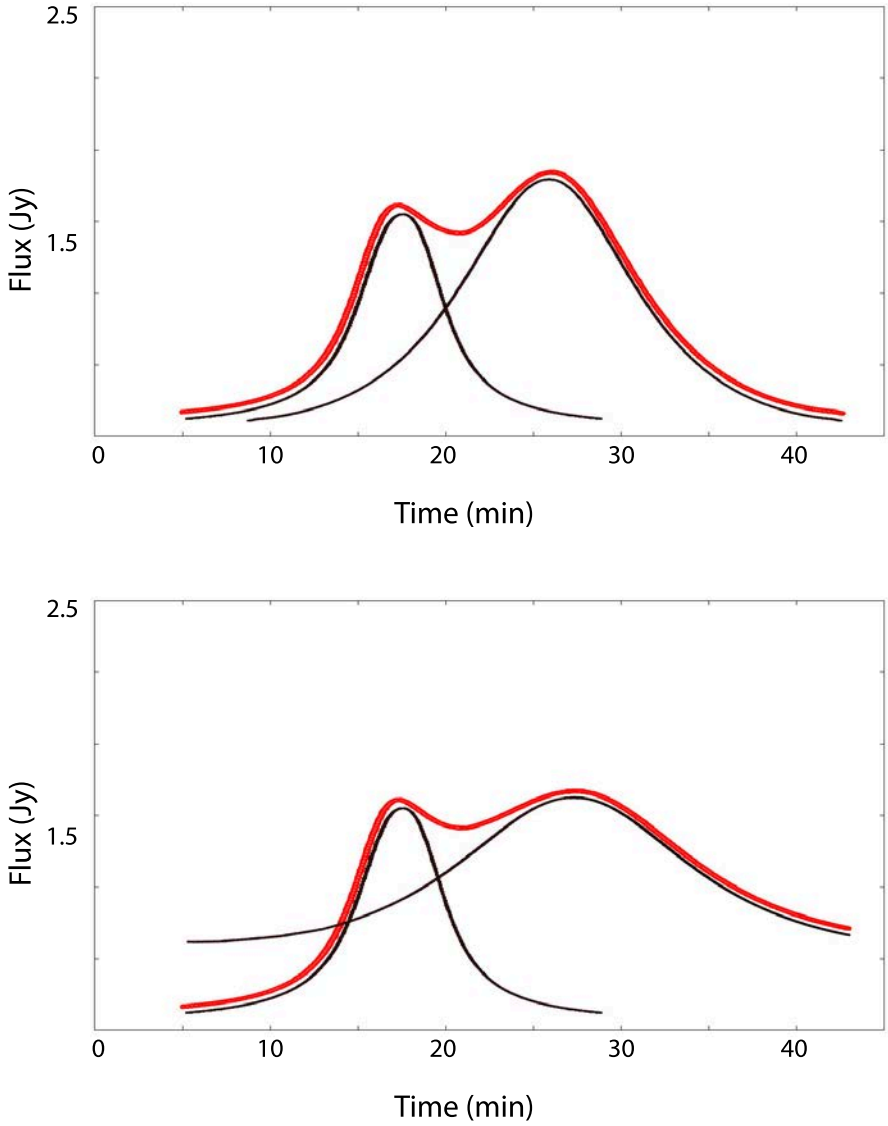

FIGURE 5.40: Light curve of a synchrotron blob that starts expanding half way through the orbit. The total duration of the entire flare event is 20 min during one single orbit. The light curve substructure shows a peak caused by the orbital relativistic effects of a steady synchrotron blob orbiting a black hole of spin $a/M = 0.998$ and a second peak caused by the intrinsic flux of the expanding blob. The blob is located at an orbital radius of $r_{\rm sp} = 4.5GM/c^2$. The radius of the blob is $R_{\rm spot} = 0.5GM/c^2$. The flare is decomposed in two separate components, the steady blob and the expanding plasmon, both shown in black. The top figure shows the light curve at 146 GHz and the bottom figure shows the same light curve at 134 GHz with a 2.5 min time delay between the plasmon peaks.

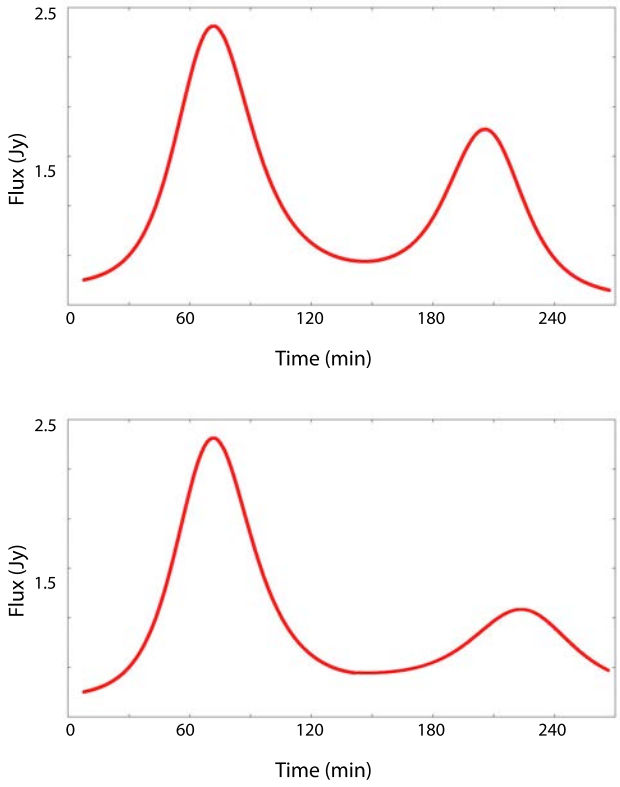

FIGURE 5.41: Light curves of a blob expanding after one orbit. The first peak is caused by relativistic effects of a steady blob and the second peak is caused by the relativistic effects of an expanding plasmon combined with optical depth effects. The blob of radius $R_{\rm spot} = 0.5GM/c^2$ is located at $r_{\rm sp} = 4.5GM/c^2$. The top figure shows the light curve at 43 GHz and the bottom figure shows the light curve at 22 GHz with a 20 min time lag between the peaks.

adiabatic expansion, implying that the flare activity might be actually associated with an outflow (Yusef-Zadeh et al. 2006). Their concept was a direct consequence of the fact that the synchrotron lifetime of sub-mm particles is about 12 hours, much longer than the 20-40 min timescale associated with the higher energetic particles from NIR emission.

The simultaneity of the NIR and X-ray light curves together with similar sub-flare structure favours a model of emission from a single region. The blob could be ejected from the region near the central black hole or formed in the disk. However, from radio/mm modelling we inferred very low expansion velocities of the plasma. Consequently, it is very possible that the blob is formed within the disk and not ejected with a relativistic speed from inner

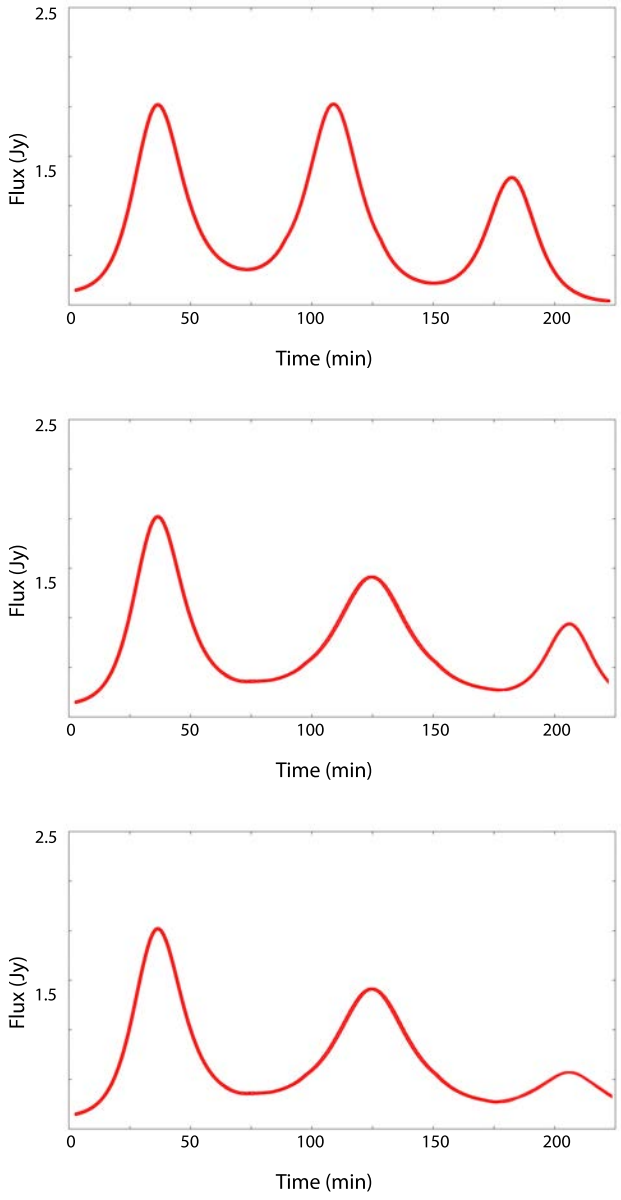

FIGURE 5.42: Light curves of a synchrotron blob that starts expanding after two orbits. The total duration of the entire flare event is three full orbits. The first peak is caused by the orbital relativistic effects of a steady synchrotron blob orbiting a black hole of spin $a/M = 0.998$. The second and third peaks are caused by the orbital relativistic effects of an expanding plasmon combined with the intrinsic flux modulation caused by optical depth effects. The blob is located at an orbital radius of $r_{\rm sp} = 4.5GM/c^2$. The radius of the blob is $R_{\rm spot} = 0.5GM/c^2$. The top figure shows the light curve at 43 GHz and the middle figure shows the same light curve at 22 GHz with a 15 min time delay between the plasmon peaks. The plasmon expands with a velocity of v=0.09. The bottom figure shows the same light curve at 22 GHz but for a blob expanding faster with the velocity v=0.4.

regions close to the ISCO of the black hole.

The inferred expansion speeds suggest a low orbital velocity speed of the blob and a disk origin rather than the relativistic ejection of emitting blobs from the underlying accretion flow (analogy with the theory of the coronal mass ejection in the Sun, see Yuan, 2010).

As we employ the extended synchrotron model, we find that the model is also able to explain the time lag feature in the radio flares observed at different frequencies, together with an understanding of the flare duration (not predicted by the adiabatically expanding plasmon model), at the same timescale with the NIR broad flaring activity.

The interplay between the variability at sub-orbital level, orbital and multi-orbital plays an important role in providing a full realistic picture of the light curve structure in both NIR and radio wavelength bands.

5.6 Estimating Sgr A* parameters

It is possible to estimate the blob orbital period and ultimately the black hole mass and spin. Since the orbital period at ISCO of a Schwarzschild black hole is longer than 20 min, this orbital period can be easily interpreted as evidence for a Kerr black hole. Modelling of a spot at different orbital radii in the accretion disk provides a good method for estimating the black hole spin.

An additional factor is employed here, to substantiate our claim for periodicity. An important result from multi-wavelength simulations here is that the process of adiabatic expansion of the source is very relevant when looking for periodicity, as the time delayed peaks in the substructure of the light curve can be eliminated on the basis that they are not of relativistic origin. A candidate for a periodic signal is most likely caused by a relativistic signature occurring during the periodic orbital motion of the blob. It is also possible that periodic signatures of intrinsic variability to be present, if we assume a flare having an intrinsic modulation exactly equal to the orbital motion. A possible instability in the disk could exhibit periodic signatures on orbital scale. We calculated the orbital period of a spot in circular orbit for Sgr A* of mass $4.31\ 10^6 M_{\odot}$, in Kerr metric. We have plotted the dependency of the orbital period as a function of orbital radius which has been normalized by the ISCO radius

(see Figure 2.4). The radius of the flare orbit and the spin parameter could be constrained by various observations of flares from Sgr A*.

If we consider the infrared observations that show a periodic variability of the light curves between approx 20 min and 22 min, we have to take into account the spot model, as there is no time delay observed.

Considering a simple spot model, these periodicities correspond to the orbiting period of the flare around the black hole. As we assume that the blob is formed near the ISCO, we use Figure 2.4 to find the spin parameter as a function of the orbital radius. As the spin estimation is done based on ISCO dependency of the spin parameter, Figure 2.4 can be used to calculate the black hole spin.

From our light curve modelling, we find an average orbital location of the flare being between $4.3R_s$ and $4.5R_s$ (with insignificant changes for different spins of the black hole) corresponding to the 1330 sec orbital period (from relativistic light curves matching the data). Consequently, if $4.5R_s$ is interpreted as ISCO in the context of our model constraints, this leads to a black hole's spin:

$$\begin{aligned} 0.4 \lesssim a \lesssim 0.5, \\ 4.3\, r_{\rm S} \lesssim r \lesssim 4.5\, r_{\rm S}. \end{aligned} \tag{5.19}$$

If this orbital period is the same with the QPO already found in simultaneous X-ray/NIR light curves, this fact substantiates the previous findings and confirms the QPO as a genuine orbital period. In this way, the time lag searching method can be used as a valid technique to find and confirm the orbital period and ultimately, the spin of the black hole.

Combined with observed quasi-periods found in X-ray and NIR, this method provides a new way in which to estimate the black hole spin.

The model also allows estimates of the inclination angle extracted from a number of initial assumptions regarding the sub-structure of the light curve.

The magnification caused by gravitational lensing varies with the orbital radius and it is a good indicator of the inclination angle of the disk (and the equatorial orbit of the blob in the

disk) relative to the line of sight of an observer located at infinity. This factor together with an estimate of the asymmetry of the light curve at orbital scales, for a given $4.5R_s$ ISCO, can constrain the viewing angle.

The flare peaks at different flux values for various inclination angles, radial locations of the spot and different spins of the black hole. We notice that for different spins, the flare peaks at lower values of the flux as the black hole spins faster.

The flare also peaks at higher values as the inclination angle of the disk relative to the observer increases. A very interesting feature is that under the ISCO limit, the flare peaks are lower as the orbital location is increased.

Further away from the black hole, the flare loses its brightness and reaches a minimum flux value for ISCO location. As we consider larger orbits than ISCO, the flux amplitude is higher as the spot is further away from the black hole. For orbits larger than the ISCO limit, the flux peaks start to increase, as less photons are falling into the black hole. As we get closer to the black hole, the flux amplitude is lower because a number of photons are captured by the black hole and plunge into the ISCO region.

The flare loses brightness in this way. Another reason for this decrease is the fact that the redshift signatures become very strong closer to the black hole, smearing the higher peak of the light curve and lowering the total amplitude of the flare.

For high inclination angles both gravitational lensing and Doppler boosting effects would play major roles in the relativistic structure and shape of the light curve. For blobs viewed at higher inclination angles, this leads to significant Doppler boosting effects, causing the black hole disk to appear asymmetric with a bright (dim) approaching (receding) side.

We have fit light curves for different gravitational lensing magnifications and Doppler boosting modulations and found that only for viewing angles ranging from 75° to nearly face-on 89° inclinations, we obtain a clear double peak sub-structure. A light curve observed at these angles will exhibit asymmetric characteristics between the approaching and receding side of the black hole.

For nearly face-on 89° inclinations, we expect very narrow profiles of the light curve. However, in some cases, the flare appears broader than the simple simulated relativistic light curve, suggesting a separate intrinsic mechanism, like the injection of fresh particles and/or

cooling processes that. Such a separate mechanism will definitely affect the asymmetry of the light curve.

Throughout the modelling, we assumed the X-ray/NR flare to be affected by the injection of high energy electrons and synchrotron cooling processes, whereas the radio flares to be subject to slow adiabatic expansion/cooling processes. If such a mechanism occurs at orbital scale, the light curve sub-structure could be affected.

The minimum inclination angle that allows for a double-peak structure in the light curve is 75°. Unfortunately, because the broadening of the light curve and the degree of symmetry could be both affected by other intrinsic energetic mechanisms in the flare, an estimate for a minimum viewing angle can't be provided accurately. However, the model allows us to strongly disfavour the low disk inclination angles and to estimate some parameters of the accretion flow, together with the spin of the black hole.

The spin parameter is constrained based on two models (hot spot and plasmon) and the assumption that the flare is forming at the ISCO. The models involved suggest an average orbital location of $4.5R_s$ ±0.2, with face-on geometries $\theta = 30°$ and very high inclination angles $\theta = 90°$ being satisfactorily ruled out.

We find consistent values of the orbital radius, providing in this way, compelling evidence for the existence of a fixed inner-disk radius. We suggest that the orbital radius is closely associated with the radius of the ISCO. This assumption postulates a firm foundation for the measurement of the black hole spin.

Unlike the inclination, the spin estimates are not so robust. While the spin is independent of the accretion dynamics, the estimation of the spin parameter is still dependent on the geometry involved and the spatial distribution of the emitting plasma surrounding the black hole. The most likely values for the spin were placed in the interval a= 0.45 ±0.2. Nonetheless, additional observations are required before this constraint can be convincingly settled.

Given the confidence limits, a non-rotating black hole can be in this way ruled out, together with very high values of the spin a $\gtrsim$ 0.9, regardless of the weak constraint. It is necessary to better distinguish between the models of emission and accretion scenarios together with including polarimetric data, in order to provide a confident prediction of the

value of the black hole spin.

5.7 Final remarks and future prospects

This Chapter represents a qualitative analysis of the relativistic signatures on Sgr A* light curves. However, we find it necessary to discuss the quality of the fit between the models used and the existing observational data, in order to provide further comparative aspects between various assumptions made e.g. expanding / non- expanding blob. We suggest that the existing data confirms the picture of a composite relativistic hot spot / expanding plasmon model at multiple wavelengths. While the constraints on Sgr A* parameters are here not very strong, a brief comparative statement can be issued. We find that a composite model that uses both the hot spot and the expanding plasmon pictures, with sub-orbital relativistic structure, is a good fit for the current simultaneous IR/NIR and mm data, suggesting a correlation or a common origin between them.

The model setup and assumptions are both based on a phenomenological approach but still provide a convincing case for a relativistic picture with sub-flare characteristics, accounting for beaming and lensing effects. Our analysis is meant to offer an insight about the nature of the flares and the inner accretion flow. Nonetheless, only additional future simultaneous multi-wavelength observational data, with better sampling rates can ultimately confirm our predictions and theoretical assumptions.

We suggest various scenarios and find that for the IR/NIR and mm data, the best fit is given by a combination between a non-expanding hot spot and an expanding self-absorbed plasmon, while the peaks formed at sub-orbital timescales account for relativistic signatures. The time delays are also found to be consistent with the existing observations.

A realistic scenario is here developed by introducing the plasmon model together with all relativistic effects and employing the hot spot scenario as an additional component, ultimately comparing to existing Sgr A* flare data. The simulated light curves contain all relativistic effects such as gravitational lensing, time delays, gravitational redshift and relativistic beaming of the photons.

Because of many timescales involved in the flare structure such as orbital motion, adiabatic cooling, injection and synchrotron cooling, time-dependent modelling of the flaring is required to understand the light curve characteristics. We analysed the structure and parameters of a blob of synchrotron emitting plasma in the vicinity of Sgr A* at various wavelengths and predict the presence of time delays between flux peaks in light curves at successive frequencies together with long-term evolution of the flare.

The method of disentangling the orbital peaks (created by relativistic effects) from the flare peaks (created by intrinsic flux modulations) by introducing the plasmon model, helps us dissociate the delayed peaks from the simultaneous ones (when observed at different frequencies). However, by eliminating most types of peaks and identify their nature, we remain only with peaks purely caused by orbital motion. being able to estimate the orbital period of the flare. The reason we introduce multiple timescales and aim to provide a complete picture of NIR/radio flaring activity is to identify the origin of each type of sub-peak in the light curve and answer the question about the orbital period, as the stepping stone helping us with a better estimation of the spin parameter of the black hole. Further observations with large frequency coverage are also required to resolve these issues.

The combination between the relativistic amplification curves with the plasmon mechanism provides us with a valid and flexible time dependent flare emission model. The emission from SgrA* can in this way be interpreted through a relativistic model with combined intrinsic emission properties of a simple synchrotron spot and an expanding plasmon.

We showed that a combined orbiting synchrotron spot and adiabatic expanding plasma blob models, together with all relativistic effects can explain the observed variability of Sgr A* across all wavelengths and the time lags observed in radio wavelengths. We tested the model by simulating light curves for expanding blobs with various expansion velocities and orbital locations, obtaining delayed flaring that confirms the derived expansion velocities in the literature as well as the predicted time lags from the plasmon model.

We presented a complementary approach to estimate the orbital parameters using the plasmon model. We also offered an estimate for the spin of the black hole and the inclination angle of the disk.

We matched the structure of the light curve profiles as well as the calculated time lags

between successive frequencies. The derived blob size, density and magnetic field strength are also in agreement with the standard accretion model.

We tested the model in a simplistic and phenomenological way, through qualitative comparison with simultaneous and delayed light curves in the literature.

Future simultaneous measurements at both optically thin and thick frequencies should be able to test the model. A further understanding of Sgr A* emission will rely on simultaneous multi-wavelength campaigns. The flare emission is most likely originating from a compact source from the inner regions of the accretion disk and could probe the dynamics and properties of the gravitational field close to an event horizon.

It may be also possible in the future to calculate with accuracy the spin of the black hole by detecting the periodic signature of the blobs close to the ISCO. The study of the temporal information in the light curve provides further constraints on possible future phenomenological models and analysis of future Sgr A* data.

5.7.1 Caveats and approximations

While the model offers a realistic picture of Sgr A* variability at several wavelengths and predicts several features in the flare emission, there are still a number of issues to be addressed. Several approximations had to be assumed in order to keep the calculations simple.

In Kerr metric, a good approximation is neglecting the gravitational field of the accreting plasma. If the disc is thick and dense, its gravity, especially farther away from the black hole, shouldn't be neglected. A more advanced version of the model that assumes a self-gravitating disc should be considered.

We also assumed that the blob is compact and rigid, neglecting any shearing effects. In a realistic scenario, the blob could vary in shape due to differential rotation within the accretion disk. In a very strong magnetic field, the blob can be considered a rigid object that retains its original shape during the flare emission event. The blob intrinsic shape is disregarded as the source is ray traced from infinity to the disk, using the geometric optics approximation. We have also ignored external influences on the light rays when they arrive at the observer. The blob follows a stable planar circular orbit near the ISCO in the equatorial plane of the disk.

A supermassive black hole is unlikely to be accreting in the same orbital plane as the black hole spin. The Lense-Thirring precession should lead to a tilted and warped disk. Eccentric orbits should eventually converge and produce non-axisymmetric standing shocks. The gravitational torque could cause the disc to precess almost as a solid body (Fragile et al. 2007). By working in 2 dimensions only, the simulation excludes the effects of misalignment between the angular momentum of the gas and the black hole. A geometrically thick accretion flow does not align with the black hole. The disc misalignment affects the dynamics and properties of the accretion flow. A tilted accretion flow could alter the observable features of Sgr A* emission and considerably affect the sub-flare structure of the light curve.

In our modeling the flare is caused by a local event close to the ISCO. In such a dynamical picture of the accretion flow, it is possible that the flaring to be produced close but not exactly at the ISCO due to instabilities and turbulent processes in the disk. For a thick disk solution, self-eclipsing of the disk might play some role in the observed emission. As the blobs could be created through magneto-rotational instabilities, shown to be present in Keplerian rotating accretion disks (Hawley Balbus 1991), a shear-flow instability may generate a turbulent flow in the disk. Excess angular momentum transport from such shock could truncate the accretion flow outside the ISCO (Fragile 2009; Dexter Fragile 2011). The flare could spread out via a shock wave and produce a temporary torus around the black hole. In this case, the spin of the black hole shouldn't be derived only based on flares located at ISCO. The light curve sub-structure could be also affected by the presence of an orbiting asymmetry in this torus causing flux modulations on orbital scales.

In order to develop a more realistic model, work should include a variable expansion speed of the plasmon. Furthermore, other types of orbital motion should be considered, such as orbits off the equatorial plane.

5.7.2 Future prospects

To provide additional insight on the nature of Sgr A* flaring activity, modelling of polarized emission should be also included in future modelling, in the context of a hot spot or an expanding synchrotron blob. A model for polarized emission of an expanding plasmon should

be considered together with the influence of relativistic effects on the polarization degree and polarization angle. Such an analysis would provide further constraints on the black hole spin and the orientation of the orbital plane.

We have studied and modelled the possibility of gravitational lensing and Doppler effects in light curves from compact orbiting blobs. The VLTI instrument GRAVITY will be able to image these plasma blobs orbiting near the ISCO. VLBI interferometry or second-generation Very Large Telescope Interferometer instrument GRAVITY is designed to detect highly relativistic motion of matter close to the event horizon. The astrometric displacement of the primary image, the presence of a secondary image that shifts the centroid of Sgr A, and the gravitational lensing effect may be detected. GRAVITY may also detect gravitational lensing effects in the NIR bands. The gravitational lensing effects around Sgr A* might be detected for the first time due to GRAVITY astrometric capacity.

Current 1.3 mm VLBI observations have shown that the mm emission arrived from a compact region from the disk (Fish et al., 2010). We used this data to constrain the black hole parameters (spin and inclination). Future additions to the VLBI array will offer the opportunity for the mm emission to be imaged directly. Millimeter VLBI offers the possibility to probe the Sgr A* emission at angular scales of only a few Schwarzschild radii and on timescales of a few seconds. The high angular resolution and fine time resolution will be used to identify the nature of the quiescent emission and detect possible periodicity in the variable component of emission. A measurement of the spin of the black hole may be done by using the observed periodic signature of the compact blobs at the ISCO. Very long baseline interferometry at mm/sub-mm wavelengths offers the highest spatial resolution at any wavelength. The inclusion of ALMA as a phased array into the VLBI network by the end of 2014 will bring high sensitivity for mmVLBI. The new ALMA capabilities will allow imaging the event horizon of the black hole and testing General Relativity theory. The new phased ALMA will offer the sensitivity needed to image the innermost regions of Sgr A* disk at all available frequencies and in polarization, with excellent angular and spatial resolution.

The time resolved monitoring observations will search for structural variability and help

with deriving the spin of the black hole. New triggered VLBI imaging using NIR variability as a trigger for direct VLBI imaging at high frequencies will be also performed. Our proposed scenario and connection between NIR and radio frequencies may be confirmed by future VLBI observations that include ALMA facilities, through a deeper analysis of the time-variable structures in Sgr A* accretion flow. Future mm-VLBI observations (Fish and Doeleman, 2009) at high frequencies as well as VLTI observations in the NIR should provide a better picture of the Sgr A* variable emission. Spatial resolution is probably the key to understanding the Sgr A* variability, hence the need for polarimetric mm-VLBI measurements. Simultaneous observations in X-ray and NIR will also allow us to constrain the location of the compact source, the nature of the expanding plasma and detect any time variable periodicity and sub-structure in the light curves.

6

Conclusions

Time variability is extremely important to the understanding of Sgr A* flaring nature and has to be considered in conjunction with general relativistic effects, especially, as seems to be the case, if the intrinsic variability time scale and the orbital scale are comparable.

This Thesis examined the contributions of GR effects associated with orbital motion to the variability of Sgr A*. Using ray-tracing techniques, we model all relativistic signatures in light curves from a continuum emitting blob in orbital motion around a Kerr black hole.

We initially studied the relativistic effects in light curves for different viewing angles, at different orbital radii and for different spins of the black hole, for an intrinsically steady spot of continuum emission within a thin accretion disk as viewed by a distant observer located at infinity. The spot was assumed to be in circular orbital motion and located in the equatorial plane of the accretion disk.

We modelled relativistic light curves by using ray tracing techniques in Kerr metric and

found that the light curve can be a useful tool to constrain the black hole parameters and understand the nature of emission. We computed the profile of the resulting light curve and the blending between Doppler shifts, lensing, relativistic beaming, and gravitational redshifting. We found that the variation in flux would arise from two major fundamental processes: Doppler shift and gravitational lensing. We showed that some of these processes leave their strongest signatures on specific portions of the light curve.

Motivated by the apparent periodicity in some Sgr A* light curves, and the clear sub-structure, suggestive of lensing and Doppler beaming effects, together with the presence of time lags at radio wavelengths, we developed a relativistic time-dependent model that includes the intrinsic variability of the emission region. We took into account all relativistic effects, and sought for relativistic signatures in the resulting light curves. Modelling of Sgr A* periodicity provided us with important clues about long-term and short-term variability, through identifying and isolating peaks of different origin in the light curves. We analysed light curves firstly under the assumption of stationary intrinsic emission and later, considered an intrinsic variable source that expands adiabatically while orbiting the black hole.

This led us to suggesting a possible connection between the NIR flaring activity and the radio emission via adiabatic expansion of a self-absorbed plasmon in orbital motion about the black hole. The observations were interpreted in the framework of a relativistic model involving a multi-component structure containing both the hot spot picture and a self-absorbed plasmon forming within the accretion flow. We showed that the intrinsic evolution of the flare could exhibit time dependent signatures in the light curve, on a different or the same timescale with signatures caused by orbital relativistic effects. The model was used for the evaluation of the spin, assuming one identifies the inner edge of the disc with the ISCO. The extended analysis of the variability timescale has led us to an estimate of the black hole spin, albeit determined entirely from the radial position of the ISCO. We find that the Sgr A* spin has rather an intermediate value $a \approx 0.45$. We also found that the minimum inclination angle allowing for the double-peak structure apparent in many of the observed X-Ray/NIR light curves is 75°.

The individual sub-flares of 20 min average separation seen in the NIR are due to a single blob in orbital motion around the black hole, with shorter term modulations caused

by lensing and Doppler effects. A relatively slow underlying process of injection of new particles accounts for the broad overall flare observed in the NIR bands. The modelling provides evidence that some sub-structural patterns present in Sgr A* flaring are due to orbiting bright structures in the accretion flow that exhibit clear small timescale sub-orbital modulations.

To provide additional insight on the nature of Sgr A* flaring activity, modelling of polarized emission should be also included in future modelling, in the context of a hot spot or an expanding synchrotron blob. A model for polarized emission of an expanding plasmon should be considered together with the influence of relativistic effects on the polarization degree and polarization angle. Such an analysis would provide further constraints on the black hole spin and the orientation of the orbital plane. We will consider in the future to calculate with accuracy the spin of the black hole by detecting the periodic signature of the blobs close to the ISCO.

As we only included a qualitative analysis of the light curves here, future work should include a quantitative follow-up task, allowing a good estimate for the location of the emission region in the accretion flow. Using near-future observational data that aims to reach the immediate vicinity of Sgr A*, we may be able to provide a better estimate of the black hole parameters, infer the properties of the spacetime around the black hole and ultimately test General Relativity.

References

[1] Abramowicz, M. A., Bao, G., Lanza, A., & Zhang, X. 1991, A&A, 245, 454

[2] Abramowicz M. A., Beloborodov A. M., Chen X.-M. & Igumenshchev I. V. (1996). A&A, 313, 334.

[3] Agol E., 2000, ApJ, 538, L121

[4] Agol E. (1997). Ph.D. Thesis.

[5] Aitken D. K., Greaves J., Chrysostomou A., Jenness T., Holland W., Hough J. H., Pierce-Price D., Richer J., 2000, ApJ, 534, L173

[6] Alberdi, A., Lara, L., Marcaide, J. M., et al. 1993, A&A, 277, L1

[7] Alexander, T. 1997, MNRAS, 285, 891

[8] An T., Goss W. M., Zhao J.-H., Hong X. Y., Roy S., Rao A. P., Shen Z.-Q., 2005, ApJ, 634, L49

[9] Anninos P., Fragile P. C., Salmonson J. D., 2005, ApJ, 635, 723

[10] An, T., Goss, W. M., Zhao, J.-H., et al. 2005, ApJ, 634, L49

[11] Armitage, P. J. & Reynolds, C. S. 2003, MNRAS, 341, 1041

[12] Arnaud K. A. (1996). In Astronomical data analysis software and systems V, volume 101, page 17. Jacoby G. & Barnes J., ASP Conf. Series.

[13] Asaoka I. (1989). PASJ, 41, 763.

[14] Aschenbach, B., Grosso, N., Porquet, D., & Predehl, P. 2004, A&A, 417, 71

[15] Baars, J. W. M., Genzel, R., Pauliny-Toth, I. I. K., & Witzel, A. 1977, A&A, 61, 99

[16] Baars, J. W. M., Martin, R. N., Mangum, J. G., McMullin, J. P., & Peters, W. L. 1999, PASP, 111, 627

[17] Backer, D. C., Zensus, J. A., Kellermann, K. I., et al. 1993, Science, 262, 1414

[18] Baganoff, F. K. 2003, in Bulletin of the American Astronomical Society, Vol. 35, Bulletin of the American Astronomical Society, 606

[19] Baganoff F. K., Bautz M. W., Brandt W. N., Chartas G., Feigelson E. D., Garmire G. P., Maeda Y., Morris M., Ricker G. R., Townsley L. K., Walter F., 2001, Nature, 413, 45

[20] Baganoff F. K., Maeda Y., Morris M., Bautz M. W., Brandt W. N., Cui W., Doty J. P., Feigelson E. D., Garmire G. P., Pravdo S. H., Ricker G. R., Townsley L. K., 2003, ApJ, 591, 891

[21] Balbus S. A., Hawley J. F., 1991, ApJ, 376, 214

[22] Balick B., Brown R. L., 1974, ApJ, 194, 265

[23] Bardeen J. M. (1973). In Black holes, page 241. C. de Witt and B. S. de Witt, Gordon & Breach, New York.

[24] Bardeen J. M., Press W. H. & Teukolsky S. A. (1972). ApJ, 178, 347.

[25] Barriere, N., et al. 2013, in AAS/High Energy Astrophysics Division, Vol. 13, #403.02

[26] Bélanger G., Goldwurm A., Melia F., Ferrando P., Grosso N., Porquet D., Warwick R., Yusef-Zadeh F., 2005, ApJ, 635, 1095

[27] Bélanger G., Goldwurm A., Renaud M., Terrier R., Melia F., Lund N., Paul J., Skinner G., Yusef-Zadeh F., 2006, ApJ, 636, 275

[28] Blandford R. D., Begelman M. C., 1999, MNRAS, 303, L1

[29] Bondi H. & Hoyle F. (1944). MNRAS, 104, 273.

[30] Blandford R. D. & Znajek R. L. (1977). MNRAS, 179, 433.

[31] Blumenthal G. R., Gould R. J., 1970, Reviews of Modern Physics, 42, 237

[32] Bower G. C., Falcke H., Wright M. C., Backer D. C., 2005, ApJ, 618, L29

[33] Bower G. C., Wright M. C. H., Falcke H., Backer D. C., 2003, ApJ, 588, 331

[34] Bower, G. C., Falcke, H., Herrnstein, R. M., et al. 2004, Science, 304, 704

[35] Bremer, M., Witzel, G., Eckart, A., et al. 2011, A&A, 532, A26

[36] Broderick A. E., 2006, MNRAS, 366, L10

[37] Broderick A. E., Fish V. L., Doeleman S. S., Loeb A., 2011, ApJ, 735, 110

[38] Broderick, A. E. & Loeb, A. 2006, MNRAS, 367, 905

[39] Broderick, A. E., Loeb, A., & Narayan, R. 2009, ApJ, 701, 1357

[40] Bromley, B.C. et al. 1997, ApJ, 475, 57

[41] Carter B. (1968). Phys. Rev., 174, 1559.

[42] Cenko, S. B., Krimm, H. A., Horesh, A., et al. 2011, arXiv:astro-ph.HE/1107.5307

[43] Chiaberge M., Ghisellini G., 1999, MNRAS, 306, 551

[44] Chandrasekhar S. (1931). ApJ, 74, 81.

[45] Chandrasekhar S. (1960). Radiative transfer. Dover publications, New York.

[46] Chandrasekhar S. (1983). The mathematical theory of black holes. Clarendon Press/Oxford University Press (International Series of Monographs on Physics. Volume 69), p. 663.

[47] Clauset, A., Rohilla Shalizi, C., & Newman, M. E. J. 2007, arXiv:physics.data-an/0706.1062

[48] Cunningham, J. M. & Bardeen, C. T. 1973, ApJ, 183, 237

[49] Cunningham C. T. (1975). ApJ, 202, 788.

[50] Cunningham C. T. (1976). ApJ, 208, 534.

[51] Damour T. (1980). Mechanical, electrodynamical and thermodynamical properties of black holes. In Gravitational Radiation, Collapsed Objects, and Exact Solutions, page 454.

[52] Damour T., Ruffini R., Hanni R. S. & Wilson J. R. (1978). Phys. Rev. D, 17, 1518.

[53] Davidson J. A., Werner M. W., Wu X., Lester D. F., Harvey P. M., Joy M., Morris M., 1992, ApJ, 387, 189

[54] Davies, R. D., Walsh, D., & Booth, R. S. 1976, MNRAS, 177, 319

[55] de Kool M., Begelman M. C., Sikora M., 1989, ApJ, 337, 66

[56] Dexter J., 2011, PhD thesis, University of Washington

[57] Dexter J., Agol E., 2009, ApJ, 696, 1616

[58] Dexter J., Agol E., Fragile P. C., 2009, ApJ, 703, L142

[59] Dexter J., Agol E., Fragile P. C., McKinney J. C., 2010, ApJ, 717, 1092

[60] Dexter J., Fragile P. C., 2012, ArXiv e-prints

[61] Devillard, N. 1999, in Astronomical Society of the Pacific Conference Series, Vol. 172, Astronomical Data Analysis Software and Systems VIII, ed. D. M. Mehringer, R. L. Plante, & D. A. Roberts, 333

[62] Dibi S., Drappeau S., Fragile P. C., Markoff S., Dexter J., 2012, ArXiv e-prints

[63] Diolaiti, E., Bendinelli, O., Bonaccini, D., et al. 2000, in Presented at the Society of Photo-Optical Instrumentation Engineers (SPIE) Conference, Vol. 4007, Proc. SPIE Vol. 4007, p. 879-888, Adaptive Optical Systems Technology, Peter L. Wizinowich; Ed., ed. P. L. Wizinowich, 879–888

[64] Do, T., Ghez, A. M., Morris, M. R., et al. 2009, ApJ, 691, 1021

[65] Dodds-Eden K., Gillessen S., Fritz T. K., Eisenhauer F., Trippe S., Genzel R., Ott T., Bartko H., Pfuhl O., Bower G., Goldwurm A., Porquet D., Trap G., Yusef-Zadeh F., 2011, ApJ, 728, 37

[66] Dodds-Eden, K., Porquet, D., Trap, G., et al. 2009, ApJ, 698, 676

[67] Dodds-Eden K., Sharma P., Quataert E., Genzel R., Gillessen S., Eisenhauer F., Porquet D., 2010, ApJ, 725, 450

[68] Doeleman S. S., Weintroub J., Rogers A. E. E., 2008, **N**, 455, 78

[69] Doeleman, S. S., Fish, V. L., Broderick, A. E., Loeb, A., & Rogers, A. E. E. 2009, ApJ, 695, 59

[70] Fish V L, Doeleman S S, Beaudoin C, Blundell R, Bolin D E, Bower G C, Chamberlin R, Freund R, Friberg P, Gurwell M A, Honma M, Inoue M, Krichbaum T P, Lamb J, Marrone D P, Moran J M, Oyama T, Plambeck R, Primiani R, Rogers A E E, Smythe D L, SooHoo J, Strittmatter P, Tilanus R P J, Titus M, Weintroub J, Wright M, Woody D, Young K H and Ziurys L M 2011 ApJ 727 L36+ (*Preprint* 1011.2472)

[71] Doeleman, S. S., Shen, Z.-Q., Rogers, A. E. E., et al. 2001, AJ, 121, 2610

[72] Doeleman, S. S., Weintroub, J., Rogers, A. E. E., et al. 2008, **N**, 455, 78

[73] Dolence J. C., Gammie C. F., Shiokawa H., Noble S. C., 2012, ApJ, 746, L10

[74] Dovčiak, M., Karas, V., Matt, G., & Goosmann, R. W. 2008, MNRAS, 384, 361

[75] Dovčiak, M., Karas, V., & Yaqoob, T. 2004, ApJS, 153, 205

[76] Eckart, A., Baganoff, F. K., Morris, M., et al. 2004, A&A, 427, 1

[77] Eckart, A., Baganoff, F. K., Morris, M. R., et al. 2009, A&A, 500, 935

[78] Eckart, A., Baganoff, F. K., Schödel, R., et al. 2006, A&A, 450, 535

[79] Eckart, A., Baganoff, F. K., Zamaninasab, M., et al. 2008, A&A, 479, 625

[80] Eckart, A., Schödel, R., García-Marín, M., Witzel, G., Weiss, A., Baganoff, F. K., Morris, M. R., Bertram, T., Dovčiak, M., Duschl, W. J., Karas, V., König, S., Krichbaum, T. P., Krips, M., Kunneriath, D., Lu, R.-S., Markoff, S., Mauerhan, J., Meyer, L., Moultaka, J., Mužić, K., Najarro, F., Pott, J.-U., Schuster, K. F., Sjouwerman, L. O., Straubmeier, C., Thum, C., Vogel, S. N., Wiesemeyer, H., Zamaninasab, M., & Zensus, J. A. 2008, A&A, 492, 337

[81] Eckart, A. & Genzel, R. 1996, **N**, 383, 415

[82] Eckart, A. & Genzel, R. 1997, MNRAS, 284, 576

[83] Eckart, A., Genzel, R., Ott, T., & Schödel, R. 2002, MNRAS, 331, 917

[84] Eckart, A., Schödel, R., Baganoff, F. K., et al. 2008, Journal of Physics Conference Series, 131, 012002

[85] Eckart, A., Schödel, R., García-Marín, M., et al. 2008, A&A, 492, 337

[86] Eckart, A., Schödel, R., Meyer, L., et al. 2006, The Messenger, 125, 2

[87] Eckart, A., Schödel, R., Meyer, L., et al. 2006, A&A, 455, 1

[88] Eckart, A., García-Marín, M., Vogel, S. N., et al. 2012, A&A, 537, A52

[89] Einstein A. (1916). Die Grundlage ger allgemeinen Relativitätstheorie. Ann. Phys. (Leipzig), 49, 769.

[90] Eisenhauer, F., Schödel, R., Genzel, R., et al. 2003, ApJ, 597, L121

[91] Emmanoulopoulos, D., McHardy, I. M., & Uttley, P. 2010, MNRAS, 404, 931

[92] Esin A. A., Narayan R., Ostriker E., Yi I., 1996, ApJ, 465, 312

[93] Falcke, H., Goss, W. M., Matsuo, H., et al. 1998, ApJ, 499, 731

[94] Falcke, H. & Markoff, S. 2000, A&A, 362, 113

[95] Falcke, H., Markoff, S., & Bower, G. C. 2009, A&A, 496, 77

[96] Falcke, H., Melia, F., & Agol, E. 2000, ApJ, 528, L13

[97] de Felice F., Nobili L. & Calvani M. (1974). A&A, 30, 111.

[98] Fish, V. L., Doeleman, S. S., Broderick, A. E., Loeb, A., & Rogers, A. E. E. 2008, ArXiv e-prints:0807.2427

[99] Fish V. L., Doeleman S. S., Beaudoin C., Blundell R., 2011, ApJ, 727, L36

[100] Fragile P. C., Gillespie A., Monahan T., Rodriguez M., Anninos P., 2012, ApJS, 201, 9

[101] Fragile P. C., Meier D. L., 2009, ApJ, 693, 771

[102] Frank J., King A. & Raine D. J. (2002). *Accretion Power in Astrophysics: Third Edition*. Cambridge University Press.

[103] Freitag, M. 2003, in American Institute of Physics Conference Series, Vol. 686, The Astrophysics of Gravitational Wave Sources, ed. J. M. Centrella, 109–114

[104] Fritz, T., Gillessen, S., Trippe, S., et al. 2010, MNRAS, 401, 1177

[105] Fuerst S. V., Wu K., 2004, A&A, 424, 733

[106] Garofalo D., 2009, ApJ, 699, 400

[107] Garcia, M. R., et al. 2010, ApJ, 710, 755

[108] Gaskell, C. M. 2004, ApJ, 612, L21

[109] Genzel, R., Schödel, R., Ott, T., et al. 2003, **N**, 425, 934

[110] Genzel R., Eisenhauer F., Gillessen S., 2010, Reviews of Modern Physics, 82, 3121

[111] Gerbal D. & Pelat D. (1981). Profile of a line emitted by an accretion disk – influence of the geometry upon its shape parameters. A&A, 95, 18.

[112] Ghez, A. M., Hornstein, S. D., Lu, J. R., et al. 2005, ApJ, 635, 1087

[113] Ghez, A. M., Klein, B. L., Morris, M., & Becklin, E. E. 1998, ApJ, 509, 678

[114] Ghez, A. M., Morris, M., Becklin, E. E., Tanner, A., & Kremenek, T. 2000, **N**, 407, 349

[115] Ghez, A. M., Salim, S., Hornstein, S. D., et al. 2005, ApJ, 620, 744

[116] Ghez, A. M., Salim, S., Weinberg, N. N., et al. 2008, ApJ, 689, 1044

[117] Ghez, A. M., Wright, S. A., Matthews, K., et al. 2004, ApJ, 601, L159

[118] Gillessen, S., Eisenhauer, F., Trippe, S., et al. 2009, ApJ, 692, 1075

[119] Gillessen S., Eisenhauer F., Fritz T. K., Bartko H., Dodds-Eden K., Pfuhl O., Ott T., Genzel R., 2009, ApJ, 707, L114

[120] Gillessen S., Genzel R., Fritz T. K., Quataert E., Alig C., Burkert A., Cuadra J., Eisenhauer F., Pfuhl O., Dodds-Eden K., Gammie C. F., Ott T., 2012, N, 481, 51

[121] Goldwurm A., Brion E., Goldoni P., Ferrando P., Daigne F., Decourchelle A., Warwick R. S., Predehl P., 2003, ApJ, 584, 751

[122] Hanisch R. J., Farris A., Greisen E. W., Pence W. D., Schlesinger B. M., Teuben P. J., Thompson R. W. & Warnock A. (2001). Definition of the flexible image transport system (FITS). A&A, 376, 359.

[123] Haubois X., Dodds-Eden K., Weiss A., Paumard T., Perrin G., Clénet Y., Gillessen S., Kervella P., Eisenhauer F., Genzel R., Rouan D., 2012, A&A, 540, A41

[124] Hawking S. W. (1971). Gravitationally collapsed objects of very low mass. MNRAS, 152, 75.

[125] Hawking S. W. (1975a). Particle creation by black holes. Commun. Math. Phys., 43, 199.

[126] Hawley J. F., Balbus S. A., 1992, ApJ, 400, 595

[127] Heeschen, D. S., Krichbaum, T., Schalinski, C. J., & Witzel, A. 1987, AJ, 94, 1493

[128] Heil, L. M., Vaughan, S., & Uttley, P. 2011, MNRAS, 411, L66

[129] Herrnstein, R. M., Zhao, J.-H., Bower, G. C., & Goss, W. M. 2004, AJ, 127, 3399

[130] Herbst T. M., Beckwith S. V. W., Shure M., 1993, ApJ, 411, L21

[131] Hilburn G., Liang E., Liu S., Li H., 2010, MNRAS, 401, 1620

[132] Hollywood, J. M., Melia, F., Close, L. M., McCarthy, Jr., D. W., & Dekeyser, T. A. 1995, ApJ, 448, L21

[133] Hornstein S. D., Ghez A. M., Tanner A., Morris M., Becklin E. E., Wizinowich P., 2002, ApJ, 577, L9

[134] Hornstein, S. D., Matthews, K., Ghez, A. M., et al. 2007, ApJ, 667, 900

[135] Huang, L., Cai, M., Shen, Z.-Q., & Yuan, F. 2007, MNRAS, 379, 833

[136] Jauncey, D. L., Tzioumis, A. K., Preston, R. A., et al. 1989, AJ, 98, 44

[137] Karas, V. & Bao, G. 1992, A&A, 257, 531

[138] Karas V. (2006). Astronomische Nachrichten, 10, 327.

[139] Kerr R. P. (1963). Gravitational field of a spinning mass as an example of algebraically special metrics. Phys. Rev. Lett., 11, 237.

[140] Kormendy, J. 2004, in Coevolution of Black Holes and Galaxies, ed. L. C. Ho, 1

[141] Kormendy J. & Richstone D. (1995). Inward bound – the search for supermassive black holes in galactic nuclei. ARA&A, 33, 581.

[142] Knuth, K. H. 2006, arXiv:physics/0605197

[143] Kraus, A., Krichbaum, T. P., Wegner, R., et al. 2003, A&A, 401, 161

[144] Krichbaum, T. P., Alef, W., Witzel, A., et al. 1998, A&A, 329, 873

[145] Krichbaum, T. P., Graham, D. A., Bremer, M., et al. 2006, Journal of Physics Conference Series, 54, 328

[146] Krichbaum, T. P., Graham, D. A., Witzel, A., et al. 1998, A&A, 335, L106

[147] Krichbaum, T. P., Witzel, A., Standke, K. J., et al. 1994, in Compact Extragalactic Radio Sources, ed. J. A. Zensus & K. I. Kellermann, 39

[148] Krichbaum, T. P., Zensus, J. A., Witzel, A., et al. 1993, A&A, 274, L37

[149] Krolik, J. H. & Piran, T. 2011, ApJ, 743, 134

[150] Krolik J. & Hawley J. F. (2002). ApJ, 573, 754.

[151] Kunneriath, D., Eckart, A., Vogel, S., et al. 2008, Journal of Physics Conference Series, 131, 012006

[152] Kunneriath, D., Witzel, G., Eckart, A., et al. 2010, A&A, 517, A46

[153] Laor A. (1991). ApJ, 376, 90.

[154] Laplace P. S. (1796). Le Système du Monde Vol. II. Des Mouvements Réels des Corps Célestes (Paris: Duprat).

[155] Lazio, T. J. W. 2004, ApJ, 613, 1023

[156] Lenzen, R., Hartung, M., Brandner, W., et al. 2003, in Presented at the Society of Photo-Optical Instrumentation Engineers (SPIE) Conference, Vol. 4841, Society of Photo-Optical Instrumentation Engineers (SPIE) Conference Series, ed. M. Iye & A. F. M. Moorwood, 944–952

[157] Lazio, T. J. W. & Fey, A. L. 2001, ApJ, 560, 698

[158] Li, J., Shen, Z.-Q., Miyazaki, A., et al. 2008, Journal of Physics Conference Series, 131, 012007

[159] Liu, S., & Melia, F. 2001, ApJ, 561, L77

[160] Liu, S., Melia, F., & Petrosian, V. 2006, ApJ, 636, 798

[161] Liu, S., Petrosian, V., & Melia, F. 2004, ApJ, 611, L101

[162] Lo, K. Y., Backer, D. C., Ekers, R. D., et al. 1985, **N**, 315, 124

[163] Lo, K. Y., Backer, D. C., Kellermann, K. I., et al. 1993, **N**, 362, 38

[164] Lo, K. Y., Shen, Z.-Q., Zhao, J.-H., & Ho, P. T. P. 1998, ApJ, 508, L61

[165] Lu, R.-S., Krichbaum, T. P., Eckart, A., et al. 2008, Journal of Physics Conference Series, 131, 012059

[166] Luminet J P 1979 *A&A* 75 228–235

[167] Marcaide, J. M., Alberdi, A., Lara, L., Pérez-Torres, M. A., & Diamond, P. J. 1999, A&A, 343, 801

[168] Markoff, S. 2005, ApJ, 618, L103

[169] Markoff, S., et al. 2001, A&A, 379, L13

[170] Marrone, D. P. 2006, PhD thesis, Harvard University

[171] Marrone, D. P., Baganoff, F. K., Morris, M. R., et al. 2008, ApJ, 682, 373

[172] Marrone D. P., Moran J. M., Zhao J.-H., Rao R., 2007, ApJ, 654, L57

[173] Marrone, D. P., Moran, J. M., Zhao, J.-H., & Rao, R. 2006, Journal of Physics Conference Series, 54, 354

[174] Martocchia A., Karas V. & Matt G. (2000). MNRAS, 12, 817.

[175] Marscher, A. P. 1983, ApJ, 264, 296

[176] Marscher, A. P. 2009, arXiv:astro-ph.HE/0909.2576

[177] Matt G., Perola G. C. & Stella L. (1993). Multiple-peaked line profiles from relativistic disks at high inclination angles. A&A, 267, 643.

[178] Mauerhan, J. C., Morris, M., Walter, F., & Baganoff, F. K. 2005, ApJ, 623, L25

[179] McKinney J. C., Tchekhovskoy A., Blandford R. D., 2012, MNRAS, 423, 3083

[180] Melia F., 1992, ApJ, 387, L25

[181] Melia F., 1994, ApJ, 426, 577

[182] Melia F., Falcke H., 2001, ARA&A, 39, 309

[183] Merloni, A., Heinz, S., & di Matteo, T. 2003, MNRAS, 345, 1057

[184] Meyer, L., Do, T., Ghez, A., et al. 2008, ApJ, 688, L17

[185] Meyer, L., Do, T., Ghez, A., et al. 2009, ApJ, 694, L87

[186] Meyer, L., Eckart, A., Schödel, R., et al. 2006, A&A, 460, 15

[187] Meyer, L., Schödel, R., Eckart, A., et al. 2007, A&A, 473, 707

[188] Meyer, L., Schödel, R., Eckart, A., et al. 2006, A&A, 458, L25

[189] Menten K. M., Reid M. J., Eckart A., Genzel R., 1997, ApJ, 475, L111

[190] Michell J. (1784). On the means of discovering the distance, magnitude, etc. of the fixed stars, in consequence of the Diminution of the Velocity of their Light, in case such a Diminution should be found to take place in any of them, and such other Data should be procured from Observations, as would be farther necessary for that Purpose. Philosophical Transactions of the Royal Society of London, 74, 35.

[191] Misner C. W., Thorne K. S. & Wheeler J. A. (1973). Gravitation. W. H. Freedman & Co., San Fransisco.

[192] Miyazaki, A., Tsutsumi, T., Miyoshi, M., Tsuboi, M., & Shen, Z.-Q. 2005, ArXiv Astrophysics e-prints:astro-ph/0512625

[193] Miyazaki, A., Tsuboi, M., and Tsutsumi, T. (2013). Time Lag in the Intra-Day Variability of Sagittarius A* between Light Curves at 90 and 102 GHz. *PASJ*, 65:L6.

[194] Mościbrodzka M., Gammie C. F., Dolence J., Shiokawa H., Leung P. K., 2011, in Morris M. R., Wang Q. D., Yuan F., eds, The Galactic Center: a Window to the Nuclear Environment of Disk Galaxies Vol. 439 of Astronomical Society of the Pacific Conference

Series, Numerical Models of Sgr A*. p. 358

[195] Mościbrodzka M., Gammie C. F., Dolence J. C., Shiokawa H., Leung P. K., 2009, ApJ, 706, 497

[196] Muñoz D. J., Marrone D. P., Moran J. M., Rao R., 2012, ApJ, 745, 115

[197] Muno, M. P., et al. 2004, ApJ, 613, 326

[198] Narayan, R. & Goodman, J. 1989, MNRAS, 238, 963

[199] Narayan R., Mahadevan R., Grindlay J. E., Popham R. G., Gammie C., 1998, ApJ, 492, 554

[200] Narayan R., Yi I., 1994, ApJ, 428, L13

[201] Neilsen, J., et al. 2013, ApJ, 774, 42

[202] Nord, M. E., Lazio, T. J. W., Kassim, N. E., Goss, W. M., & Duric, N. 2004, ApJ, 601, L51

[203] Novikov I. D. & Thorne K. S. (1973). Astrophysics of black holes. In Black holes, page 343. C. de Witt and B. S. de Witt, Gordon & Breach, New York.

[204] Nowak, M. A., et al. 2012, ApJ, 759, 95

[205] Ott, T., Eckart, A., & Genzel, R. 1999, ApJ, 523, 248

[206] Pariev V. I. & Bromley B. C. (1998). ApJ, 508, 590.

[207] Pariev V. I., Bromley B. C. & Miller W. A. (2001). ApJ, 547, 649.

[208] Penrose R. & Floyd G. R. (1971). Nature Physical Science, 229, 177.

[209] Plotkin, R. M., et al. 2012, MNRAS, 419, 267

[210] Porquet D., Grosso N., Predehl P., Hasinger G., Yusef-Zadeh F., Aschenbach B., Trap G., Melia F., Warwick R. S., Goldwurm A., Bélanger G., Tanaka Y., Genzel R., Dodds-Eden K., Sakano M., Ferrando P., 2008, A&A, 488, 549

[211] Porquet D., Predehl P., Aschenbach B., Grosso N., Goldwurm A., Goldoni P., Warwick R. S., Decourchelle A., 2003, A&A, 407, L17

[212] Price R. H. & Thorne K. S. (1986). Phys. Rev. D, 33, 915.

[213] Pringle J. E. & Rees M. J. (1972). A&A, 21, 1.

[214] Priestley, M. B. 1982, Spectral Analysis and Time Series, sixth edn. (Academic Press,

London)

[215] Quataert E., 2002, ApJ, 575, 855

[216] Quataert E., Gruzinov A., 2000a, ApJ, 545, 842

[217] Quataert E., Gruzinov A., 2000b, ApJ, 539, 809

[218] Rafelski, M., Ghez, A. M., Hornstein, S. D., Lu, J. R., & Morris, M. 2007, ApJ, 659, 1241

[219] Rauch K. P. & Blandford R. D. (1994). Optical caustics in a Kerr space-time and the origin of rapid X-ray variability in active galactic nuclei. ApJ, 421, 46.

[220] Reid M. J., 1993, ARA&A, 31, 345

[221] Reid, M. J. 2009, International Journal of Modern Physics D, 18, 889

[222] Reid, M. J., Broderick, A. E., Loeb, A., Honma, M., & Brunthaler, A. 2008, ApJ, 682, 1041

[223] Reid, M. J., Menten, K. M., Zheng, X. W., et al. 2009, ApJ, 700, 137

[224] Fabian C.S. et al. (1989). MNRAS, 238, 729.

[225] Revnivtsev, M. G., Churazov, E. M., Sazonov, S. Y., et al. 2004, A&A, 425, L49

[226] Richstone, D., Ajhar, E. A., Bender, R., et al. 1998, N, 395, A14

[227] Rogers, A. E. E., Doeleman, S., Wright, M. C. H., et al. 1994, ApJ, 434, L59

[228] Roy, S. & Pramesh Rao, A. 2003, Astronomische Nachrichten Supplement, 324, 391

[229] Rybicki G. B., Lightman A. P., 1986, Radiative Processes in Astrophysics

[230] Sabha, N., Witzel, G., Eckart, A., et al. 2010, A&A, 512, A2

[231] Shakura N. I. & Sunyaev R. A. (1973). Black holes in binary systems. Observational appearance. A&A, 24, 337.

[232] Sharp N. A. (1979). General Relativity and Gravitation, 10, 659.

[233] Schödel R., Eckart A., Mužić K., Meyer L., Viehmann T., Bower G. C., 2007, A&A, 462, L1

[234] Schödel R., Morris M. R., Muzic K., Alberdi A., Meyer L., Eckart A., Gezari D. Y., 2011, A&A, 532, A83

[235] Schödel, R., Najarro, F., Muzic, K., & Eckart, A. 2010, A&A, 511, A18

[236] Schödel, R., Ott, T., Genzel, R., et al. 2002, N, 419, 694

[237] Schwarzschild K. (1916). From the observatory. PASP, 28, 269.

[238] Shen, Z.-Q. 2006, Journal of Physics Conference Series, 54, 377

[239] Shen, Z.-Q., Lo, K. Y., Liang, M.-C., Ho, P. T. P., & Zhao, J.-H. 2005, N, 438, 62

[240] Shakura N. I., Sunyaev R. A., 1973, A&A, 24, 337

[241] Shcherbakov R. V., Penna R. F., McKinney J. C., 2010, ArXiv e-prints

[242] Shcherbakov, R. V., & Baganoff, F. K. 2010, ApJ, 716, 504

[243] Serabyn, E., Carlstrom, J., Lay, O., et al. 1997, ApJ, 490, L77

[244] Simonetti, J. H., Cordes, J. M., & Heeschen, D. S. 1985, ApJ, 296, 46

[245] Speith R., Riffert H. & Ruder H. (1995). Computer Physics Communications, 88, 109.

[246] Stark, R. F. & Connors, P. A. 1977, N, 266, 429

[247] Stepney S., Guilbert P. W., 1983, MNRAS, 204, 1269

[248] Stolovy S. R., Hayward T. L., Herter T., 1996, ApJ, 470, L45

[249] Su M., Finkbeiner D. P., 2012, ApJ, 753, 61

[250] Sunyaev, R. & Churazov, E. 1998, MNRAS, 297, 1279

[251] Telesco C. M., Davidson J. A., Werner M. W., 1996, ApJ, 456, 541

[252] Terrier, R., Ponti, G., Bélanger, G., et al. 2010, ApJ, 719, 143

[253] Theiler, J., Eubank, S., Longtin, A., Galdrikian, B., & Doyne Farmer, J. 1992, Physica D Nonlinear Phenomena, 58, 77

[254] Thorne K. S. (1974). Disk-accretion onto a black hole. II. Evolution of the hole. ApJ, 191, 507.

[255] Thorne K. S., Price R. H. & MacDonald D. A. (1986). New Haven: Yale University Press.

[256] Timmer, J. & Koenig, M. 1995, A&A, 300, 707

[257] Tokunaga, A. T. 2000, Infrared Astronomy (Cox, A. N.), 143

[258] Trippe, S., Paumard, T., Ott, T., et al. 2007, MNRAS, 375, 764

[259] Trap, G., et al. 2010, Advances in Space Research, 45, 507

[260] Uttley, P. & McHardy, I. M. 2001, MNRAS, 323, L26

[261] Uttley, P., McHardy, I. M., & Papadakis, I. E. 2002, MNRAS, 332, 231

[262] Uttley, P., McHardy, I. M., & Vaughan, S. 2005, MNRAS, 359, 345

[263] van der Laan, H. 1966, N, 211, 1131

[264] Vaughan, S., Edelson, R., Warwick, R. S., & Uttley, P. 2003, MNRAS, 345, 1271

[265] Viergutz S. U. (1993). A&A, 272, 355.

[266] Wald R. M. (1974). Phys. Rev. D, 10, 1680.

[267] Wald R. M. (1998). Chicago: University of Chicago Press.

[268] Walker M. & Penrose R. (1970). Commun. Math. Phys., 18, 265.

[269] Wang, Q. D., et al. 2013, Science, 341, 981

[270] Wilkinson, P. N., Narayan, R., & Spencer, R. E. 1994, MNRAS, 269, 67

[271] Witzel, G., Eckart, A., Buchholz, R. M., et al. 2011, A&A, 525, A130

[272] Witzel, G., et al. 2012, ApJS, 203, 18

[273] Xu, Y.-D., et al. 2006, ApJ, 640, 319

[274] Young, A. J., et al. 2007, ApJ, 669, 830

[275] Yuan F., Markoff S., Falcke H., 2002, A&A, 383, 854

[276] Yuan F., Quataert E., Narayan R., 2003, ApJ, 598, 301

[277] Yuan, F., Quataert, E., & Narayan, R. 2004, ApJ, 606, 894

[278] Yuan, F. 2011, in Astronomical Society of the Pacific Conference Series, Vol. 439, The Galactic Center: a Window to the Nuclear Environment of Disk Galaxies, ed. M. R. Morris, Q. D. Wang, & F. Yuan, 346

[279] Yuan, F., et al. 2009, MNRAS, 395, 2183

[280] Yuan, F., Yu, Z., & Ho, L. C. 2009, ApJ, 703, 1034

[281] Yusef-Zadeh F., Arendt R., Bushouse H., Cotton W., Haggard D., Pound M. W., Roberts D. A., Royster M., Wardle M., 2012, ArXiv e-prints

[282] Yusef-Zadeh, F., Bushouse, H., Dowell, C. D., et al. 2006, ApJ, 644, 198

[283] Yusef-Zadeh, F., Bushouse, H., Wardle, M., et al. 2009, ApJ, 706, 348

[284] Yusef-Zadeh, F., Cotton, W., Wardle, M., Melia, F., & Roberts, D. A. 1994, ApJ, 434, L63

[285] Yusef-Zadeh, F., Roberts, D., Wardle, M., Heinke, C. O., & Bower, G. C. 2006, ApJ, 650, 189

[286] Yusef-Zadeh, F., Wardle, M., Heinke, C., et al. 2008, ApJ, 682, 361

[287] Yusef-Zadeh, F., Wardle, M., Cotton, W. D., Heinke, C. O., & Roberts, D. A. 2007, ApJ, 668, L47

[288] Zamaninasab, M., Eckart, A., Meyer, L., et al. 2008, Journal of Physics Conference Series, 131, 012008

[289] Zamaninasab, M., Eckart, A., Witzel, G., et al. 2010, A&A, 510, A3

[290] Zeldovich Y. B. & Novikov I. D. (1964). Dokl. Acad. Nauk. SSSR, 58, 811.

[291] Zhao, J.-H., Bower, G. C., & Goss, W. M. 2001, ApJ, 547, L29

[292] Zhao, J.-H., Herrnstein, R. M., Bower, G. C., Goss, W. M., & Liu, S. M. 2004, ApJ, 603, L85

[293] Zhao, J.-H., Young, K. H., Herrnstein, R. M., et al. 2003, ApJ, 586, L29

[294] Zubovas, K., Nayakshin, S., & Markoff, S. 2012, MNRAS, 421, 1315